Gerhard Sommer

Mechanical Properties of Healthy and Diseased Human Arteries

Monographic Series TU Graz

Computation in Engineering and Science

Series Editors

G. Brenn	Institute of Fluid Mechanics and Heat Transfer
G.A. Holzapfel	Institute of Biomechanics
M. Schanz	Institute of Applied Mechanics
O. Steinbach	Institute of Computational Mathematics

Monographic Series TU Graz

Computation in Engineering and Science   Volume 7

Gerhard Sommer

_____

Mechanical Properties of Healthy and Diseased Human Arteries

Insights into Human Arterial Biomechanics and Related Material Modeling
_____

Abstract

Major causes of atherosclerosis are biochemical and biomechanical changes in the wall of a blood vessel with a subsequent narrowing of its lumen. Untreated this disease can cause ischemic stroke or heart attack. An increase in lumen can be achieved by applying, for example, balloon angioplasty and stenting, which represents a mechanical solution for a clinical problem. These procedures can fail due to restenosis. The processes behind this failure are partly unclear.

Therefore, this thesis focussed on the determination of the mechanical properties of healthy and diseased human arteries and their underlying layers and tissue components. The layer-specific mechanical behavior of healthy coronary arteries, of tissue components in highly stenotic iliac arteries, and the dissection properties of human abdominal aortic media were determined by means of uniaxial *in vitro* tensile tests. Furthermore, by means of *in vitro* extension-inflation tests the biaxial mechanical properties of carotid arteries, and their adventitia and media-intima tubes were determined. These experimental data were fitted to a novel constitutive model appropriate for finite element implementation and able to describe the typical mechanical features of soft biological tissues.

Zusammenfassung

Die Hauptursachen für Atherosklerose sind biochemische und biomechanische Veränderungen in der Arterienwand mit der Folge einer Verkleinerung des Lumens. Unbehandelt kann diese Krankheit zu einem ischämischen Schlaganfall oder zu einem Herzinfarkt führen. Eine Lumenvergrößerung kann z.B. durch Anwendung der Ballon Angioplastie mit Stenting, welches eine mechanische Lösung für ein klinisches Problem darstellt, erreicht werden. Diese Methode kann durch eine Wiederverengung des Lumens versagen (Restenose). Die damit verbundenen Mechanismen sind zum Teil unklar.

Diese Dissertationsarbeit konzentrierte sich deshalb auf die Bestimmung des mechanischen Verhaltens gesunder und kranker menschlicher Arterien und deren Schichten und Gewebskomponenten. Mittels uniaxialer *in vitro* Zugversuche wurden das schichten-spezifische mechanische Verhalten gesunder Koronararterien,

von Plaquekomponenten von hoch-stenotischen Beckenarterien, und die Dissektionseigenschaften von menschlichen Bauchaorten bestimmt. Weiters wurden mittels *in vitro* Inflationsversuchen das biaxiale mechanische Verhalten von gesunden Karotisarterien und deren Adventitia- und Media-Intima-Röhren ermittelt. Diese experimentellen Daten wurden einem für finite Elemente kompatiblen neuen konstitutiven Modell angepasst. Dieses Modell ist in der Lage die mechanischen Charakteristika von weichen biologischen Geweben wiederzugeben.

CONTENTS

1 INTRODUCTION AND MOTIVATION

1.1 Cardiovascular Disease

The generic name given in the literature for any abnormal function of the cardiovascular system is *cardiovascular disease* (CVD). CVD is established to be the leading cause of death in the developed countries, accounting for 49% of all death in Europe (by sex, 43% women and 55% of men) [1] and 38% in the US. This number increases to 60% if total mortality, where CVD was either primary or a contributing cause of death, is accounted. CVD is strongly related to age, with a large proportion of fatal events occurring at 65 years of age or later [2].

CVD is also a heavy economic burden for both public and private institutions. The total estimated cost of CVD health care in the European Union was 105 billion Euros, with another 65 billion Euros in indirect costs like productivity loss. In the US, the direct and indirect costs associated with CVD have been estimated to be 449 billion USD for 2008 [2].

A sizable part of the direct costs above can be attributed to the drugs/medicaments needed by the patients. Indeed, the first line of defence against the CVD is prevention, which involves medication of risk groups. Sometimes, these strategies are not effective, or the disease has already advanced too much to be handled with medication before being diagnosed. The preferred alternative is to perform *angioplasty*, a minimum-invasive procedure where a balloon-tipped catheter is guided in the narrowing (called *stenosis*) and expanded, widening the vessel lumen and restoring blood flow to the affected organ. When the expansion was performed with the catheter alone, often requiring more than one inflation in order to have enough permanent deformation and to ensure success of the intervention. With this technique alone there appears complications, e.g., the vessel closes again after a few days or weeks.

In order to overcome this, Dr. Palmaz introduced an expandable tube made of a metal mesh [3–7], that remains inside the vessel after expansion and prevented its closure. This devise is called *stent*. The mid-term complications that appeared with the first stent designs, such as *in-stent restenosis* (tissue growth inside the stent, narrowing its section), have been partially overcome with improved models, where details such as fabrication technique and strut shape and placement are taken into account along with parameters like overall flexibility or target vessel size. The results are stents with lower restenosis rates, although this still remains a weak point of these devices.

More recently a further improvement had come with the *Drug Eluting Stents* (DES), which promise to lower restenosis rates even more while long-term patency of these devices. Essentially, DES are normal stents with a special coating, which releases drugs that regulate the metabolic activity of the surrounding vascular tissue, preventing adverse reactions [8].

Stents have the great advantage of being easy and fast to deploy, as they do not require the patient to stay in hospital. This also lowers the cost and risk of the intervention. For these reasons, it is not surprising that percutaneous techniques are established as the first choice in interventional cardiology.

In spite of these advances, there are cases where the only alternative to treat a lesion is to perform surgery. Usually the reasons are that disease has advanced so much that the catheter cannot placed reliably, that the patient has multivessel disease (more than two arteries obstructed is eligible for surgery), that the lesion is at a difficult location or that a previously implanted stent has failed, for example, due to restenosis.

Moreover, there are two ways to restore blood flow to the affected organ. The first one is to remove the diseased segment and join the remaining ends, stretching the native vessel. This procedure is used for certain cases of aneurysm in large arteries. For occlusive lesions, which occur more often in narrow vessels, the choice in this case is to replace this segment with a *graft*, i.e. an alternative conduit.

The second way is to provide an alternative path for the blood to circulate, performing a bypass without removing the diseased segment. This method is preferred in coronary surgery, where replacement of the diseased segment would involve risk of trauma for the heart.
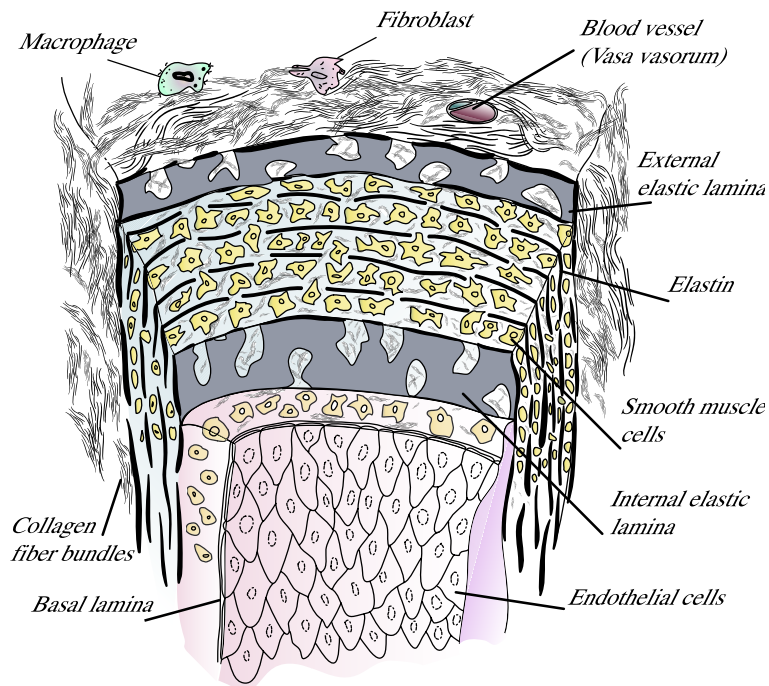
Figure 1.1: Schematic representation of an elastic artery. Adapted from Rhodin [9].

The onset and progression of cardiovascular disease have been linked, among other, to hemodynamics. However, there is evidence that physiological activity is dependent on variables such as stress and strain within the tissue. Additionally, the procedures outlined above affect the vessels mechanically, so it is essential to understand the mechanical behavior of the vessel wall in order to improve the outcome of these treatments.

1.2 The Healthy Arterial Wall

All blood vessels share some common characteristics, for example, they consist of three distinct layers or *tunicae*: The *tunica intima, tunica media* and *tunica adventitia*.

In young human arteries the intima is a thin endothelial layer that lines the inside walls, and sits on a very thin (~80 nm) basal lamina of a net-like type IV

collagen. In general, the endothelial cells tend to be elongated in the direction of the blood flow. They act as a semipermeable membrane, through which nutrients and chemical signals can reach the cells in the vessel wall from the bloodstream. The intima has also a key role in regulating the active response of the vessel: as a membrane, it is the conduit through which pressure regulating agents reach the media. Additionally, it is known that the intima produces NO (nitric oxide), which relaxes smooth muscle cells in the media and thus helps control the *vascular tone*. Despite its great functional importance, due to its small thickness in young arteries the intima is usually neglected when considering the different layer contributions to the global mechanical resistance of the vessel wall. The intima is separated from the media by the *internal elastica lamina*, a fenestrated sheet of elastin.

The media is formed primarily by smooth muscle cells (SMC) that are embedded in an extracellular plexus of elastin and collagen (mainly types I and III) and an aqueous ground substance that also contains proteoglycans. Depending on the internal arrangement of the smooth muscle cells in the media, it is distinguished between *elastic arteries* and *muscular arteries*. The former tend to be large-diameter vessels close to the heart, and include the aorta, the main pulmonary artery, the common carotid and common iliac arteries. Their most characteristic histological feature is the so-called *lamellar unit*, a sandwich-like 'sublayer' of smooth muscle cells and thin elastic laminae. Histological sections of elastic arteries show concentric ring-like structures (see Fig. 1.1), as many as 40 to 70 in thick vessels like in the human aorta, that are tied together by radially oriented collagen. In muscular arteries, the media appears as a single thick ring of smooth muscle cells. The SMC are embedded in a loose connective tissue matrix and arranged as a sequence of concentric layers of cells, which can reach numbers of 25-40 in larger vessels like in the femoral artery.
Sometimes it is difficult to identify clearly between elastic and muscular arteries, due to the fact that abrupt changes do not occur in continuous structures like the vasculature. These transitions occur smoothly and the corresponding artery segments loose their characteristical lamellar structure progressively, as happens in the internal and external carotid arteries.

Finally, the adventitia is the outermost layer of the vessel wall. It consists of a dense network of type I collagen fibers with scattered fibroblasts, elastin and nerves. In

medium and large arteries there is also the *vasa vasorum*, an intramural network of arterioles, capillaries and venules that supply large vessels where the distance from the main bloodstream to the outer sections of the wall does not allow for proper interchange of O_2, CO_2, nutrients and metabolites. The presence of nerves in the adventitia allows innervation of smooth muscle in the outer media, via the diffusion of neurotransmitters. As for the fibroblasts, they are responsible for collagen production, particulary type I, and thus regulate the connective tissue.

Although the outer limits of the adventitia are difficult to identify, due to its fibrous nature, it is definitely thinner in elastic arteries than in muscular arteries, where it is approximately as thick as the media [9]. One notable exception are cerebral arteries, which are muscular in character but often completely lack an adventitia. They are in direct contact with the cerebrospinal fluid, which might explain this feature.

The fibers of the adventitia generally appear undulated at physiological pressures, arranged in groups or bundles that form the aforementioned network. At higher pressures, the fibers gradually straighten, confirming the hypothesis that the adventitia serves as a protective sheath, preventing rupture of the vessel due to acute increase in pressure.

1.3 Atherosclerosis

Atherosclerosis is a local inflammatory disease of the arteries that primarily alters the conduit function by reducing the lumen, sometimes completely blocking blood flow. Atherosclerosis appears preferably at junctions and branches of conduit arteries (like coronary arteries and carotid bifurcation), always at sites of altered flow patterns.

The natural history of atherosclerosis starts with the formation of fatty streaks by a specific trapping and retention of lipoproteins at lesion prone sites, due to an imbalance between the LDL (low density lipoprotein) concentration in the tissue with respect to the plasma. When this happens, the lipids are trapped in the extracellular matrix, in the basal zone of the intima. If this trapping is pathologic, there is an increase of leukocytes that adhere to the endothelial surface, supported
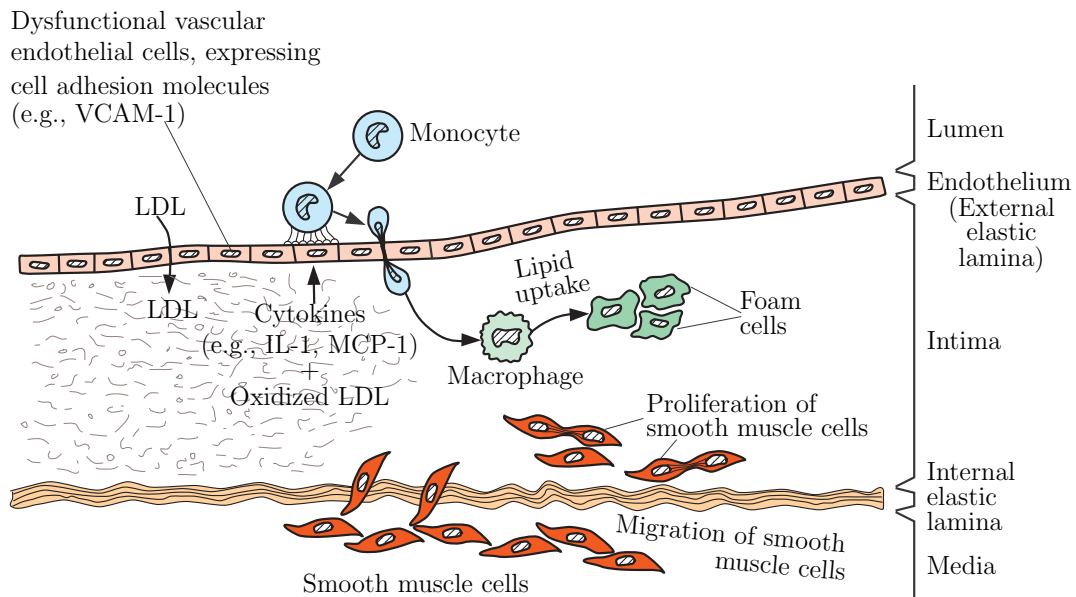
Figure 1.2: Progression of atherosclerotic disease. From the initial state, where LDL migrate through the endothelium in the intima (left side) to the beginning of intima thickening (right side). Illustration adapted from [10].

by the expression of specific adhesion molecules. This is seen as the start of the inflammatory response. As a result, monocytes enter the artery wall and rapidly differentiate into tissue macrophages, subsequently transforming into foam cells by ingesting trapped and modified lipoproteins. Many of the foam cells within the lesion become activated to express a large number of additional factors that likely play important roles in the atherogenic process, from inducing anomalous behavior of healthy cells to providing a favorable biochemical environment for disease progression (see Fig 1.2).

A more advanced lesion is hallmarked by the formation of a *fibrous cap* [11, 12]. In this process, smooth muscle cells migrate from the media to the intima and change phenotype, switching from being contractile to a cell type which proliferates and produces large amounts of connective tissues [13]. The fibrous cap acts as a protective shield for the underlying lipid pool, which has a necrotic core with interspersed microscopic calcium nodules. At this stage, there is a significant dysregulation of the vascular tone, likely due to a reduction in NO availability to

the now atrophic media.

In the final stage, the atheromatous plaque described above may either become stable, in which case it only impairs blood flow, or unstable, where it is at risk of rupturing and developing its highly thrombogenic contents into the blood stream. It has been established that it is the plaque composition, rather than its size, that determines its instability [14, 15].

From this short description, it is obvious that the structure and the mechanics of the wall changes dramatically in the event of atherosclerosis.

1.4 Arterial Mechanics

The mechanical behavior of blood vessels has been a subject of research for over 100 years, with the first reports of Marey [16] and Roy [17] dating back to the late 19th century.

1.4.1 Residual Stresses

A salient characteristic of the vascular mechanical behavior is the existence of *residual stresses* in an otherwise unloaded vessel. If an arterial ring is cut radially it springs open and an axial strip excised from the artery bends away from its vessel axis. These observations expose the existence of residual stresses in the wall, both in axial and circumferential direction.

It was Bergel in 1960 [18], who first reported about residual stresses in arteries and it was the independent work of Fung and Vaishnav, however, that definitely drew attention to this matter. The authors presented their work at two different conferences in 1983 [19, 20]. Shortly after, Chuong and Fung [21], and Takamizawa and Hayashi [22] quantitatively showed the consequences of residual stresses in the arteries and in soft tissues in general.

The fact that the vascular ring opens when cut radially implies that the luminal part is under compression, while the external part is under tension. *In vivo*, however, the internal pressure equilibrates these stresses, and the whole wall supports a more uniform level of stress throughout the radius [21–23]. In this line of thought,

Skalak suggested that these stresses may be a result of growth [24], and that they may be needed for 'compatible growth' [25]. This idea about the origin of residual stresses is widely accepted, and for this reason the term stress is preferred over strain: residual stresses are a result of growth and remodeling, not of physical deformations.

By selectively digesting components of the arterial wall, it has been demonstrated that elastin is largely responsible for the residual stress [26]. These effects are manifested externally, in that the internal elastic lamina is wavier in histological samples of the load-free state than those of the stress-free configuration or under *in vivo* conditions [27].

The existence of residual stresses immediately suggests the question about a *stress-free* configuration and its measure. Chuong and Fung [21] suggest the opening angle of the vascular sample as the only measure to quantify the residual circumferential deformation of the vessel. This is a popular measure due to its simplicity, and is routinely found in the literature. Besides, it has been shown that a single cut releases most of the residual stresses, and that the opening angle is relatively insensitive to the exact location [28–31]. Contrasting these findings, it has been shown that the opening angle is different for each layer [32–34], and even between the inner and outer parts of the media [35]. Matsumoto et al. [36] have found that even in this macroscopic stress-free configuration, the lamellar unit in the aorta is subject to residual stresses at microscopic level. All these results are mutually compatible if the stress-free configuration is considered as a boundary value problem: if the boundary conditions change (for example, the vessel layers are separated), the equilibrium configuration will change accordingly.

1.4.2 Anisotropy

Another fundamental characteristic of the vascular tissue is its marked anisotropy, indicated by different behavior in the circumferential and axial directions. Patel and Fry [37] were the first to treat the tissue symmetry, concluding that the global response was cylindrically orthotropic. Experiments on dog carotids indicate that they are stiffer in the circumferential direction than in the axial direction, which is consistent with Chuong and Fung's experiment in rabbits [21], but conflict with

von Maltzahn's, who performed the same test in cows [38].

In spite of these discrepancies, most researches agree that the mechanical response of arterial tissue is anisotropic with respect to the load-free configuration, based on the comparison of the material parameters associated to circumferential and axial directions [22, 38–40].

1.4.3 Incompressibility, Viscoelasticity and Pseudoelasticity

The high water content of the vascular wall (70-80%) justifies the usual assumption that it is incompressible. Although this is not strictly true, as there may be certain (small) movements of fluids within the tissue induced by stress gradients, vascular samples undergo isochoric deformations under a large variety of loads, notable the physiological state. Experimental observations support this statement: Lawton [41] and Dobrin and Rovick [42] measured isovolumetric deformations under different loads, concluding that incompressibility is maintained at least globally. Such conclusions were also reached by Carew et al. [43], who performed a detailed study of the compressibility of dog aortic tissue under a wide range of deformations.

Regarding atherosclerotic arteries, this assumption has to be revisited. Indeed, as discussed above, the lesions have a composition that is very different from healthy tissues. They may have a high lipid content which is compressible. On the other hand, we are not aware of similar studies on atherosclerotic arteries to those cited above.

Nearly all soft tissues present a certain degree of viscoelastic response, which is revealed by the stress relaxation they suffer when subject to sustained deformations and by the hysteresis they display under cyclic loads. This may be attributed in part to fluid transport within the solid matrix, and to the friction between its fluids and solid constituents. After being *preconditioned*, the tissue displays highly repetitive behavior, so that it can be considered *pseudoelastic*, that is elastic but behaving differently in loading and unloading [23].

1.4.4 Mechanical Behavior

A sizable part of knowledge we have of the general mechanical behavior of arterial tissues comes from the experiments of Cox [44–54] and Dobrin [42, 55–60] in the 70's and 80's. These pioneering works have influenced subsequent experiments in the 80's and 90's by many other researchers.

Like most soft tissues, arteries display a highly nonlinear behavior, progressively stiffening with increasing applied loads. In addition, blood vessels show increased circumferential stiffening with increasing axial stretch, though the axial force-length behavior is less sensitive. Interestingly, the axial force needed to keep the vessel stretched to a constant length at physiological pressures is nearly zero when this is the *in vivo* length [61, 62]. This implies that the artery does no axial work *in vivo*, which is energetically advantageous and reinforces the principle of optimal operation.

The heterogeneity of arterial walls is also taken into account in the literature by considering distinct layers, in other words the individual layers are considered to be homogeneous. This is justified by the regularity of the composition within each layer [63, 64], and has been later confirmed by mechanical tests [35].
The first study that tried to quantify the nonlinear mechanics of the arterial wall by considering its layered structure was carried out by von Maltzahn and coworkers [65]. In a later experiment [38], they performed multiaxial tests (pressure-diameter, for different axial stretches, whose values were kept constant) in bovine carotids, both intact and free from the adventitia. Their conclusions were that both layers are anisotropic, with a stiffer media that support higher stresses than previously thought. Both layers were stiffer in the axial direction.

Vito and Demiray [66] were the first to publish mechanical data on the mechanical response of the individual layers. They performed uniaxial experiments in the circumferential and axial directions of the adventitia and media-intima composite of the canine aorta. Their results seemed to indicate that the adventitia was stiffer than the media, though both were practically isotropic. Later, however, the same authors suggested that the media was cylindrically orthotropic [67], following Patel and Fry [37].

These and other studies confirm the intuition, acquired from the histological description of the wall, that the media and adventitia behave differently. The stress-strain characteristic of both layers, however, is very similar in high loads, well outside the physiological range; for lower loads, however, the media is stiffer. The possible cause for this behavior is that, structurally, the only relevant component in the adventitia is the fibrillar collagen, which is wavy, and can, therefore, be considered to be unloaded. When the stretch augments, the collagen fibers are stretches and the stiffness of tissue grows very rapidly. In the media, on the other hand, the SMC contribute to the load-bearing capacity of the vessel together with the elastin and collagen, so that the stiffening happens more steadily. The parallel stress-strain curves of both layers for very high load may indicate that the fibrillar collagen present in both tissues is responsible for the stiffness in this range.

Layer-specific data on the behavior of human vessels is nevertheless scarce due to the complexity of the layer separation and the difficulty in obtaining samples, mainly derived from ethical concerns. Recent data on a variety of vessels have been published by the group of Holzapfel [34, 68–80], and are probably the most comprehensive studies to date. From the results it is apparent that aged arteries experience a more sudden stiffening in both layers than young ones. For the media, this may be related to fatigue induced fracture of elastic laminae; for the adventitia, it might be a consequence of increased cross-linking among collagen fibers, derived from remodeling process.

1.5 Organization of the Thesis

The thesis is a compilation of eight scientific papers, dealing with the determination of the mechanical behavior and the constitutive modeling of human arteries in health and disease.

1. The study *'Anisotropic Mechanical Properties of Human Atherosclerotic Plaques'* quantifies the mechanical properties of the different tissue components in atherosclerotic plaques of human iliac arteries and discusses their differences. For this purpose uniaxial tensile tests of strip samples in two di-

rections (circumferential and axial) were performed. Associated anamnesis were reported and ultimate tensile stress and associated stretches investigated. Novel direction-dependent stress-strain data and fracture stress and stretch of all plaque types and healthy surrounding tissues were described. The data shows the need for anisotropic models and may help to perform computational analyses of plaques within mechanical interventional therapies such as balloon angioplasty with higher accuracy.

G.A. Holzapfel, G. Sommer and P. Regitnig, *Anisotropic mechanical properties of tissue components in human atherosclerotic plaques*, ASME Journal of Biomechanical Engineering, 126 (2004), 657–665.

2. The study *'Layer-specific Mechanical Properties of Human Coronary Arteries'* explores the underlying mechanics of the adventitia, media, and intima of human coronary arteries with non-atherosclerotic intimal thickening. A recently proposed constitutive model was used to represent the deformation behavior for each tissue type over the entire loading range. The study showed the need to model non-stenotic human coronary arteries with non-atherosclerotic intimal thickening as a composite structure composed of three solid mechanically relevant layers with different mechanical properties. The intima showed significant thickness, load-bearing capacity, and mechanical strength when compared with the media and the adventitia.

G.A. Holzapfel, G. Sommer, C.T. Gasser and P. Regitnig, *Determination of the layer-specific mechanical properties of human coronary arteries with nonatherosclerotic intimal thickening, and related constitutive modeling*, American Journal Physiology – Heart Circulation Physiology, 289 (2005), H2048–2058.

3. The study 'In situ *Tensile Testing of Human Aortas by Small-Angle X-ray Scattering'* studies the macro- and nanoscopic mechanical tensile behaviors of human aortas using a newly designed tensile testing device and synchrotron radiation. The collagen diffraction patterns of human aortas under uniaxial tensile test conditions were investigated by synchrotron small angle X-ray scattering. Using a recently designed tensile testing device the orientation and d-spacing of the collagen fibers in the adventitial layer were measured

in situ with the macroscopic force and sample stretching under physiological conditions. The results showed a relation between the orientation and extension of the collagen fibers on the nanoscopic level and the macroscopic stress and strain. This may be attributed first to a straightening, second to a reorientation of the collagen fibers, and finally to an up-take of the increasing loads by the collagen fibers.

F. Schmid, G. Sommer, M. Rappolt, C.A.J. Schulze-Bauer, P. Regitnig, G.A. Holzapfel, P. Laggner and H. Amenitsch, *In situ tensile testing of human aortas by time-resolved small angle X-ray scattering*, Journal of Synchrotron Radiation, 12 (2005), 727–733.

4. The study *'Bidirectional Tensile Testing Cell for Small Angle X-ray Scattering'* illustrates the development of a tensile testing device, where the center of the sample was fixed with respect to the X-ray at all times. Two linear μ-translation stages were used to symmetrically — i.e. bidirectionally — stretch the sample. A video-extensometer was installed to record geometrical changes of the sample during the measurements which allowed to determine (true) stresses and strains. The sample could be immersed in a liquid and heated. We demonstrated the advantages over common unidirectional tensile testing devices without length measurement systems by comparing different mechanical and diffraction data sets of human arterial tissue.

F. Schmid, G. Sommer, M. Rappolt, P. Regitnig, G.A. Holzapfel, P. Laggner and H. Amenitsch, *Bidirectional tensile testing cell for in situ small angle X-ray scattering investigations of soft tissue*, Nuclear Instruments and Methods in Physics Research Section B: Beam Interactions with Materials and Atoms, B 246 (2006), 262–268.

5. The study *'Layer-Specific 3D Residual Deformations of Human Aortas with Non-Atherosclerotic Intimal Thickening'* describes the investigation of three-dimensional residual deformations for intact strips and for their separate layers from human aortas. For the study, 16 pairs of rings and axial strips were harvested. The images of the resulting geometries were recorded in different

time-steps and the strips were separated into their three layers. Image processing and analysis was then used to quantify residual stretches and curvatures. The study showed that residual deformations were three-dimensional and cannot be described by a single parameter such as 'the' opening angle.

G.A. Holzapfel, G. Sommer, M. Auer, P. Regitnig and R.W. Ogden, *Layer-specific 3D residual deformations of human aortas with non-atherosclerotic intimal thickening*, Annals of Biomedical Engineering, 35 (2007), 530–545.

6. The study *'Dissection Properties of the Human Aortic Media: an Experimental Study'* presents the investigation of dissection properties of the human abdominal aortic media by means of direct tension and peeling tests. The direct tension test demonstrated the dissection strength of the media in the radial direction, while the peeling test explored the fracture energy required to propagate a dissection. The study was performed by histological investigations at different stages of the peeling test in order to explore the development of irreversible changes on the microscale during medical dissection. The study showed, that the dissection properties of the human aortic media were anisotropic within the dissection plane.

G. Sommer, T.C. Gasser, P. Regitnig, M. Auer and G. A. Holzapfel, *Dissection properties of the human aortic media: an experimental study*, ASME Journal of Biomechanical Engineering, 130 (2008), 021007-1–021007-12.

7. The study *'Biaxial Mechanical Properties of Human Carotid Arteries'* presents the passive biaxial mechanical behavior of human common arteries, internal carotid arteries, and related adventitial and media-intima composite layers. Cyclic, quasi-static extension-inflation tests at different axial stretches were performed on pre-conditioned tube specimens. Moreover, stress-free configurations of the intact wall, the adventitia and the media-intima composite were determined. The obtained comprehensive data are intended to serve for improving constitutive laws, determination of constitutive parameters, and enhancing our knowledge of the mechanical functions of arteries and their associated layers in specific physiological and clinical problems such as hypertension and balloon angioplasty and stenting.

G. Sommer, P. Regitnig, L. Költringer and G.A. Holzapfel, *Biaxial mechanical properties of intact and layer-dissected human carotid arteries at physiological and supra-physiological loadings*, American Journal Physiology – Heart Circulation Physiology, submitted.

8. The study *'3D Modeling of the Mechanical Response of Human Carotid Arteries'* shows the fitting of the experimental data from a series of biaxial tests (axial extension and inflation) on the intact carotid artery (common and internal) walls, and subsequently, their corresponding layer-dissected intact adventitia and media-intima composite tubes to an established novel, three-dimensional, and structure-based strain-energy function. The zero stress states of the investigated tubes were considered by the kinematic formulation in the fitting process. Therefore, the obtained constitutive (material) parameters included the zero stress state and the mechanical behavior of the utilized tissues. The 3D constitutive model will serve as a foundation for the formulation of layer-specific boundary value problems in human carotid physiology and pathology.

G. Sommer and G.A. Holzapfel, *Three-dimensional constitutive modeling of the biaxial mechanical properties of intact and layer-dissected human carotid arteries considering residual stretches*, ASME Journal of Biomechanical Engineering, submitted.

In addition, the following 11 conference contributions, in form of abstracts, are also a result of the thesis:

G. Sommer, P. Regitnig, L. Költringer and G.A. Holzapfel, *Biaxial mechanical properties of intact and layer-dissected human carotid arteries at physiological and supra-physiological loadings*, 8th World Congress on Computational Mechanics (WCCM8), 5th European Congress on Computational Methods in Applied Sciences and Engineering (ECCOMAS 2008), Venice, Italy, June 30–July 5, 2008.

D. Balzani, S. Brinkhues, G. Sommer and G.A. Holzapfel, *Modeling of damage hysteresis in overstretched soft biological tissues*, 8th World Congress on Computa-

tional Mechanics (WCCM8), 5th European Congress on Computational Methods in Applied Sciences and Engineering (ECCOMAS 2008), Venice, Italy, June 30–July 5, 2008.

G.A. Holzapfel, G. Sommer and T.C. Gasser, *Modeling of arterial dissection*, IX International Conference on Computational Plasticity (COMPLAS IX), within the Invited Session on 'Computational Methods in Biomechanics and Mechanobiology', Barcelona, Spain, September 5–7, 2007.

G.A. Holzapfel, G. Sommer, T.C. Gasser and P. Regitnig, *Patient-specific biomechanical analysis of plaque rupture during balloon angioplasty using MRI and mechanical testing*, 11th International Conference on 'Human Biomechanics 2006', Hrotovice, Czech Republic, November 13–16, 2006.

G.A. Holzapfel, C.T. Gasser and G. Sommer, *Rupture analysis for human atherosclerotic plaques*, 19th Nordic Seminar on Computational Mechanics hosted by Lund University, Faculty of Engineering, Lund, Sweden, October 20–21, 2006.

G.A. Holzapfel, C.T. Gasser, G. Sommer and R.W. Ogden, *Constitutive modeling of soft biological tissue: applications to arterial walls*, 6th European Solid Mechanics Conference, Budapest, Hungary, August 28–September 1, 2006.

G. Sommer, P. Regitnig and G.A. Holzapfel, *Biomechanics of human carotid arteries: experimental testing and material modeling* (within the Mini-Symposium: Vascular wall mechanics). 5th World Congress of Biomechanics, Munich, Germany, July 29–August 4, 2006.

T.C. Gasser, M. Landuyt, G. Sommer, M. Auer, P. Verdonck, J. Swedenborg and G.A. Holzapfel, *A histologically based anisotropic model of the abdominal aortic aneurysm* (within the Mini-Symposium: Computational biomechanics of arteries in health and disease). 5th World Congress of Biomechanics, Munich, Germany, July 29–August 4, 2006.

G.A. Holzapfel, T.C. Gasser, G. Sommer and P. Regitnig *Computational analyses of dissection-type of failure of atherosclerotic arteries following balloon angioplasty*, 14th European Society of Biomechanics (ESB) conference, Mini-Symposium on 'Intravascular devices', 's-Hertogenbosch, The Netherlands, July 4–7, 2004.

G.A. Holzapfel, M. Auer, F. Cacho, G. Franceschini, C.T. Gasser, D. Kiousis, G. Sommer and M. Stadler, *Was kann die Ingenieurwissenschaft zur Verbesserung von therapeutischen Eingriffen an atherosklerotischen Blutgefäßen beitragen?* Workshop: Zukunft durch Forschung - Forschung heißt Zukunft gestalten, Forum Technik und Gesellschaft an der Technischen Universität Graz, November 28, 2003.

C.A.J. Schulze-Bauer, G. Sommer, M. Rappolt, H. Amenitsch, P. Laggner and G.A. Holzapfel, *Layer and age specific tensile testing of human aortas: A small angle X-ray scattering study,* 2nd International Conference on Materials for Advanced Technologies (ICMAT) & IUMRS-ICA 2003, Symposium J - Synchrotron Radiation for Advanced Materials Analysis and Processing, Suntec Singapore International Convention & Exhibition Centre, Singapore, 29 June–4 July, 2003.

2 ANISOTROPIC MECHANICAL PROPERTIES OF HUMAN ATHEROSCLEROTIC PLAQUES

Abstract. Knowledge of the biomechanical properties of human atherosclerotic plaques is of essential importance for developing more insights in the pathophysiology of the cardiovascular system and for better predicting the outcome of interventional treatments such as balloon angioplasty. Available data are mainly based on uniaxial tests, and most of the studies investigate the mechanical response of fibrous plaque caps only. However, stress distributions during, for example, balloon angioplasty are strongly influenced by all components of atherosclerotic lesions. A total number of 107 samples from nine human high-grade stenotic iliac arteries were tested; associated anamnesis of donors reported. Magnetic resonance imaging was employed to test the usability of the harvested arteries. Histological analyses has served to characterize the different tissue types. Prepared strips of 7 different tissue types underwent cyclic quasi-static uniaxial tension tests in axial and circumferential directions; ultimate tensile stresses and stretches were documented. Experimental data of individual samples indicated anisotropic and highly nonlinear tissue properties as well as considerable interspecimen differences. The calcification showed, however, a linear property, with about the same stiffness as observed for the adventitia in high stress regions. The stress and stretch values at calcification fracture are smaller ($179.0 \pm 56\,$kPa and 1.02 ± 0.005) than for each of the other tissue components. Of all intimal tissues investigated, the lowest fracture stress occurred in the circumferential direction of the fibrous cap ($254.8 \pm 79.8\,$kPa at stretch 1.182 ± 0.1). The adventitia demonstrated the highest and the non-diseased media the lowest mechanical strength on average.

2.1 Introduction

Atherosclerosis is a vascular disease associated with the accumulation of lipids leading to invasion of leucocytes and smooth muscle cells into the intima, a process which may proceed in the formation of atheroma. Biomechanical and biochemical mechanisms are then involved in the development of a lesion known as an atherosclerotic plaque, which is composed primarily of fibrous tissue of varying density and cellularity. In addition, calcium, extracellular lipid, and lipid-laden foam cells are present, each constituting 5 to 10% of the remaining area. Advanced atherosclerosis may lead to lesions which can reduce or block the flow of the oxygen-containing blood leading to oxygen deficiency in the tissues. Clinical emergencies such as myocardial infarction and stroke can result from plaque rupture and subsequent release of highly thrombogenic material and lipids into the blood stream. It is important to point out that the danger of suffering a myocardial infarction or a stroke is particularly high in cases of unstable or vulnerable plaques, which are thought to have a thin fibrous cap, a large lipid core, and significant inflammatory cell infiltration (see, for example, [81–83]). Atherosclerotic cardiovascular disease remains the leading cause of death and disability in North America [84]. In all European countries cardiovascular disease is the main cause of death in women and the main cause of death in men except in France [85].

A frequently used and well-established therapeutical intervention for reducing the severity of atherosclerotic plaques is balloon angioplasty with or without stenting (see [86] and references therein). It represents a mechanical solution for a clinical problem in which, for example, disease-free (medial) tissue is overstretched (damaged), plaques are disrupted or dissected, and redistribution inside the wall and lipid extrusion occur. These mechanisms alter the mechanical environment such that a cascade of biological responses occur, which may cause restenosis or thrombosis. Besides the knowledge of the composition and the geometry of the plaque, applied loads and parameters of balloon catheters and stents, it is the detailed information on the biomechanical behaviors of atherosclerotic plaques and non-diseased cardiovascular tissues that is crucial for a complete mechanical description of this interventional procedure. Understanding of the mechanical behavior of plaques under various loading conditions is an essential contributor

for developing more insight in the physiology and pathophysiology of the cardiovascular system and new procedures for preventing or reducing restenosis, and for better predicting the outcome of interventional treatments on a plaque- or patient-specific basis.

To motivate further the need to understand the constitutive behavior of atherosclerotic plaque, consider the following recent statement by Richardson [87]: *'There are relatively few data on the mechanical properties of arterial tissues, especially for the separate layers of a vessel wall, and the materials-testing protocols have varied between the measurements that have been published. This is probably the most uncertain aspect in the whole body of study of plaque fracture.'*

We summarize now the work performed on mechanical plaque testing and data available in the literature (see also the surveys [88, 89]). The first uniaxial tensile tests on ulcerated and non-ulcerated thoracic plaque caps and adjacent intima from human aortae seem to have been performed by Lendon et al. [90]. Results showed marked differences between plaques and heterogeneity within individual plaque caps. Fracture stresses ranged from 12 to 1938 kPa. Uniaxial tension tests on axial strips of aortic plaques were also performed by Born and Richardson [91], although little detail was provided of the results. Lendon et al. [92] compared aortic plaque caps, which had undergone rupture (ulceration), with caps of intact plaques. Caps of ruptured aortic plaques showed a significant increase in macrophage density, an increase in extensibility and a decrease in the ultimate stress when compared with caps from intact plaques. Lee et al. [93, 94] performed dynamic and static uniaxial compression tests on aortic plaque caps, which were classified as cellular, hypocellular and calcified. All caps demonstrated an increase in stiffness with increasing frequencies of stress ranging from 0.05 to 10 Hz. Values of plaque 'moduli' are presented as a function of the plaque type. McCord [95] performed cyclic bending tests on fresh human arterial ring segments that allowed the passive collapse of an artery, which may occur downstream of a stenosis. The author's studies indicate that cyclic bending and compression may cause artery fatigue and plaque rupture. Lendon et al. [96] show preliminary results of the stress-strain relationships of four (non-ulcerated and ulcerated) plaque caps of human aortas. The findings for the caps are very different, the stress-strain curves are qualitatively similar to that of the normal arterial wall. Loree et al. [97] investigated the uniaxial tensile behavior

of circumferentially oriented samples of human aortic plaque caps with correlation of the underlying composition (cellular, hypocellular and calcified). This seems to be the first study where the samples were pre-conditioned with three cycles at physiological tensile stresses followed by progressive loading until fracture occurred. The authors concluded that the static circumferential tangential modulus of the samples is not significantly affected by the degree of cellularity and calcification determined by histological characterization. Topoleski et al. [98] studied the radial compressive behavior of different plaque compositions of human aorta-iliac arteries segments. Data showed that plaques exhibit composition- and history-dependent nonlinear and inelastic responses under finite deformations. They also found that the area of the hysteresis loop tended to decrease with subsequent cycles. Topoleski and Salunke [99] investigated the multiple cyclic compression and stress-relaxation response of diseased and healthy specimens, while a more recent work [100] demonstrated composition-dependent differences and different responses of plaques to successive relaxation tests in uniaxial compression.

All of these studies have the common limitation that they are based on tests in one direction and that most of the mechanical testing is focused primarily on the properties of the plaque cap, which was isolated from the underlying plaque core and vessel wall. Our aim is to separately quantify the mechanical properties of the different tissue components in the atherosclerotic plaques of human iliac arteries, and to discuss their differences. For this purpose we have performed uniaxial extension tests of human strip samples in two directions (axial and circumferential). Additionally, we report the associated anamnesis, since mechanical properties of arteries depend on several clinical factors. Finally, the ultimate tensile stresses and associated stretches of the different high-grade stenotic arterial segments were investigated. Such systematic direction-dependent and tissue-specific experimental results for human stenotic arteries including ultimate stresses and stretches are not yet available in the literature. These data may serve for theoretically-based quantification in terms of constitutive equations, which can be used in finite element programs to better model the biomechanics of atherosclerotic lesions.

Table 2.1: *Anamnesis*

Specimen	*I*	*II*	*III*	*IV*	*V*	*VI*	*VII*	*VIII*	*IX*
Type of iliac artery	EIA	CIA	IIA	CIA	CIA	IIA	CIA	IIA	CIA
Age (yrs)	65	90	80	64	81	60	60	87	87
Sex	f	m	f	f	f	m	m	f	f
Primary disease	CS	GS	AS	CS	CS	CS	AS	GS	GS
Cause of death	MI	MI	BP	MI	MI	GHD	MI	BP	BP
Atherosclerosis									
Type of atherosclerotic lesions [101]	V	VII	V	VIII	VII	VII	VII	VII	VIII
Adjoining Vessels	y	y	y	y	y	n	y	y	y
Peripheral	y	y	y	y	y	n	y	y	y
Coronary	y	y	y	y	y	y	y	y	y
Cerebral	y	y	n	n	y	n	n	y	y
Renal	y	y	y	n	y	n	n	y	y
Cardiovascular treatments	n	AH	n	BS	n	n	n	n	n

CIA ... common iliac artery; EIA ... external iliac artery; IIA ... internal iliac artery; AH ... antihypertensives; AS ... atherosclerosis; BP ... bronchopneumonia; BS ... bypass surgery; CS ... coronary sclerosis; GHD ... global heart dilation; GS ... generally atherosclerosis; MI ... myocardial infarction. Types of atherosclerotic lesions are according to Stary et al. [101]. Assessment of atherosclerosis is based on autopsy reports (y ... medium or high grade, n ... no or low grade).

2.2 Methods

2.2.1 Material

Iliac arteries are of particular clinical and biomedical interest, since they are atherosclerotic-prone vessels, which frequently undergo endovascular treatments. They are relatively easy to access for vascular diagnostic procedures [73]. Therefore, nine atherosclerotic iliac arteries (*I-IX*) from eight corpses (74.9 ± 12.5 yrs, mean $\pm$ SD) were harvested during autopsy within 24 hours from death. From one corpse two arteries (*VIII-IX*) were obtained. Information about the different types for the iliac arteries and their related anamnesis are summarized in Table 2.1. The arteries were required to have an atherosclerotic lesion of type V or higher according to Stary et al. [101] (for a partitioning of the pathogenesis of atherosclerosis into different stages of plaque formation see Fig. I therein). A type V lesion (or fibroatheroma), for example, contains mainly reparative smooth muscle cells and
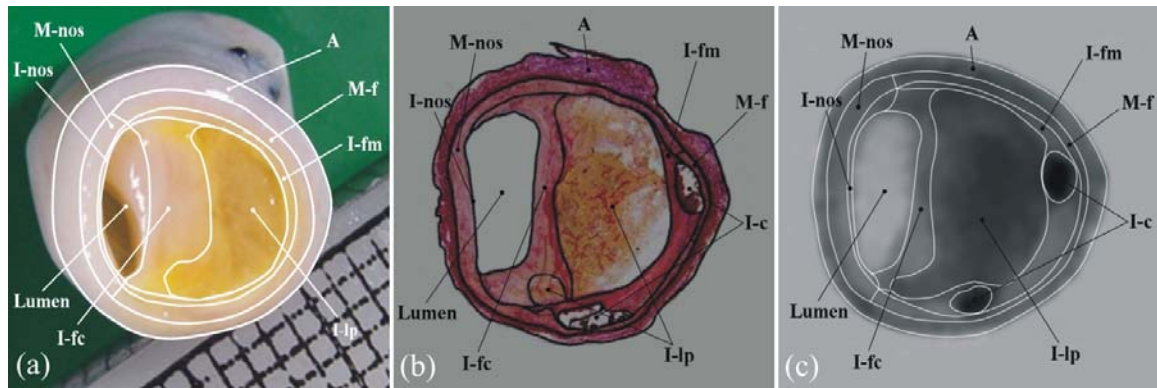
Figure 2.1: Human external iliac artery, specimen *I*: (a) segmented macroscopic view, (b) segmented histological section (EVG coloring) — transmitted light microscopic photograph, (c) high resolution magnetic resonance image of the same artery, filtered and (manually) segmented. The histological section and the magnetic resonance image are taken from the same location.

fibrous tissue and, additionally, two or more lipid pools of unequal size separated from each other by cells and fibrous tissue. Cross-sectional macroscopic views of the investigated nine stenotic iliac arteries investigated are provided in Figs. 2.1(a) and 2.2.

The lesions were classified by a pathologist by means of histological sections and **h**igh **r**esolution **M**agnetic **R**esonance **I**mages (hrMRI). The specimens were stored in a 4°C calcium-free and glucose-free Tyrode solution (in mmol: NaCl 136.9, KCl 2.7, MgCl$_2$ 1.05, NaHCO$_3$ 11.9, NaHPO$_4$ 0.47, EGTA 2.0). The axial *in situ* prestretch, defined as the ratio of *in situ* length to *ex situ* length, was calculated to be 1.06 ± 0.05. Use of autopsy material from human subjects was approved by the Ethics Committee, Medical University Graz in Austria.

2.2.2 hrMRI Examination and Histology

hrMRI Examination. In order to identify the usability of the harvested arteries in regard to the experimental tests to be performed, and, additionally, to detect the three-dimensional geometry for reconstruction purposes (documented in a follow-up paper), we use high resolution magnetic resonance imaging. The arteries were tethered with superficial surgical sutures to a grid of nylon threads fixed in a
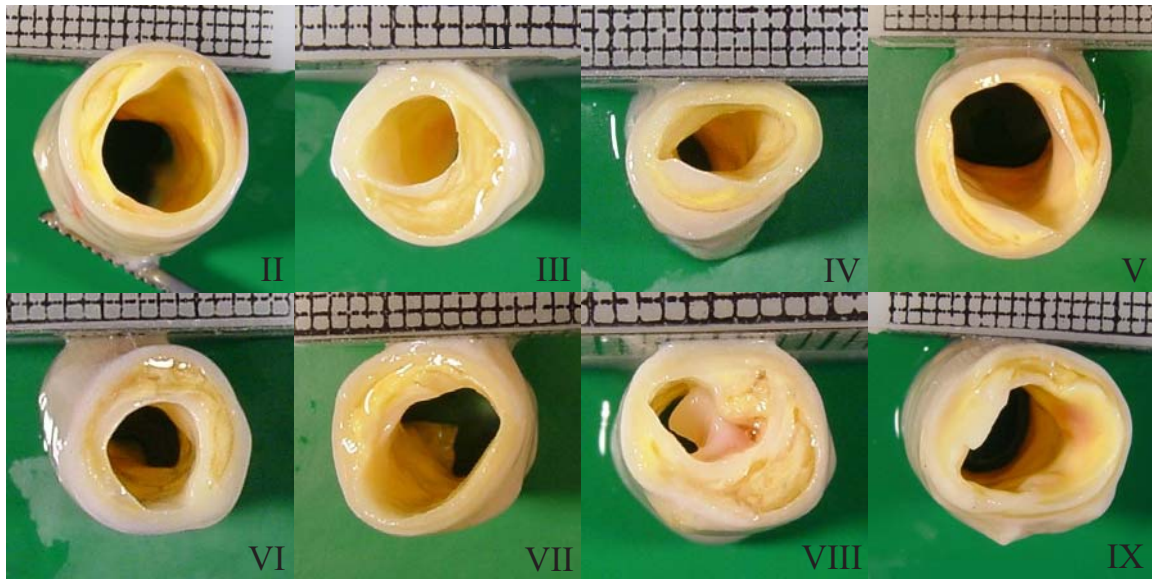
Figure 2.2: Macroscopic view of eight human stenotic iliac arteries, specimens *II-IX*. Top ruler scale: one side of a square characterizes 1 mm.

Perspex frame filled with physiological 0.9 % NaCl solution maintained at 37 °C (see Fig. 1(a) in [102]), and then scanned on a 1.5 T whole body system (Philips ACS-NT, maximum gradient strength = 23 mT) within 24 hours after autopsy. The lateral resolution was about 0.25 mm, while the axial resolution was 0.6 mm. Figure 2.1(c) shows a typical (corrected and noise-filtered) hrMR image of a stenotic artery (specimen *I*).

After MR-imaging the arteries were marked for histology by injecting black ink at a nylon thread crossing, and then cut through transversely into two halves. One half was used for corresponding histological analyses to allow material characterization, while the other halves of the arteries were dissected anatomically into their major components. We used only lesions that were relatively uniform along their length of about 20 mm. We identified uniformity by means of hrMRI.

Histology. The histological analysis is necessary since it allows direct identification the underlying tissue type. The ink-marked half of the vessel segment was fixed in 8% buffered formaldehyde solution (pH 7.4), decalcified with EGTA, embedded in paraffin, and serially sectioned at 0.6 mm intervals. 5 μm thick sections were stained with Elastica van Gieson (EVG) and Hematoxylin and Eosin (H&E).

Figure 2.1(b) shows a transmitted light microscopic photograph of a typical histological section of an external iliac artery (specimen *I*), which corresponds to the hrMRI cross-section shown in Fig. 2.1(c).

The histological section close by the other half of the artery devoted to anatomical dissection, was segmented by a pathologist, who drew the border of the different tissues on the microphotograph. Eight different tissue types were considered: the non-diseased intima I-nos[1], fibrous cap I-fc (fibrotic part at the luminal border), fibrotic intima at the medial border I-fm, calcification I-c, lipid pool I-lp, non-diseased media M-nos, diseased fibrotic media M-f and adventitia A [86, 103]. The histological analysis of the tissue component M-f, i.e. a very thin portion of the media adjacent to the plaque, showed a higher amount of collagenous tissue. Since this tissue component differed in its mechanical behavior from the remaining (non-diseased) portion of the media M-nos, we have considered it in the mechanical test protocol. Remarkably, for two atherosclerotic lesions we observed morphological features such as calcification with secondary bone formation and typical bone marrow cells. For the mechanism of mineralization during evolution of atherosclerotic plaques see, for example, [104].

The classification introduced here has served as a basis for the separation of the diseased vessel wall and the segmentation process of the histology (compare with Fig. 2.1). Each of the tissue components so classified is mechanically relevant and contributes to the overall mechanical response. The separation of the diseased vessel wall was physically feasible using surgical instruments.

2.2.3 Mechanical Testing

Mechanical tests were performed on a computer-controlled, screw-driven high-precision tensile testing machine. The system was based on a commercial class 1 machine (Messphysik, μ-Strain Instrument ME 30-1, Fürstenfeld, Austria), which was adapted for small biological specimens by integrating a tissue bath at (37 ±

---

[1]The abbreviation 'nos' is frequently used in histopathology and stands for **n**ot **o**therwise **s**pecified. In the context of the present study it means 'no appreciable disease', or, more precisely 'non-atherosclerotic'.
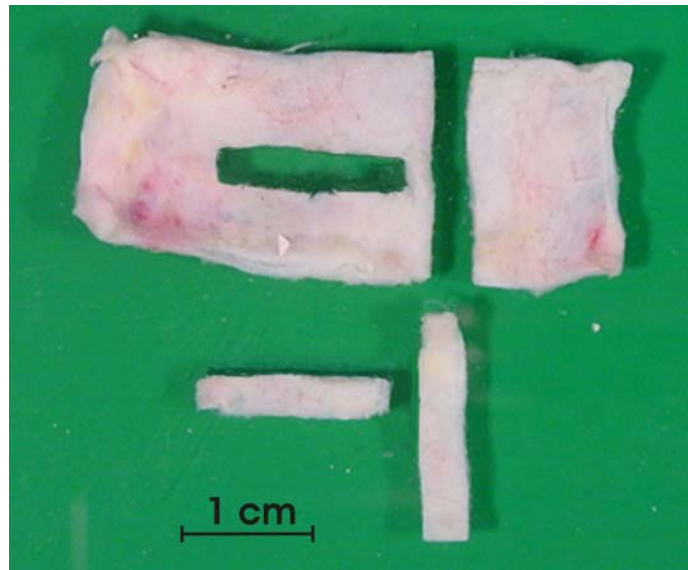
Figure 2.3: Representative axial and circumferential strips excised from a dissected adventitial layer.

0.1) °C maintained by a heater-circulation unit (model E 200, Lauda; Lauda-Königshofen, Germany). The crossheads are driven in opposing directions, allowing a fixed position of the sample center. A crosshead stroke resolution of $0.04\,\mu$m and a minimum load resolution of $1\,$mN using a $25-$N load cell is specified by the manufacturer. Gauge length and width are measured optically using a PC-based CCD-camera videoextensometer that allows automatic gauge mark and edge recognition. Dimensional measurements are performed with a total resolution of 16 bit with regard to the camera's field of view.

The lipid pools I-lp and the bone marrows were excluded from mechanical testing. The lipid pool was not tested because of its liquid ('butter-like') consistence, while the bone marrow was not tested because of its small size. The lipid pools are assumed to behave as a nearly incompressible fluid [103, 105–107] not able to sustain shear stress [108].

For the determination of the passive, quasi-static stress-stretch response of the individual tissue components, rectangular strip samples with axial and circumferential orientations were excised from the specimen. Representative axial and circumferential strips from a dissected adventitial layer are shown in Figure 2.3. The samples varied from 7 to 17 mm in length, from 2.2 to 5.6 mm in width, and
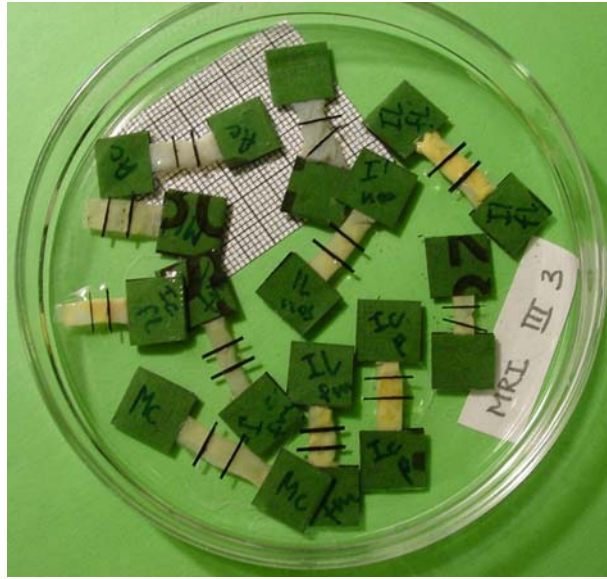
Figure 2.4: Eleven strip samples prepared for mechanical testing (from specimen
          V). Samples for the tissue types A, M-nos, I-nos, I-fc and I-fm in both
          directions, and one sample for the calcification I-c in circumferential
          direction.

from 0.24 to 1.7 mm in thickness. Pieces of emery paper were attached to the ends
of the samples to prevent slippage during testing. Two black colored straw chips
were glued transversely in parallel onto the middle part of the samples to act as
gauge markers for the axial deformation measurements. The strip samples were
allowed to equilibrate for $30 - 60$ min in a calcium-free physiological 0.9 % NaCl
solution at 37 °C. A collection of strip samples from specimen *V*, which were
prepared for mechanical testing, is illustrated in Fig. 2.4.

Pre-conditioning was achieved by executing up to five successive loading-unloading
cycles for each test. Then the samples underwent one cyclic quasi-static uniaxial
extension test with continuous recording of tensile force, width and gauge length
at a constant crosshead speed of 1 mm/min. Finally, the strain was increased until
fracture occurred. Sometimes it happened that the fracture occurred outside the
gauge section of the sample close to one of the grips so that another sample was
prepared and tested if enough material was available. It was usually possible to
get a second sample for the tissue types A, M-nos and I-fc. A photograph of a
fractured tissue component is shown in Fig. 2.5. A total number of 107 samples
were tested, and 82 are documented in the present paper (18 for A, 18 for M-nos,
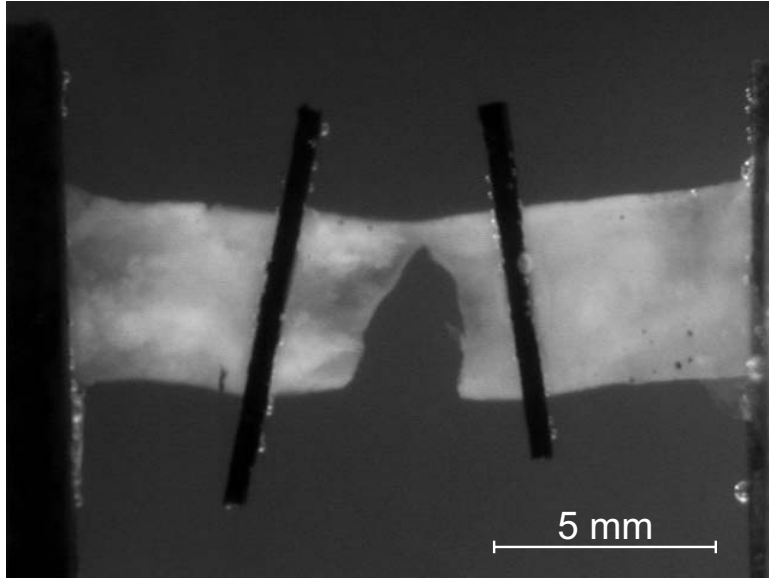
Figure 2.5: Photograph of a fractured tissue component (specimen *I*), non-diseased intima I-nos tested in circumferential direction).

12 for I-nos, 17 for I-fc, 8 for I-fm, 5 for M-f and 4 for I-c). The four I-c samples were obtained from three specimens, i.e. *I* (samples in both directions), *IV* (sample in axial direction) and *V* (sample in circumferential direction). After tensile testing the sample's thickness was measured by means of the videoextensometer.

The stretch ratio λ was computed as l/L, where l and L are the measured gauge lengths in the loaded and unloaded configurations, respectively. Based on the global equilibrium, the incompressibility condition, and the experimental data, it is straightforward to compute the associated Cauchy stress, denoted as σ. Incompressibility requires $LWT = lwt$, where w, t and W, T are the width and the thickness of the strip sample in the loaded and unloaded configurations, respectively. Thus, $\sigma = f/wt$, and, therefore,

$$\sigma = \frac{f}{WT}\lambda,$$ (2.1)

where f is the actual tensile force. Hence, the computation of σ requires the measurements of the five parameters f, W, T, l, L. The Cauchy stresses were then plotted versus the stretch ratio.

Finally, we compute the hysteresis loop area $A \in [0, 100]$ within a typical loading-

unloading cycle defined to be $A = 100(A_l - A_u)/A_l$, where A_l is the area below the σ/λ-curve during tissue loading, and A_u is the area below the σ/λ-curve during unloading.

2.3 Results

Table 2.1 documents the anamnesis of the donors from which the specimens *I-IX* were obtained. The set of specimens consists of five common iliac arteries (CIA), three internal iliac arteries (IIA) and one external iliac artery (EIA). The table documents data on age, sex, primary disease, cause of death, type of atherosclerotic lesions, and cardiovascular treatments. Moreover, the condition of the adjoining vessels and the remaining parts of the arterial vasculature in regard to atherosclerosis is shown. These factors were proven to affect the mechanical properties of arteries (see, for example, the review [109]), and are important for a complete registration of arterial mechanics of aged patients.

Figure 2.1 illustrates the marked heterogeneity of a lesion and the good correlation between the different images. In a comparative study Figs. 2.6 and 2.7 exhibit the highly nonlinear and anisotropic (except for the fibrotic intima at the medial border I-fm) mechanical responses, i.e. Cauchy stress versus stretch, of the different tissue types (A, M-nos, M-f, I-nos, I-fc, and I-fm) of the investigated specimens *I-IX*. In particular, a comparison is provided between the responses in the circumferential direction and in the axial direction. The loading-unloading paths showed only small hysteresis (Table 2.2), and, therefore, the unloading path is not shown in the plots. Some measurements of the samples close to the fracture appeared to be rather noisy and are not shown in the plots. Only for the adventitia A and the non-diseased media M-nos were complete sets of strip samples from all specimens available (Figs. 2.6(a)-(d)). For the diseased fibrotic media M-f, unfortunately, only five sample could be tested (Figs. 2.6(c),(d)).

The calcification I-c has shown very stiff and linear mechanical responses (not shown in the plots) with an average Young's modulus of 12.6 ± 4.7 MPa, mean $\pm$ SD.

Table 2.2: *Calculated mean values in* (%) *and associated standard deviation (SD) of the hysteresis loop area of all tissue types (obtained from specimens* I-IX*) tested in the circumferential direction* c *and the axial direction* a.

	Tissue type											
	A		**M-nos**		**M-f**		**I-nos**		**I-fc**		**I-fm**	
Hysteresis (%)	*c*	*a*	*c*	*a*	*c*	*a*	*c*	*a*	*c*	*a*	*c*	*a*
mean	17.3	13.6	13.8	8.8	5.8	4.7	12.8	7.9	16.7	13.1	11.1	10.6
SD	9.1	6.3	9.8	3.1	5.4	3.0	7.1	5.4	3.9	5.2	6.1	8.6

The ultimate tensile stress characterizes the maximum resistance to fracture. It is equivalent to the maximum load that can be carried by the cross-sectional area when the load is applied as a tensile force, see Eq. (2.1). The ultimate tensile stresses (in kPa) and the associated ultimate stretches, denoted as σ_{ult} and λ_{ult}, of all tested samples that fractured within the gauge section are summarized in Table 2.3. Values that are related to samples tested in the circumferential direction are denoted by *c*, and to samples tested in axial direction by *a*. Missing values indicate either that the test was unsatisfactory or that a sample was not available. The ultimate values in the table are related to the plots of the samples shown in Figs. 2.6 and 2.7. Furthermore, the mean values and the standard deviations (SD) of the ultimate tensile stresses, denoted as $\overline{\sigma}_{ult}$, and the ultimate stretches, denoted as $\overline{\lambda}_{ult}$, are documented. The calcification has shown an average ultimate tensile stress of 179 ± 56 kPa, mean $\pm$ SD at an average stretch of 1.02 ± 0.005, mean $\pm$ SD.

2.4 Discussion

Histopathological investigations suggested that plaque rupture involves plaque cap failure. Therefore, most of the mechanical studies focused primarily on the properties of fibrous plaque caps. However, plaque stability cannot be dependent only on the mechanical properties of the plaque cap. The stress distribution in the plaque cap is strongly influenced by all surrounding components of the atherosclerotic lesion so that a systematic, direction-dependent and tissue-specific experimental testing is needed. Even the adventitia is in strong interaction with the
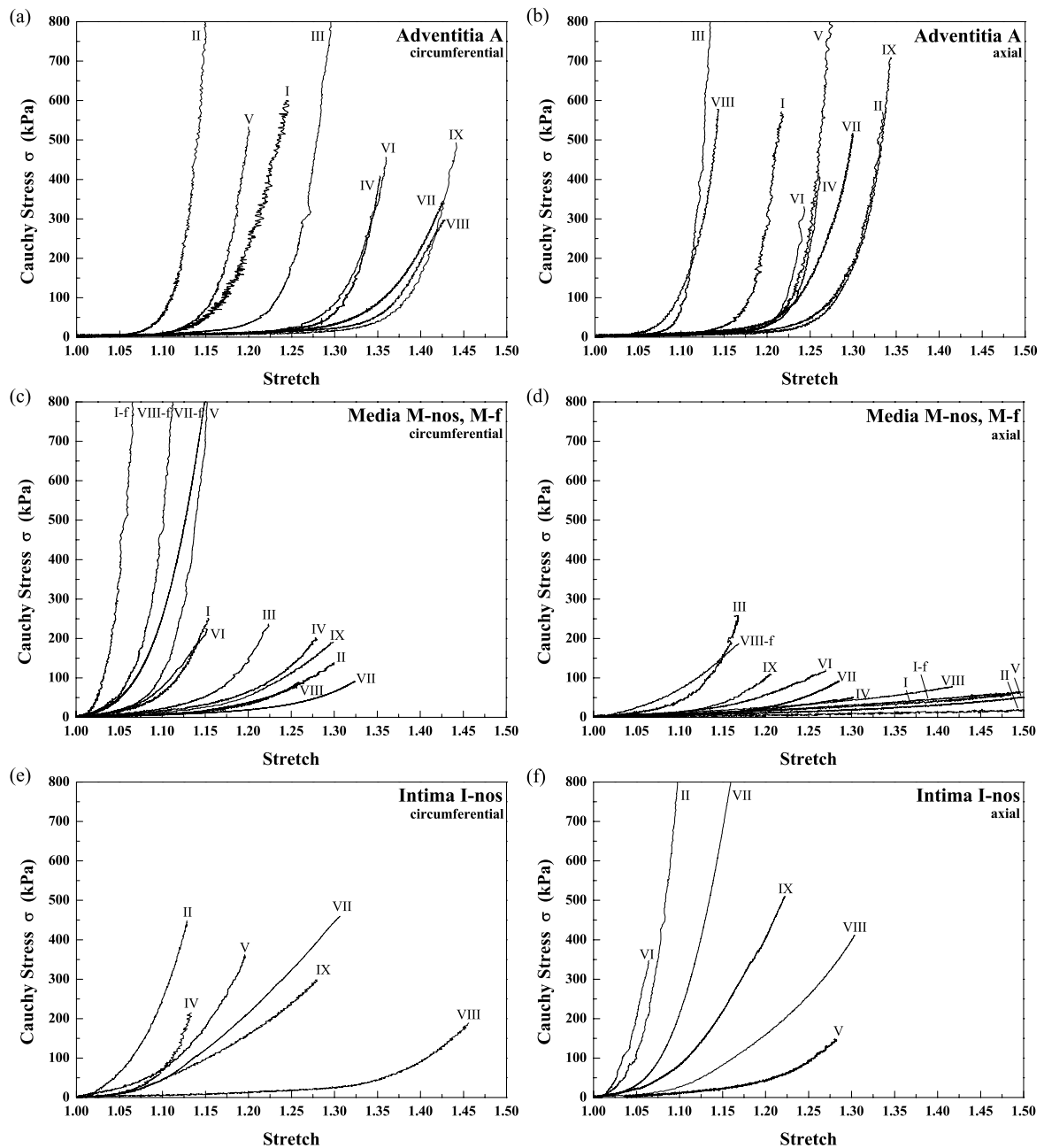
Figure 2.6: Uniaxial tensile stress-stretch responses of different human tissues in the circumferential and axial directions. (a),(b) are stress-stretch plots for the adventitia A, (c),(d) are plots for the healthy and diseased media (M-nos and M-f), and (e),(f) are related to the healthy intima I-nos. Labels *I-f, VII-f* and *VIII-f* in (c),(d), indicate fibrotic media samples from specimens *I, VII* and *VIII*, respectively.
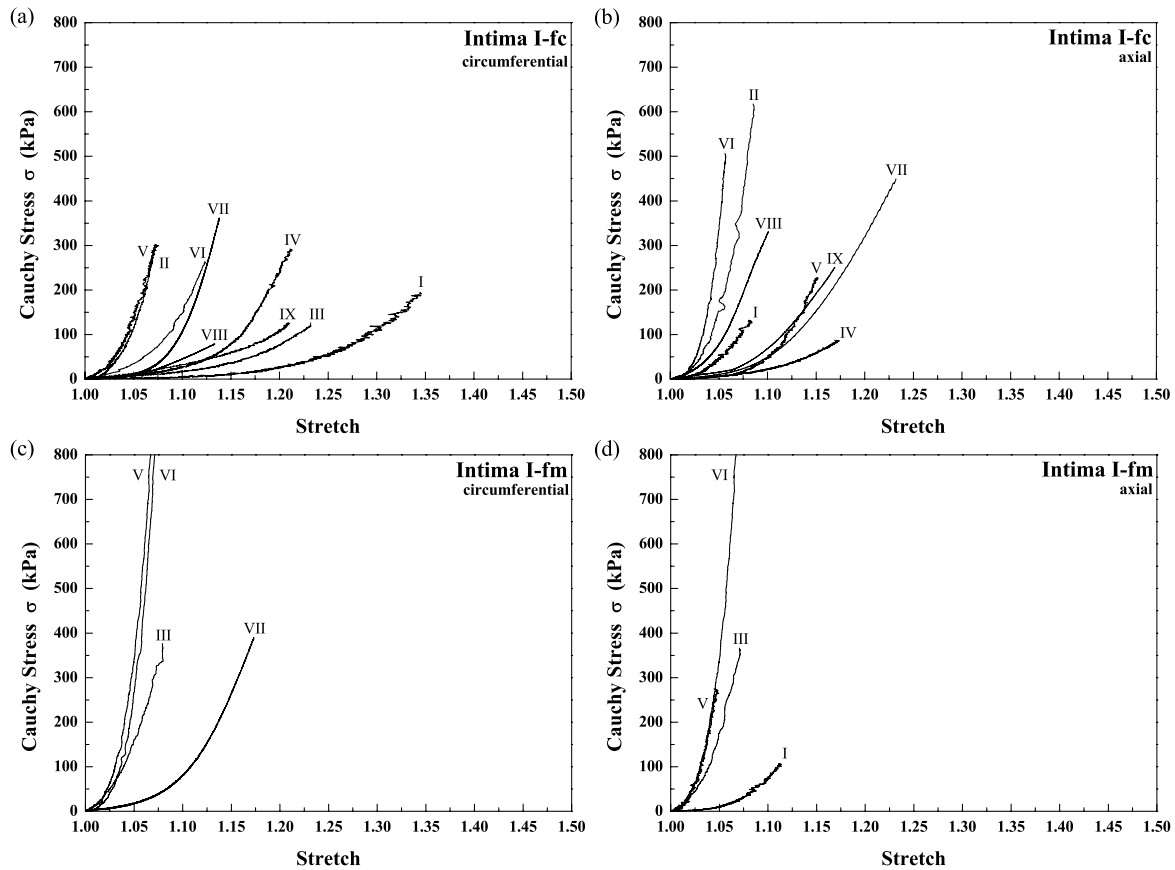
Figure 2.7: Uniaxial tensile stress-stretch responses of different human tissues in the circumferential and axial directions. (a),(b) are stress-stretch plots for the fibrous cap *I-fc*, while (c),(d) are plots for the fibrotic intima samples at the medial border *I-fm*.

plaque cap and plays a crucial role in plaque loading. Recent studies have shown that for aged human arteries the adventitia is a significant carrying structure [69], and that disrupted plaques exhibit increased incidence of adventitia inflammation [110]. This is the reason why we investigated the mechanical properties of different tissue components in human atherosclerotic plaques and the healthy surrounding tissues. Lendon et al. [92] showed that the mechanical properties of human aortic intima did not significantly alter when stored at 4°C for time periods up to 64 hours. Berberian and Fowler [111] showed that minimal enzymatic changes occur in rabbit aortas within 48 hours when stored at 4°C. For this reason all mechanical tests were finished within 48 hours after autopsy.

Knowledge of the mechanical properties of atherosclerotic plaque is of fundamen-

Table 2.3: *Ultimate tensile stress σ_{ult} (kPa) and associated ultimate stretch λ_{ult} (1) of the different types of tissue of all specimens* I-IX *tested in the circumferential direction* c *and the axial direction* a. *Associated mean values $\overline{\sigma}_{\mathrm{ult}}$ and $\overline{\lambda}_{\mathrm{ult}}$ and standard deviations (SD).*

		Tissue type
		A		**M-nos**		**I-nos**		**I-fc**		**I-fm**		**M-f**	
Specimen		**c**	**a**	**c**	**a**	**c**	**a**	**c**	**a**	**c**	**a**	**c**	**a**
I	σ_{ult}	618.5	737.6	261.5	183.7			205.6	509.8		171.8	1278.1	181.5
	λ_{ult}	1.243	1.223	1.156	1.863			1.374	1.121		1.135	1.076	1.797
II	σ_{ult}	832.3	667.6	212.9	128.4	435.2	1321.9	299.3	617.5				
	λ_{ult}	1.173	1.392	1.409	2.005	1.129	1.117	1.073	1.068				
III	σ_{ult}	1188.3	1276.6	229.7	261.6			126.4			366.5		
	λ_{ult}	1.479	1.157	1.249	1.169			1.232			1.071		
IV	σ_{ult}	845.4	886.6	201.6				292.2					
	λ_{ult}	1.424	1.299	1.280				1.213					
V	σ_{ult}		990.7		432.7	356.4		301.3		941.1	294.3		
	λ_{ult}		1.282		1.830	1.201		1.076		1.071	1.057		
VI	σ_{ult}	802.3		298.2	121.8			287.9	506.1	999.2			
	λ_{ult}	1.413		1.177	1.283			1.126	1.058	1.078			
VII	σ_{ult}	1479.5		108.9	92.5	473.9	796.2	360.1	449.2	390.1		869.0	
	λ_{ult}	1.676		1.323	1.284	1.320	1.159	1.138	1.232	1.173		1.154	
VIII	σ_{ult}	1090.1	1005.3	93.7	141.3	368.2	703.8		402.3				193.2
	λ_{ult}	1.458	1.458	1.260	1.583	1.648	1.435		1.121				1.176
IX	σ_{ult}	1396	1097.9	209.9	148.1	809.1	952.9	165.8	326.9				
	λ_{ult}	1.652	1.658	1.313	1.267	1.357	1.309	1.222	1.208				
mean $\overline{\sigma}_{\mathrm{ult}}$		1031.6	951.8	202.0	188.8	488.6	943.7	254.8	468.6	776.8	277.5	1073.6	187.4
SD		306.8	209.0	69.8	110.9	185.6	272.3	79.8	100.1	336.2	98.4	289.3	8.3
mean $\overline{\lambda}_{\mathrm{ult}}$		1.440	1.353	1.270	1.536	1.331	1.255	1.182	1.135	1.107	1.088	1.115	1.487
SD		0.175	0.168	0.081	0.327	0.199	0.146	0.100	0.071	0.057	0.042	0.055	0.439

tal importance for identifying plaque rupture, the most common antecedent of myocardial infarction. In this study we have investigated the mechanical properties of nine atherosclerotic lesions — their mechanical responses indicate significant variations, as seen in the plots of Figs. 2.6 and 2.7. All tissue components investigated, with the exception of the calcification I-c, show a highly nonlinear behavior, which was also found for aortic fibrous caps in the studies by, for example, Lendon

et al. [96] and Loree et al. [97]. Because of the nonlinear responses of the tissues a measure of stiffness would only be meaningful for certain stress or stretch levels, not provided here. Several authors found, however, that diseased arterial tissue is stiffer than healthy tissue (see Born and Richardson [91], Topoleski et al. [98] among others). In regard to our study, by comparing the slopes of the stress-stretch curves at low and high stresses there is a clear tendency that diseased tissues are stiffer than healthy ones. For example, all diseased fibrotic media M-f tested are stiffer than the non-diseased samples M-nos (see Figs. 2.6(c),(d)); there is also a clear tendency that the diseased intima tissue (fibrous cap I-fc and I-fm) is stiffer than the non-diseased tissue I-nos (compare with Figs. 2.6(e),(f), and Fig. 2.7).

The present plots allow also a unique and interesting comparison of the mechanical response of a sample oriented and tested in the circumferential direction with the associated sample oriented and tested in the axial direction. For example, as can be seen from Figs. 2.6(c),(d), the mechanical response of the healthy media M-nos in the axial direction tends to be weaker than in the circumferential direction, in which the smooth muscle cells are mainly oriented [112] (samples from specimens *III*, *VII* and *IX* exhibit a stiffer response in the axial direction). The fibrotic media M-f tested show also a weaker behavior in the axial direction than in the circumferential direction (labeled as *I-f, VIII-f* in the plots of Figs. 2.6(c),(d)), where, however, only two comparable samples were available for testing. The adventitia A (Figs. 2.6(a),(b)), the non-diseased intima I-nos (Figs. 2.6(e),(f)) and the fibrous caps I-fc (Figs. 2.7(a),(b)) tested in the axial direction indicate the tendency to be stiffer than associated samples in the circumferential direction. Interestingly, as can be seen from Figs. 2.6(a),(b), all samples of the adventitia tested demonstrate a similar, very high stiffness behavior in the high-stress domain.

Strip samples of the fibrotic intima at the medial border I-fm show almost isotropic behavior for all comparable samples obtained from specimens *III*, *V* and *VI* (Figs. 2.7(c),(d)). The sample from specimen *VI* obtained from a 60 year old male donor (IIA) shows almost the same behavior as the sample from specimen *V* obtained from a 81 year old female donor (CIA).

Our study indicates that the calcification I-c has about the same stiffness as that of the stiffest tissue component tested, i.e. the adventitia A in both directions or

the diseased fibrotic media M-f in the circumferential direction in the high stress domain at which the response is almost linear. All other tissues show a softer mechanical response than the calcification does. By defining a plaque 'moduli', Lee et al. [93] found that calcified caps of abdominal aortic plaques are $4 - 5$ times stiffer than cellular caps in radial compression tests at room temperature.

In our study, the adventitia A shows the highest average ultimate tensile stresses $\overline{\sigma}_{\mathrm{ult}}$, while the non-diseased media M-nos shows the lowest average values (for this comparison the diseased fibrotic media M-f was excluded since ultimate values of only four samples were available); see Table 2.3. It is the adventitia, which demonstrates very high average tensile strength having significant load-carrying capabilities at higher pressures at which it changes to a stiff 'jacket-like' tube, that prevents the smooth muscle from acute overdistension (see also [69, 89]). From the mechanical perspective, it is the non-diseased media that is the most significant (load-carrying) layer in a healthy artery under physiological conditions.

The average ultimate tensile stress $\overline{\sigma}_{\mathrm{ult}}$ of fibrous caps I-fc in the circumferential direction was $254.8 \pm 79.8\,\mathrm{kPa}$ at an associated stretch of 1.182 ± 0.1. The stress values are in good agreement with stress values obtained by, for example, Lendon et al. [92], who have performed uniaxial tensile tests on strips from human ulcerated aortic plaques in the circumferential direction. However, the associated stretch values they obtained were about 1.5, which deviate significantly from our findings. Cheng et al. [113] reported maximum circumferential stresses of $545 \pm 160\,\mathrm{kPa}$ in human fibrous caps that ruptured. These (indistinct) values were calculated by means of a linear elastic finite element analyses without a failure criterion. Thereby, ruptured lesions were discretized and a mean intraluminal pressure of $110\,\mathrm{mmHg}$ applied. The ultimate tensile stresses of human aortic fibrous caps in the circumferential direction investigated by Loree et al. [97] ranged from 149 to $701\,\mathrm{kPa}$, with a mean of $484 \pm 216\,\mathrm{kPa}$ and the ultimate tensile stretches ranged from 1.15 to 1.60, with a mean ultimate tensile stretch of 1.30 ± 0.16. Limitations in this study were the small number of specimens (six) that fractured within the gauge section and that uniaxial testing was performed at room temperature.

It turns out that of all intimal tissues investigated (I-nos, I-fc and I-fm) the lowest fracture stress is for the fibrous cap in the circumferential direction, which supports

the hypothesis of Richardson et al. [108] that peak circumferential stress may be a critical factor in plaque rupture. Interestingly, both the stress and stretch at calcification I-c fracture, i.e. $179.0 \pm 56\,\text{kPa}$ and 1.02 ± 0.005, respectively, are smaller than for each of the other tissues tested. Except for the medial tissues M-nos and M-f, all others show, on average, higher ultimate tensile stretches $\overline{\lambda}_{\text{ult}}$ in the circumferential direction than in the axial direction.

Table 2.2 shows the mean areas of the hysteresis loops for all tissue types tested. Remarkably, all tissue components oriented in the circumferential direction show a larger hysteresis than those oriented in the axial direction.

Limitations of our study concern the number of samples tested, which were too small in order to recognize age-specific, gender-specific, artery type-specific or atherosclerotic type-specific differences of the mechanical properties. In addition, due to the small size of the specimen, appropriate strip samples could not always be prepared. It was especially difficult to get samples from the fibrotic media M-f, because the M-f is a very thin tissue located behind the fibrous intima at the medial border I-fm. A possible improvement in measurement of the tensile properties of micro-sized specimens would be the use of micro-testers. Quite a number of fracture tests failed in the sense that the fracture occurred outside the gauge section, although a second sample could sometimes be prepared and tested. Due to the small size of many strip samples the idea of running experiments with dumb-bell shaped samples would also not have been successful.

2.5 Conclusion

This study has attempted to systematically investigate and quantify the anisotropic mechanical responses of the different tissue components of nine human stenotic iliac arteries selected by means of MRI; associated anamnesis of donors were reported. From anatomical dissections into eight different tissue types, which were based on histological images, a total number of 107 samples could be obtained for experimental tensile testing at a temperature of $37\,^\circ\text{C}$. Gauge length and width were appropriately measured optically using a PC-based CCD-camera videoextensometer. Novel direction-dependent stress-strain data and fracture stress and

stretch of all plaque types and healthy surrounding tissues are described.

This approach presents a step toward a better understanding of the biomechanical behavior of atherosclerotic lesions as a function of their components; however, because of the variability of the lesions and their marked heterogeneity the need for more data remains. The data presented indicate the general characteristics of the mechanical response of individual arterial tissue types and may serve as a basis for the design of related constitutive models, a task that is performed in an upcoming paper. The present study shows the need for anisotropic models and may help to perform computational analyses of plaques within mechanical interventional therapies such as balloon angioplasty with greater accuracy.

Nomenclature

$$
\begin{aligned}
\text{A} &= \text{Adventitia} \\
\text{CIA} &= \text{Common iliac artery} \\
\text{EIA} &= \text{External iliac artery} \\
f &= \text{Tensile force} \\
\text{hrMRI} &= \text{High resolution magnetic resonance imaging} \\
\text{IIA} &= \text{Internal iliac artery} \\
\text{I-c} &= \text{Calcification} \\
\text{I-fc} &= \text{Fibrous cap} \\
\text{I-fm} &= \text{Fibrotic intima at the medial border} \\
\text{I-lp} &= \text{Lipid pool} \\
\text{I-nos} &= \text{Non-diseased intima} \\
L, l &= \text{Gauge length in the load-free (reference) and current configurations} \\
\text{M-f} &= \text{Diseased fibrotic media} \\
\text{M-nos} &= \text{Non-diseased media} \\
\text{SD} &= \text{Standard deviation} \\
T, t &= \text{Thickness in the load-free (reference) and current configurations} \\
W, w &= \text{Width of the strip sample in the load-free (reference) and current} \\
&\quad\ \ \text{configurations} \\
\lambda &= \text{Stretch ratio} \\
\sigma &= \text{Cauchy stress} \\
\sigma_{\text{ult}}, \lambda_{\text{ult}} &= \text{Ultimate tensile stress and associated ultimate stretch} \\
\overline{\sigma}_{\text{ult}}, \overline{\lambda}_{\text{ult}} &= \text{Mean values of the ultimate tensile stresses and associated ultimate} \\
&\quad\ \ \text{stretches}
\end{aligned}
$$

3 LAYER-SPECIFIC MECHANICAL PROPERTIES OF HUMAN CORONARY ARTERIES

Abstract. At autopsy 13 non-stenotic human left anterior descending (LAD) coronary arteries (71.5 ± 7.3yr, mean±SD) were harvested and related anamnesis documented. Cyclic quasi-static uniaxial tension tests of 78 pre-conditioned pre-pared strips of mid-LAD segments from the individual layers in the axial and circumferential directions were performed; ultimate tensile stresses and stretches were documented. The ratio of outer diameter to total wall thickness was 0.189 ± 0.014; ratios between thickness of adventitia, media, intima and the total wall were 0.4 ± 0.03, 0.36 ± 0.03, 0.27 ± 0.02; axial *in situ* stretch was 1.044 ± 0.06, and decreased with age. The stress-stretch responses for the individual tissues showed pronounced mechanical heterogeneity. The intima is the stiffest layer over the whole deformation domain, while the media in the longitudinal direction is the softest. All specimens exhibited small hysteresis, behaved anisotropically and strongly nonlinearly in both loading directions. The media and intima showed similar ultimate tensile stresses, which are on average *three* times smaller than ultimate tensile stresses in the adventitia (1430 ± 604kPa circumferential, 1300 ± 692kPa longitudinal). The ultimate tensile stretches are similar for all tissue layers. A recently proposed constitutive model was extended and used to represent the deformation behavior for each tissue type over the entire loading range. The study showed the need to model non-stenotic human coronary arteries with non-atherosclerotic intimal thickening as a composite-structure composed of three solid mechanically relevant layers exhibiting different mechanical properties. The intima showed significant thickness, load-bearing capacity and mechanical strength when compared with the media and adventitia.

3.1 Introduction

One central aim in cardiovascular solid mechanics is the investigation of the mechanobiological behavior of arteries in health and disease, which may better explain their function on the basis of their structure and mechanics, i.e. vital information for clinical treatments of artery diseases, for designs of vascular implants such as stents and grafts, and for tissue engineering. For example, there were $1265,000$ PCI procedures performed in the US in 2005 [2]. For improving our understanding of the mechanisms involved in PCI procedures, and for improving stent designs, it is fundamental to better explore the mechanical properties and role of the separate arterial layers of coronary arterial walls, and additionally to develop efficient computational models.

Most of the studies have focused on the mechanical properties of animal coronary arteries (see, e.g., [114], [115], [66], [116], [117], [118], [119]). Besides a collagenous adventitia and a medial layer (comprised of smooth muscle, collagen and some elastin), a coronary arterial wall, however, may consist of a complex intimal layer, which develops rapidly in early years, and continues to grow in size gradually throughout life [120]. This is not observed in animals. The intima is a prominent layer with a distinctive organization of layered groups of collagen fibers which condense into a few separate alignment families [121]. Another fundamental difference from animal subjects is the fact that the intima of aged human specimens exhibit s considerable mechanical strength (see, e.g., [102]). The axial pre-stretch of aged human arteries is much smaller than for animal arteries; the axial pre-stretch can even be smaller than 1.0, i.e. the vessel then elongates axially upon excision [102]. Hence, the constitutive parameters found for animal arteries are of limited value for the development of, e.g., appropriate stents and vascular grafts or tissue engineered substitutes that are functional. In particular, from the mechanical point of view, grafts, e.g., should be designed with material properties nearly identical to those of the host vessel, since only then is there no compliance mismatch at the anastomosis.

Only a few *in vitro* data on the mechanical properties of human coronary arteries are available in the literature (see, e.g., [122], [123], [124], [91], [125], [126], [127]);

three-dimensional constitutive models that are able to describe the typical non-linear and anisotropic material response and which are of practical use for finite element methods are rare. Since human coronary arteries with non-atherosclerotic intimal thickening are composed of three (thick-walled) layers a better understanding of their mechanical function at the tissue level requires a layer-specific experimental approach and the design of constitutive descriptions that can be implemented efficiently in numerical computations. It appears that Vito and Demiray [66] were the first to document separate mechanical response data for the media and adventitia from canine aorta, which they obtained from uniaxial strip tests in the axial and circumferential directions. Later, Richardson and Keeny [124] performed mechanical measurements during uniaxial tests of intima segments taken near the junction region between the left circumflex and the human LAD coronary arteries. There is considerable uncertainty about the mechanical properties and role of the adventitia, media and intima (including failure). To the authors' knowledge a systematic study of the layer-specific mechanical response of human coronary arteries is not available to date.

With the long term goal of improving our understanding of the mechanisms involved in PCI procedures, and for improving stent designs, we explore the underlying mechanics of the adventitia, media and intima of human coronary arteries with non-atherosclerotic intimal thickening. Since LAD coronary arteries are of central importance in heart and circulatory pathophysiology (restenosis after stenting is more common in the LAD compared with other coronary locations [128], [129]) the present work focuse s on examination of this arterial segment. One specific aim is the experimental investigation of the passive mechanical properties of arterial strips taken from each of the three layers of the mid regions of human LAD coronary arteries, and the mechanical role of the intima attracts particular attention. Another goal is the determination of three-dimensional constitutive models for the description of the mechanical response of each of the tissues tested.

Table 3.1: *Anamnesis*

	Specimen No.												
	I	*II*	*III*	*IV*	*V*	*VI*	*VII*	*VIII*	*IX*	*X*	*XI*	*XII*	*XIII*
Age, yr	80	73	80	64	73	75	73	75	72	77	69	64	54
Gender	F	M	F	F	M	M	M	M	M	M	M	M	M
Primary disease	PT	HC	PN	CK	PC	PN	CC	PC	LC	DE	HT	SA	BC
Cause of death	PAE	GHD	GHD	UR	IL	GHD	MOF	GHD	PN	PN	AP	AP	GHD
Atherosclerosis													
Aorta	√	√	√	√	√	√	√	√	√	√	-	√	√
Coronary arteries	√	-	-	√	√	√	√	√	√	√	-	-	-
Cerebral arteries	-	-	-	-	√	√	-	√	-	-	-	√	-
Renal arteries	√	-	-	√	-	-	-	-	-	√	√	-	√

M … male; F … female; AP … apoplexy; BC … bronchus carcinoma; CC … colon carcinoma; CK … polycystic kidney disease; DE … demencia; GHD … global heart dilation; HC … hydrocephalus internus with tetraparesis; HT … hypertension; IL … ileus; LC … liver carcinoma; MOF … multiple organ failure; PAE … pulmonary artery embolism; PC … pancreas carcinoma; PN … pneumonia; PT … phlebothrombosis of the leg; SA … salmonelloses; UR … uraemia. Assessment of atherosclerosis is based on autopsy reports: √ … medium or high grade atherosclerosis, - … no or low-grade atherosclerosis.

3.2 Materials and Methods

Specimens

Thirteen hearts (71.5 ± 7.3 yr, mean ± SD; range 54 to 80) were harvested within 24 h from death (female/male = 3/10). The axial *in situ* length of a LAD coronary artery was determined by measuring the distance between two superficial surgical knots of the considered segment, made of surgical fibers, and prepared by a pathologist. The *ex situ* length was measured after one hour of equilibration of the excised artery in 0.9 % physiological saline solution at 37 ± 0.1°C. Thereafter, the axial *in situ* stretch, defined as the ratio of *in situ* segment length to *ex situ* segment length, was computed.

Information about the anamnesis of the coronary arteries investigated is summarized in Table 3.1. Only straight segments without palpable circumscribed wall hardening were used. An artery was rejected if during preparation (i) the straight

segment showed an atherosclerotic plaque, or if (ii) eccentric intimal thickening were macroscopically visible [130]. Therefore a total number of 27 hearts were investigated, and 14 were rejected.

The segments were harvested from the location between the first and the second diagonal branch, which is a part of the mid-LAD (segment 13 according to the coronary artery surgery study – CASS [131]). Use of autopsy material from human subjects was approved by the Ethics Committee, Medical University Graz, Austria.

Layer Preparation

Since our own preliminary studies revealed that for aged human coronary arteries the intima is a prominent layer of considerable thickness and mechanical strength we aimed for an anatomical separation of the heterogeneous arterial wall structure into three layers. Preliminary preparation tests on aged human coronary arteries indicated that it was impossible to obtain intact (leak-free) tubes of the adventitia, media and intima for performing inflation and extension experiments. In recent work [69], however, we succeeded in separating the adventitia from the media/intima layer of aged human femoral arteries, which are much larger in diameter than coronary arteries and lack multiple branches.

The harvested arteries were pruned from remaining adipose and connective tissues, and then they were cut along the axial direction to obtain flat rectangular sheets. From each sheet neighboring strips of axial orientation (the long side of the strip is aligned with the axial direction) and of circumferential orientation of the arterial wall were cut out with a sharp knife (for prepared strip samples see, e.g., Fig. 3 in [75]). The rectangular form of the samples was verified repeatedly during the preparation using a ruler. Sample length, width and thickness were measured by means of a videoextensometer.

For the anatomical separation of the arterial sample in its three layers we tried to find suitable location s at which the layer separation process can easily be initiated. Then, by pulling apart the layers, and through careful disconnection of the inter connective tissue with a scalpel, which was sometimes necessary, the arterial layers could be separated. According to the authors' experience, this

technique is much more difficult or may even be impossible for arteries of young experimental animals. Note, however, that the layer preparation process was not always successful since either macroscopic inspection or the histological images inspected afterwards have established that the result was not the desired single arterial layer (intima, media or adventitia). If this was the case the experimental data were not used, but data from a neighboring strip were obtained if the layer separation was performed successfully. Hence, a total number of 55 entire arterial strips were used from the 13 LADs, and $6 \times 13 = 78$ separated strips which were used for the study.

Pieces of sand paper were mounted at the ends of the prepared strip samples with superadhesive gel to facilitate a defined clamping in the tensile testing machine and to prevent slippage during testing. Finally, two black colored chips of a straw were glued transversely in parallel onto the middle part of the samples to act as gage markers for the axial deformation measurements (for representative tissue samples see, e.g., Fig. 4 in [75]). The strip samples were allowed to equilibrate for $30 - 60$ min before testing in a calcium-free 0.9 % physiological saline solution at $37 \pm 0.1°$C.

Mechanical Testing

Uniaxial tensile tests with bi-dimensional measurements of coronary strip specimens were performed on a computer-controlled, screw-driven high-precision tensile testing machine adapted for small biological specimens (Messphysik, μ-Strain Instrument ME $30 - 1$, Fürstenfeld, Austria). The specimens were investigated in a perspex container filled with 0.9 % physiological saline solution maintained at $37 \pm 0.1°$C by a heater-circulation unit (type Ecoline E 200, Lauda; Lauda-Königshofen, Germany) and the tensile force was measured with a 25 N class 1 strain gage-load cell (model F1/25N, AEP converter). The upper and lower crossheads of the testing machine are moved in opposite directions so that the gage region of the samples is always in the same field of view. A crosshead stroke resolution of 0.04 μm and a minimum load resolution of 1 mN of the 25 N load cell is specified by the manufacturer. Digital control of the electric drive of the machine as well as data acquisition of the crosshead position and applied load were performed by an external digital controller (EDC 25/90W, DOLI; Munich,

Germany) especially designed for screw-driven tensile testing machines. Gage length and width were measured optically using a PC-based (CPU 586) videoextensometer (model ME 46-350, Messphysik) utilizing a full-image charge-coupled device (CCD) camera, that allows automatic gage mark and edge recognition [75]. The corresponding deformation data were averaged with respect to the measuring zone and sent to the data-processing unit in real time.

Prior to testing, pre-conditioning was achieved by executing five loading and unloading cycles at a constant crosshead speed of 1 mm/min for each test to obtain repeatable stress-strain curves. Thereafter, the sample underwent a cyclic quasi-static uniaxial extension test with continuous recording of tensile force, gage length and width at the same crosshead speed of 1 mm/min. After tensile testing the sample thickness was measured. Finally, for the determination of the ultimate tensile stress and associated stretch the sample was re-clamped into the testing machine and the strain was increased with the same crosshead speed of 1 mm/min until fracture occurred. Since the width (and thickness) of the samples inside and outside the gage region was similar it sometimes happened that the fracture occurred outside the gage region of the sample close to one of the clamps so that another sample was prepared and tested if enough material was available.

After each test, the strip samples were inserted into a 4 % buffered formaldehyde solution (pH 7.4) for fixation and further histological evaluation.

Histology

The separated tissues were embedded in paraffin, sectioned at $3\,\mu$m, and consecutive sections were stained with Hematoxylin and Eosin (H&E) and with Elastica van Gieson (EvG). Histological investigations were accomplished in order to confirm primarily correct layer separation. The membrana elastica interna and the membrana elastica externa – both seen in H&E and EvG stained sections – served as structural components to ensure the correct separation of the arterial layers. Additionally, histological sections were used to assess the histostructural homogeneity of the different layers, particularly of the intimas, i.e. without circumscribed atherosclerotic plaques. With this additional histological investigation all specimens were classified as appropriate, as described above.

Analysis and Data Fitting

Arterial tissue subject to loading exhibits strong nonlinearity (with a typical exponential stiffening effect at higher loads), and anisotropy, and it also undergoes finite strains. Thus, a formulation of the material behavior needs to be derived within the realm of nonlinear continuum mechanics [132], [133].

Each arterial sample is regarded as incompressible [43], which requires that $\lambda_r\lambda_\theta\lambda_z = 1$, where λ_r, λ_θ and λ_z are the principal stretches of the deformation (when there is no shear) associated with the radial, circumferential and axial directions. In order to model the general mechanical characteristics of the arterial tissues we use a strain-energy function Ψ (per unit volume), which extends a recently proposed multi-layer model for arterial walls [134], [135] (see also [136]). This is

$$\Psi = \mu(I_1 - 3) + \frac{k_1}{k_2}\{\exp\{k_2[(1-\rho)(I_1 - 3)^2 + \rho(I_4 - 1)^2]\} - 1\}, \tag{3.1}$$

where $I_1 = \lambda_\theta^2 + \lambda_z^2 + (\lambda_\theta\lambda_z)^{-2}$ and $I_4 > 1$ are invariants [133], $k_2 > 0$, $\rho \in [0,1]$ are dimensionless parameters and $\mu > 0$ and $k_1 > 0$ are stress-like parameters. Note that (3.1) describes the strain energy stored in a composite reinforced by two families of (collagen) fibers which are arranged in symmetrical spirals — here assumed to be mechanically equivalent. For the considered specific loading state (no shear loads), and the assumption that the fibers are all embedded in the tangential surface of the tissue (no components in the radial direction), I_4 in (3.1) can then simply be expressed as

$$I_4 = \lambda_\theta^2\cos^2\varphi + \lambda_z^2\sin^2\varphi. \tag{3.2}$$

Note that the anisotropic term in (3.1) contributes to Ψ only when $I_4 > 1$ (see the discussion in [135]). The parameter φ in (3.2) is the angle between the fiber reinforcement (orthotropy) and the circumferential direction in the individual layers, which, therefore, acts as a *geometrical parameter*. Since the structural orientation of the individual layers was not investigated the parameter φ is here used as a phenomenological variable. The function (3.1), with (3.2), is sufficiently general to capture the typical features of each arterial response. It ensures mechanically and mathematically reliable behavior in the sense discussed in [134], [135]. Since each layer responds with similar mechanical characteristics we use subsequently

the same form of strain-energy function (but a different set of material parameters) for each layer.

The five parameters $(\mu, k_1, k_2, \varphi, \rho)$ in (3.1), (3.2) are obtained by means of the standard nonlinear Levenberg-Marquardt algorithm. We minimize the 'objective function'

$$\chi^2 = \sum_{i=1}^{n} \left[w_1 (\sigma_{\theta\theta} - \sigma_{\theta\theta}^{\Psi})_i^2 + w_2 (\sigma_{zz} - \sigma_{zz}^{\Psi})_i^2 \right], \tag{3.3}$$

where n is the number of considered data points, w_1 and w_2 are weighting factors, and

$$\sigma_{\theta\theta i}^{\Psi} = \left(\lambda_\theta \frac{\partial \Psi}{\partial \lambda_\theta} \right)_i, \qquad \sigma_{zzi}^{\Psi} = \left(\lambda_z \frac{\partial \Psi}{\partial \lambda_z} \right)_i \tag{3.4}$$

are the Cauchy stresses in the circumferential and axial directions of the artery predicted by the function Ψ for the i–th data record. The associated experimental Cauchy stresses, $\sigma_{\theta\theta}$ and σ_{zz}, are calculated directly from the original data as $\sigma_{\text{tens}} = f\lambda_{\text{tens}}/A$, where σ_{tens} stands for the Cauchy stress in the circumferential or axial direction, and $\lambda_{\text{tens}} = l/L$ for the associated stretch ratio, with gage lengths l and L measured in the loaded and unloaded configurations, respectively. The current tensile force is denoted by f, and A is the cross-sectional area of the specimen in the unloaded configuration. For the fitting process we have just considered data points on the loading branches. This is justified by the small hystereses between loading and unloading branches observed for all the arteries investigated, as can be seen below.

As a measure for the 'goodness of fit' the RMS error measure ε is used. It is based on the value of χ^2 of a certain constitutive model, and defined as

$$\varepsilon = \frac{\sqrt{\dfrac{\chi^2}{n-q}}}{\sigma_{\text{ref}}}, \tag{3.5}$$

where n is the number of data points considered, q is the number of parameters of the strain-energy function, which in our case is five, and hence $n-q$ is the number of degrees of freedom. The value σ_{ref} is the sum of all Cauchy stresses for each

data point divided by the number of all data points.

3.3 Results

Anamnesis

Table 3.1 shows the anamnesis of the patients (specimens *I-XIII*) in terms of age, sex, primary disease, and cause of death. Furthermore, the condition of the aorta, coronary, cerebral and renal arteries with regard to atherosclerosis, taken from the postmortem report, is provided. It is evident that there is a correlation between the anamnesis of a patient and the mechanical properties of arteries (see, e.g., the review article [109]), and hence it seems to be important to get a complete picture of the arterial mechanics of aged patients (see also [73], [75]).

Geometry and Axial In Situ Stretch

The outer diameter of the mid-LADs (middle segments of LADs) investigated from 13 hearts is 4.5 ± 0.3 mm (mean ± SD). Mean values and related SDs of length, width, and thickness of the total wall for the 55 samples prepared are 7.21 ± 1.21, 2.81 ± 0.38 and 0.87 ± 0.23 mm, respectively, with a length/width ratio of 2.61 ± 0.70. It is most likely that this length/width ratio implies the desired homogeneous stress-strain state within the gage range (Saint-Venant's principle). The ratio of the total wall thickness to outer diameter of all specimens *I-XIII* investigated is 0.189 ± 0.014 (mean ± SD), and the average wall thickness computed from the number of samples for each segment was related to the respective outer diameter. The thickness values for each arterial layer, i.e. adventitia, media, intima, for all specimens *I-XIII* investigated ($n = 26$ for each layer) are 0.34 ± 0.08, 0.32 ± 0.11, 0.24 ± 0.17 (mean ± SD; dimensions in mm), respectively. The values for the ratios between the adventitia, media, intima, and the total wall thickness are 0.40 ± 0.03, 0.36 ± 0.03, 0.27 ± 0.02 (mean ± SD), respectively.

The axial *in situ* stretch is 1.044 ± 0.06 (mean ± SD). Statistical analysis was performed to test for significant correlations between age and axial *in situ* stretch. For this, Pearson's correlation coefficient (*r*) was calculated, and the *P* value was determined based on Student's *t*-distribution. $P < 0.05$ was considered significant.
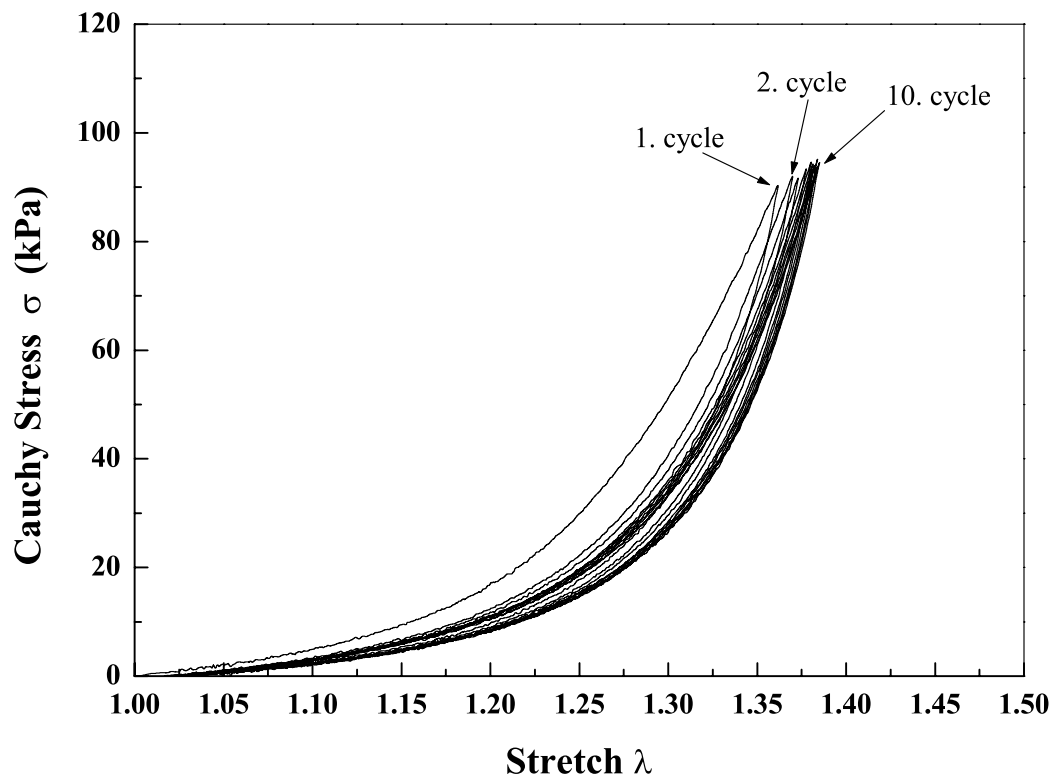
Figure 3.1: Preconditioning behavior of a human coronary artery layer (intima strip sample in circumferential direction from specimen *IV*).

There were significant negative correlations between age and axial *in situ* stretch ($r = -0.80, P = 0.017$). This suggests that axial *in situ* stretches of human LAD decrease with age.

Tissue Preconditioning, Stress-Stretch Behavior

Figure 3.1 shows a representative plot of the pre-conditioning behavior of an intima strip sample with 10 load-cycles. As can be seen, the hysteresis loops shift during repeating loading-unloading cycles towards a larger deformation and converge to a certain deformation with smaller hysteresis. We know that the number of pre-conditioning cycles depends on the origin of the specimen (species, localization, type, age, etc), and in the literature up to 15 pre-conditioning cycles are used [116]. It turned out that for the pre-conditioning of the present specimens five loading-unloading cycles were sufficient.

The stress-stretch plots in Figs. 3.2-3.4 show the mechanical responses, i.e. Cauchy stress σ versus stretch λ, of the different arterial tissues in the circumferential

(a)

(b)
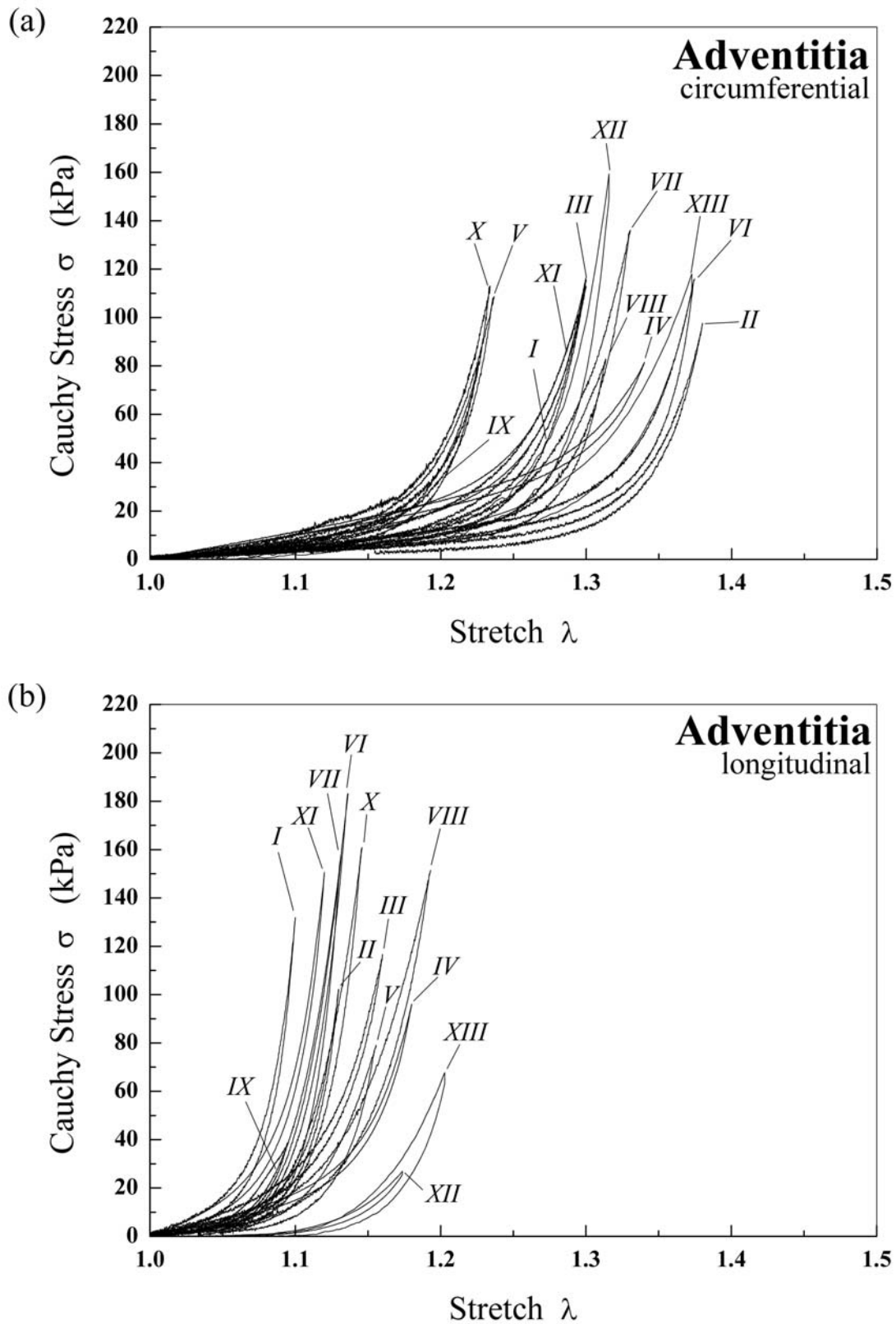
Figure 3.2: Uniaxial tensile stress-stretch responses for adventitia samples *I-XIII* in the circumferential (a) and longitudinal (b) directions.

and longitudinal directions for all specimens *I-XIII* investigated. As can be seen, all three tissue types exhibit a pronounced anisotropic and nonlinear mechanical response with remarkably small hysteresis over finite strains.

In order to check whether the tissue properties do change over the time period between death and mechanical testing or not, we correlated that time period with the stretch at 40 kPa (Cauchy) stress for all tested media strip samples. We computed Pearson's correlation coefficients of $r = -0.426, P = 0.147$ (for circumferential samples) and $r = 0.064, P = 0.870$ (longitudinal), while $P < 0.05$ was considered significant. Hence, this data indicate insignificant correlation. Additionally, we have computed Pearson's correlation coefficients for the intima and adventitia samples, which also indicate insignificant correlation. This result was expected since intima and adventitia samples are bradytrophic tissues for which the proteolytic activity is delayed for several days after death.

Ultimate Tensile Stresses and Related Stretches

The ultimate tensile stresses of the coronary arterial tissues, say σ_{ult}, were computed from the experimentally determined fracture forces according to

$$\sigma_{\mathrm{ult}} = \frac{f_{\mathrm{f}}}{WT} \lambda_{\mathrm{ult}}, \tag{3.6}$$

where f_{f} is the fracture tensile force, W, T are the width and the thickness of the strip sample in the unloaded configuration, respectively. The ultimate stretch ratio λ_{ult} was computed as l/L, where l and L are the measured gage lengths in the loaded (state at fracture) and unloaded configurations, respectively. The average ultimate tensile stresses $\overline{\sigma}_{\mathrm{ult}}$ and the associated ultimate stretches $\overline{\lambda}_{\mathrm{ult}}$ for the individual tissues from two separate orientations, which fractured in the gage region are indicated in Table 3.2. (There were 40 samples.)

Histology

Histological analyses of the specimens showed homogeneous diffuse intimal hyperplasia (see Fig. 3.5), which occurs due to a non-atherosclerotic process [130] — intimal cells (mainly myofibroblasts) proliferate concentrically and lead to an increase of extracellular matrix (containing mainly collagen fibers), and to thickening of the intima to restore baseline wall stress. In the present study the mean

(a)

(b)

Figure 3.3: Uniaxial tensile stress-stretch responses for media samples *I-XIII* in the circumferential (a) and longitudinal (b) directions.

Table 3.2: *Ultimate tensile stresses and stretches for samples obtained from (adventitia, media, intima) of specimens* I-XIII.

| | Arterial Layer and Orientation | | | | | |
| | Adventitia | | Media | | Intima | |
	AC ($n = 5$)	AL ($n = 6$)	MC ($n = 9$)	ML ($n = 7$)	IC ($n = 6$)	IL ($n = 7$)
$\overline{\sigma}_{\mathrm{ult}}$, kPa	1430.0 ± 604.0	1300.0 ± 692.0	446.0 ± 194.0	419.0 ± 188.0	394.0 ± 223.0	391.0 ± 144.0
$\overline{\lambda}_{\mathrm{ult}}$	1.66 ± 0.24	1.87 ± 0.38	1.81 ± 0.37	1.74 ± 0.28	1.60 ± 0.29	1.55 ± 0.40

Values are mean ± SD; n ... number of specimens which fractured within the gage region. σ_{ult} ... Ultimate tensile stress; λ_{ult} ... ultimate stretch; AC and AL ... circumferential and longitudinal adventitia; MC and ML ... circumferential and longitudinal media; IC and IL ... circumferential and longitudinal intima.

thickness value of the intima was 27% of the total wall thickness. The occurrence of the elastic lamellae in the media was not easily discernable.

Constitutive Modeling

The constitutive parameters μ, k_1, k_2, φ, ρ for the individual tissue layers of all 13 specimens are summarized in Table 3.3. Additionally, the error measures, mean values and related standard deviations are stated.

Figure 3.6 shows a comparative study between the circumferential and longitudinal stress-stretch responses of samples obtained from the three arterial layers (specimen *IX*). In particular, a comparison between experimental data, indicated by circles and squares, with numerical results obtained from the strain-energy function (3.1), indicated by solid lines, is provided. Figure 3.7 summarizes the stress-stretch model results by using mean constitutive parameters taken from Table 3.3.

3.4 Discussion

One important issue in cardiovascular solid mechanics is the determination of the mechanical properties of human arterial walls with non-atherosclerotic intimal thickening under various loading conditions. Clearly, aged human arterial
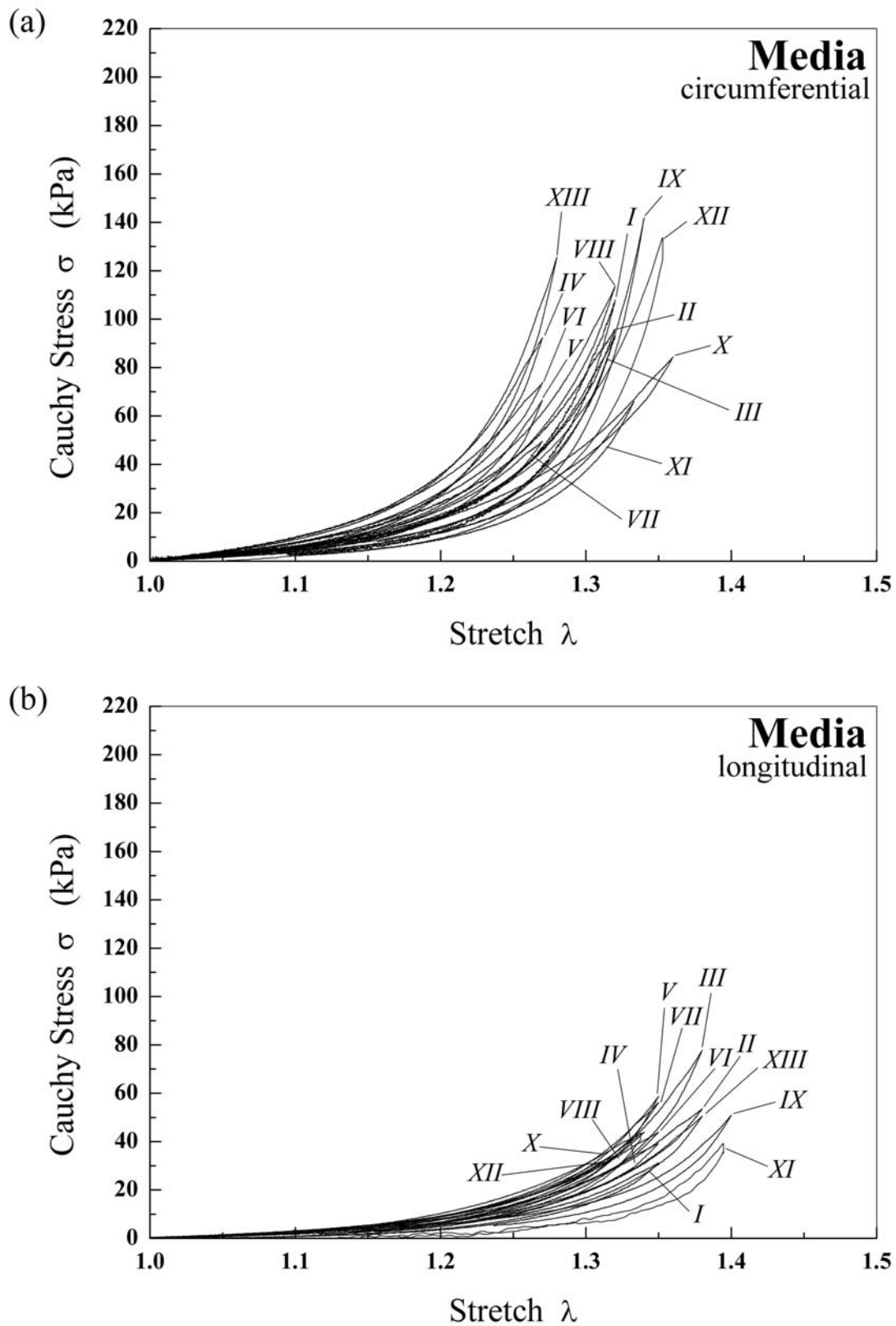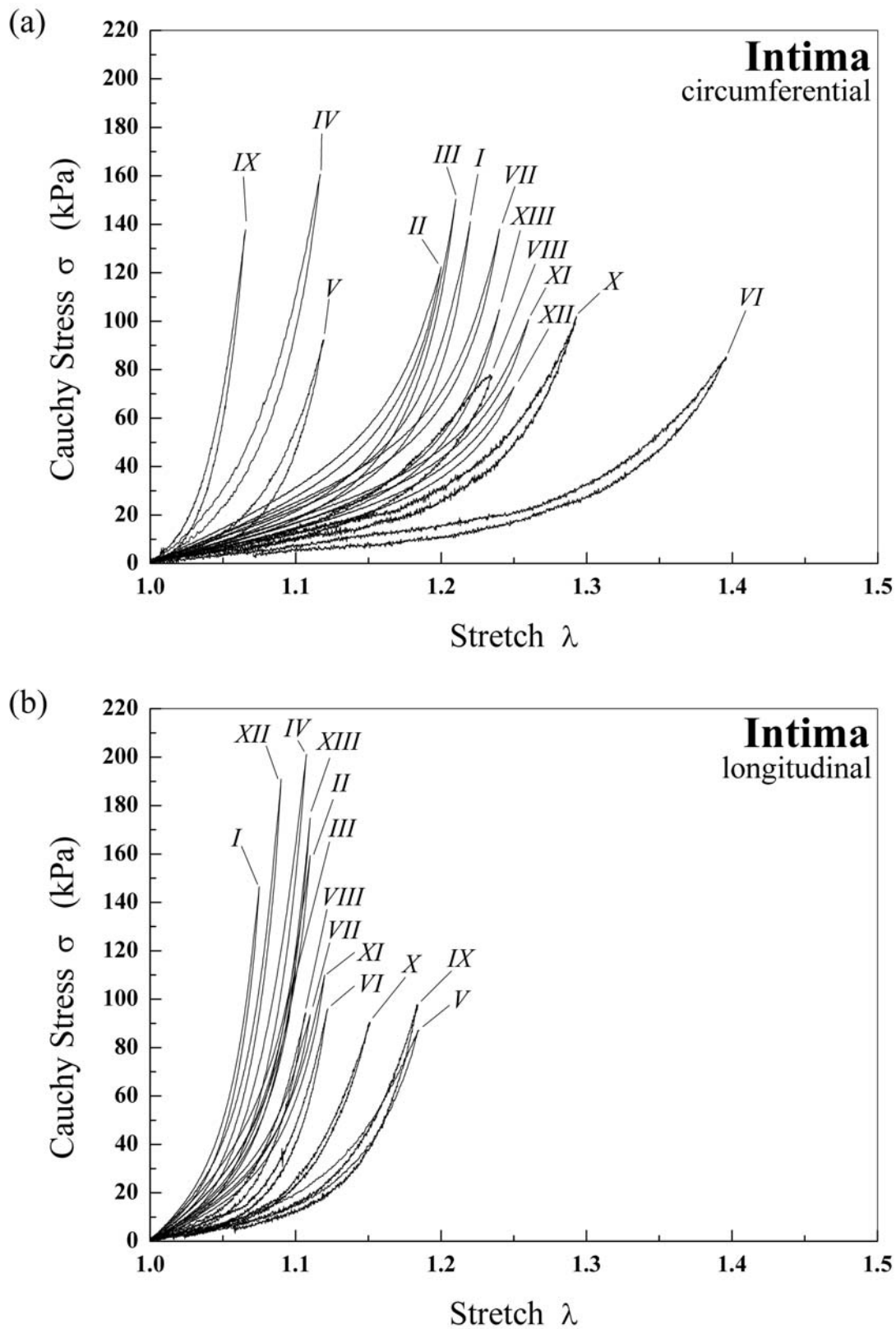
Figure 3.4: Uniaxial tensile stress-stretch responses for intima samples *I-XIII* in the circumferential (a) and longitudinal (b) directions.

walls are heterogeneous three-layered composites with layer-specific histological features and mechanical functions. There is a need to better characterize the underlying mechanics of the individual tissue types, in particular of LAD coronary arteries. This issue is of clinical importance *vis à vis* morbidity and mortality, and also of crucial interest for the stent producing industry.

Geometry and Axial In Situ Stretch

A few studies report the LAD diameter and thickness of human subjects; however, sometimes the location is not documented. Based on four (male) human LAD coronary arteries (63.5 ± 7.9 yr, mean ± SD), Canham et al. [121] reported outer diameters for proximal LADs (4.30 ± 0.47 mm) and for distal LADs (2.5 ± 0.37 mm). They used histological sections from which measurements were obtained. According to [121] the outer diameter decreases significantly from the proximal to the distal region, and the intimal layer shows decreasing dominance for the more distal segment, but remains the dominant layer in comparison to the media and adventitia. Kang et al. [137] report a luminal diameter of 2.9 ± 0.2 mm (15 mid-LAD segments) by using quantitative coronary angiography (47.4 ± 2.5 yr, male/female = 9/6), which coincides very well with the values obtained in our study. Besides atherosclerotic LAD coronary arteries, Gradus-Pizlo et al. [138] measured the geometry of mid-LADs of 5 patients with normal coronary angiograms (mean age: 57; range 48 to 77) by using high-frequency transthoracic and epicardial echocardiography. From the images the average outer diameter (4.0 mm) and wall thickness (1.0 mm) were measured (average wall thickness/diameter ratio = 0.25). Richardson and Keeny [124] reported thicknesses of intima samples of human coronary arteries in the range of 0.15-0.35 mm. Lu et al. [119] presented morphometric data for porcine coronary arteries (RCA and LAD), documenting a wall thickness/luminal diameter ratio at a transmural pressure of 100mmHg of 0.05. The mean intima/media/adventitia thickness ratio for the human mid-LAD segments investigated is 27/36/40, while in aged human iliac arteries this ratio is 13/56/31 [73].

In the literature no data concerning the axial *in situ* stretches of human and animal coronary arteries can be found. They are, however, of fundamental importance for the computation of *in situ* stress states. In the present study the axial *in situ*

(a)

(b)

(c)
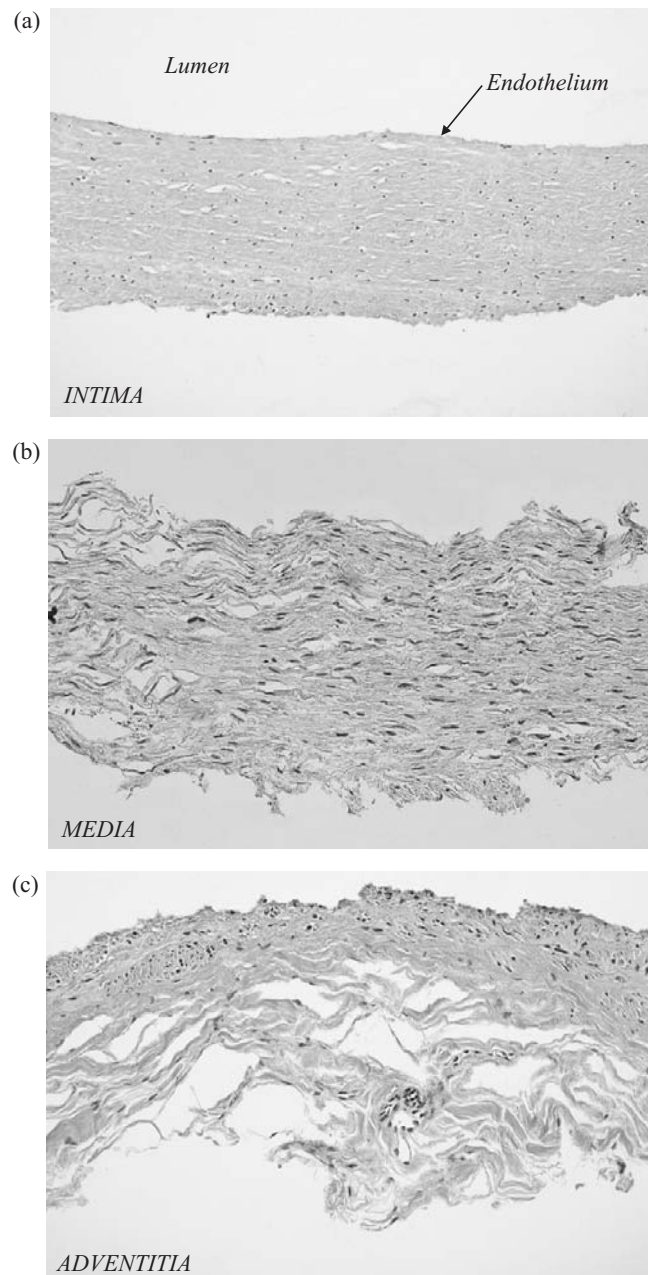
Figure 3.5: Photomicrographs of 3-μm-thick hematoxylin-and-eosin-stained sections from wall layers in longitudinal direction stemming from the gauge section after anatomical separation and mechanical testing. (a): intima. Note homogeneous thickening due to diffuse intimal fibrous hyperplasia. (b): media. Note mainly short-appearing nuclei and muscular fibers, indicating longitudinal direction of the artery; separation of some smooth muscle cells may have occurred during testing. (c): adventitia. Note tendency to separate because of loose collagen fibers in the outer part. Original magnification 200x.

Table 3.3: *Constitutive parameters and error measure for adventitia, media, and intima of specimens* I-XIII.

Specimen No.	μ	k_1	k_2	φ	ρ	ε
			Adventitia			
I	4.04	32.50	103.63	72.7	0.65	0.043
II	2.41	13.78	81.02	67.6	0.75	0.056
III	4.91	67.23	49.47	61.3	0.50	0.026
IV	16.41	8.42	37.16	75.7	0.95	0.028
V	9.65	82.06	144.98	53.4	0.40	0.070
VI	7.92	25.36	67.85	70.3	0.70	0.072
VII	7.07	23.86	7.01	74.5	0.55	0.080
VIII	2.25	37.06	48.36	65.8	0.40	0.046
IX	6.16	32.89	167.31	75.3	0.30	0.045
X	14.93	119.25	213.81	53.4	0.60	0.074
XI	12.71	35.14	84.65	69.3	0.60	0.063
XII	3.13	17.20	67.92	55.3	0.40	0.085
XIII	6.69	6.60	32.18	76.2	0.35	0.075
Mean	7.56	38.57	85.03	67.0	0.55	0.059
±SD	±4.66	±32.53	±58.94	±8.5	±0.18	±0.020
			Media			
I	0.94	13.28	10.81	21.0	0.25	0.024
II	1.09	25.77	5.93	25.8	0.30	0.063
III	1.79	21.01	5.77	23.0	0.20	0.023
IV	1.63	26.40	9.57	25.6	0.40	0.037
V	2.54	16.67	13.85	17.0	0.20	0.078
VI	0.73	30.61	5.36	18.7	0.30	0.036
VII	0.93	24.91	7.52	12.3	0.15	0.053
VIII	0.32	27.95	5.43	10.9	0.20	0.034
IX	2.31	8.45	12.84	24.9	0.30	0.065
X	0.85	31.17	2.57	16.4	0.10	0.023
XI	1.21	12.98	8.41	29.7	0.30	0.046
XII	0.96	21.54	7.77	20.5	0.15	0.015
XIII	1.19	20.10	10.87	22.2	0.40	0.082
Mean	1.27	21.60	8.21	20.61	0.25	0.045
±SD	±0.63	±7.12	±3.27	±5.5	±0.09	±0.022
			Intima			
I	28.62	124.01	180.43	69.5	0.55	0.054
II	42.43	264.32	286.97	53.7	0.70	0.067
III	25.30	234.48	176.34	57.8	0.50	0.075
IV	53.95	1860.70	454.42	46.8	0.40	0.043
V	24.75	369.53	343.14	39.9	0.70	0.057
VI	15.93	35.45	42.66	71.3	0.72	0.107
VII	34.66	54.80	92.74	72.3	0.35	0.157
VIII	26.17	60.10	110.34	74.2	0.35	0.070
IX	20.30	182.59	228.58	13.1	0.40	0.039
X	27.47	32.42	72.38	66.0	0.40	0.056
XI	26.16	56.26	77.80	66.3	0.50	0.066
XII	16.50	80.22	73.72	78.2	0.65	0.041
XIII	20.39	72.75	81.94	74.7	0.45	0.035
Mean	27.90	263.66	170.88	60.3	0.51	0.067
±SD	±10.59	±490.95	±125.47	±18.2	±0.14	±0.033

μ (kPa), k_1 (kPa), k_2 (dimensionless), φ (degrees), and ρ (dimensionless) are from Eqs. (3.1) and (3.2), and ε (dimensionless error measure) is from Eq. (3.5).

(a)

Circumferential experimental data

Longitudinal experimental data

Model prediction

Adventitia of specimen *IX*

$\mu = 6.16\,\text{kPa},\ k_1 = 32.89\,\text{kPa},\ k_2 = 167.31$
$\varphi = 75.3°,\ \rho = 0.30$

(b)

Circumferential experimental data

Longitudinal experimental data

Model prediction

Media of specimen *IX*

$\mu = 2.31\,\text{kPa},\ k_1 = 8.45\,\text{kPa},\ k_2 = 12.84$
$\varphi = 24.9°,\ \rho = 0.30$

(c)

Circumferential experimental data

Longitudinal experimental data

Model prediction

Intima of specimen *IX*

$\mu = 20.30\,\text{kPa},\ k_1 = 182.59\,\text{kPa},\ k_2 = 228.58$
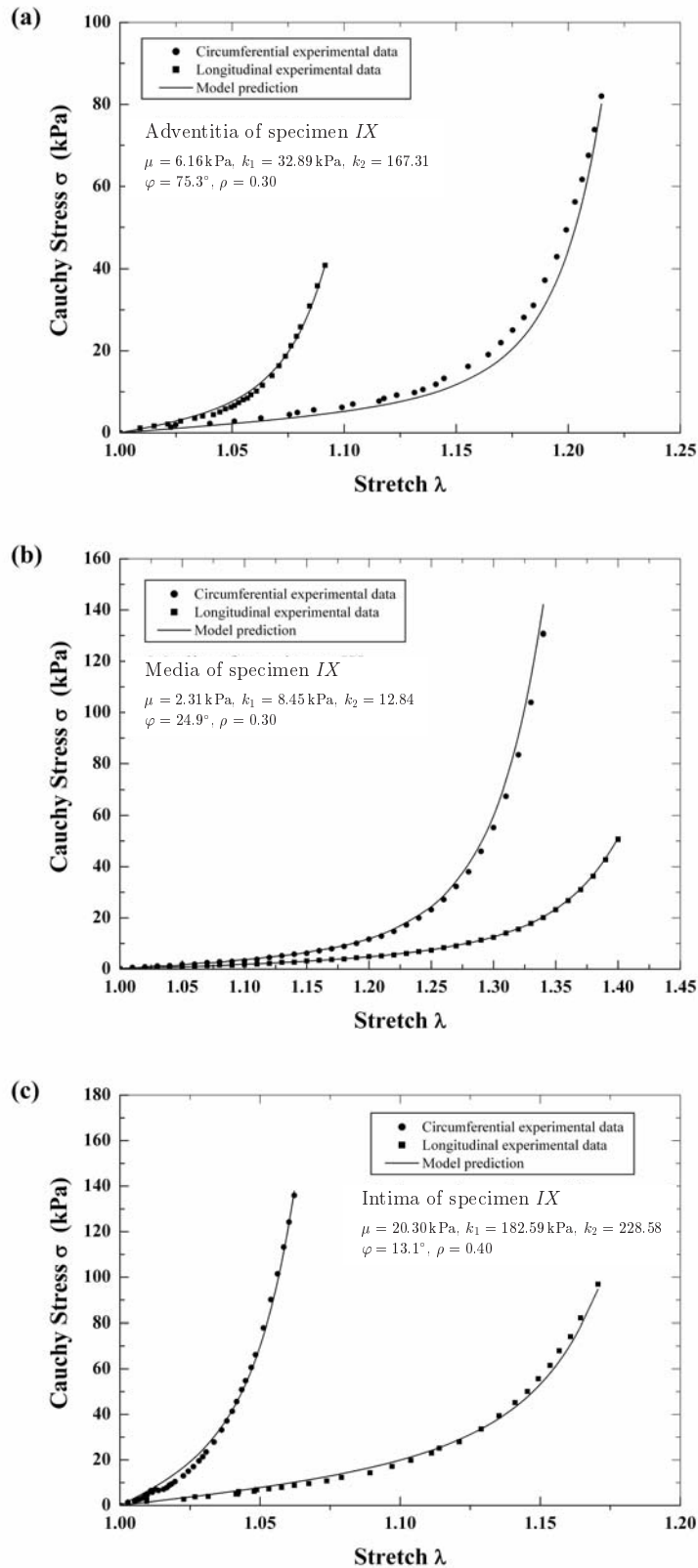$\varphi = 13.1°,\ \rho = 0.40$

Figure 3.6: Circumferential and longitudinal stress-stretch responses of samples from layers of a human LAD coronary artery (specimen *IX*). (a): adventitia. (b): media. (c): intima. Experimental data (● and ■) are compared with numerical results obtained from the strain-energy function (Eq. (3.1), solid lines).

stretches were determined to be 1.044 ± 0.06 (mean $\pm$ SD), which is an average of about 5% pre-stretch with respect to the load-free length. For iliac arteries, e.g., Schulze-Bauer et al. [73] measured an axial *in situ* stretch of 1.071 ± 0.087 (10 external iliac arteries; 52-87 yrs). Note, however, that Fung et al. [139] reported axial *in situ* stretches of 1.5 for rabbit iliacs.

Layer-Specific Stress-Stretch Behavior

As can be seen from Figs. 3.2-3.4 the different arterial tissues exhibit a marked mechanical heterogeneity. In the light of these data it is clear that a single layer approach for characterizing the mechanical response of human coronary arteries and for performing local stress analyses is inappropriate. In addition, pronounced nonlinear, inelastic, and anisotropic mechanical responses over finite strains for all arterial tissues are observed. The adventitia samples and the samples of the intima tested in the longitudinal direction show the most pronounced nonlinearity. All tissues tested indicate initially compliant, but then stiffer behavior over finite stretches for both orientations. This justifies the model assumption of a rather soft matrix material, into which the collagenous fibers are embedded. By 'stiffness' we shall mean subsequently the ratio of the Cauchy stress to the associated extension ratio, i.e. stretch -1. Hence a small gradient indicates low stiffness (e.g., see specimen *VI* in Fig. 3.4(a)), while a larger gradient indicates higher stiffness (e.g., see specimen *IX* in Fig. 3.4(a)). Another common mechanical characteristic is the occurrence of relatively small hysteres is, although coronary arteries are of the muscular type. Small hysteres is indicate s how energy dissipation in the material during load cycles.

Next, we discuss briefly the major mechanical features of the individual tissue s. The stress-stretch curves for the adventitia indicate quite a large dispersion amongst the individual samples, and a clear anisotropic behavior is evident (see Fig. 3.2). The adventitia samples oriented in the circumferential direction stiffens at a much higher stretch than those tested in the longitudinal direction. The dispersion of the stress-stretch curves for the media samples is much smaller than for adventitia samples (see Fig. 3.3). Also the media shows a clearly pronounced anisotropic behavior, with the mechanical response of strips in the longitudinal direction tend ing to be softer than for those in the circumferential direction. The
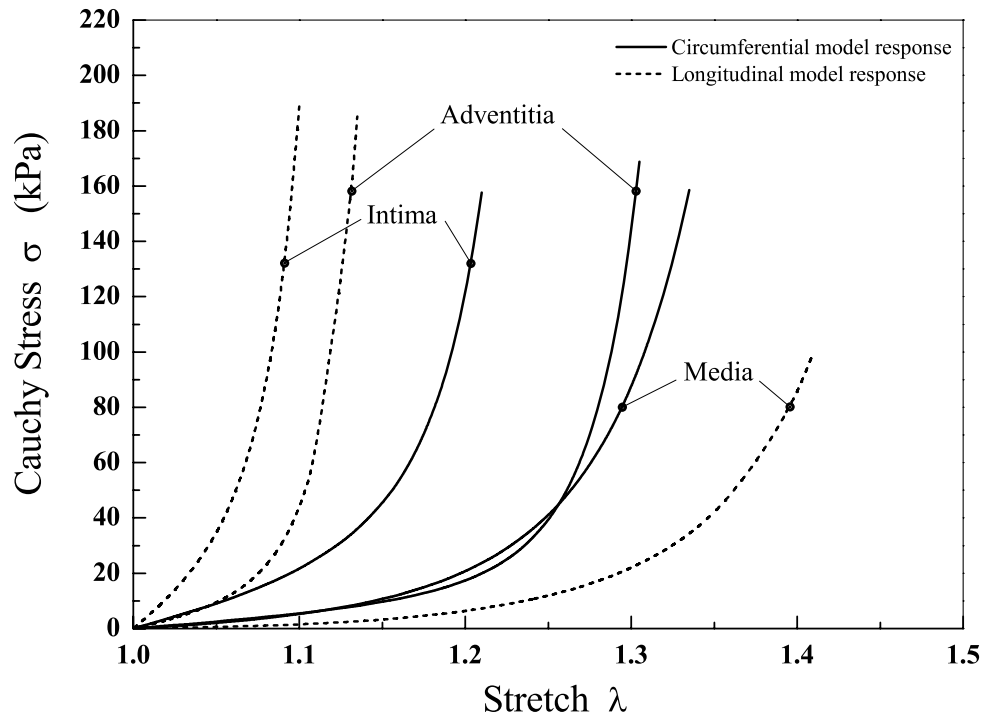
Figure 3.7: Stress-stretch model response representing the mean of all mechanical data of adventitia, media, and intima in circumferential and longitudinal directions obtained from the midportion of human left anterior descending coronary specimens *I-XIII*. Mean constitutive parameters are from Table 3.3.

dispersion of the intimal stress-stretch curves obtained from samples tested in the longitudinal direction is much smaller than for samples in the circumferential direction (see Fig. 3.4). Interestingly, adventitia and intima samples tested in the longitudinal direction (Figs. 3.2(b) and 3.4(b), respectively) exhibit a tendency to be stiffer than corresponding samples in the circumferential direction, while for the media samples the opposite is the case. The proceedings [124] also documents significant anisotropy in human coronary intima, with the same characteristics as shown in the present study. The apparent anisotropy, in particular for the adventitia and the intima, may be caused by the organization of the collagen fibers, which are almost entirely responsible for the resistance to stretch in the high loading domain [140].

Based on the experimental data obtained the media seems to be the softest layer over the whole deformation domain, and the intima and adventitia exhibit con-

siderable stiffness, particularly in the high loading domain.

Ultimate Tensile Stresses and Related Stretches

The values for the ultimate tensile stresses of the media and intima are (very) similar, and there appears no systematic difference between the longitudinal and circumferential directions. As far as the intima samples are concerned this finding is analogous to that in [124], where stress at fracture varied over the range from 133-490 kPa. In our study the strip samples from the adventitia, however, show, on average, about three times higher ultimate tensile stresses than for the related media and intima samples (see Table 3.2). The ultimate tensile stretches are similar for all layers. Similar experiments on strip samples of human descending aortas were performed by Mohan and Melvin [141]. Their results on ultimate tensile stresses and stretches are comparable with those obtained from the adventitial samples in our study, although Mohan and Melvin tested non-separated strips.

Constitutive Model

Dictated by the anisotropic and nonlinear mechanical response of the arterial tissue, an extended version of a previously published constitutive model was used ([134], [135], see also [136]). The model involves a small number of material parameters so that a least-square procedure avoids problems of non-uniqueness associated with their sensitivity to small changes in the data, as pointed out, e.g., by Fung [23], Section 8.6.1, or [134].

The average stiffness of the tissue s in the low loading domain (at which the non-collagenous matrix material is mainly active) is lowest for the media ($\mu = 1.27 \pm 0.63$ kPa), and highest for the intima ($\mu = 27.90 \pm 10.59$ kPa), see Table 3.3. The average stiffness of the individual tissue in the high loading domain, dominated by the recruitment of collagenous fibers, is governed by the parameters k_1, k_2. They are also lowest for the media ($k_1 = 21.60 \pm 7.12$ kPa, $k_2 = 8.21 \pm 3.27$ kPa), and highest for the intima ($k_1 = 263.66 \pm 490.95$ kPa, $k_2 = 170.88 \pm 125.47$ kPa). This indicates that also in the high loading domain the intima shows significant stiffness.

The dimensionless parameter $\rho \in [0, 1]$ ranges between zero and one. If $\rho = 0$ the second term of eq. (3.1) reduces to an isotropic (rubber-like) model, similar to that proposed in [142]. If $\rho = 1$ the second term in eq. (3.1) reduces to an

anisotropic model proposed in [134]. Hence, the parameter ρ is a measure of anisotropy. In the present study the mean values of ρ are similar for the adventitia and intima ($\rho = 0.55 \pm 0.18$ and $\rho = 0.51 \pm 0.14$, respectively), and smaller for the media ($\rho = 0.25 \pm 0.09$), which indicates less anisotropic behavior than for the other two tissues.

The error measure ε is very close to zero for all arterial layers. This indicates a very good correlation between the model and the experimental data for all arterial layers and specimens (see, e.g., Fig. 3.6, which relates to specimen *IX*). This supports the use of the constitutive model (3.1) employed. By taking the mean values of the five constitutive parameters for each arterial layer (Table 3.3) we get a kind of 'standard model', which reflects the mean of all mechanical data obtained from the human mid-LAD specimens tested. Although the variances among individual specimens are large the different mechanical characteristics of the individual tissues become clear. The standard model response s in the form of stress-stretch curves are illustrated in Fig. 3.7, which may serve as a constitutive basis for addressing more complex boundary-value problems.

Implications for Vascular Physiology and Mechanobiology

Our experimental data attempt to emphasize the heterogeneous properties of the arterial wall and the importance to model a mid-LAD coronary artery with non-atherosclerotic intimal thickening as a structure composed of three solid mechanically relevant layers with layer-specific constitutive behavior. This is particularly relevant if stress-strain distributions through the wall thickness are of interest. This study reveals that the intimal samples of the human vessel segments investigated demonstrate remarkable thickness, load-bearing capacities and mechanical strengths. The intima may therefore contribute significantly to vascular physiology. In addition, ultimate tensile stress data suggest that at higher levels of pressure the adventitia changes to a stiff 'jacket-like' tube which prevents the artery from overstretch and rupture; see also the discussion in [69].

The exciting challenge of vascular mechanobiology (and mechanopathology) is to explore the correlation between biological processes such as growth, remodeling and disease, and the mechanical environment of the different vascular tissues expressed in terms of quantities such as stresses and strains. Hence, constitutive

models for the individual vascular tissues with biomechanical, mathematical and computational efficacy are needed. To date many of the existing arterial wall models are based on a (single-layer) homogeneous wall structure, and, therefore, on the assumption that the mechanical properties do not change through the wall thickness. Increased insight in to the mechanical properties and geometrical dimensions of the individual vascular tissues, in particular, from human coronary arteries, are also of pressing need for applications in biomedical engineering. For example, we know that the dimensions of stent struts, which are in contact with the intimal surface of the arterial wall, have a strong effect on the stress concentration in the intima, and in the clinical outcome after stenting (see, e.g., [143], [136]); stent struts may lead to intimal laceration and to endothelial cell denudation (see, e.g., [144], [145]), which is a local effect. Hence, in that specific case, e.g., knowledge of the mechanical properties of the intima is important.

Limitations and Open Problems

The determination of the passive mechanical properties of arterial walls is not only based on the distribution and orientation of tissue elements (layers) but also on their coupling, which was not investigated here. Hence, continued research is required in order to identify the related mechanics of tissue interconnection. In addition, a relatively small number of tissue samples was investigated so that a meaningful correlation between biomechanical properties of the different arterial tissues and related anamnesis could not be quantified.

Another limitation of the study is the fact that the structural integrity at the lateral edges of the strips is disturbed. For example, collagenous fibers that are cut off during preparation may retract spontaneously, which can lead to alterations in the tensile response. Although the strips tested in the axial and circumferential directions were always taken from neighboring locations, they are different samples with probably more or less different (composition and) mechanical properties. Since we were only able to prepare strip samples for uniaxial extension tests, the data provided do not cover the whole physiological domain. The design of a new micro-tester that can measure the biaxial properties of small specimens may help to extend the present data. Note, however, that it is theoretically impossible to characterize the 3D response of anisotropic elastic materials by planar biaxial tests

alone. In this context biaxial tests (or, equivalently, extension-inflation tests) have little if any advantage over separate uniaxial tests at different orientations. Composition of the specimens may also vary throughout their dimension. The assumption of homogeneity, in particular for the adventitia, may result in an under-estimate of stress values for the inner part of the adventitia, because the outer parts, in which the collagenous fibers are less tightly packed (see Fig. 3.5(c)), are likely to be less load bearing. Similarly, to consider the individual tissues as incompressible materials may also lead to an under-estimate of stress values, because a stress-induced fluid extrusion, in particular from the outer part of the adventitia, as documented in Fig. 3.5(c), would be associated with smaller cross-sections and thus with higher stress values.

In addition, a small number of samples fractured within the gage section, although a second sample could sometimes be prepared and tested. Dumb-bell shaped samples might increase the success rate of fracture tests. Since fiber angles can directly enter the constitutive formulation it would also be valuable to obtain information about the concentration and three-dimensional structural arrangements of collagen and (medial) smooth muscle components in the different tissues. More research is needed in order to characterize this important aspect of vascular physiology. The present study has focused on the heterogeneity of the arterial wall of human LAD coronary arteries with non-atherosclerotic intimal thickening, although residual stretches were not accounted for. Considering the marked differences in the mechanical properties of the three arterial tissues, one may anticipate that there must be layer-specific residual stresses that ensure balanced stress distributions in the loaded configuration.

Despite strong legal and institutional restrictions imposed on the use of human material, the high inter-specimen variation and the occurrence of irregular specimens due to atherosclerosis, investigators of vascular solid mechanics should consider the use of human arteries for at least two reasons: (i) they allow an anatomical separation into their tissue components and, therefore, the investigation of the underlying mechanics of the individual tissue types, and (ii) an exploration of the mechanics of human arteries from aged patients is most likely to have direct and significant clinical implications, because several cardiovascular diseases occur later in life and are treated by vascular implants. Although aged human arteries

represent only a specific group of vessels, they seem to provide a promising basis for significant advances in the field of layer-specific vascular physiology and mechanobiology.

4 *IN SITU* TENSILE TESTING OF HUMAN AORTAS BY SMALL-ANGLE X-RAY SCATTERING

Abstract. The collagen diffraction patterns of human aortas under uniaxial tensile test conditions have been investigated by synchrotron small angle X-ray scattering. Using a recently designed tensile testing device the orientation and d-spacing of the collagen fibers in the adventitial layer have been measured in situ with the macroscopic force and sample stretching under physiological conditions. The results show a direct relation between the orientation and extension of the collagen fibers on the nanoscopic level and the macroscopic stress and strain. This is attributed first to a straightening, second to a reorientation of the collagen fibers, and last to an up-take of the increasing loads by the collagen fibers.

4.1 Introduction

According to WHO World Health Report cardiovascular diseases make up for roughly 30% of total global deaths (WHO, 2004) [146]. With a percentage of about 50%, the situation is even more alarming in developed countries (Petersen et al., 2004; Statistik Austria, 2008) [147, 148]. Major causes for cardiovascular disease are biochemical and biomechanical changes in the wall of a blood vessel or a narrowing of its diameter. This narrowing of the artery is the cause for 'classic' diseases such as ischemic stroke and heart attack. An increase of the diameter can be achieved by applying, e. g. an angioplasty, which represents a mechanical solution for a clinical problem. It is the most frequent therapeutical intervention world wide (Fleisch and Meier, 1999) [149] with great and steadily growing medical, socioeconomical and scientific interest (American Heart Association, 2008) [2]. Although this is meanwhile a standard procedure, there is still a lack of understanding of the detailed mechanisms during this treatment. A profound description requires an in-depth knowledge of the function and interaction of the relevant biological tissues based on their (macro- and nano-) structure and mechanics. Elastomechanical and

structural studies have been carried out mostly on tendons (Mosler et al., 1985; Sasaki et al., 1999; Fratzl et al., 1998; Puxkandl et al., 2002; Wess et al., 1998; Orgel et al., 2001; Parry & Craig, 1979; Parry, 1988; Castellani et al., 1983; Marchini et al., 1986) [150–159]. Few investigations were performed on collagen-poor tissues such as rat skin or bovine perimysium (Purslow et al., 1998) [160]. Measurements on blood vessels have been done on the basis of uniaxial and biaxial extensions tests or on inflation tests with internal pressure (Roveri et al., 1980; Bigi et al., 1981; Bigi et al., 1984) [161, 162]. However, animal tissue has been used. Experiments on human arteries investigating the layer-specific macroscopic stress-strain behavior have been carried out by Holzapfel et al. (Holzapfel et al. 2004, Holzapfel et al. 2005) [75, 76]. These experiments on human tissue were sufficient to study the mechanical responses of the different arterial layers on the macroscopic level. However, they did not provide nano-structural information about the collagen orientation. In earlier studies, layer-specific tests on different animal arteries have been carried out to relate smooth muscle fiber and collagen fiber orientation (Re et al., 1979; Re et al., 1980ab) [163–165]. Collagen fiber orientations of different human arteries at constant stretch have been studied by the group of Canham using polarized light microscopy (Canham et al., 1989, 1991, 1992; Finlay et al., 1995, 1998; Rowe et al., 2003) [121, 166–170]. These studies provided approximate information about the orientation and the quantity of collagen fibers at the fixed states. A thorough understanding of the macro- and nano-structural interaction under stress in arterial tissue is still missing. Eventually, macromolecular structural changes and their relation to physiology and pathology are the key to clinical application. Many of the experiments mentioned above have been performed under non-physiological conditions and did not use human tissue. The tendon tests were mainly performed to understand the principal behavior of collagen itself. Some tests (Bigi et al., 1981; Re et al., 1979; Roveri et al., 1980) [161–163] provided 'snapshots' and no continuous in situ information. Layer-specific quasi-static tests on human arterial tissue using time-resolved synchrotron radiation and related physical and numerical models provide information for the development of clinical applications. In this in situ study synchrotron radiation was used to investigate time-resolved changes in the orientation and d-spacing of collagen fibers in the individual layers of human aortas, which consist of three major layers. The results for two samples taken from the adventitia — the outermost layer
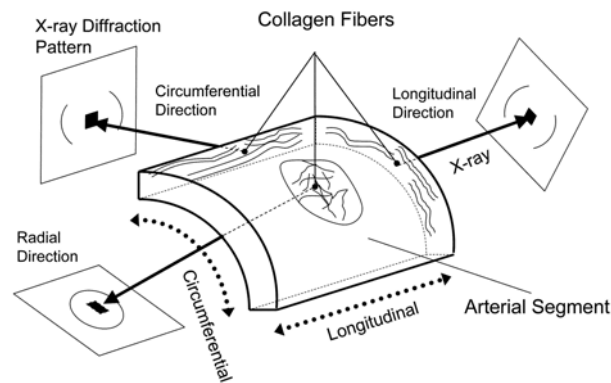
Figure 4.1: Sketch of an arterial segment and the embedded collagen fibers. The corresponding expected diffraction patterns of the meridional peak from the gap-overlap periodicity of collagen are shown for different directions. The collagen fibers are oriented in axial layers inside the arterial wall, but show no correlation between them in radial direction. As a consequence, due to the random orientation, an almost circular diffraction pattern is measured in radial direction.

— are presented here. The samples were cut from the same artery, one in the longitudinal and the other one in the circumferential direction. The adventitia can be considered as a composite made up from extracellular matrix and embedded fibers, such as collagen and elastin fibers (see for example, (Silver et al., 2001) [171]). The sketch in Fig. 4.1 shows the fiber alignment in the arteria according to Purslow and others (Purslow et al., 1984) [172]. Our sample strips were measured in radial direction only and were kept in a physiological environment during uniaxial tensile tests. Representative parameters such as force, displacement and lateral contraction were recorded simultaneously. Further details on the sample preparation, the descriptions of the tension cell and on the data analysis are given in section 4.2. Results of the macro- and nanostructural changes during tensile testing are demonstrated with an example, and discussed in section 4.3. Finally, a summary and an outlook is given in section 4.4.

4.2 Materials and Methods

4.2.1 Sample Preparation

The arteries from human cadavers were excised during autopsy within 24 h from death and were frozen directly after they became available. Use of autopsy material from human subjects was approved by the Ethics Committee, Medical University Graz, Austria. Before preparation, the excised arteries were defrosted and stored in a 0.9% physiological saline solution at a temperature of 37±0.1°C. The samples considered for testing were prepared on the day before the X-ray measurement. The arteries were pruned from remaining connective tissues and cut in axial direction to get a rectangular flat sheet. The layers were separated by pulling apart and — where necessary — through careful disconnection of the interconnective tissue with a scalpel. The layer preparation process was not always successful since either macroscopic inspection or the prepared histological images inspected afterwards have proven that the result was not the desired single arterial layer. From these separated layer sheets strips in axial and circumferential orientations were cut out with a sharp knife (for prepared strip samples see, for example, Fig. 3 in Holzapfel et al. (2004) [75]). Pieces of sand paper were then attached to the ends of the strip samples for better clamping and to prevent slippage during testing. Two black markers were glued point wise with cyanoacrylate adhesive gel (Henkel, Vienna, Austria) in parallel onto the middle part of the samples, which served as gauge markers for the axial deformation measurements with the video extensometer (Fig. 4.2). For representative tissue samples see, for example, Fig. 4 in Holzapfel et al. (2004) [75]. Thickness of the sample in the gauge region was measured before testing.

Also during measurements the samples were immersed in a calcium-free 0.9 % physiological saline solution at a temperature of 37±0.1 °C. Finally, after experimental testing and X-ray measurements the samples were stored in alcohol for histological examinations.
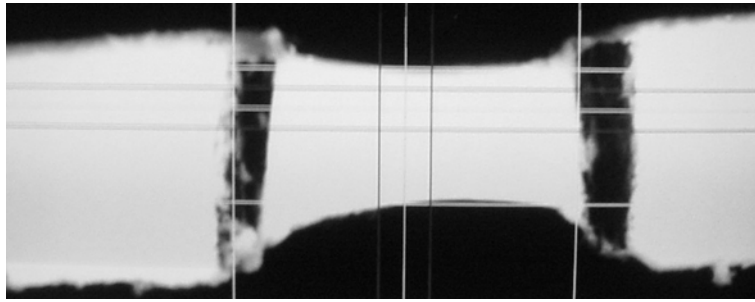
Figure 4.2: Stretching of a representative sample as viewed by the video-extensometer. The black vertical lines are the markers for length measurements (length is in the horizontal direction in the image).
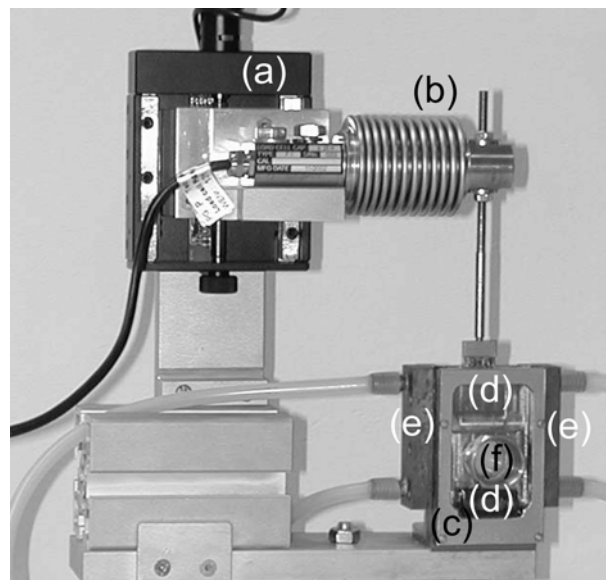
Figure 4.3: Tension cell: the sample is mounted between two clamps (d), of which the upper one is moved by a translation stage (a). Force is measured using a load cell (b), on which the upper clamp is mounted.

4.2.2 Sample Stage and Mechanical Measurements

The sample stage shown in Fig. 4.3 was designed specifically for uniaxial experiments. The sample was mounted inside the sample container (c) between two clamps (d). The upper clamp was mounted onto the 25 N load cell (b) (Type F1/25N, class 1 according to DIN 51220, Messphysik, Fürstenfeld, Austria), which itself was

attached to the motorized linear translation stage (a) M-126 (Physikinstrumente (PI), Karlsruhe, Germany). The minimum incremental motion was 0.1 μm and the maximum velocity was 1.5 mm/s. With the given travel range of 25 mm a maximum extension of at least 3% might be achieved. The sample container was made from a U-shaped stainless steel bar. The front plate was made from Plexiglas which, for sample-mounting, could be easily attached and removed. Rubber sealings kept the tension cell leak proof. The back plate was made from stainless steel. Both plates contained circular-shaped X-ray windows (f), of which the distance was adjustable to minimize background scattering and absorption arising from water. These X-ray windows were made of 10 μm thin poly-ethylene-terephthalate film (Kalle GmBH, Wiesbaden, Germany), and were tested to give negligible contribution to the measured intensities. Two copper blocks (e) on either side of the container were used as a heat exchanger. The temperature was controlled by a water bath within $0.1°$C in the range of 0–90°C (Unistat CC, Huber, Offenburg, Germany). Prior to testing, the samples were subjected to cyclic loading and unloading until the typical stress softening effect diminished and the material exhibited a nearly repeatable cyclic behavior (the material is then said to be 'pre-conditioned'). It turned out for the preconditioning of the present specimens that three loading-unloading cycles were sufficient. We have used a constant crosshead speed of <0.05 mm/s, and the final length was the same for all subsequent tests. After these three cycles the force at maximum elongation remains rather constant. The uniaxial extension tests documented in this work were performed as a displacement-driven process at a very slow constant speed (<0.05 mm/s). A video-extensometer ME-46 (Messphysik, Fürstenfeld, Austria) determined online the change of length and width of an area in the middle of the sample. Using a 50 mm lens and an OS-65-D camera (Mintron, Taipei, Taiwan) with a frequency of 25 Hz a resolution of better than 1 μm was achieved. The video-extensometer calculated the distance between the two black markers that were carefully attached onto the comparably bright sample set perpendicular to its length axis (Fig. 4.2). Two coldlight sources with optical fiber light guide illuminated the sample and the surrounding area to give a bright and contrast rich image for the video-extensometer camera. The edge of the bright sample and the dark background defined another pair of lines that were analyzed by the video-extensometer to measure the lateral contraction.
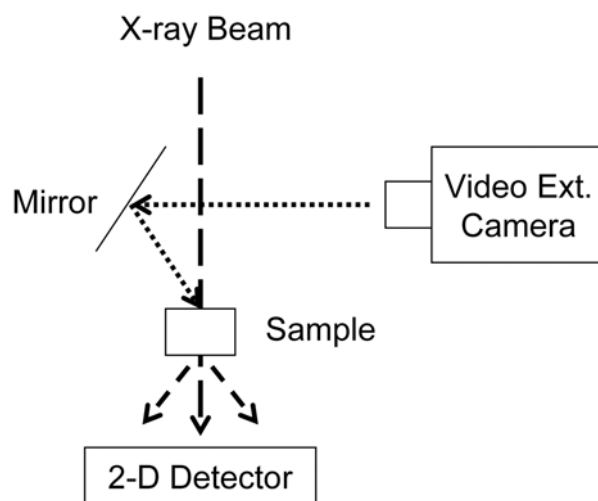
Figure 4.4: Schematic drawing of the set-up as installed in the beamline.

Figure 4.4 shows the set-up of the measurement schematically. A visible image of the sample was reflected by a mirror to the video-extensometer camera. Correction for the distortion of the video-extensometer image — caused by the position of the mirror — was performed. For further details concerning the X-ray set-up see 2.3 X-ray Measurements. All instruments and process variables of the sample stage were controlled and logged, respectively, by a PC using specifically developed programs in LabView (National Instruments, Austin, Texas, USA).

4.2.3 X-ray Measurements

All diffraction patterns were recorded at the Austrian SAXS beamline at ELET-TRA, Trieste (Amenitsch et al. 1998; Bernstorff et al. 1998) [173, 174] using a two-dimensional image intensified CCD detector (Model CV 12, Photonic Science Ltd., Millham, UK). The sample to detector distance was set to 2.3 m to cover the corresponding s-range ($s = 2\sin(\Theta)/\lambda$, with Θ as Bragg angle, and λ as X-ray wave length) of interest from about $1/980\,\text{Å}^{-1}$ to $1/55\,\text{Å}^{-1}$ at an X-ray energy of 8 keV. The angular calibration of the detector was performed with dry rat tail tendon, which has a d-spacing of 640 Å (Bigi et al., 1991) [175]. Two images taken with rat tail collagen oriented in the horizontal and vertical direction were used to determine

the beam center. During the time course of the mechanical stretch and release the diffraction patterns were taken continuously with an integration time of about 10 s each depending on the scattering power of the samples.

4.2.4 Data Analysis

All the SAXS images were corrected for electronic dark noise, spatial distortion and detector efficiency. Furthermore, they were transformed from Cartesian (Q_x, Q_z) into polar coordinates (radial component Q_R , azimuthal angle φ, see also Fig. 4.5) ((Purslow et al., 1998) [160], as prior suggested by (Roveri et al., 1980) [161]). This data reduction was performed with the software package Fit2D (Hammersley et al., 1995) [176]. All the following steps were performed using specially developed routines written in Mathematica (Wolfram Research, Champaign, USA). The images were normalized for intensity fluctuations of the primary beam, occasional 'zingers' were eliminated with a median filter. After the background was subtracted by fitting 3rd order polynomials to the intense 3rd order Bragg peak, the resulting peak data were analyzed both in azimuthal and radial directions. Therefore, a boxed area around the peak was integrated in the desired directions (compare inset of Fig. 4.5). The first outcome represents the azimuthal intensity distribution, whereas the center of the radial intensity distribution was used for the determination of the d-spacing. For intensity distributions of one complete experiment, all the corresponding frames were assembled and smoothed with a median and a 'Lee' filter (Lee, 1986) [177]. Both, the azimuthal and the radial distributions were fitted with Gaussians. The force F and the geometrical parameters of the sample delivered from the video-extensometer, i.e. the current sample length L and the current sample thickness W, are used to calculate stress and strain of the different specimens. Knowing the initial sample volume $V_0 = L_0 \cdot W_0 \cdot T_0$, in uniaxial extension tests the current stress σ is given by

$$\sigma = \frac{F \cdot L}{L_0 \cdot W_0 \cdot T_0},$$ (4.1)

where L_0, W_0 and T_0 denote the initial length, width and thickness of the sample, respectively. The strain ε is defined as

$$\varepsilon = \frac{L - L_0}{L_0}.$$ (4.2)

During elongation the thickness T of the sample decreases, and hence also the diffracted intensity diminishes. This effect has been accounted for by normalizing the intensity I to the sample thickness

$$\tilde{I} = \frac{I}{T} \propto I \cdot L \cdot W,$$ (4.3)

where $\tilde{I}$ is the normalized intensity.

4.3 Results and Discussion

Measurements were carried out on all samples (in the longitudinal and circumferential directions) obtained from the three layers of the excised aortas. The results presented here refer to two samples taken from the adventitia along the longitudinal and the circumferential directions.

Two representative static X-ray diffraction patterns for the adventitial sample in the circumferential direction are shown in Fig. 4.5, which were taken before preconditioning (left) and at maximum stretch in the last precondition cycle (right). The diffraction patterns display an intensity distribution which is typical for wet connective tissue samples containing collagen fibers (type I and III). The d-spacing of the collagen structure was determined to be 654 Å which agrees well with the value of Folkhard et al. (1987) [178]. Generally, in the unstretched state, the collagen fibers in the sample are rather homogenously distributed as seen in the broad arch of the 3rd order reflection (left), whereas at the maximum stretch (right) an orientation of the fibers towards the load axis is apparent (small arch). To quantify the orientation of the fibers the azimuthal intensity distribution of the strong 3rd order peak has been analyzed as shown in the insert of Fig. 4.5 (see also subsection 4.2.4.). In the unstretched state (left hand side in Fig. 4.5) the Full Width at Half Maximum (FWHM) of the azimuthal intensity distribution $\Delta\varphi$ has a value of 63.9°, which decreases to 21.9° for the stretched sample (right hand side in Fig. 4.5). After preconditioning the FWHM of the relaxed sample is 56.2°. For the longitudinal sample, the corresponding values were determined to be 87.0°, 38.0° and 78.0°, respectively. Thus, preconditioning, the requirement to reach steady state mechanical conditions, results already in a pronounced alignment of the collagen fibers towards the applied force.

Figure 4.5: Typical diffraction patterns of an unstretched, not preconditioned (left) and a stretched (right) adventitia cut in circumferential direction. The load axis is in Q_z direction. The strongest meridional peaks of collagen are indicated by their orders. The Half Widths at Half Maximum (HWHM) of the azimuthal intensity distributions are given explicitly for both load cases in the corresponding diffraction pattern. Further the transformation from Cartesian (Q_x, Q_z) into polar coordinates (Q_R, φ) is indicated. In the insert the 3rd order reflection of the stretched adventitia is represented in polar coordinates. The boxed region indicates the area for the radial and azimuthal integration, respectively. The peak shape in both, φ and Q_R direction are nearly Gaussian.

During a dynamic measurement the general behavior of the mechanical parameters are demonstrated in Fig. 4.6A. With elongation of the sample, the force increases and the sample undergoes lateral contraction (width and thickness). On release the inverse phenomena are observed. For a series of diffraction patterns (about 200 frames) recorded during the tensile test (load/unload) the azimuthal intensity distribution of the 3rd order reflection is extracted to obtain the fiber orientation in situ. The result is presented in Fig. 4.6B for a strip oriented in the longitudinal
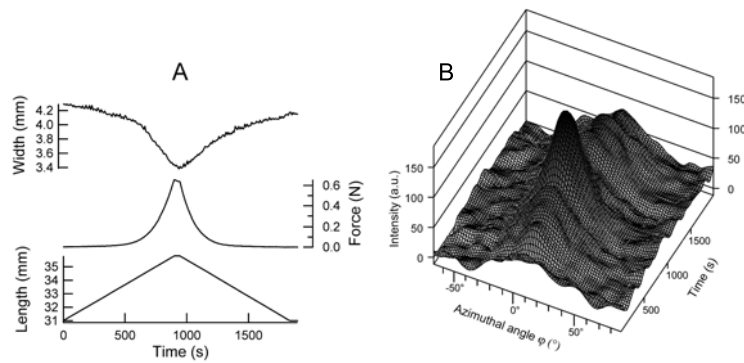
Figure 4.6: Typical time course of width, force and length during a tensile test. A circumferential adventitia was stretched at constant speed corresponding to an initial strain rate of 0.005min^{-1}. At maximum extension a strain of about 0.2 was reached. B: Azimuthal intensity distribution of the 3rd order Bragg peak during a complete cycle. After about 1000s the maximum load is reached, and the azimuthal intensity distribution is clearly sharper than at the beginning of the experiment (no load), i.e. the fiber orientation has reached its maximum at this point (compare also with Fig. 5). Thereafter the fibers get relaxed (time > 1000s) and the azimuthal intensity distribution smears out again.

direction. During elongation of the sample a continuous alignment of the collagen fibers in the loading direction can be observed, i.e. the azimuthal intensity distribution clearly narrows.

The two stress-strain plots of a loading/unloading cycle of adventitia samples in circumferential and longitudinal directions are shown in Fig. 4.7. Similar to tendon and other soft biological tissues, there is a toe region at low strains, in which strain increases without a significant increase in stress. This is followed by a heel region, when stress increases, and finally turns into a locking region at high strains, which is due to the stiffening of the collagen fibers in the tissue (see, for example, Misof et al., 1997; Holzapfel, 2001) [179, 180]. The slight hysteresis is typically seen in tensile tests of soft biological materials and is caused by small viscoelastic effects remaining after preconditioning. To assess the qualitative observation of Fig. 4.6B, the FWHM of the azimuthal intensity distribution $\Delta\varphi$, i.e. the degree of the collagen fiber orientation in the load direction, is given for both strips in Fig. 4.8.
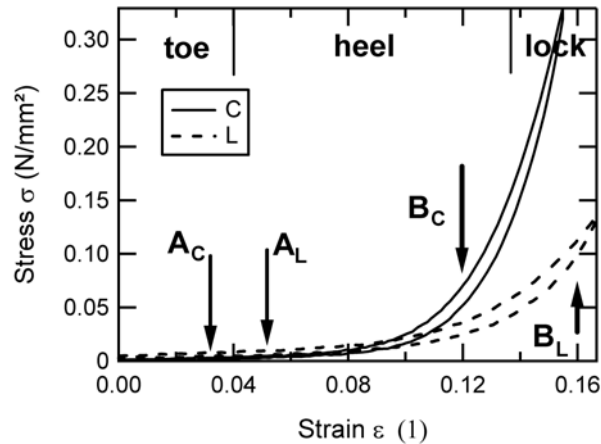
Figure 4.7: Stress-strain plots (loading and unloading) for two samples of an adventitia tested in the circumferential (C) and in the longitudinal (L) directions. Three ranges of the stress-strain plots - toe (till A), heel (range between A, B), and lock (larger than B) - are indicated. A_C, B_C and A_L, B_L give the ranges for the circumferential and the longitudinal directions, respectively.

From the azimuthal integration of the 3rd order peaks the change of the collagen d-spacing has been determined. The correlation between the increase of the fibrillar strain, i. e. the relative increase of the collagen d-spacing, and the macroscopic strain ε is shown in Fig. 4.9 again for a complete cycle. The result is qualitatively similar to the macroscopic measured stress-strain curve (Fig. 4.7). Comparing Fig. 4.7, 4.8 and 4.9, the regions — toe, heel, lock — can be identified and discussed as follows:

(i) In the toe region (until A_C, A_L) all curves show just weak dependencies on the strains. The extension is mainly caused by a macroscopic extension of the elastin in the matrix material. Moreover a microscopic straightening of the wavy collagen fibers appears (wave period about 100 μm). This is discussed for tendon collagen in the toe region in Fratzl et al., (1998) [152] and for biological tissue in Holzapfel, (2001) [180].

(ii) At the macroscopic strains ε indicated by A_C and A_L (heel region), the collagen fibers start to reorient themselves into the load direction driven by the extension of the matrix material, as it is evidenced by the continuous decrease of the fiber
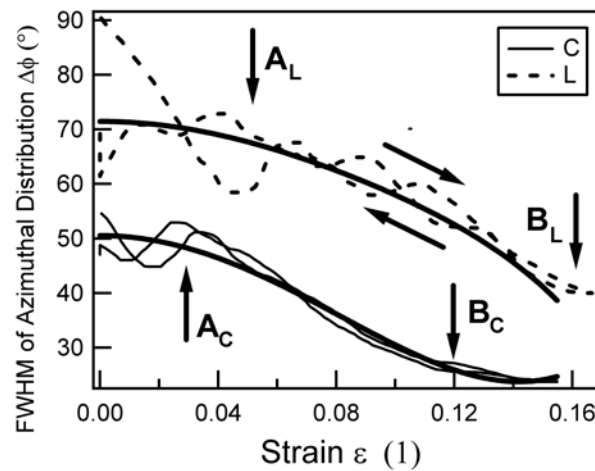
Figure 4.8: FWHM of the azimuthal intensity distribution $\Delta\varphi$ of a circumferential (C) and a longitudinal (L) adventitial sample as a function of strain ϵ for a loading/unloading cycle. The points A and B identifying the three regions of the stress-strain plot are indicated as in Fig. 7.

distribution's FWHM $\Delta\varphi$ (Fig. 4.8). This relation of the FWHM versus the strain ε was also found by Roveri et al., (1980) [161]. Around this point the fibers start to contribute to the stress, as it can be observed in the increase of the fiber strain (Fig. 4.9), although, the macroscopic stress σ still remains relatively small compared to the stress reached in the locking domain (Fig. 4.7).

(iii) At the points indicated by B_C and B_L in the Figs. 4.7 and 4.8 (locking domain), the collagen fibers reach their maximum orientation. The load is transferred from the elastin fibers to the collagen fibers, which leads to the stiffening of the adventitia.

In general, as seen from Fig. 4.9, the fibrillar strain is about one order of magnitude smaller than the macroscopic strain ε over the loading/unloading domain for both samples. This supports the assumption reported in the literature, e. g. (Purslow et al., 1998) [160], that the macroscopic strain is only partly determined by the fiber strain. Consequently the elongation of the matrix material, in which the collagen fibers are embedded, is the main driving force for the macroscopic strain. This is also found in studies of Fratzl et al., (1998) [152] and Sasaki et al., (1996) [181] for tendon collagen, in which the proteoglycan matrix is mainly responsible for the extension. In particular, for soft biological tissue, the nano- /macro-strain relation
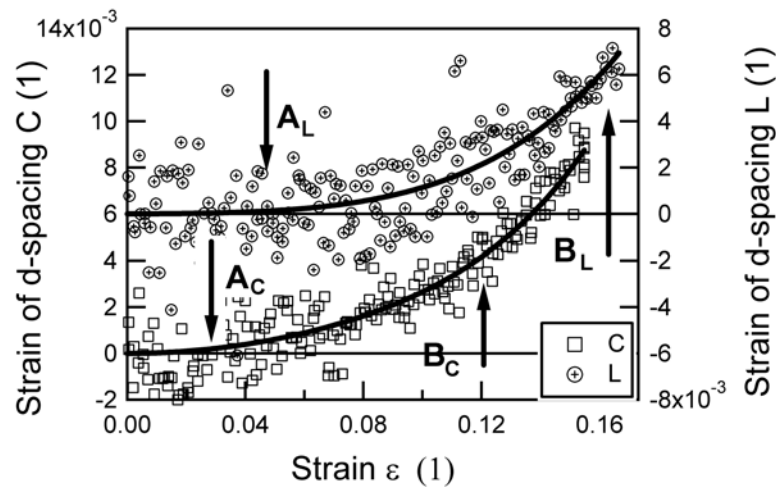
Figure 4.9: Strain of collagen d-spacing as a function of the strain ϵ for a circumferential (C) and longitudinal (L) adventitial sample. The nomenclature for the points A and B is the same as in Fig. 7 and 8.

has been discussed by Purslow et al., (1998) [160] and Bigi et al., (1981) [162]. The authors conclude that the matrix material, as in our case, is the main factor for the macroscopic strain. Comparing the data obtained from the circumferential and longitudinal samples, an important finding is that the degree of collagen fiber orientation (Fig. 4.8) is directly related to the stiffness of the arterial tissue (Fig. 4.7). The increased stiffness in the locking region of the circumferential adventitia is caused by the increased alignment of the collagen fibers into the load direction (25° circumferential against 40° for the longitudinal direction in the stretched condition (Fig. 4.8)).

This predominant alignment of the collagen fibers, consequently the increased stiffness, in circumferential direction was also attributed to the fact (Bigi et al., 1981) [162], that for a cylinder geometry under inflation pressure load the circumferential stress is twice the longitudinal one (law of Laplace). Therefore, for the adventitia, the in vivo stresses occurring in a blood vessels match the material requirements for stiffness in the corresponding directions.

4.4 Conclusion and Outlook

Biomechanics of arteries cover nearly nine orders of magnitude in size: vessels have to withstand mechanical deformation in the millimeter regime, straightening of embedded fibers occurs on a microscopical level, and the collagen fiber stretches on a nanoscopic scale. The presented method and the data of this study demonstrate the unique possibility of synchrotron radiation to investigate this complex nano- and macroscopic interplay during tensile testing experiments of biological soft tissues in situ. The three distinct regions of the macroscopic measured stress-strain diagram (heel, toe, lock) are explained by fiber straightening, fiber reorientation and fiber strain on the nanoscopic scale. This multilevel analysis is an essential prerequisite to understand the overall mechanisms in loaded biological tissues. At present a thorough analysis of the quasi-static data of all samples from the three layers is under way, and will be documented elsewhere. Nevertheless, a next step is to focus on the investigation of the viscoelastic phenomena of human soft tissues, as they occur during relaxation and creep tests. Another important perspective will be the study of the rupture behavior of human soft tissues in order to investigate the related damage/failure mechanism on the nanoscopic scale. As the ultimate goal we aim to contribute to the mathematical formulation of the existing constitutive arterial models, which may enable numerical simulations of arteries on layer-specific and nano-structural biophysical models.

5 BIDIRECTIONAL TENSILE TESTING CELL FOR SMALL-ANGLE X-RAY SCATTERING

Abstract. An X-ray cell for the acquisition of one-dimensional mechanical force-displacement diagrams of soft tissue samples has been developed. The combination of X-ray and mechanical data allows new insights into the coupling of the macroscopic behavior and nanoscopic structural changes during the application of load. Two linear μ-translation stages are used to symmetrically — i. e. bidirectionally — stretch the sample. A video-extensometer is installed to record geometrical changes of the sample during measurement which allows to determine true stresses and strains. The sample can be immersed in a liquid and heated. We demonstrate the advantages over common unidirectional tensile testing devices without length measurement systems by comparing different mechanical and diffraction data sets of human arterial tissue.

5.1 Introduction

Nowadays there is a growing interest in composite materials, both in basic and applied research. The mechanical properties of composites combine the advantages of different materials and can be tailored to specific needs. Examples of artificially produced reinforcement materials include silicon-carbide-fibers and assemblies of carbon-nano-tubes [1] [182]. Biological examples are hierarchically structured fibers such as cellulose and collagen (for a review see [2] [183]), which are found in an abundance of biological tissues. Collagen fibers are used in varying amounts in a large number of tissues to provide mechanical strength. Their concentration, distribution and orientation greatly influence the response of the tissue to applied mechanical load. This coupling of the nanostructure to macroscopic observations has been investigated in great detail [3-7] [153, 160, 161, 181, 184]. Further, understanding the mechanics of animal soft tissue is an essential requirement for the design of numerical models to simulate physiological tissue behavior, interaction

with other materials and to design tissues with similar properties. Our ultimate goal is mathematical modeling of the mechanical behavior of soft tissue with particular attention to medical intervention. For example in balloon angioplasty [8] [185], where physiologically extreme loads are applied to human blood vessels to enlarge their diameter. A balloon is inserted into an area of diminished diameter of the artery — vulgo referred to as a 'calcification' — and inflated. After deflation the restored vessel diameter enables proper bloodflow and hence the supply of tissue with oxygen. Even though this is a common procedure worldwide, the mechanical processes during the treatment are not well understood. We aim to increase the safety and success of this medical intervention. We hope to reduce the number of fatal incidences during the dilatation and to optimize the long term stability of the created lumen by none invasive analysis and computer simulation prior to intervention. A common way to understand the constitutive relationship between stress and strain of a material under uniaxial load is the comparison of stress-strain curves. However, this issue is complex for composite materials, where the constitutive equations have to describe different materials as well as their interaction. Stress is deduced from force, while strain is calculated from elongation. Therefore, the basis for a stress-strain relationship is a force-elongation curve recorded with a tensile testing device. As described in an earlier work [9] [77], geometrical changes necessary for the calculation of true stress and strain (see Fig. 5.1) can be recorded using optical techniques like a video extensometer or laser speckles [10] [186]. Contactless techniques are of crucial importance when dealing with extremely delicate samples, since any mechanical interference would falsify the measured geometrical deformations and the determination of the load. Additionally, our setup allows tensile tests of various tissue samples simultaneously with the acquisition of SAXD images at a synchrotron light source. In this manner macroscopic mechanical properties can be correlated with nanoscopic structural changes.

The present work illustrates our latest developments for a tensile testing device. Stretching is now done with two motors instead of only one. The center of the sample is fixed with respect to the direct X-ray beam at all times, i.e. during stretch the beam does no longer scan axially over a sample area (see Fig. 5.2). This avoids artifacts arising from possible tissue inhomogeneities, when neighboring tissue
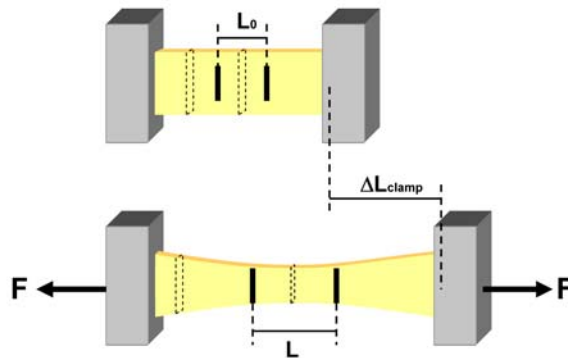
Figure 5.1: A soft tissue sample in unloaded state and stretched with the force F. The sample is mounted between two clamps. The nonlinear shrinkage of the sample width is illustrated. The central part — defined by two markers — of a sufficiently long sample can be considered as roughly cuboid. The distance of the markers allows the reconstruction of the cross sectional area and hence the calculation of the true stress.

areas contain different amounts of scattering matter.

Further we demonstrate the importance to measure the true cross section and sample length during the stretch to retrieve correct stress and strain data, respectively. In contrast, the approach to use the initial cross section and clamp distance leads to erroneous results.

5.2 Materials and Methods

5.2.1 Stress and Strain

Stress-strain diagrams are essential for the comparison of the tensile behavior of materials. They are derived from force and elongation, respectively, which are then normalized to the geometry of the sample. Force is usually normalized by dividing it by the sample cross section perpendicular to the direction of the force. The corresponding stress σ is defined as $\sigma = \frac{F}{A}$ with F being the force applied to stretch the sample and A the area of the cross section. Assuming constant volume of the sample during elongation, the diameter of the sample must shrink and with it the cross section. Due to the holding clamps, soft tissue changes from a cuboid

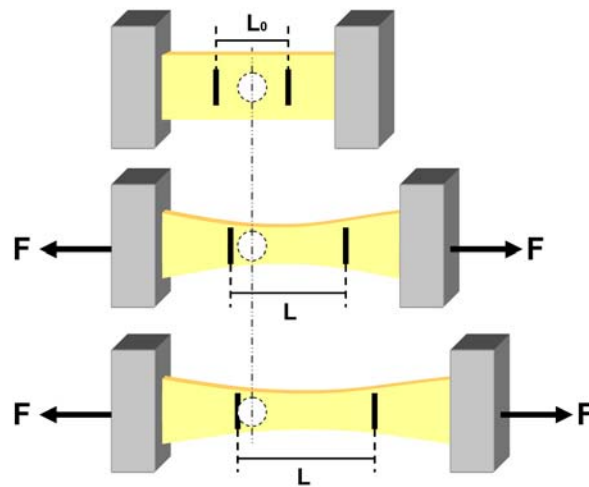Figure 5.2: Problems with inhomogeneities in the sample on unidirectional stretch. In this example the left clamp is fixed and only the right clamp moves. As the position of the X-ray beam (indicated by the dashed circle) stays constant, the part of the tissue viewed by the beam changes. In the case of an inhomogeneous composition of the tissue this will cause inconsistent signals in the diffracted images.

shape to a bone shape upon elongation, broader at the ends than in the middle. Further from the clamps, the cross section diminishes significantly to stay rather constant over a certain length in the center of a sufficiently long and homogenous sample. This behavior is shown in Fig. 5.1. Accordingly, also elongation depends on the position on the sample. Strain ε is calculated by dividing the current sample elongation $L - L_0$ by the initial sample length L_0, which results in strain $\varepsilon = \frac{L - L_0}{L_0}$. Recording the geometrical changes of the shape, however, turns out to be a non trivial task, particularly when it comes to small sample sizes, small forces and the presence of sample environments that do not allow contact measurement of the change of lengths. The approach of using the initial cross section and the current clamp distance to calculate stress and strain, respectively, underestimates the true values. Depending on the geometrical deformation, also qualitative deviations from the true stress/strain curve can result. However, this constant cross section method might be applicable to compare homogenous samples of same dimensions. For reasons of mechanical stress homogeneity, in our studies we use a small part in the center of a sample to measure and calculate true stress and strain. Only the

part of the sample defined by the markers (see Fig. 5.1) is considered and its length L and width W are measured. The initial volume of this part is $V_0 = L_0 \cdot W_0 \cdot T_0$ with L_0, W_0 and T_0 being the initial length, width and thickness, respectively. $\frac{V_0}{L \cdot W}$ equals the current thickness T. According to Carew and colleagues [11] [43] the soft tissue studied in this work can be considered as quasi incompressible, i.e. $A = \frac{V_0}{A}$. Thus, the true stress σ is given by $\sigma = \frac{F \cdot L}{V_0}$.

5.2.2 Bidirectional Stretch of the Sample

A unidirectional tensile stretching setup as described in [9] [77] is perfectly suitable for homogenous samples. However, homogeneity can not always be taken for granted in the case of biological material, like the soft tissue used in this study. If one side of the sample is fixed, every point of the sample is moving towards the end of the sample that is pulled away. Normally this does not cause problems for the macroscopic observation of the image with the video extensometer, which is only following the markers. However, if very large extensions are needed — such as in rupture experiments — it is important to keep the sample centered in the X-ray window, as only a centered sample enables the maximum stretching distance. As soon as one marker on the sample moves outside the X-ray window, the video extensometer camera can not detect it any more and the extension measurement fails. In addition, in unidirectional stretching devices problems might arise with the X-ray images (compare Fig. 5.2). Since the X-ray beam is fixed in its position, a number of different areas of the tissue are passing through the beam during the measurement. If these parts of the tissue contain different amounts of diffracting material they change the diffraction pattern, which may yield to ambiguous results and correct interpretation becomes problematic. Therefore, a second translation stage was installed to circumvent these two problems. First, this enables centered mounting of the sample to use the full size of the X-ray windows. Second, the illuminated tissue portion should stay the same unless the tissue is extremely inhomogeneous. A loss in scattered intensity should be observed, since a certain amount of tissue is constantly removed from the beam area due to the thinning of the material.
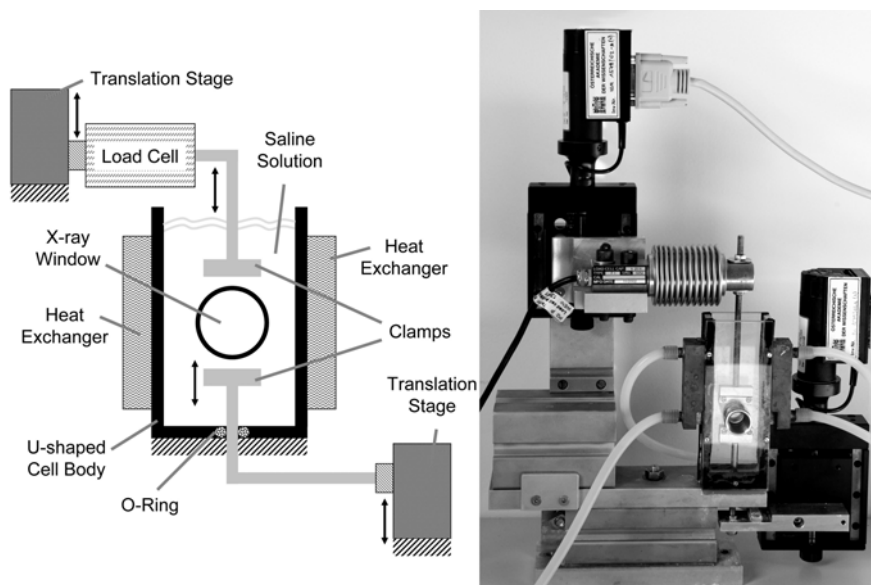
Figure 5.3: Tension cell: the sample is mounted between the two clamps, which can both be moved by PC controlled translation stages. Force is measured by a load cell mounted on the upper translation stage. Heat exchangers on either side of the cell allow to maintain a constant temperature of the tissue bath. X-rays pass through two X-ray windows.

5.2.3 Sample Stage and Mechanical Measurements

A schematic drawing and a photography of the sample stage, which is designed specifically for uniaxial tensile experiments, are shown in Fig. 5.3. The sample is mounted between two clamps inside the sample container. Both the clamps can be moved independently by motorized linear translation stages M-126 (Physikinstrumente (PI), Karlsruhe, Germany). These allow a minimum incremental motion of $0.1\,\mu$m and a maximum velocity of 1.5 mm/s. A 25 N load cell (Type F1/25N, class 1 according to DIN 51220, Messphysik, Fürstenfeld, Austria) is inserted between the clamp and the upper translation stage for force measurement.

The main part of the sample stage is a U-shaped stainless steel bar. Plexiglas plates are attached on the front and back of it with Neoprene sealings in between. An axially adjustable X-ray window covered with a $10\,\mu$m thin poly-ethylene-terephthalate film (Kalle GmbH, Wiesbaden, Germany) is mounted on either plate. This allows minimization of absorption and scattering arising from the solution,
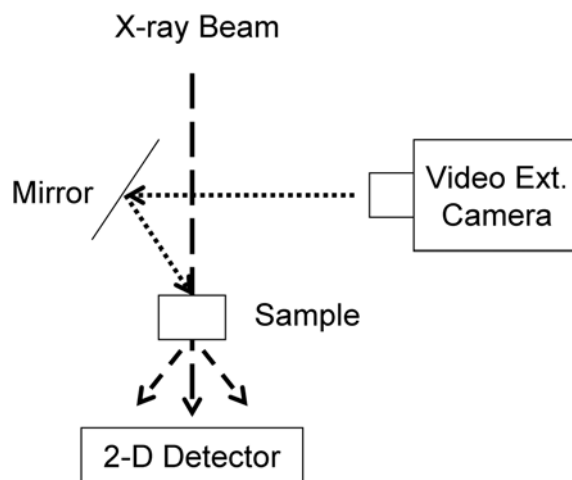
Figure 5.4: Schematic drawing (top-view) of the setup as installed in the beam-line. A mirror reflects the image of the sample to the video camera. The angle between the mirror and the X-ray beam equals almost 45ř, hence distortion of the image is negligible. Moreover the camera is calibrated to each sample.

whereas the film itself was found to give negligible contribution to the measured signal. The temperature of the tissue bath is controlled by an external water bath that can be adjusted with a precision of $0.1°C$ in the range of $0–90°C$ (Unistat CC, Huber, Offenburg, Germany). Two copper blocks are attached to either side of the U-shaped steel bar of the container for heat transfer. A video-extensometer ME-NG (Messphysik, Fürstenfeld, Austria) is used to determine online the change of length and width of the area defined by the markers in the center of the sample (see Fig. 5.4 and Fig. 5.5). The working principle of a video-extensometer is to recognize significant changes in contrast in an image that is acquired by a camera. We used the sample edges to measure lateral contraction and the artificial markers for longitudinal elongation. A coldlight source with an optical fiber light guide is used to ensure a contrast rich image. In the present setup, a 75 mm lens with a 2x converter and a digital camera (FLEA HIBW-CS, Point Grey Research, Vancouver B.C., Canada) connected to the FireWire port of a 2.4 GHz AMD computer is used. This allows theoretical data read-out frequencies of more than 200 Hz (limited by the frame rate of the camera) and a resolution better than 1 μm.
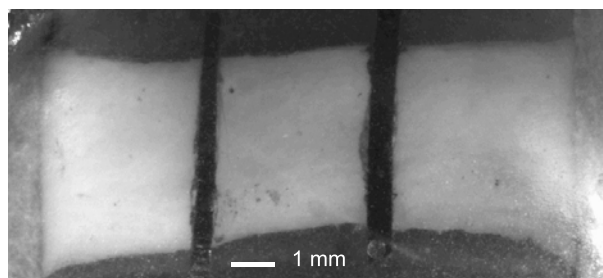
Figure 5.5: A sample as viewed by the video-extensometer. The black vertical
          lines are the markers that are used for length measurements. The
          load axis is in the horizontal direction in the image.

Fig. 5.4 shows a top view scheme of the complete setup. The X-ray beam impinges
on the sample and the diffracted image (dashed line) is recorded with a CCD
camera. The camera for the video extensometer is mounted perpendicular to the
beam. It is facing a mirror which reflects a visible image of the sample during mea-
surement. To minimize aberration errors, the mirror is set at an angle as close as
possible to 45° with respect to the X-ray beam. Before each measurement the video
extensometer is calibrated to the sample geometry. The whole setup is PC con-
trolled using specifically designed programs in LabView (National Instruments,
Austin, Texas, USA).

5.2.4 X-ray Measurements

All diffraction patterns were recorded at the Austrian SAXS beamline at ELETTRA,
Trieste ([12] [187]) using a two-dimensional image intensified CCD detector (Model
CV 12, Photonic Science Ltd., Millham, UK). The sample to detector distance was
set to 1.22 m to cover the corresponding s-range ($s = 2\sin\Theta/\lambda$, with Θ as Bragg
angle, and λ as X-ray wave length) of interest from about $1/380\,\text{Å}^{-1}$ to $1/27\,\text{Å}^{-1}$ at an
X-ray energy of 8 keV. The beamsize was 0.5 mm in axial and 1.5 mm in transversal
sample direction. The angular calibration and the beam center was determined
with silver behenate [13] [188]. For this the programs Fit2D [14,15] [176, 189]
and FibreFix from CCP13 [16] [190] were used. During the time course of the
mechanical stretch and release the diffraction patterns were taken continuously
with an integration time of typically 4 s, which varied depending on the scattering

power of the samples.

5.2.5 Sample Preparation and Conditioning

Arteries used in this study were taken during autopsy and frozen immediately. The use of the human material was approved by the Ethics Committee, Medical University Graz, Austria. Before preparation, the arteries were thawed and stored in a 0.9% physiological saline solution. The artery was cut open along the length axis and dissected into the three major arterial layers, the adventitia, media and intima, being the outer, middle and inner layer, respectively. Strips in longitudinal and circumferential direction were cut from these tissue sheets (for prepared strip samples see, for example, Fig. 5.3 in [17] [75] and Fig. 5.5). For better clamping, pieces of sandpaper were glued to the end of the samples. Further, two black markers (see Fig. 5.5) were glued perpendicular to the length axis at a distance of a few millimeters in the middle of the sample with cyanoacrylate adhesive gel (Henkel, Vienna, Austria). These markers serve as reference for the video extensometer which measures the distance of the markers. Human arteries show a non-linear stress-strain diagram. However, a number of cycles are needed to eliminate the stress softening typical of soft tissues before a nearly reproducible curve is reached. These load-unload cycles, which are done before the tests, are called 'pre-conditioning'. We found three cycles to be adequate. We have used a constant crosshead speed of <0.05 mm/s. Elongation was adapted to each sample and then kept the same for all the tests on the sample. During measurements the samples were immersed in a calcium-free buffered 0.9% physiological saline solution at a temperature of 37±0.1°C. After experimental testing the samples were stored in alcohol for histological examinations.

5.3 Performance

A typical force-elongation diagram recorded with our cell is shown in Fig. 5.6. As can be seen in panel A, the sample tests are linear clamp-displacement driven stretch-release cycles. The exponential increase of force with increasing displacement is typical for fiber reinforced soft tissues, such as the arteries tested here,
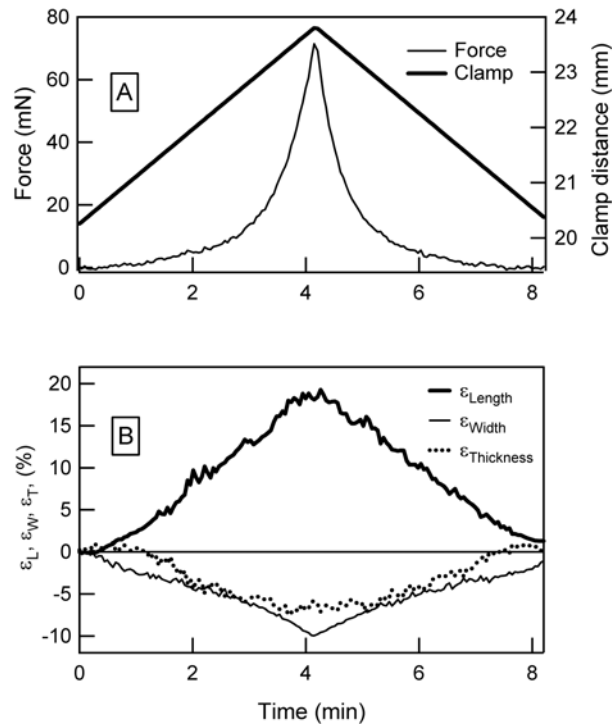
Figure 5.6: Course of different data during a stretch-release cycle. Panel A shows force and clamp distance over time. The stretch cycle was linearly displacement driven. Change of the length, width and thickness of the central part of the sample are plotted in panel B. The non-linear response of the tissue is clearly visible.

and is attributed to the fiber structure and the fiber-matrix interaction [4] [160]. Force-elongation as well as stress-strain curves of soft tissue often consist of three major regions: a rather flat 'toe' region, where no significant increase in stress is observed, followed by the onset of stress in the 'heel' region. Lastly, stress increases rather linearly in the so called 'lock' region [5,18] [153, 171]. In aortic tissue, this sequence of behaviour was attributed to first a straightening of the fiber bundles, then a rotation of the bundles towards the tensile axis and finally the extension of the fibers themselves [9] [77].

Other structural parameters determined with our setup are displayed in Fig. 5.6 B. The time course of the distance of the markers ('length') and the width of the sample in the central area are measured directly with the video extensometer (see
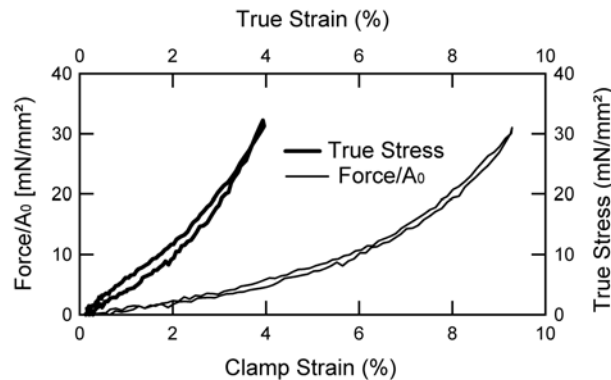
Figure 5.7: Comparison of a force/A_0-clamp strain and a true stress-strain curve. The thick line represents true stress over true strain, calculated from the marked area in the middle of the sample. In comparison, the thin line shows force divided by the initial sample cross section over clamp strain, a commonly used method to calculate stress if online length data is not available.

subsection 5.2.5). Comparing Fig. 5.6 A and B it can be seen that non-linearity strongly depends on elongation. The visco-elastic behaviour of the tissue is also shown: in panel A, the stretch and release part are not identical (i.e. not mirrored); in panel B at the end of the cycle, when the clamps have returned to their initial position, length and width have not. Sample thickness can be calculated from length and width and allows correction of the measured intensity for variation of the thickness. This is important if the absolute scattering cross section per unit volume (see e. g. [19] [191]) is derived from the measurement.

Furthermore, we would like to demonstrate that the curve of the directly measured force divided by the initial cross section (force/A_0) and clamp distance can vary significantly from the calculated true stress and strain of a particular part of the sample. Not only the absolute values, but also the shape of the curves may differ greatly. This is demonstrated with data of another sample in Fig. 5.7, where the clamp strain is very different from the true strain. We believe that the whole sample was not homogeneous in terms of strain, because strain of the total sample is larger than of the central area, which should not be the case in homogenous tissue. The maximum values for true stress and force/A_0 are nearly equal. This, however, is coincidence: the curves are generally different, because the cross sectional area
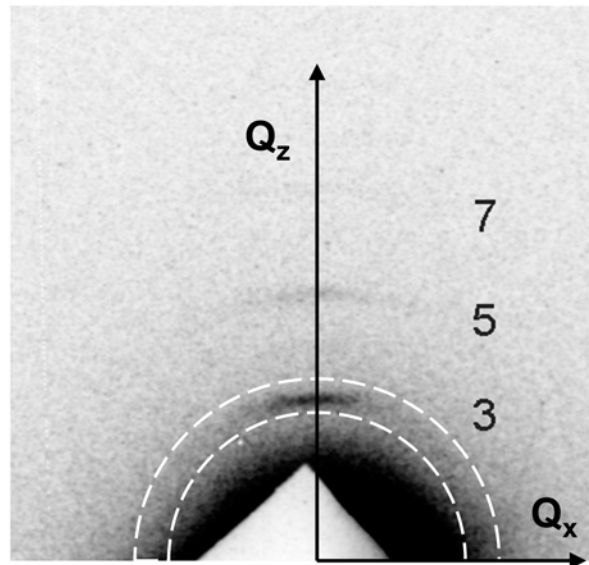
Figure 5.8: A SAXD image showing the collagen I and III diffraction peaks (indicated by numbers). The area defined by the dashed line indicates the area that was used for fitting a gaussian in radial and azimuthal direction.

diminishes during stretch (compare width and thickness in Fig. 5.6, section 2.1).

Fig. 5.8 shows a typical SAXD image of a sample in stretched state. The diffraction peaks of collagen (type I and III) are indicated with numbers. The dashed line marks the area around the 3rd order peak that was used to fit a Gaussian to the azimuthal intensity distribution (see [9] [77]). The problems that might arise in the diffraction pattern using a unidirectional stretching device are demonstrated in Fig. 5.9. In the graph the peak intensity of the Gaussian fit is plotted versus time during a stretch-release cycle for two samples. Due to the increased order of the collagen fibers under strain along the tensile axis the peak intensity should follow the course of strain. This is shown by Purslow et al. in [4] [160] for the meridional 3rd and 5th order peaks of rat skin and in Misof et al. [20] [179] for the equatorial diffuse scattering intensity of rattail tendon. The upper panel in Fig. 5.9 shows a sample with the expected relation. The data was recorded using the bidirectional stage. In the lower panel, however, the curve shows strong intensity fluctuations, yet it is still mirrored. That experiment has been done with the unidirectional stage, the clamp has been moved around 10 mm. The size of the
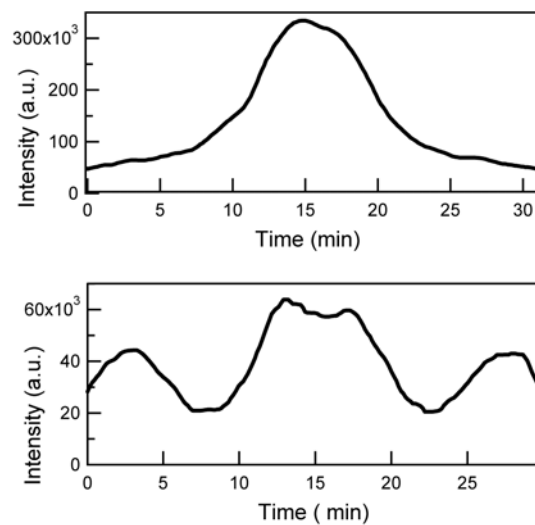
Figure 5.9: Peak intensity during a stretch-release cycle. The amplitude of the Gaussian fit of two stretch-release experiments is plotted versus time. In the upper panel a measurement taken with the bidirectional stage is shown. The increase in intensity roughly follows the course of stretch of the sample. The lower panel depicts the intensity of a unidirectionally stretched sample. There is clear evidence that the beam scanned across areas of different homogeneity, as the curve is irregular yet mirrored with the centre being at around 15 minutes when stretch turned into release.

beam of only 0.5 mm in the direction of load and the movement of the sample due to the unidirectional stretch support the assumption that the unexpected changes in signal intensity arise because the beam is scanning across sample regions of varying collagen content. It can be assumed, that an area containing such different amounts of scattering tissue also varies in mechanical properties. Hence, it is particularly important to make sure to probe only one single spot of the sample instead of scanning a continuously changing area.

5.4 Summary and Outlook

Uniaxial stretching devices cause a continuous movement of all the spots of a sample in respect to a fixed point of reference, the X-ray beam for instance (see Fig. 5.2).

In case of tissue inhomogeneities, this might introduce artifacts, as is explained in detail in section 5.3 and Fig. 5.9. A bidirectional stretching device, however, ensures the stability of the position of the center of a sample, hence the X-ray beam is constantly probing the same spot on the sample. A further advantage is the full use of the size of the X-ray window, which is particularly important for experiments where sample stretch is much larger than in normal stretch-release experiments, such as at controlled rupture. With a bidirectional device a misalignment of sample center and beam is no longer inherent to the system and in normal cases the center of the sample stays practically constant during stretch. However, severe tissue inhomogeneities might still cause central deviation and the initially illuminated sample volume might not remain perfectly aligned with the X-ray beam. Consequently, an auto alignment system shall be installed to correct for this and to keep the sample centered at all times. The issue that will be addressed in the future is the extension to a second axis while conserving full functionality. A biaxial stretching device using 4 motors but without force measurement has been described by Liao et al. [21] [192]. The strategy to replace two uniaxial measurements with one biaxial test is important, as two perpendicular uniaxial tests represent only the two extreme cases of 2-dimensional stretch.

6 LAYER-SPECIFIC 3D RESIDUAL DEFORMATIONS OF HUMAN AORTAS

Abstract.   Data relating to residual deformations in human arteries are scarce. In this paper we investigate three-dimensional residual deformations for intact strips and for their separate layers from human aortas in their passive state. From 11 abdominal aortas with identified anamnesis, 16 pairs of rings and axial strips were harvested, and the rings cut open. After 16 h images of the resulting geometries were recorded, and the strips were separated into their three layers; after another 6 h images were again recorded. Image processing and analysis was then used to quantify residual stretches and curvatures. For each specimen histological analysis established that the intima, media and adventitia were clearly separated, and the separation was atraumatic. Axial *in situ* stretches were determined to be 1.196 ± 0.084. On separation, the strips from the adventitia and media shortened (between 4.03 and 8.76% on average), while the intimal strips elongated on average by 3.84% (circumferential) and 4.28% (axial) relative to the associated intact strips. After separation, the adventitia from the ring sprang open by about 180° on average, becoming flat, the intima opened only slightly, but the media sprang open by more than 180° (as did the intact strip). The adventitia and intima from the axial strips remained flat, while the media (and the intact strip) bent away from the vessel axis. This study has shown that residual deformations are three dimensional and cannot be described by a single parameter such as 'the' opening angle. Their quantification and modeling therefore require consideration of both stretching and bending, which are highly layer-specific and axially dependent.

6.1 Introduction

For over a century it has been considered that when removed from the body blood vessels are stress free [39, 44, 58, 62, 193–198], although this assumption has been questioned [39]. Bergel [18] appears to be the first, in 1960, to allude to residual

stress in arteries. However, it was Y.C. Fung [19] and R.N. Vaishnav [20] and their colleagues who initiated the study of residual stress and deformation in arteries. This was followed by the work of Choung and Fung [21] and Takamizawa and Hayashi [22], who documented the important implications of the influence of residual stress in arteries. Understanding of residual stresses is crucial in consideration of vascular growth and remodeling [199]. The existence of residual stress is manifest in the springing open of an arterial ring when it is cut in the radial direction. This opening relieves the residual stress, the circumferential component of which is compressive on the inner part of the ring and tensile on the outer part. Indeed, the compression of the inner part can be seen in a macroscopic view of an unloaded intact ring of a human artery (see Fig. 6.1), in which the intima buckles and delaminates from the media.

2 mm
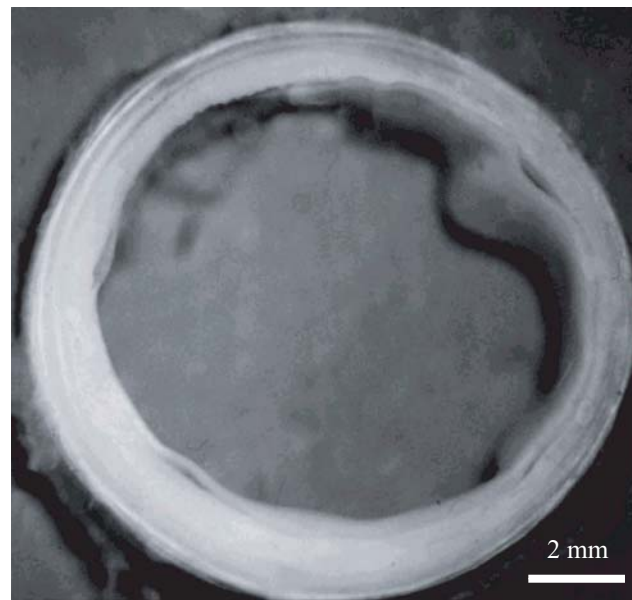
Figure 6.1: Ring of a fresh human iliac artery (donor: female, 81 years) in a tissue bath
($37 \pm 0.1°$C, Ca^{2+}-free 0.9% physiological saline solution) showing spontaneous buckling and delamination of the intimal layer from the media. This indicates that the intima is compressed in the circumferential direction in the unloaded wall. This macroscopic phenomenon is analogous to the observed microscopic wrinkling of internal elastic laminas in unloaded arterial rings [27].

Several authors have shown that although residual stresses are small compared with *in vivo* wall stresses they have a strong influence on the *in vivo* stress dis-

tribution [22, 134, 135, 200]. In particular, the residual stresses seem to have the effect of homogenizing the circumferential stress within each layer in the physiological load state [89, 134, 200]. Without residual stresses relatively large stress gradients would occur in the arterial wall. In some works the strain rather than the stress is considered to be uniform [22]. Consequences of the assumptions of uniform circumferential stress and/or strain have also been discussed in the literature [201]. In fact, it has been shown that hypertension [202], aging [203], and atherosclerosis [204] are accompanied by changes in the residual deformation.

Several studies have characterized the zero-stress configuration in terms of a single parameter, the opening angle; see Humphrey [89], Chapter 7, for detailed references. The opened sector is then frequently assumed to be stress free. However, it has been demonstrated that separation of the inner and outer ring portions leads to additional deformation, [32] and hence further stress release. Greenwald et al. [33] performed a series of experiments to investigate this observation. It is important to emphasize that there are also residual stresses in the axial direction of the vessel, and they may vary significantly throughout the arterial wall [32, 205, 206]. In particular, since the arterial layers exhibit marked differences in histological structure and cellular constituents [101], and mechanical behavior and *in situ* loads [38, 69], it is an obvious conclusion that residual stresses are tailored in order to meet the specific requirements of the layers and are therefore strongly layer specific. The residual stresses also, in general, vary through each layer.

Arteries of laboratory animals have only two layers that are mechanically significant (media and adventitia); however, in human aged arteries the intima is a third mechanically significant layer of considerable thickness and mechanical strength [76]. This is caused by 'diffuse intimal hyperplasia', which is the result of a nonatherosclerotic process [130] in which intimal cells proliferate concentrically, leading to an increase in extracellular matrix and thickening of the intima to restore baseline wall stress. Arteries so affected are non-diseased by definition and have intima/media ratios of about 0.1 to 1.0 or even more [130]. For iliac arteries of aged subjects, e.g., an average intima/media/adventitia ratio of 13/56/31 has been documented [73]. Thus, for the investigation of residual stresses and deformations in human arteries with non-atherosclerotic intimal thickening, the intima must also be considered.

Basically, two types of residual deformation exist in an arterial layer, namely bending and stretching. Without residual deformations a pressurized thick-walled cylinder exhibits circumferential tensile stress that is maximal at its inner boundary, where the circumferential stretch is also maximal. However, if an open (stress-free) sector is deformed into a cylinder then the circumferential stress gradient through the wall thickness is reduced by subsequent inflation as compared with the situation without residual deformations. This is because the compressive stress at the inner boundary and tensile stress at the outer boundary generated by the closing up of the sector reduce the stress gradient in the pressurized configuration. While this feature is well recognized in arterial wall mechanics [89, 134], the effects of individual layer stretching have largely been ignored. However, for the human femoral adventitia, e.g., it has been demonstrated that (i) there are layer-specific residual stretches in the circumferential and axial directions, and (ii) residual stretches have a crucial influence on the mechanical function of the adventitia [69]. In particular, without residual deformations the adventitia has low stiffness, but becomes a relatively stiff layer that carries about a third of the physiological mechanical loads when residual deformations are accounted for. According to the authors' knowledge, there is no study available that is concerned with layer-specific residual deformations (bending and stretching) for either the circumferential or axial direction.

In view of the importance of residual deformations and associated stresses and the clear differences in the mechanical properties of the different layers, the objective of the present *in vitro* study is to investigate in detail the layer-specific residual deformations for the intima, media and adventitia separately. In order to elucidate the three-dimensional nature of the residual deformations we obtain data for both the axial and the circumferential directions for each layer from eleven human aged aortas with non-atherosclerotic intimal thickening, from which 16 pairs of rings and axial strips were harvested. A total of 2 (ring + strip) ×3 (layers) ×16 (pairs) = 96 specimens was obtained and tested according to a systematic protocol. This study aims, in particular, to highlight the significance of layer-specific residual deformations for the understanding of vascular physiology and pathology. In this connection, it is worth mentioning that there is general agreement that vascular cells respond to their mechanical environment. Consequently, a thorough un-

derstanding of the mechanobiological aspects of regular vessel function, growth, remodeling, adaptation, repair, disease, etc., requires the quantification of the local stress and deformation states, and, therefore, identification of the residual stress state of the arterial wall.

6.2 Materials and Methods

6.2.1 Specimen Preparation and Histology

Eleven abdominal aortas from human cadavers (48.0 ± 12.5 years, mean $\pm$ SD) were excised during autopsy between 6 and 24 h from death. The abdominal aorta was chosen because it is relatively easy to access during autopsy, and its large dimension is particularly advantageous for layer dissection and for making residual deformation measurements. Information about the anamnesis of the abdominal arteries investigated is summarized in Table 6.1. Aortas with no or minimal signs of atherosclerotic disease were used in this study. In addition, the abdominal aortas from donors *V*, *VI* and *IX*, although having medium- or high-grade atherosclerosis, had sufficient portions that were free from atherosclerotic admissions and were also used for the study. It is worth noting that donors *V*, *VI* and *IX* were the oldest (aged 54, 66 and 74). Use of autopsy material from human subjects was approved by the Ethics Committee, Medical University Graz, Austria. The axial *in situ* lengths of the aortas were determined by measuring, for each considered segment, the distance between two superficial surgical knots made of surgical fibers and prepared by a experienced pathologist. The location of the proximal knot was approximately 0.5 cm distal of the renal artery and the distal knot was located approximately 1 cm proximal of the aorta bifurcation. The *ex situ* length was measured after one hour of equilibration of the excised artery in a Ca^{2+}-free 0.9% physiological saline solution at a temperature of $37 \pm 0.1°C$. Thereafter, the axial *in situ* stretch, defined as the ratio of *in situ* segment length to *ex situ* segment length, was computed.

Loose connective tissue was carefully removed from the surface of the artery. Although it has recently been reported that the peri-adventitial tissue has important

Table 6.1: *Anamnesis*

Donor	*I*	*II*	*III*	*IV*	*V*	*VI*	*VII*	*VIII*	*IX*	*X*	*XI*
Age (yrs)	40	36	43	47	66	74	41	37	54	38	52
Sex	m	f	m	f	f	m	m	m	f	f	f
Primary disease	BO	AML	LC	NHL	PC	CA	IA	HC	BC	IA	SEC
Cause of death	GHD	GHD	GHD	GE	ME	MI	SAH	CH	ME	SAH	STB
Atherosclerosis:											
Aorta	n	n	n	n	√	√	n	n	√	n	n
Coronary arteries	n	n	n	n	n	√	n	n	n	n	n
Cerebral arteries	n	n	n	n	n	√	n	n	n	n	n
Renal arteries	n	n	n	n	n	√	n	n	n	n	n

The following abbreviations are used: AML (acute myeloid leukaemia), BC (breast carcinoma), BO (brain oedema), CA (coronary arteriosclerosis), CH (cerebral hemorrhage), GE (generalization), GHD (global heart dilation), HC (hypertrophic cardiomyopathy), IA (intracranial aneurysm), LC (liver cirrhosis), ME (metastasis), MI (myocardial infarction), NHL (Non-Hodgkin-lymphoma), PC (pancreas carcinoma), SAH (subarachnoid hemorrhage), SEC (squamous epithalial carcinoma of soft palate), STB (severe tumor bleeding). Assessment of atherosclerosis is based on autopsy reports. The abbreviations √ and n stand for 'medium or high-grade atherosclerosis' and 'no or low grade atherosclerosis', respectively.

effects on smooth muscle tone control [207, 208], removal of the perivascular adventitial adipose tissue should not effect the passive behavior of the arterial tissues on which we are focusing. A ring was then cut from each aorta, and an 'axial strip', i.e. a strip whose long sides were aligned with the vessel axis, was cut from the anterior site of each aorta (a schematic illustration of the protocol of specimen preparation is provided in Fig. 6.2).

From five aortas it was possible to harvest five additional ring and axial strip pairs so that a total number of 16 pairs were obtained. Typical specimen dimensions were 15 mm × 5 mm (diameter × height) for the rings and 20 mm × 5 mm (length × width) for the axial strips. The specimens were placed in a tissue bath (Ca^{2+}-free physiological saline solution), which was maintained at a temperature of $37 \pm 0.1°C$ using sensors and a thermostatically controlled heating plate. Each ring was allowed to equilibrate in the bath for 30 min, and thereafter glued pointwise with cyanoacrylate adhesive on to a cylindrical plastic tube of diameter 7 mm.

This procedure provided load-free suspension of the specimen and allowed proper orientation of the specimen edges towards a digital camera. Finally, a scaled digital image of the ring was taken. Similarly, the axial strip was glued to a cylindrical plastic tube immediately after specimen preparation, and a scaled digital image was taken. The results are illustrated in the next section (see Figs 6.6(a) and (f) therein). The schematic in Fig. 6.2 shows that the specimens are symmetric about the point of attachment, while for the images shown in Figs 6.6 and 6.7 this is clearly not the case. This is due partly to the inhomogeneity of the tissue and partly to the difficulty of identifying the optimal location on the tissue for gluing. It is possible that the movement of the segment as it approaches the zero-stress state may be impeded by surface tension and/or drag between the vessel and the base of the tissue bath. There have been no reports of attempts to quantify these effects, although observations by Rachev and Greenwald [209] suggest that they may account for the rather large variability in opening angle between adjacent ring segments from the same vessel. We avoided these effects by glueing the specimen pointwise to a cylindrical plastic tube such that the distances between the specimen and the base of the tissue bath and the fluid surface were at least 2 mm. Another possible solution to this problem is to attach the cut ring to the tip of a micropipette by suction [210].

For each aortic ring a radial cut through the wall was made. A release of circumferential compressive residual stress at the inner vessel wall and tensile residual stress at the outer surface of the wall was manifest by the ring deforming into a sector, which was rarely shaped as a circular arc. Note that axial residual stress is also released in this process but this is not apparent from the resulting geometry. This specimen is referred to as a 'circumferential strip'. The subsequent time dependence of the arterial tissue properties led to changes in their sizes and shapes (i.e. further deformation). We took pictures $1, 2, 4, 8$ and 16 hours after the radial cut and the excision of the axial strip. We did not observe any geometrical change after 8 hours. It therefore seemed that the specimens had already reached thermodynamic equilibrium 8 hours after cutting.

Next, the intimal layers of each circumferential and axial strip pair were separated very carefully with minimal force using anatomical instruments, and then the media was separated from the adventitia (the technique for separation is illustrated
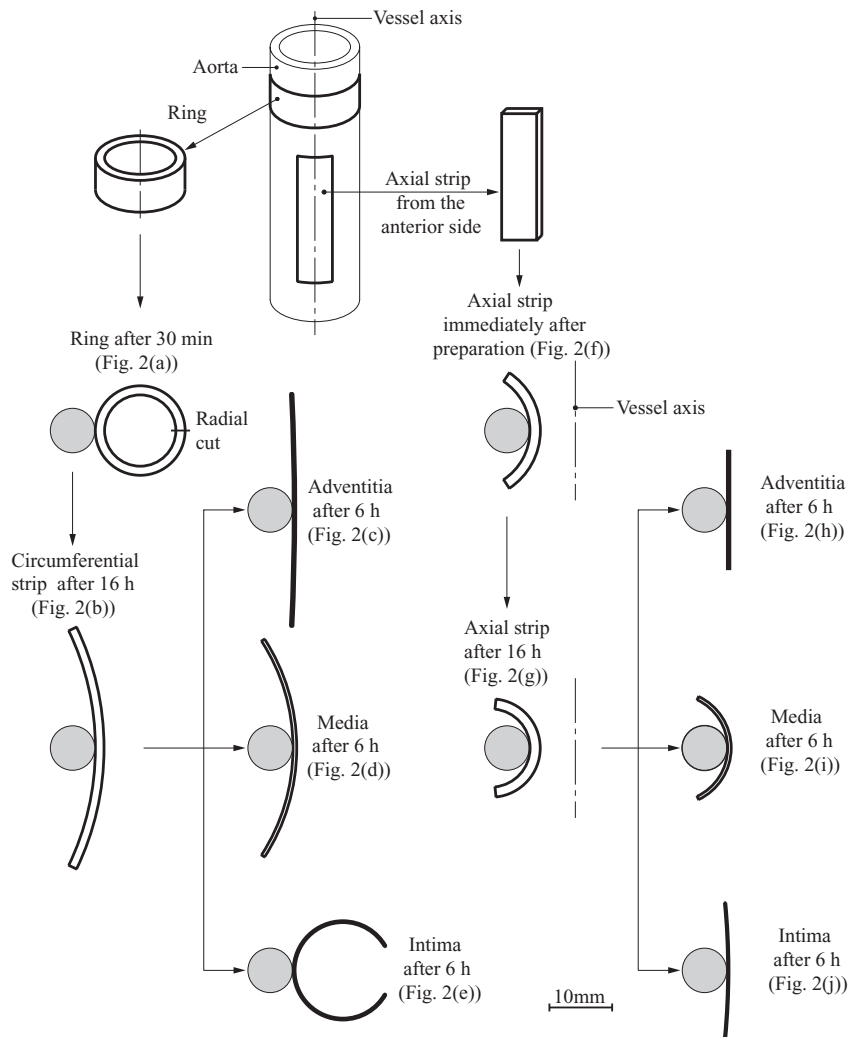
Figure 6.2: Schematic illustration of the specimen preparation: ring and axial strip obtained from the aorta, ring after 30 min of equilibration, and axial strip immediately after preparation; circumferential strip (after a radial cut of the ring) and axial strip after 16 h of equilibration; circumferential and axial strips from the intima, media and adventitia after 6 h of equilibration. All specimens were glued pointwise to cylindrical plastic tubes (with diameter of 7 mm), which provided load-free suspension of the specimens within the tissue bath, and allowed proper orientation of the specimen edges towards the camera. At each stage of the preparation a digital image was taken. The geometries of the individual arterial segments are drawn to the correct scale.

in Fig. 6.3). Sometimes it was necessary to use a scalpel to achieve a complete separation of the interconnective tissues. Six strips were obtained, two for each layer, three oriented circumferentially and three axially. Surprisingly, we found
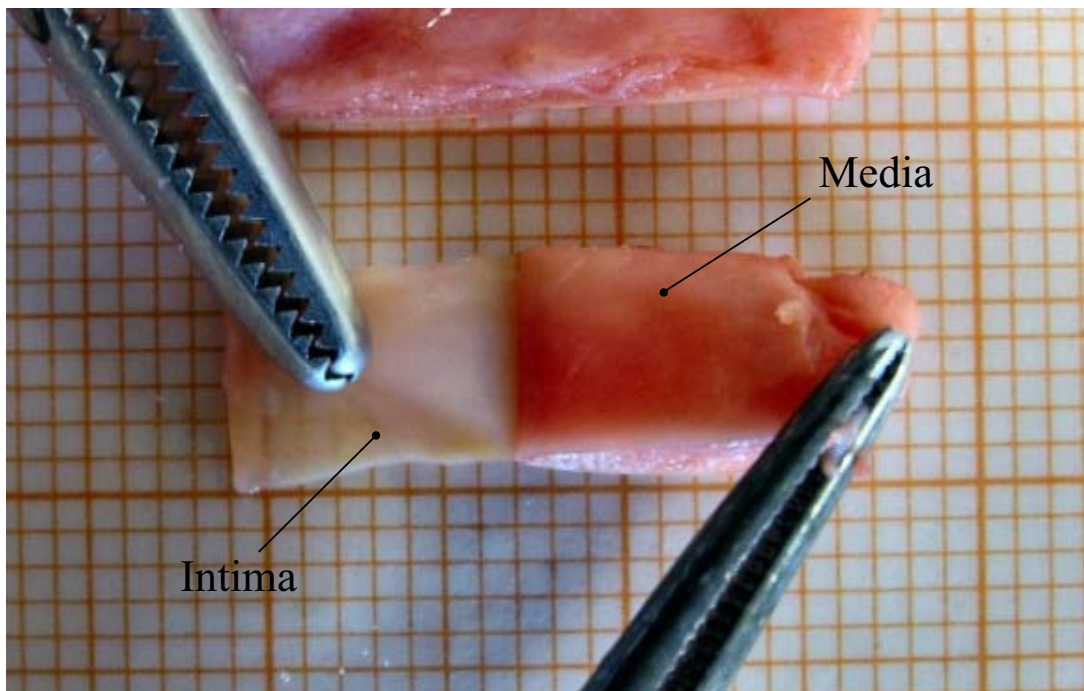
Figure 6.3: Layer separation of an aortic patch from an aged human subject (donor *IV*) using anatomical instruments.

that it was relatively easy to identify the tissue boundaries and to separate the layers. In order to confirm correct layer separation and that the separation did not induce damage, histological images were prepared for all samples considered in the study and examined by an experienced pathologist. Macroscopic inspection showed that for most samples the layer separation process was successful, but for the small number of samples for which this was not the case the specimen were discarded. The remaining tissues were selected for histological analysis. The procedure, as performed for the non-separated ring and the non-separated axial strip, was then repeated for these specimens, which were glued to the cylindrical plastic tubes in the tissue bath. The internal and external surfaces of the strips were marked and the strips were allowed to equilibrate in the tissue bath for about 6 h, and then scaled digital images were taken (Figs 6.2(c)-(e) and (h)-(j)). All tests were completed within 24 h of excision. We emphasize that the tissue used was treated as carefully as possible during transportation, storage, layer separation and test preparations.

A set of images was that contained new information on the initial geometries of the

non-separated specimens and the final geometries of the separated layer-specific strips was then obtained, which are now assumed to be stress free. The curved shapes of the strips with circumferential and axial orientations in the tissue bath enabled the biaxial residual stretches and bending deformations to be determined on a layer-specific basis.

The separated layers were embedded in paraffin, and then sectioned at $3\,\mu$m. Consecutive sections were stained with Elastica van Gieson (EvG) and histological investigations were conducted in order, primarily, to confirm correct layer separation through the external and internal elastic laminas and to ensure relatively atraumatic separation of the intact layers. The resulting histological sections were evaluated by an experienced pathologist and those for which clear atraumatic separation was not achieved the associated specimens and experimental data were discarded. If the histological analysis showed that no damage had occurred to the individual tissue layers (intima, media or adventitia) and that clear separation was confirmed then the experimental data obtained were retained for the study.

6.2.2 Image Processing

The algorithm for the segmentation of the individual images is performed semi-automatically, and is based on the discretization of NURBS (non-uniform rational B-splines) curves (determination of the geometries). The computations of the geometrically relevant vessel parameters were implemented in the image processing software IDL (Interactive Data Language) of RSI (Research System Inc.).

The image-processing software was developed in order to assist the user with a simple image segmentation problem. For example, the cylindrical plastic tube, which serves here as a reference object in the image, is found automatically. The 7 mm diameter of the tube was measured in the image in terms of pixels in order to determine the scaling factor. Vessel parameters such as diameter, thickness, length, and curvature were then scaled appropriately. The CCD (Charge Coupled Device) camera was placed so as to avoid scaling (measurement) error associated with image distortion, and its distance from the object was more than ten times the dimension of the object itself. Hence, the distance of the CCD camera from the object was adjusted according to the field of view in order to obtain nearly

parallel projection. The surface of the tube and the section of the whole vessel segment should have been placed in the same horizontal plane in order to have the same distance of depth, although this was not always achieved exactly. The largest difference in depth between the planes of the tube and the object was about 1 cm.

The approximate region of the (black) tube was identified by using an intensity threshold. The tube boundary was computed using the Sobel operator. To determine the diameter of the tube we used the Hough transform of a circle [211], which enabled the diameter to be measured accurately. The Hough transform maps each point of the Sobel-based edge image into the parameter space, from which position and diameter of the circle are obtained.

The approximate region of the specimen, which, after several hours in a physiological saline solution, appears as a nearly white object, can be found similarly by using an intensity threshold followed by a basic morphological operation such as opening and closing. The Sobel operator provided an edge image, which was used to fit NURBS curves to the boundaries of the specimen. These curves are, however, only approximations of the boundaries, and have to be improved manually because a fully automatic and exact determination of the boundaries is not possible. The reason for the solution being approximate is the fact that overlaps and non-unique determination of the faces of the specimen may occur. The use of NURBS provided an analytical description of the boundaries and allowed adaptation of the boundaries with a few manual interventions such as adjustments in a number of control points of the NURBS. Finally, the user had to determine which of the two boundaries belonged to the inner or outer boundary of the arterial segment. This is important for the subsequent computations and vessel parameter determination.

6.2.3 Image Analysis – Computation of Vessel Parameters

The use of NURBS permits the accurate computation of the required geometrical parameters. To measure the length of a boundary curve we choose, therefore, equidistant steps for the curve parameter so that we obtain 100 points on the curve. The total length of the curve is then the sum of the 99 segment lengths. The

		Ring	Circumferential strip	Adventitia	Media	Intima
Pre-stretch	inside	$\dfrac{l_i}{\overline{L}_i}$	$\dfrac{\overline{L}_{Ee}}{L_{Ai}}$	$\dfrac{\overline{L}_{Ei}}{L_{Mi}}$	$\dfrac{\overline{L}_i}{L_{Ii}}$	
	outside	$\dfrac{l_o}{\overline{L}_o}$	$\dfrac{\overline{L}_o}{L_{Ao}}$	$\dfrac{\overline{L}_{Ee}}{L_{Mo}}$	$\dfrac{\overline{L}_{Ei}}{L_{Io}}$	
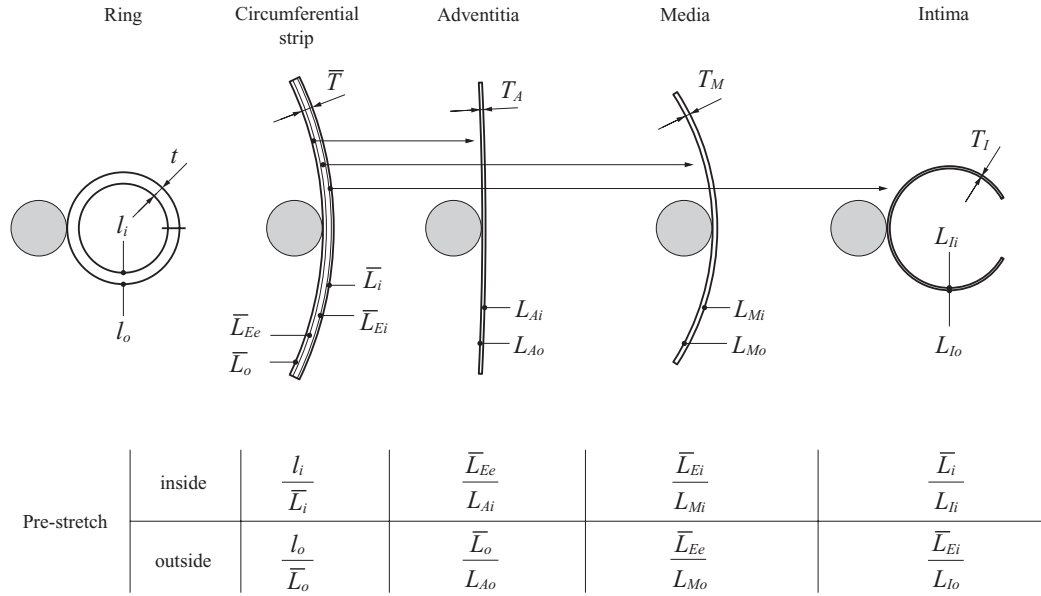
Figure 6.4: Definitions of the different lengths at the inner and outer boundaries of the ring and of the different segments oriented in the circumferential direction. The lengths of the elastica interna $\overline{L}_{Ei}$ and the elastica externa $\overline{L}_{Ee}$ were computed by linear interpolation of the lengths at the inner and outer boundaries; all other lengths were determined by image analysis. Pre-stretches at the inner and outer boundaries of the individual segments were then determined from the computed lengths.

outer diameter of the ring is the average value of the local diameters measured from the discrete points. The local diameter at a point is defined as the distance between that point and the most distant point on the curve. This procedure is repeated for the inner diameter.

In order to compute the mean thickness of a particular segment we proceed as follows: we select one curve (e.g., the outer boundary curve of the segment) and determine the normal vector and the corresponding normal line at each of the 100 points. We then determine the corresponding intersection points of the normal lines with the other boundary curve (e.g., the inner boundary of the segment). The distances between the 100 points and the associated intersection points then give 100 local thicknesses. Finally, we compute the mean thickness by averaging all the local thicknesses. Note, however, that the sum $T_A + T_M + T_I$ of the average thicknesses of the adventitia, media and intima does not, in general, coincide with the average thickness, denoted $\overline{T}$, of the intact strip before separation. In fact, the
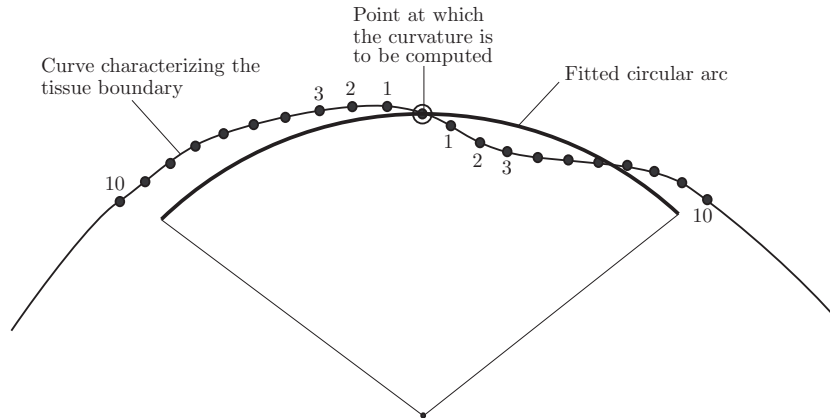
Figure 6.5: Computation of the local curvature at an individual point of the tissue boundary characterized by a segmented curve. A set of 20 neighboring points on the curve was considered. The curvature of the fitted circular arc represents the local curvature of the point in question.

sum $T_A + T_M + T_I$ is, in general, smaller than $\overline{T}$. The reason for this is that, due to the separation process, residual stresses are released and, therefore changes in the geometries of the individual layers occur.

Next we compute the lengths of the different segments at the inner and outer boundaries, as detailed in Fig. 6.6 for the ring and for the segments oriented in the circumferential direction. The inside and outside lengths of the ring (l_i, l_o), the circumferential strip ($\overline{L}_i$, $\overline{L}_o$), adventitia (L_{Ai}, L_{Ao}), media (L_{Mi}, L_{Mo}), and intima (L_{Ii}, L_{Io}) are computed by image analysis from the sum of 99 line segments, as described above. Since the intima/media and media/adventitia boundaries are difficult to find in the images of the circumferential and axial strips, the lengths of these boundaries, i.e. of the elastica interna $\overline{L}_{Ei}$ and the elastica externa $\overline{L}_{Ee}$, were computed by adopting a linear interpolation process as follows: the lengths $\overline{L}_{Ei}$ and $\overline{L}_{Ee}$ were assumed to be interpolated proportionately to the thicknesses T_A, T_M, T_I of the arterial layers. Since the sum of these thicknesses does not coincide with the thickness $\overline{T}$ of the segment before separation, the individual layer thicknesses are scaled by the factor $\overline{T}/(T_A + T_M + T_I)$. The computations of the lengths of the arterial segments in the axial direction were done similarly. The pre-stretches of the ring and the individual wall segments in the circumferential direction are determined from the computed lengths according to Fig. 6.6, and the computations for segments in the axial direction were performed likewise.

Next, we attempt to characterize the curvatures of the individual tissue components. For the axial strips the opening angle is not a characteristic quantity for residual deformations since the angle depends on the strip length. Furthermore, the cut specimens rarely take the form of circular arcs; however, the opening angle method remains popular, presumably because of its technical simplicity. Images of the zero-stress state illustrate clearly that many, if not most, of the specimens spring open unsymmetrically. The residual stretch states in the individual specimens were, therefore, described by changes in geometry. Since the shape of each segment considered deviated from that of a circular arc, the curvature was computed locally for each of the 100 points of the curve, i.e. the curve consisting of 99 segments (see Fig. 6.5). For this computation we used a set of 20 neighboring points on the curve, 10 to the left and 10 to the right of the actual position. Then, based on a least squares fit, we computed the curvature of the circle that approximated the curve. For a point on the end of a curve we used 10 points on the curve together with 10 points obtained by appropriate extension of the curve using symmetry. The mean curvature is then obtained by computing the average over all the 100 local curvatures.

Mean values of the diameter, length, pre-stretch, and curvature of each specimen were then determined by averaging the values for the inner and outer boundaries. Finally, the vessel parameters (diameter, thickness, length, pre-stretch, curvature) were obtained by computing the mean values and associated standard deviations for the 16 specimens.

6.3 Results

With reference to the protocol shown in Fig. 6.2, results for a selection of specimens are illustrated in Fig. 6.6. We emphasize that the images are representative but not taken from the same specimen. Therein, solid curves highlight the outer boundaries, while the dashed curves specify the inner boundaries of the specimens. The image processing tool that we have developed allows the boundaries of the ten specimens to be segmented from the images, as illustrated in Fig. 6.6, in about 45 min.

Adventitia
(c)

Ring
(a)

Circumferential
strip
(b)

Media
(d)

Intima
(e)

Axial strip
(f)

Axial strip
(g)

10mm

Adventitia
(h)

Media
(i)

Intima
(j)
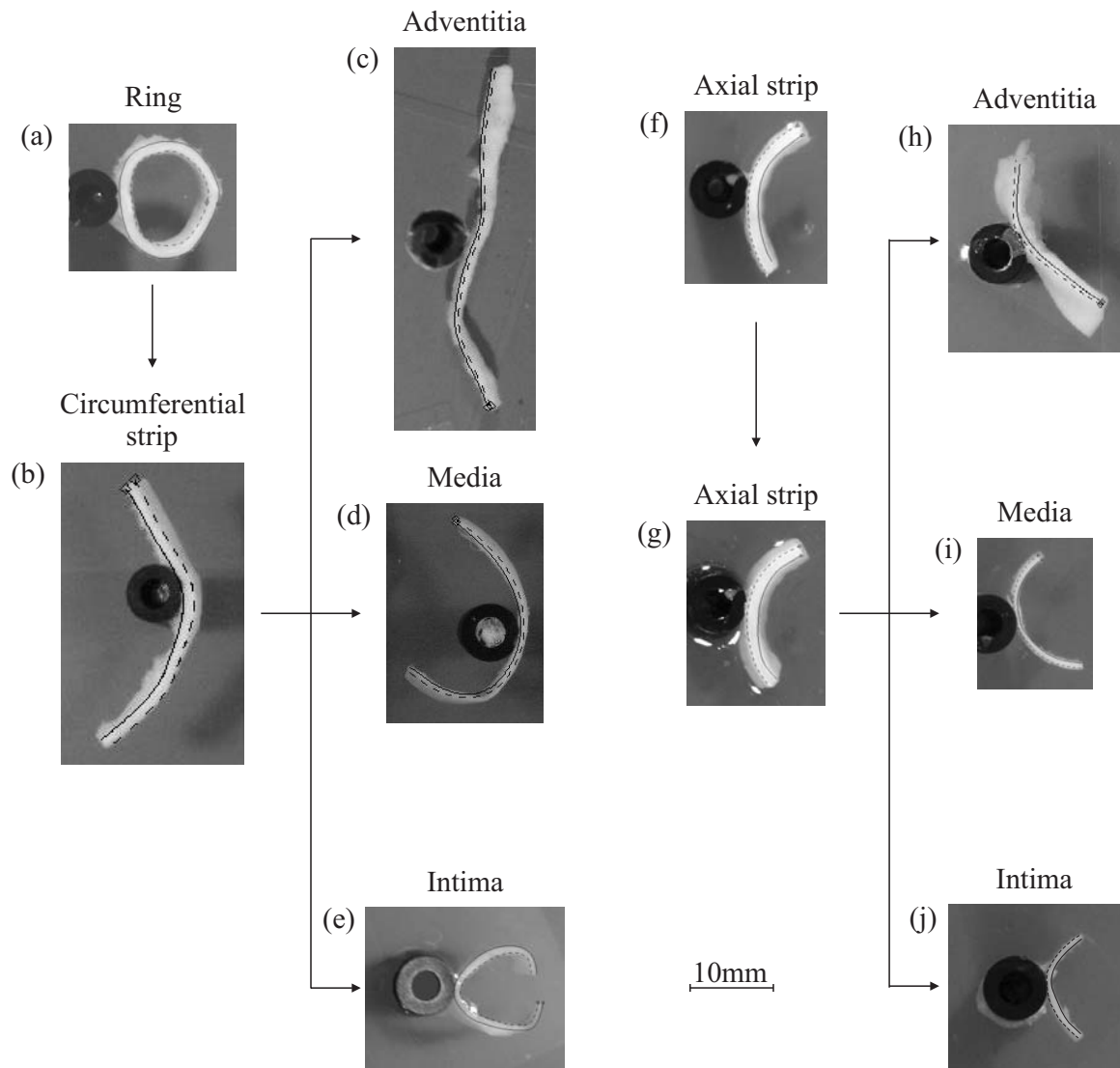
Figure 6.6: Ring after 30 min of equilibration (a), and axial strip immediately after specimen preparation (f); ring after a radial cut (b) and axial strip (g) after 16 h of equilibration; circumferential strips (c)-(e) and axial strips (h)-(j) from the adventitia, media and intima after 6 h of equilibration (specimens from donor *VIII*). All specimens are in a Ca^{2+}-free physiological saline solution at a temperature of $37 \pm 0.1°C$. Although the strips are from one non-separated specimen their geometries differ significantly, which indicates layer-specific residual stretches. The solid curves indicate the outer boundaries, while the dashed curves indicate the inner boundaries of the specimens. For the protocol of the specimen preparation see Fig. 6.2. We emphasize that the images are representative but not taken from the same specimen.
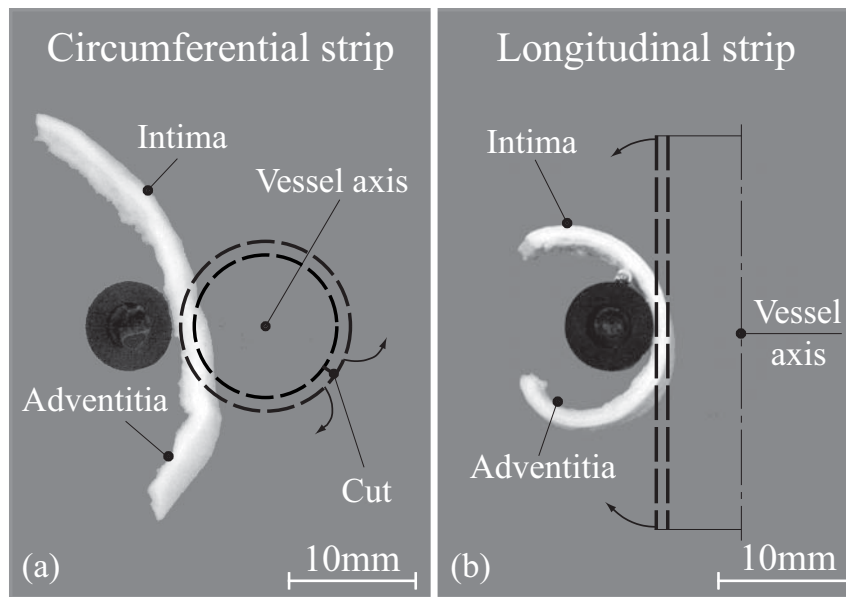
Figure 6.7: Circumferential strip (after a radial cut through the wall of the aortic segment) (a) and axial strip (strip whose long sides are aligned with the vessel axis) (b) in a Ca^{2+}-free physiological saline solution at a temperature of $37 \pm 0.1°C$ (specimens from donor *III*). The specimens are attached to a cylindrical plastic tube with diameter of 7 mm. Images were taken after about 16 h of equilibration. The black dashed circles and lines illustrate the initial (unloaded) configurations of the aorta. The thin black pairs of curves designate the boundaries of the considered sample. Outside these boundaries loose connective tissue can be seen.

After 30 min of equilibration in the physiological bath at 37°C, the mean inner and outer diameters of the aortic ring segments ($n = 16$) were determined to be 11.22 ± 2.18 mm and 14.09 ± 1.92 mm (mean $\pm$ SD), respectively. These values were determined from images of the type illustrated in Fig. 6.6(a). The mean ratio of the wall thickness of the ring to its outer diameter for all specimens was 0.106 ± 0.034 (mean $\pm$ SD).

Figure 6.7 shows images of aortic samples from donor *III* after 16 h of equilibration. The black dashed circles and lines illustrate the initial configurations in the unloaded (but stressed) configurations of the aorta. The pictures indicate that both specimens bend away from the vessel axis after stress release.

Figure 6.8, e.g., shows the distribution of the thicknesses along the (normalized) length of the boundaries for both the circumferential and axial strips of donor
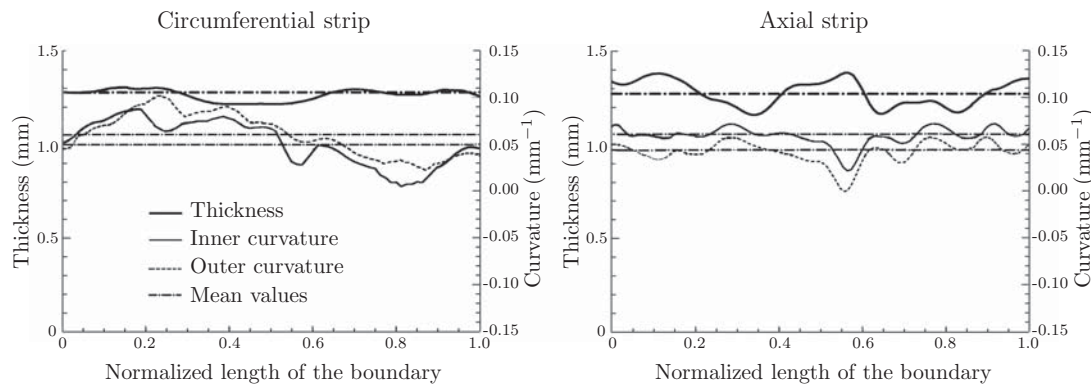
Figure 6.8: Distributions of the thicknesses and the (inner and outer) curvatures along the (normalized) lengths of the circumferential and axial strips of donor *VIII*. The dash-dot lines indicate the associated mean values.

VIII. The dash-dot lines represent the associated mean thicknesses of the strips. Figure 6.2 also shows the distribution of the curvatures along the (normalized) lengths of the inner and outer boundaries for the circumferential and axial strips of donor *VIII*. The dash-dot lines indicate the associated mean curvatures of the inner and outer boundaries of the strips. Note that both the thicknesses and the curvatures for the strips are slightly different at the two ends for some samples, which is not surprising because of the inhomogeneity of the material and of the residual stresses.

The specimens exhibited a heterogeneous structure with three layers (Adventitia A, Media M, Intima I) with significant thicknesses. Figure 6.9 shows column plots of the thickness values of the rings, the strips and the separated layers (A, M, I) oriented in the circumferential and axial directions ($n = 16$). Note that the specimen thicknesses change during stress release. Hence, e.g., the thickness of the intact ring differs from that of both the (non-separated) circumferential strip (ring after a radial cut) after 16 h of equilibration and the sum of the thicknesses of the separated adventitia, media and intima. The thickness ratios adventitia : media : intima oriented in the circumferential direction were calculated as 32 : 46 : 22, and for the axial direction 33 : 48 : 19. The axial *in situ* stretch is 1.196 ± 0.084 (mean ± SD) calculated from seven samples.

The column plots in Fig. 6.10 represent the pre-stretches (mean values and associated standard deviations) of the aortic sector strips before (left-hand panel) and

(a)   (b)
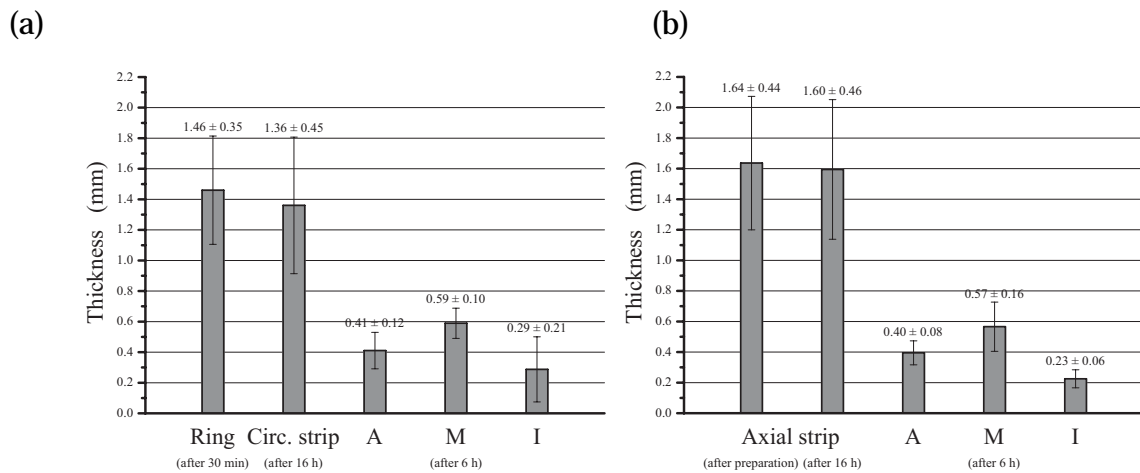
Figure 6.9: Column plots (mean values and related standard deviations) of the thick-
nesses of the aortic wall and the separated layers (Adventitia A, Media
M, Intima I) oriented in the circumferential (a) and axial (b) directions
($n = 16$). Thicknesses of the aortic ring after 30 min of equilibration and
of the axial strip immediately after specimen preparation (compare with
Figs 6.6(a),(f)); circumferential strip (ring after a radial cut) and axial strip
after 16 h (Figs 6.6(b),(g)), and separated layers after 6 h of equilibration
(Figs 6.6(c)-(e) and (h)-(j)). The error bars represent standard deviations.

after separation (right) into their three layers (Adventitia A, Media M, Intima I)
oriented in the circumferential and axial directions ($n = 16$ for each direction). Val-
ues for the strips before separation refer to a state after about 16 h of equilibration,
and the separated layers refer to a state after about 6 h of equilibration. For the
pre-stretch computation, see the caption of Fig. 6.4. Figure 6.10 indicates that the
adventitia and the media seem to be slightly stretched in the environment of the
intact arterial strip for each orientation (circumferential and axial), whereas the
intima seems to be compressed in both orientations. These changes in dimensions
correspond to shortening of the adventitia and the media by between 4.03% and
8.76% on average, and lengthening of the intima by 3.84% (circumferential) and
4.28% (axial) on average on separation. The compression of the intima has al-
ready been noted in the introduction with reference to Fig. 6.1. These features are
highlighted in Fig. 6.11, in which the intima, media and adventitia patches from
donor *VII* from the circumferential and axial directions are pictured after separa-
tion along with the corresponding intact patches. The patches were moisturized,
and because of placement on a moisturized smooth surface 'creep recovery' was
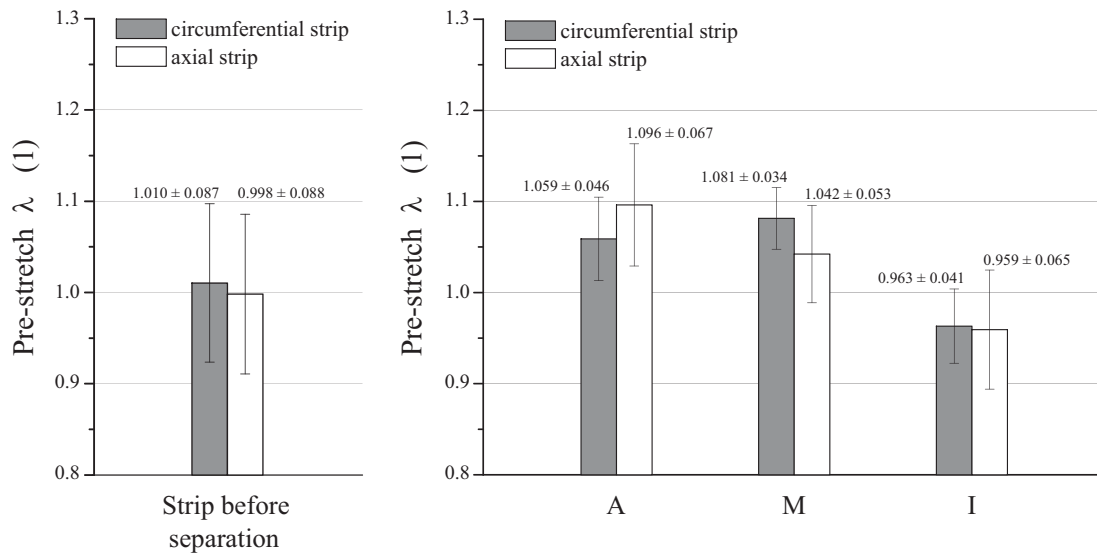
Figure 6.10: Column plots (mean values and associated standard deviations) of the pre-stretch of the aortic wall before and after separation into the three layers (Adventitia A, Media M, Intima I) oriented in the circumferential and axial directions ($n = 16$ for each direction). Values for the strips before separation refer to a state after about 16 h of equilibration, and the separated layers refer to a state after about 6 h of equilibration. The error bars represent standard deviations.

allowed for. As can be seen from Fig. 6.11, there are significant differences in the dimensions of the separate patches, whose lengths and breadths before separation were equal. This emphasizes that there are layer-specific residual stretches in the circumferential and axial directions. In particular, we note that the intima, the innermost layer, is the longest of the three after separation in both directions, indicating again that the intima is compressed in the unloaded state.

The column plots in Fig. 6.12 show the curvatures of the individual specimens. Strips of the adventitia appear to be relatively flat in both directions, while strips of the media exhibit negative curvatures in both directions. Circumferential strips of the intima have pronounced positive curvatures, while axial strips are relatively flat (slight negative curvature). The associated standard deviations are relatively small. As can be seen from Fig. 6.12 the residual deformations are very pronounced and characteristic for each layer and specimen direction. Note that in Figs 6.2(a)-(j) the curvatures of the individual arterial segments are drawn to the correct scale, which is also the case for other vessel parameters such as the diameter of the
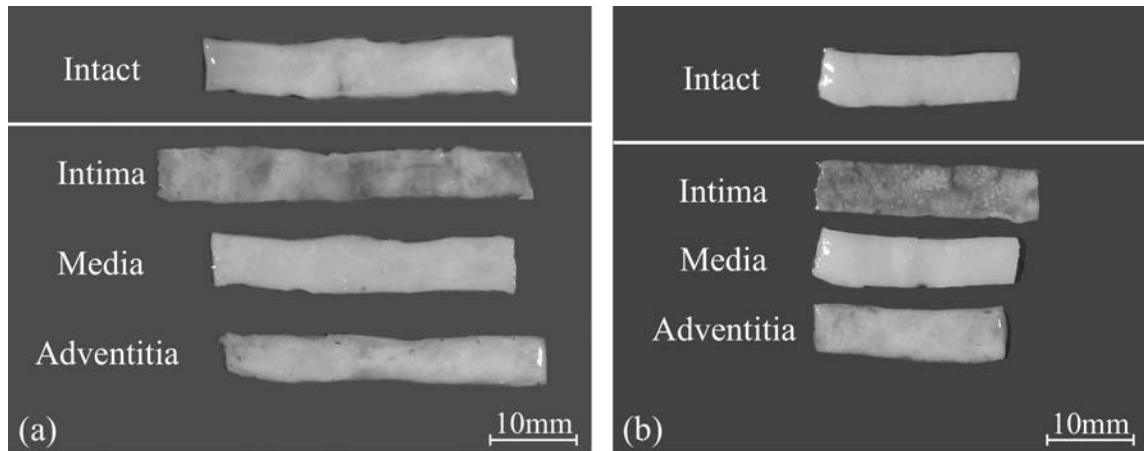
Figure 6.11: Anatomical separation of a fresh human aortic patch oriented in circumferential (a) and axial direction (b) from donor *VII* into isolated patches of intima, media, and adventitia. In each case the intact patch is shown at the top. Although, before separation, the separate layers had the same in-plane dimensions their dimensions differ significantly after separation. This phenomenon indicates that there are layer-specific residual stretches in the circumferential and axial directions.
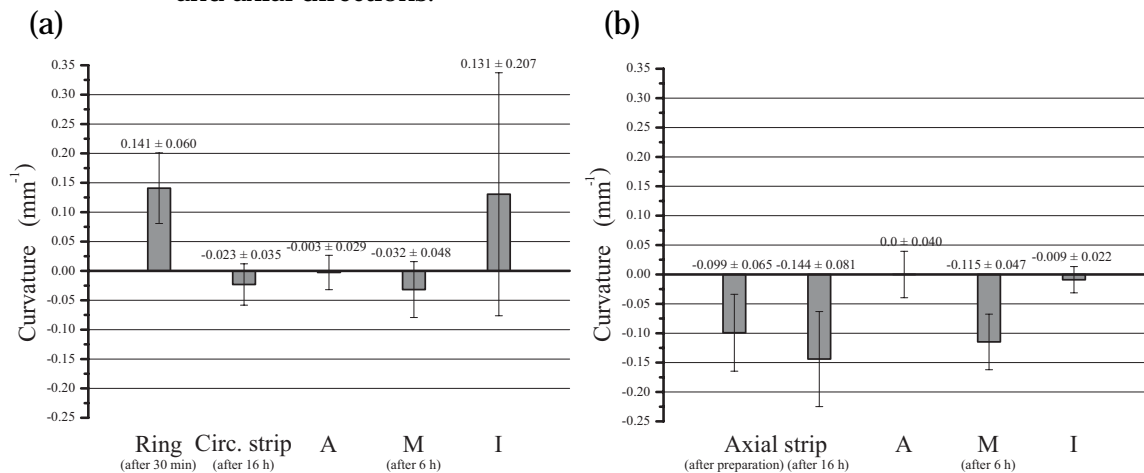
Figure 6.12: Column plots (mean values and associated standard deviations) of the curvature of the mean aortic ring after 30 min of equilibration, the circumferential strips after 16 h, and the separated layers (Adventitia A, Media M, Intima I) oriented in the circumferential direction after 6 h (a) ($n = 16$); the axial strip immediately after preparation and after 16 h, and the separated layers (A, M, I) oriented in the axial direction after 6 h of equilibration (b) ($n = 16$). The error bars represent standard deviations.

ring, thicknesses and lengths. As we have seen, the residual deformations in the different layers are different, but it should be pointed out that these are not uniform

(a) (b)
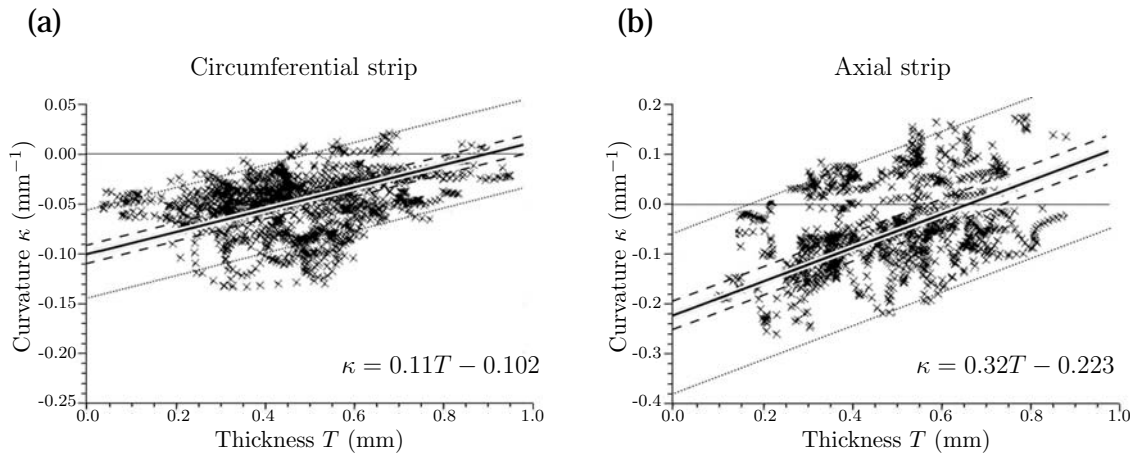
Figure 6.13: Relationship between the local curvature κ and the local thickness T for each individual point of the media oriented in the circumferential (a) and the axial direction (b) ($n = 16$ for each direction). The values of the curvature refer to the mean of the inside and the outside of the boundary curvatures. Linear regression lines (solid) for all data ($n = 16 \times 100$). Best-fit functions for the values of the curvature are $\kappa = 0.11T - 0.102$ ($p = 0.036$), and $\kappa = 0.32T - 0.223$ ($p = 0.048$) for the circumferential and axial strips, respectively. Dashed lines indicate the 95% confidence interval for the regression line and dotted lines show the 95% prediction interval of curvatures.

through each layer. Likewise, residual stresses are distributed inhomogeneously through the layer thickness.

Saini et al. [212] observed a clear and highly significant sex difference in opening angle at all ages and at all positions along the human aorta. We found, that the sector strips and individual tissue strips oriented in the circumferential and axial directions reveal a decreasing curvature with increasing age, with the exception of the intima strips oriented in the circumferential direction, which show an increasing curvature with increasing age. For the circumferential direction, the sector strips show the most pronounced decrease of curvature with increasing age ($r = -0.52, p = 0.04$), and, for the axial direction, the media shows the most pronounced decrease of curvature with increasing age ($r = -0.48, p = 0.06$). Furthermore, curvatures of male sector strips and also of the individual tissue strips were on average always smaller than curvatures of female strips.

A detailed analysis of all the data was carried out with the aim of identifying any particular trends in the data. The main outcome was that for the media a

(a)

(b)

(c)
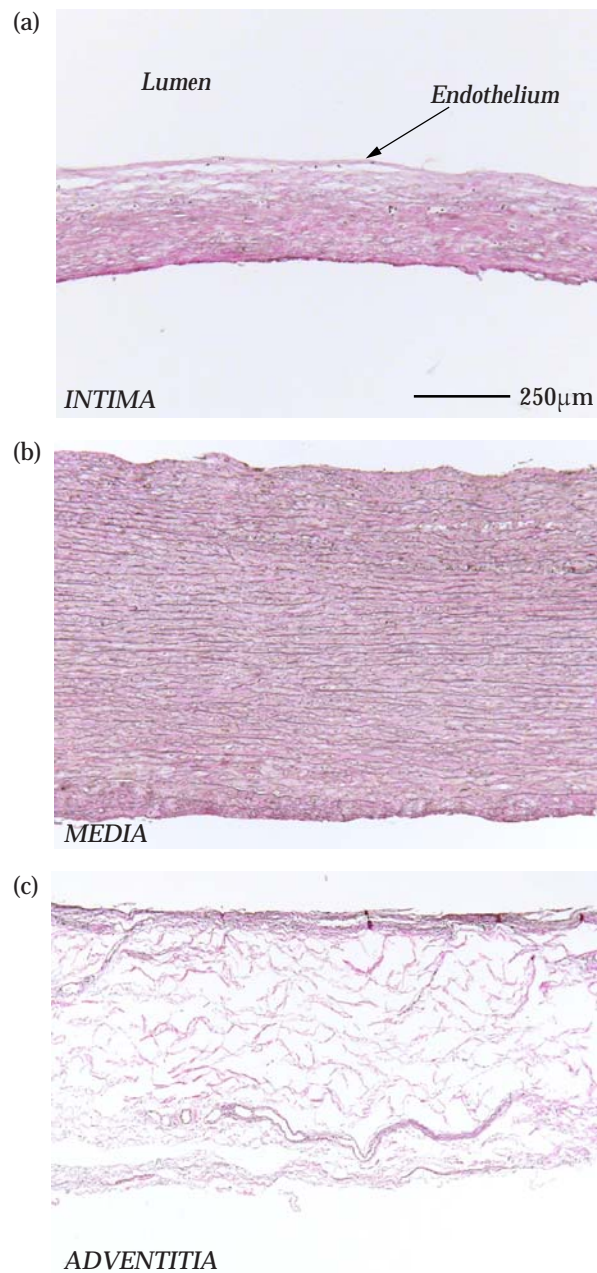
Figure 6.14: Photomicrographs of $3\,\mu$m-thick Elastica van Gieson-stained sections from wall layers in the circumferential direction from an abdominal aorta (donor *V*) after anatomic separation and mechanical testing: (a) intima; note the homogeneous thickening due to diffuse intimal hyperplasia in an aged patient. The outer part (lower part of the image) includes elastic fibers from the membrana elastica interna; (b) media; note that the surface irregularities are caused by histological processing during embedding; (c) adventitia; note the tendency to separate after microtome cutting, because of the loose collagen fibers in the outer part (histologic artefact). Original magnification 40x.

definite trend was found in the relationship between the curvature κ and thickness T (the subscript M has now been dropped from T_M for simplicity). This is shown in Fig. 6.13 for the circumferential and axial strips separately. In each case the curvature increases with thickness, and this increase is characterized by a linear regression which gives best fit functions of $\kappa = 0.11T - 0.102$ ($p = 0.036$) for the circumferential strip and $\kappa = 0.32T - 0.223$ ($p = 0.048$) for the axial strip. For the linear regression line all the data were used ($n = 16 \times 100$). In Fig. 6.13 the dashed lines indicate the 95% confidence interval for the regression lines, while the dotted lines show the 95% prediction interval of curvatures.

An illustration of the layers separated in the circumferential direction for the abdominal aorta of donor V is shown in Fig. 6.14. Histological analyses of the specimens showed homogeneous diffuse intimal hyperplasia, as discussed in the introduction. The different structures within each layer are very clearly seen. Corresponding photomicrographs were obtained for each specimen, and showed clearly the atraumatic separation of the wall layers.

In addition to the experimental and analytical investigations of the residual deformations, uniaxial extension tests were performed on the layer specimens. The associated data will be presented elsewhere and will form the basis for physical modeling of the layer-specific response and, consequently, the computation of residual stresses.

6.4 Discussion

It is now clear that residual deformations and stresses play a very significant role in the function of arterial walls, and therefore in the understanding of vascular physiology and disease. They characterize implicitly the mechanical environment required by the arterial tissues and cells for their normal functions. Changes in the mechanical environment due to, e.g., elevated blood pressure or the formation of a thick and stiff intimal layer lead to biological responses and consequently to alterations in the residual deformations in order to adjust the homeostatic state of stress. In particular, vascular cells regulate their structure and composition and that of the surrounding extracellular matrix. Hence, residual deformations may be seen as a

'mechanical fingerprint' of the biological state of a vessel, which can be thought of as a dynamic control system that adapts continuously its geometry and mechanical properties in order to meet the demands of its components, i.e. the cells, extracellular matrix, etc. Systematic investigation of this 'mechanical fingerprint' promises to improve significantly our knowledge of arterial mechanobiology. Without appropriate data on layer-specific residual deformations and associated constitutive models incorporating them, stress-deformation analysis at a tissue level is incomplete. The residual stresses and deformations are crucial for understanding the interaction between the mechanics and the associated biological responses such as growth, atrophy, remodeling, adaptation, etc. It is therefore important to develop a comprehensive collection of data concerning residual stresses and deformations.

In the present study we have obtained significant results towards this objective. In particular, novel results on human aortas with non-atherosclerotic intimal thickening presented here demonstrate distinct layer-specific residual deformations and provide generic information that quantifies the state of the mechanical environment. In the light of these data it seems to be highly unlikely that residual deformations in the inhomogeneous arterial wall can be characterized appropriately by a single parameter such as the opening angle of a wall sector. However, to date, due to lack of three-dimensional data, the opening angle method has been in common use because of its simplicity. The present study aims to highlight the essential features of arterial layers with respect to residual deformations by using a series of images. For this purpose a simple approach to the measurement of kinematical quantities characterizing the layer-specific residual deformations of arteries has been introduced and demonstrated. Moreover, the study has focussed on human tissue and, although access to human specimens is restricted, this material is to be favored since the separation of the wall into three layers is feasible, unlike the situation for animals normally used in such studies, and it is most relevant from the point of view of human physiology. In addition, according to the authors' experience, the separation of intact strips into their layers is much more difficult or even impossible to achieve for animal arteries or even for healthy young human arteries. Note, however, that in these cases the intima consists merely of a monolayer of endothelial cells lining the arterial wall and resting on a thin basal membrane, and is not significant from the solid mechanics point of view.

There are several novel features of the results presented here: first, residual deformations (stretching and bending) have been determined for circumferential and axial strips from intact aortic tissue; second, corresponding deformations have been recorded for the three separate layers in both the circumferential and axial directions; third, the deformations have been quantified by using image analysis. The study has shown that the intima has a significant thickness when compared with the media and adventitia. Hence, it is meaningful to model human aged aortas with non-atherosclerotic intimal thickening as a composite structure composed of three layers. In the literature no data concerning the axial *in situ* stretches of human aortas can be found. Such data are, however, of fundamental importance for the computation of *in situ* stress states. In the present study the axial *in situ* stretches were determined to be 1.196 ± 0.084 (mean $\pm$ SD), which is an average of about 20% pre-stretch with respect to the load-free length. This is significantly larger than values found for other human aged arteries such as iliac arteries (axial *in situ* stretch of 1.071 ± 0.087) [73], coronary arteries (1.044 ± 0.06) [76], and femoral arteries (1.1 ± 0.091 at 100 mmHg) [69]. By contrast, Fung et al. [139] reported axial *in situ* stretches of 1.5 for rabbit iliac arteries.

With reference to Figs 6.10 and 6.11, the following observations with respect to pre-stretches in the intact wall and the associated separate layers are important to note: first, the intact axial strip (before separation) undergoes negligible change in stretch, while the circumferential intact strip shortens by only about 1%; second, on separation both the circumferential and axial strips from the intimal elongate, but, by contrast, the adventitia and the media shorten significantly. For circumferential strips the media shortens on average more than the adventitia, while for the axial strip the reverse is the case. This suggests that in the intact wall both the media and the adventitia are under tension, while the intima is under compression, thereby emphasizing that in order to characterize residual deformations it is insufficient to consider just the opening angle since both bending and stretching have an influence.

These pronounced differences in the pre-stretches (and in distensibility) of the individual layers are the cause of the occurrence of relatively high tractions at the layer interfaces during load changes in aged arteries. These tractions, in combination with the compressive hoop stress in the intimal layer, may lead to

spontaneous layer delamination and resulting buckling of the intima (see Fig. 6.1). The relatively high tractions may also be the underlying reason for the feasibility and accuracy of anatomical layer dissection for human aged arteries in a relatively atraumatic way.

By referring to Fig. 6.2, in which the curvatures of the individual arterial segments are drawn to the correct scale, and to Fig. 6.12 the changes in curvatures can be identified. In particular, the flatness of the adventitial strips, the negative curvatures of the medial strips, the significant positive curvatures of the circumferential intimal strips, and the relative flatness of the axial intimal strips after separation should be emphasized. The changes in curvature can be associated with the release of the through-thickness stress distributions, in particular the transition from compressive to tensile circumferential stress through the wall from the intima to the adventitia. A particular feature to emphasize is that the behavior of the media with regard to bending follows the pattern of the intact strips, and that is for both directions. This suggests that the medial layer is dominant in this respect. Finally, a specific and interesting trend has been observed in respect of the media, based on 1600 sample measurements: for both the circumferential and axial directions the local curvature increases with the total wall thickness from negative values for relatively thin walls to positive values for thicker walls. A possible explanation of this phenomenon is as follows: while for thin walls the residual stresses are relatively small, for thicker walls the larger changes in curvature may be related to the significant and inhomogeneous through-thickness distribution of residual stress.

6.4.1 Limitations

The method developed is based on human aortas with non-atherosclerotic intimal thickening, but it is applicable in principle to other human arteries for which two or more tissue components can be separated, including atherosclerotic plaques. In order to draw conclusions concerning the effect of the anamnesis summarized in Table 6.1 on the state of residual stress many more samples would be required than we have used here. The method assumes that the separated strips are stress free. This, of course, is an approximation, as also indicated by Liu and Fung [28], where

it was suggested that further cuts were necessary to reach the zero-stress state. Ideally, circumferential and axial strips of the same dimensions should be used in order to avoid comparative size effects. Here we used circumferential and axial strips of approximately the same widths, but we were not able to obtain axial strips that were more than about half the length of the circumferential strips because of the location of atherosclerotic material. Study of the effect of specimen size on residual deformations might yield further valuable information. A common limitation of studies of this kind is the fact that damage to the material is caused locally near the edges of the strips when they are cut from the surrounding material and on the faces of the strips by the separation process. Both these could affect the residual deformation distribution.

Since we are concerned with the passive behavior of the tissue, we used a Ca^{2+}-free physiological saline solution in order to avoid muscular activity. Nevertheless, the absence of calcium from the bath may not preclude intracellular calcium stores in the tissue from inducing muscular contraction. A disadvantage of using the physiological saline solution is that its pH-value is somewhat lower than that of the normal pH-value of blood. The effect of this difference on the residual deformation distribution is not clear. The main alternative solution, i.e. phosphate-buffered saline (PBS), has the pH-value of blood, but was not used because it contains potassium chloride (KCl), which is likely to cause muscle activation. Also, so as to avoid any active response of smooth muscle cells, substances such as acetylcholine and histamine were not used during the experiments, and neither was electrical stimulation. Factors such as the time of measurement after post-mortem and/or rigor mortis might influence the behavior of smooth muscle cells in arterial walls, but not of the bradytrophic tissue components such as collagen or elastic fibers. We note, however, that all measurements started at least 6 hours post mortem, suggesting that there was no (non-reversible) ischemic damage of smooth muscle cells. We therefore claim that only the passive response of the arterial wall layers has been tested. To take the intravital active reaction of smooth muscle cells into account would have required a more complicated experimental setup. This issue was not addressed here, but should be examined in a subsequent study. In our experimental procedure we used warm ischaemia. We did not determine the influence of cold ischaemia on the mechanical properties of arterial wall layers.

We recall that in the determination of the curvatures we have approximated the real geometry by using circular arcs for both directions. Strictly this gives a crude approximation to the three-dimensional geometry, which can be improved by using ellipsoidal patches. Further information on layer-specific 3D residual deformations could be provided by cutting strips at orientations different from axial or circumferential orientations. For identifying the relevant dimensions of the individual tissue samples we used imaging-processing software that was specifically developed for this purpose. The results for the thickness-measurements were validated with corresponding measurements from the video-extensometer, thereby confirming the accuracy of the measurements. However, it should be pointed out that the exact 3D geometries of the tissue samples were not known, and therefore an accuracy measure of the 3D tissue boundaries could not be determined.

The fixing of the tissue samples on the cylinder was essential for the feasibility of the experimental investigation. The choice of cyanoacrylate adhesive seems to be the most reliable since this adhesive does not diffuse into the surrounding tissue. The potential effect of the adhesive is, therefore, very localized, and does not influence the global deformation behavior of the tissue samples.

6.5 Concluding Remarks

The data provided in this paper serve as a sound basis for the development of a three-dimensional kinematic model of the residual deformation state in the aortic wall. This model can then be used for the construction of constitutive and computational models of the material that incorporate the associated residual stresses. This will be helpful for clarifying the role of layer-specific 3D residual stresses and deformations in vascular mechanobiology. It is important to emphasize that for a thorough understanding of the complex mechanobiology of human aged arteries, appropriate physical models that account for all three layers of the wall with layer-specific data on the residual deformations are then required. The images shown in the present study draw attention to these characteristic features, and hence point to novel challenges in contemporary arterial wall mechanics. As indicated above, these layer-specific patterns of deformation show systematic differences. It may be hypothesized that these distinctive phenomena reflect the specific functions

of the various vascular cells in respect of their mechanical environment. After all, it is these cells that sense continuously the mechanical stresses and deformations and are responsible for geometrical changes and material remodeling. The mechanobiological role of the residual stresses and deformations in the individual layers requires clarification in order to improve our understanding of the complex interactions between mechanical quantities and biological processes.

7 DISSECTION PROPERTIES OF THE HUMAN AORTIC MEDIA: AN EXPERIMENTAL STUDY

Abstract.   Aortic dissection occurs frequently and is clinically challenging; the underlying mechanics remain unclear. The present study investigates the dissection properties of the media of 19 human abdominal aortas (AAs) by means of direct tension tests (n=8) and peeling tests (n=12). The direct tension test demonstrates the strength of the media in the radial direction, while the peeling test allows a steady state investigation of the dissection propagation. To explore the development of irreversible microscopic changes during medial dissection, histological images (n=8) from four AAs at different peeling stages are prepared and analyzed. Direct tension tests of coin-shaped medial specimens result in a radial failure stress of 140.1 ± 15.9 kPa (mean±SD, n=8). Peeling tests of rectangular-shaped medial strips along the circumferential and axial directions provide peeling force/width ratios of 22.9 ± 2.9 mN/mm (n=5) and 34.8 ± 15.5 mN/mm (n=7); the related dissection energies per reference area are 5.1 ± 0.6 mJ/cm^2 and 7.6 ± 2.7 mJ/cm^2, respectively. Although Student's t-tests indicate that force/width values of both experimental tests are not significantly different ($\alpha = 0.05$, $p = 0.125$), the strikingly higher resisting force/width obtained for the axial peeling tests is perhaps indicative of anisotropic dissection properties of the human aortic media. Peeling in the axial direction of the aorta generates a remarkably 'rougher' dissection surface with respect to the surface generated by peeling in the circumferential direction. Histological analysis of the stressed specimens reveals that tissue damage spreads over approximately 6-7 elastic laminae, which is about 15-18% of the thickness of the abdominal aortic media, which forms a pronounced cohesive zone at the dissection front.

7.1 Introduction

Arterial dissections may occur spontaneously or non-spontaneously as a result of a traumatic injury and have been observed in several arterial branches including the aorta. Aortic dissections frequently result from an intimal tear (see [213] and references therein) or from a perforation of the intima as, for example, caused by intramural hemorrhage and hematoma formation [214]. Moreover, mechanical traumatization of the intima due to cannulation for catheter-based diagnostic and/or therapeutic interventions have been identified as initiating aortic dissections [215]. These intimal defects can cause concentrations of mechanical stress of the pressurized aorta and may be the trigger for the propagation of the medial dissection. In addition, blunt traumatic aortic rupture following motor vehicle accidents carries a high mortality, and occurs in 21% of car occupant deaths in the UK [216]. Traumatic aortic dissection is one consequence for blunt thoracic trauma patients [217]. In a population-based long-term study, 86 cases of aortic dissection were found in 84 patients (mean age of 65.7 yr), 66 patients were hospitalized and 18 non-hospitalized [218]. A total of 22.7% of the hospitalized patients died within the first 6 h, 33.3% within 12 h, 50% within 24 h, and 68% in total died within the first 2 days after admission. Untreated, a dissection may propagate until it runs either back into the lumen, resulting in the reduplication of the aortic lumen (false lumen), or it ruptures through the adventitia, often with a lethal outcome [214]. For example, in the absence of intervention, acute aortic dissections have a 90% chance of mortality, and the majority of these deaths occur within 48 hours [219].

The incidence of spontaneous aortic dissection is 5 to 30 cases per million people per year, and it strongly depends on the presence of risk factors. Among many others, chronic systemic hypertension, atherosclerosis, Marfan's and Ehlers-Danlos syndromes, aortic dilatation (aneurysm), and coarctation of the aorta are well-established predisposing factors for aortic dissection [214, 220]. Chronic systematic hypertension is the most common predisposing factor and has been present in 62 to 78% of patients with aortic dissection [214].

A common cause of media dissection is balloon angioplasty, an established and effective therapeutical intervention to reduce the severity of atherosclerotic stenosis [221]. Balloon angioplasty involves denudation of endothelium, disruption of

the intima and the atherosclerotic plaque with frequent separation from or dissection of the media, and overstretching of non-diseased portions of the arterial wall, see, for example, [89] and references therein. In particular, dissection is a characteristic form of arterial trauma involving laceration and/or cleavage of the arterial wall. Plaque fracture and/or dissections are major contributors to the gain in lumen following balloon angioplasty [221]. Moreover, dissection has been implicated as a contributing factor to both acute procedural complications (abrupt re-closure, ischemia, myocardial infarction, emergency surgery, and coronary microembolization [222–226]), and chronic restenosis of the treatment site [227]. Luminal gain, tissue injury and the risk of wall fracture are quantities for consideration with this interventional procedure. Dissection secondary to tear propagation is a particular form of balloon angioplasty-induced arterial trauma, and serves as an important predictor of clinical outcome after balloon angioplasty intervention [228].

The rubber-like protein elastin, the stiff fibrous protein collagen and smooth muscle cells influence the mechanical properties of arterial walls. In the media of elastic arteries (like the aorta) these three components are found to be organized in medial lamellar units [229], each of which is about 10μm thick [112]. These laminated structures may be prone to separation creating a cleavage plane parallel to the elastic lamellae [230], and hence provide the mechanism to propagate a dissection in parallel to the lumen [231]. Spontaneous aortic dissections typically show steady-state like failure propagation, which might indicate a kind of fatigue mechanism caused by the pulsatile loading of the aorta. By contrast, balloon angioplasty causes extraordinarily high mechanical loading to the (stenotic) tissue during one or more episodes of treatment, and hence (quasi)-static failure mechanisms seem to apply. Although arterial dissection is a frequently occurring phenomenon and a challenging clinical entity the underlying biomechanical properties remain largely unclear.

The present study was carried out with the goal to investigate the dissection properties of the aortic media. Direct tension and peeling experiments of the media of human abdominal aortas were performed. The direct tension test demonstrates the dissection strength across the lamellae of the media in the radial direction, while the peeling experiment explores the fracture energy required to propagate a dissection. Under certain assumptions, the performed experiments allow an

estimation of the constitutive properties of medial dissection within the abdominal aorta. The gathered data have served as a basic input for the finite element modeling of the experiments, presented in the companion paper [232]. From the combined experimental and numerical investigation an accurate prediction of the dissection properties is feasible. To this end the material parameters in the finite element model, which affects the dissection process, are varied until the numerical prediction matches the experimental data. In addition the mechanical study is enhanced by histology at different stages of the peeling test to explore the development of irreversible changes on the microscale level during medial dissection.

7.1.1 Fracture Properties of the Aorta

To our knowledge the approach in this study is new. However, a variety of methods have been developed and implemented with the goal to explore the failure properties of aortic tissue. A summary of related experimental data is given in Table 1 with respect to tensile, inflation, tearing, splitting and peeling tests performed on human and porcine aortic tissues.

The following tests have been performed to determine the tensile strength of aortic tissue: – uniaxial tensile tests in radial directions [235], circumferential and axial directions [141, 236], inflation tests on circular specimens incorporating bubble inflation techniques [237], inflation tests of intact arteries [238], and tearing tests of arterial strips [239] were performed to determine the tensile strength of aortic tissue. Beside that, in the literature only a few techniques have been presented to investigate the dissection properties of the aortic media. A commonly used approach has been to create a bleb by infusing a fluid into the media, as it was presented for human aortas decades ago [244, 245]. This idea has been adopted by Roach and colleagues to investigate dissection properties of the canine thoracic aortas [231], the porcine aorta [240, 242] and the human aorta [241]. Moreover, they applied this method to isolated and pressurized porcine aortas in order to explore the mechanisms of dissection propagation under more physiological circumstances [230, 243].

The experimental data from tensile tests on aortas indicate that they are dependent

Table 7.1: *Failure properties of arterial tissue according to tensile, inflation, tearing, splitting and peeling tests. Mean values are presented with standard deviations.*

Tensile test				
Tissue	Circ. strength (MPa)	Axial strength (MPa)	Radial strength (MPa)	Reference
Human descending mid-thoracic aorta	1.72 ± 0.89	1.47 ± 0.91	——	[141]
Human abdominal aorta	——	1.21 ± 0.33	——	[233]
Human descending thoracic aorta	1.76 ± 0.22	1.95 ± 0.60	——	[234]
Porcine thoracic aorta	——	——	0.061 ± 0.004	[235]
Human ascending thoracic aorta	1.80 ± 0.24	1.71 ± 0.14	——	[236]
Human abdominal aorta	——	——	0.140 ± 0.016	Present study

Inflation test		
Tissue	Ultimate stress (MPa)	Reference
Human descending mid-thoracic aorta	0.114 ± 0.032	[237]
Human descending thoracic aorta	2.7 ± 1.5	[238]

Tearing test		
Tissue	Circ. breaking stress (MPa)	Axial breaking stress (MPa)	Reference
Porcine upper descending thoracic aorta	2.19 ± 0.57	0.18 ± 0.44	[239]
Porcine lower descending thoracic aorta	3.64 ± 0.53	0.87 ± 0.34	[239]

Media splitting test		
Tissue	Max. pressure (MPa)	Splitting energy (mJ/cm^2)	Reference
Porcine descending thoracic aorta	0.077 ± 0.002	15.9 ± 0.9	[240]
Human thoracic and abdominal aorta	0.079 ± 0.029	0.17	[241]
Porcine upper thoracic aorta	0.106 ± 0.022	2.84 ± 1.19	[242]
Porcine lower thoracic aorta	0.109 ± 0.019	2.90 ± 1.21	[242]
Porcine upper abdominal aorta	0.095 ± 0.037	1.88 ± 0.89	[242]
Porcine lower abdominal aorta	0.085 ± 0.027	11.34 ± 4.05	[242]
Porcine thoracic aorta	0.071	——	[230]
Porcine descending thoracic aorta	0.073	——	[243]

Peeling test		
Tissue	Circ. dissection energy (mJ/cm^2)	Axial dissection energy (mJ/cm^2)	Reference
Human abdominal aorta	5.1 ± 0.6	7.6 ± 2.7	Present study

on the anatomical site of the vessel and that the tensile failure behavior is perhaps anisotropic (see Table 1). The aortic strength in the axial direction seems to be slightly lower than in the circumferential direction;however, the large standard deviation makes this finding inconclusive. The failure properties obtained from tensile tests suggest that the tensile strength of the human aorta is decreasing with increasing distance from the heart.

Tensile or inflation tests of soft biological tissue are poorly suited to quantify the fracture energy of the tissue, since these testing methods cause unstable (dynamic)

failure, i.e. its propagation cannot be controlled. In contrast, tearing experiments, as conducted in [239], lead to controlled failure propagations of tissues and allow a quantification of the fracture energy. That paper [239] documents that the circumferential 'breaking stress' (evaluated through axial tearing experiments) exceeds the axial 'breaking stress' (evaluated through circumferential tearing experiments), which is in accordance with findings from tensile tests. Media splitting showed that the maximum splitting pressure is fairly constant; however, the splitting energy decreases with distal position along the aorta. For comparative purposes the results from the direct tension and the peeling tests of the present study are included in Table 1. Note that the experimental approach of the peeling test is fundamentally different from the 'Tearing Test' and the 'Media Splitting Test', which was noted by the introduction of a separate category in the table.

7.2 Material and Methods

7.2.1 Material

In the present study, 19 human abdominal aortas (AAs) (age range 36 to 75 yrs, 10 males and 9 females) were harvested during autopsy within 24 h from death. We have taken segments from the infrarenal portion of the AA. It was a requirement that pathological changes such as severe atherosclerosis were not present in the specimens. In order to satisfy this requirement the condition and texture of the intima were closely inspected by a trained pathologist. After harvesting, the specimens were stored in a calcium-free and glucose-free 0.9% physiological saline solution at $4\,^\circ$C until use. Use of autopsy material from human subjects was approved by the Ethics Committee, Medical University Graz, Austria. All tests were performed within 48 h from death.

7.2.2 Specimen Preparation

We conducted two different mechanical failure tests of the media of the AA specimens – denoted by (i) *direct tension tests* and (ii) *peeling tests*. The peripherally attached adipose and loose connective tissues were carefully removed from the adventitia of the aortic patch. The AAs were then cut along the axial direction to
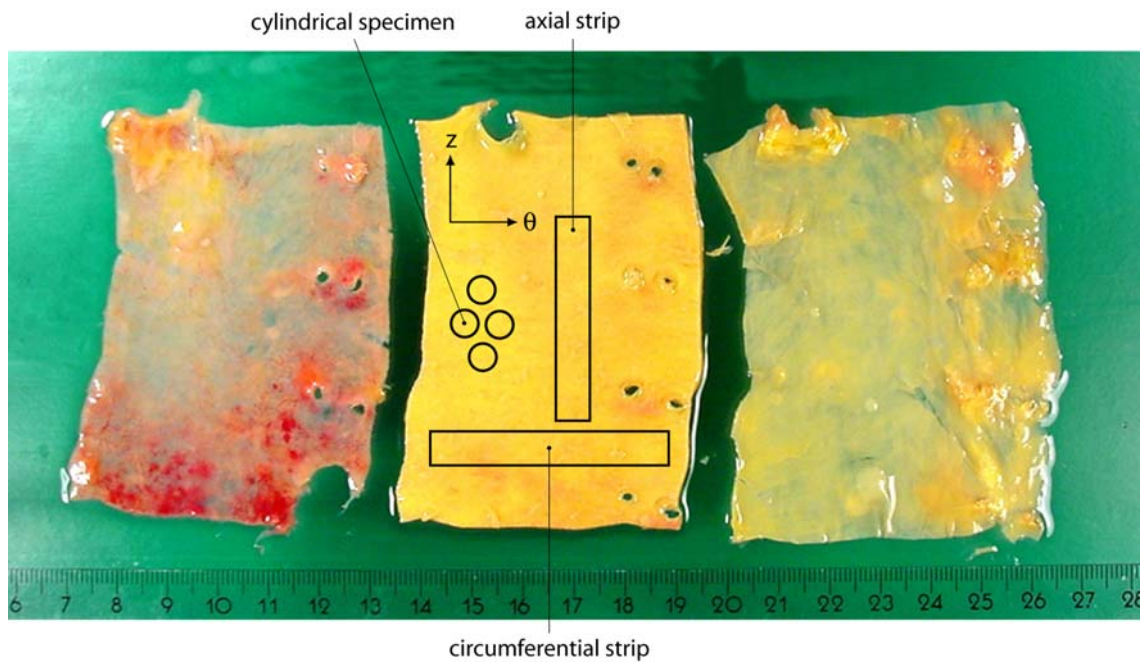
Figure 7.1: Arterial layers prepared from an aortic patch (adventitia, media, intima – from left to right) – donor: male, 63 yr. The arrangement of the test specimens with respect to the medial patch is shown schematically on the central photograph. Cylindrical (coin-shaped) specimens were prepared for the direct tension test, and circumferential and axial oriented strip specimens for the peeling tests. The circumferential and axial directions of the artery are indicated by θ and z, respectively. The photographed centimeter scale provides a dimensional reference.

obtain flat rectangular tissue sheets. For the anatomical separation of the three layers we tested various locations at which the layer separation process can easily be initiated. The arterial layers were separated with careful dissection techniques and with the aid of a surgical scalpel. Reflected light microscopy was used to inspect the layer preparation process. The structured media could easily be distinguished from the intimal and the adventitial tissues. In addition, for all specimens considered in the study, related histological images were prepared and investigated in order to confirm that specimens consisted only of medial tissue. This technique has been successfully applied in the past (see [76], [34]). Particular attention has been paid to minimize the mechanical damage of the media including tissue immersion in a 0.9% physiological saline solution throughout the whole separation process. Figure 7.1 shows photographs of the separated intimal, medial and adventitial layers (from left to right), where it can be seen that even perforating vessels have

not caused any difficulties during the separation process.

While intimal and adventitial tissues were not further considered, the medial patches were used to prepare the specimens for the conducted mechanical testing and for subsequent histological investigations. A cylindrical blanking tool was used to punch out 8 coin-shaped specimens for the direct tension test (6.0 mm diameter, and 1.16 ± 0.15 mm (mean±SD), thickness), subsequently denoted as *D I – D VIII*. These 8 radial tension test specimens were obtained from three different AAs. Several specimens were obtained from the same aorta, as indicated in Fig. 7.1, but note that only about 1 out of 5 direct tension tests was successful. A total of 12 rectangular-shaped strip specimens were cut out with a surgical scalpel for the peeling tests, whereas each peeling sample was from a different AA. From Fig. 7.1 it can be seen that the rectangular strips are either oriented in the circumferential direction θ or in the axial direction z. Five specimens were cut out along the circumferential direction of the aorta, subsequently denoted as *PC I – PC V*, and seven specimens were cut out along the axial direction of the aorta, subsequently denoted as *PA I – PA VII*.

In order to get the specimens ready for testing, some final preparations were required. After mounting the specimens for the direct tension test on the testing machine an incision of about 1.0 mm depth around the circumference of the circular specimen was cut with an especially adapted surgical knife. This undercut provided the site for the initiation of failure (and reduced the tissue diameter from 6.0 to 4.0 mm). The specimens devoted to the peeling test were split at one end to get two 'tongues' (8-10 mm in length) of about equal thickness for mounting them on the testing machine. We used a superadhesive gel to glue rectangular pieces of sandpaper (Grit: 320) at both sides of the 'tongues' to avoid slipping of the specimen in the clamps of the testing machine during loading. A representative specimen, ready for a peeling test, is shown in Fig. 7.2. The individual dimensions of the aortic test specimens are summarized in Tables 2-4. Note that the dimensions refer to the prepared medial patches, and that the effective lengths of the peeling test specimens in the circumferential and axial directions are denoted as L_{pc} and L_{pa}, respectively.
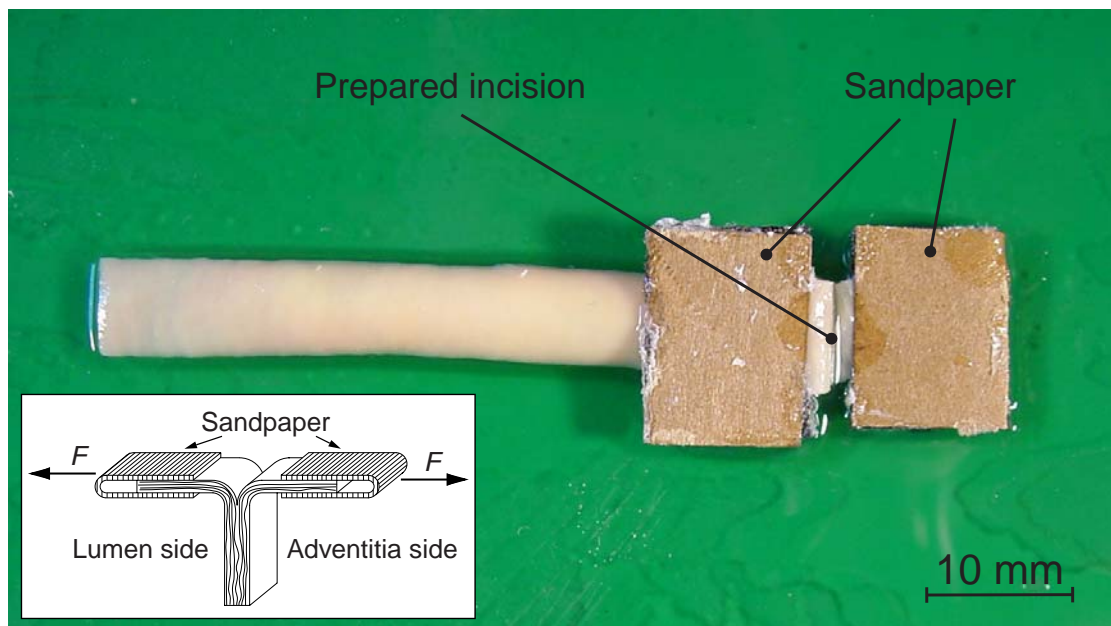
Figure 7.2: Macroscopic view of a representative specimen ready for a peeling test, and sketch showing the 3D nature of the figure.

7.2.3 Mechanical Testing

Device

Mechanical tests were performed on a computer-controlled, screw-driven high-precision tensile testing machine (Messphysik, μ-Strain Instrument ME 30-1, Fürstenfeld, Austria), which was adapted for small biological specimens (experimental setup shown in Fig. 7.3). The specimens were investigated in a perspex container filled with 0.9% physiological saline solution maintained at $37.0 \pm 1.0\,°C$ by a heater-circulation unit (type Ecoline E 200; Lauda, Lauda-Königshofen, Germany) and the tensile force were measured with a 10 N class 1 strain gauge-load cell (type TCA 10 N, code CTCA1K5; AEP transducers, Modena, Italy). The upper and the lower fixing clamps of the testing machine are moving in opposite directions, which keeps the center of the specimen fixed in space. A position control resolution of 0.04 μm of the upper and the lower crosshead of the tensile testing machine (see Fig. 7.3) and a combined error of 0.03% of the 10 N load cell is specified by the manufacturer. For our case this means that a combined error of 0.6 mN may occur at a maximum occurring force of 2 N. While the specimens for the peeling test could directly be mounted on the testing machine, an especially developed
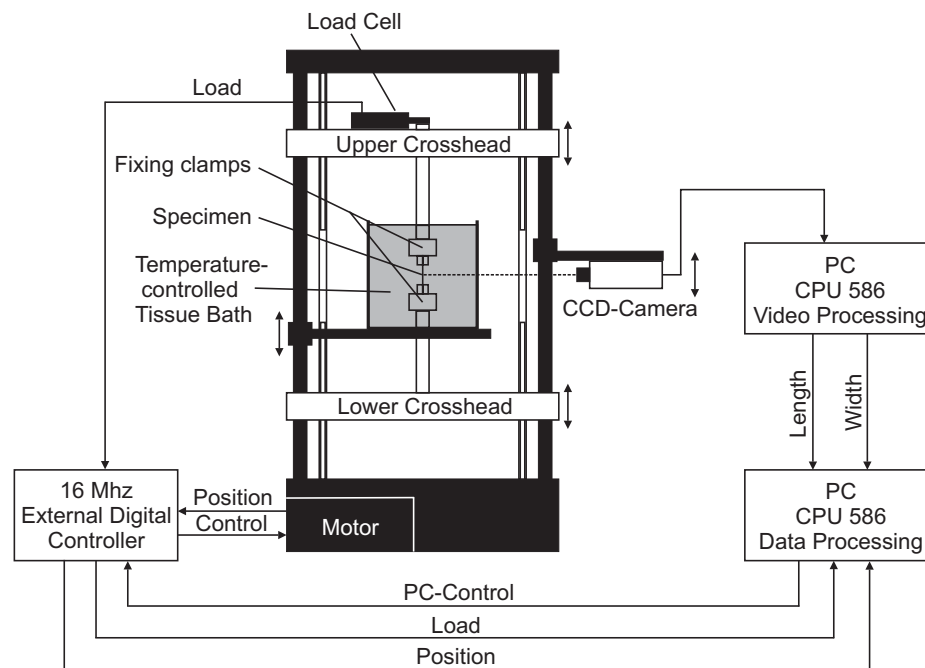
Figure 7.3: Schematic experimental setup.
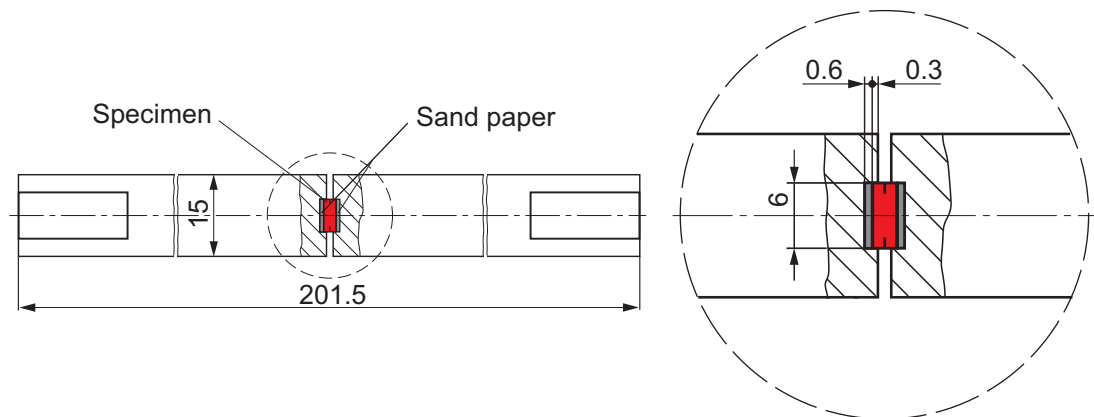
Figure 7.4: Schematic direct tension fixing tool with a detailed drawing of the specimen-rod connection. Dimensions are given in mm.

specimen holder was used for the direct tension test.   A small cylindrical-shaped recess (deepening) in each plastic rod, with fixed sandpaper (Grit: 320) therein, leads to a strong specimen-rod connection. The coin-shaped specimens were then glued with cyanoacrylate glue onto the fixed sandpapers on the two plastic rods for mounting on the testing machine (Fig. 7.4).

Table 7.2: *Thickness of the specimens* D I – D VIII *for the direct tension test*

Specimen	Thickness (mm)
D I	1.34
D II	1.20
D III	0.97
D IV	1.04
D V	1.27
D VI	1.07
D VII	1.34
D VIII	1.01
mean±SD	1.16±0.15

Table 7.3: *Length* L_{pc}, *width and thickness of the circumferential peeling test specimens* PC I – PC V.

Specimen	Length L_{pc} (mm)	Width (mm)	Thickness (mm)
PC I	30.1	6.5	0.96
PC II	31.5	8.3	1.58
PC III	27.4	8.3	0.93
PC IV	27.1	9.3	1.15
PC V	31.0	8.1	1.20
mean±SD	29.4±2.0	8.1±1.0	1.16±0.26

Table 7.4: *Length* L_{pa}, *width and thickness of the axial peeling test specimens* PA I – PA VII.

Specimen	Length L_{pa} (mm)	Width (mm)	Thickness (mm)
PA I	15.0	8.3	2.43
PA II	18.0	7.8	1.74
PA III	30.0	8.2	1.53
PA IV	35.0	8.9	1.43
PA V	33.5	8.6	1.57
PA VI	25.0	8.2	1.39
PA VII	15.0	7.4	1.82
mean±SD	24.7±8.0	8.2±0.5	1.70±0.36
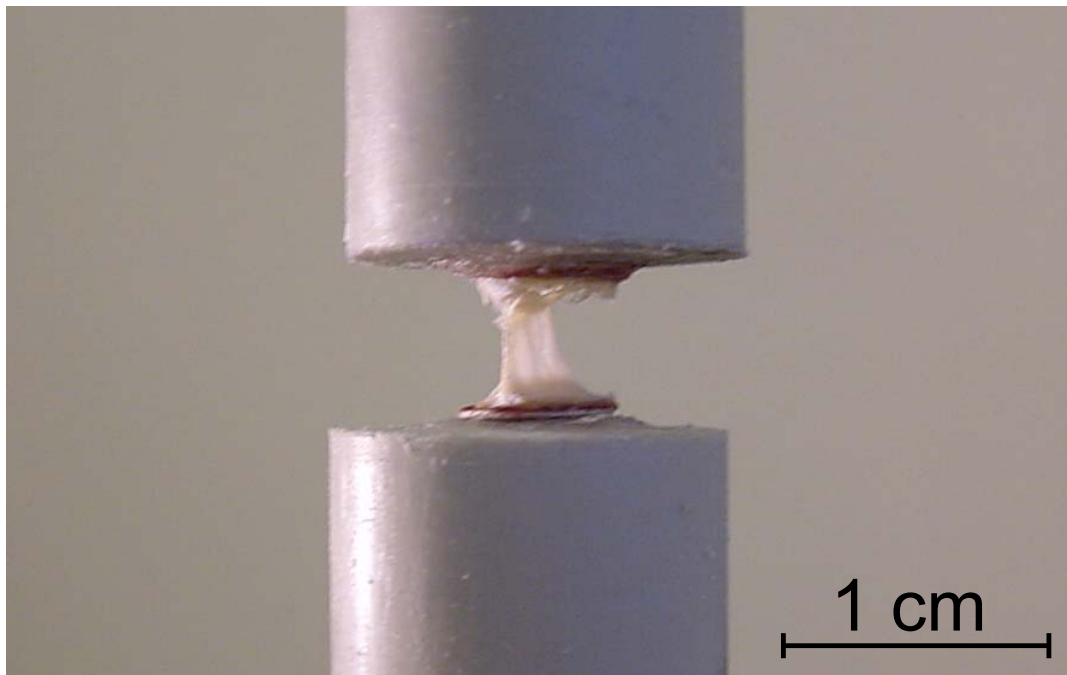
Figure 7.5: Representative photograph of the end stage of a successful direct tension test.

Protocol

Direct tension test. Cyanoacrylate glue was placed on the sandpaper into the cylindrical recess of the upper and lower rods of the specimen holder. The lower rod was then mounted on the testing machine and the circular test specimen was placed in the cylindrical recess. The upper rod of the specimen holder was mounted on the testing machine, and a compression force of 1.0 N was applied to the specimen for about 5 minutes to allow the adhesive to react. Before testing, the specimen was moistened with 0.9% physiological saline solution. Throughout the whole test the extension rate of 1.0 mm/min was controlled and the resisting force recorded. Moreover, the whole test was recorded by a CCD-camera and saved in SVHS-format. After the specimen was completely separated the zero load level was defined and the failure surface has been visually inspected. Frequently it happened that failure occurred at the region where the specimen was glued to the specimen holder and not at the location where the incision was placed. If that was the case the test was rejected. A representative photograph of the end stage of a successful direct tension test is shown in Fig. 7.5.
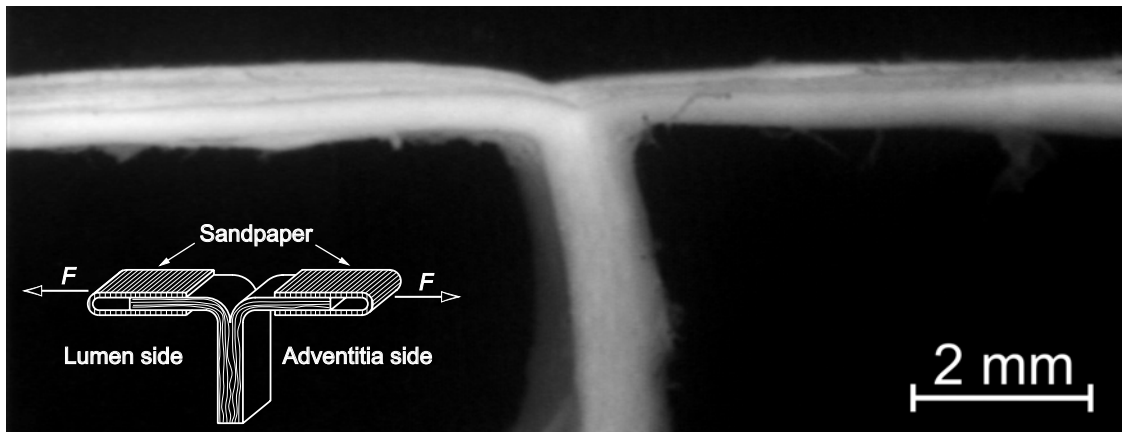
Figure 7.6: Representative image of a circumferentially oriented strip specimen during a peeling test acquired from the videoextensometer, and sketch showing the 3D nature of the image.

Peeling test. Both tongues of the specimen were mounted on the testing machine. Similar to the tension direct tension test, the extension rate of 1.0 mm/min was controlled, and the measured force recorded. The whole test was recorded, saved in SVHS-format, and the zero load level was defined after complete separation of the specimen. In order to account for effects of buoyancy the testing machine's 'buoyancy-force-displacement' curve was subtracted from the achieved results. This curve was recorded for a particular level of fluid in the perspex container but without a test specimen. A representative image of the medium stage of a circumferentially oriented strip specimen during a peeling test is shown in Fig. 7.6.

Measurement of specimen dimensions. The geometrical dimensions (length, width, thickness) of the test specimens were measured optically before the individual tests by using a PC-based videoextensometer utilizing a full-image CCD camera. For the length and width measurements the strip samples were positioned in air on a black plate in front of the CCD camera. After calibration of the videoextensometer its automatic edge recognition capability was used to quantify the dimensions. For the thickness measurement the strip sample was positioned in air on a black colored object plate of known thickness (1 mm). One lateral side of the gage region of the strip sample was in plane with the lateral side of the object plate and oriented towards and perpendicular to the CCD-camera. Then the thickness of the contour

(sample plus object plate) was measured by the videoextensometer within the gage region. The resulting thickness value of the sample was determined then as the average of the contour thickness along the gage region minus the thickness of the object plate.

7.2.4 Histology

In order to investigate irreversible changes of the tissue's microstructure due to dissection, 8 additional rectangular-shaped strips (4 circumferentially and 4 axially oriented) were prepared from 4 AAs. In contrast to the aforementioned peeling tests, these strips were not dissected throughout their whole length. We stopped the peeling approximately in the middle of the strip length. For that reason we designed a specimen holder in order to 'freeze' the loading state of the tissue sample (Fig. 7.7). After mounting the tissue in the specimen holder it was fixed in 7% neutral-buffered formaldehyde solution (pH 7.4), embedded in paraffin using standard techniques and prepared for histological investigations.

The media which was partly dissected was then sectioned at $4\,\mu$m and stained with Elastica van Gieson. The applied technique allowed us to investigate, histologically, the gradual development of the damage state in the media subjected to supra-physiological loading, and to trace and study the irreversible effects in the medial tissue due to mechanical loading.

7.3 Results and Interpretation

7.3.1 Direct Tension Test

Figure 7.8 presents the measured force-displacement response of all 8 coin-shaped media specimens during the direct tension test. The thick (solid) curve characterizes the mean response of the individual tissue tests, which are denoted by thin curves. Note that after a radial extension of approximately 4.5 mm some curves drop down to zero so that less than 8 specimens are included in the averaging process above 4.5 mm. The mean curve represents the arithmetic mean calculated with the data analysis software OriginPro 7.5 (OriginLab Corporation).
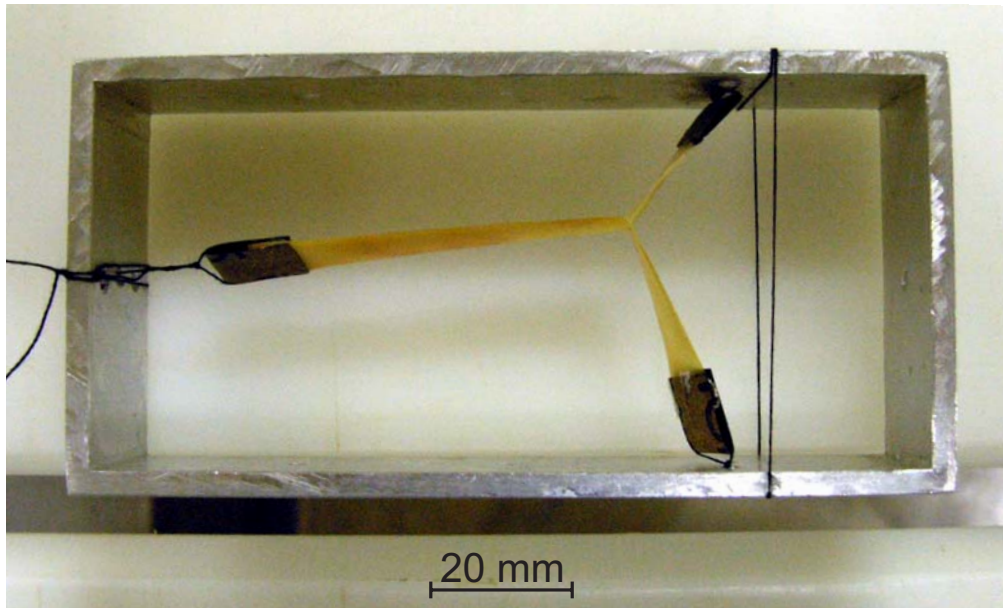
Figure 7.7: Photograph of a mechanically fixed specimen in the specimen holder.

During the increasing displacement, the force-displacement response shows a characteristic sequence, which we subsequently denote by the three regions: *S1* for elastic, *S2* for damage and *S3* for failure (see Fig. 7.8). The region *S1*, i.e. the initial phase of the force-extension curve, is assumed to represent the tissue's elastic response and is characterized by a steep slope in the force-displacement curve. It is governed by the geometry of the test specimen (diameter, thickness and incision depth) and the material properties of the media of the human AA. At about 1.25 N the 'elastic limit' is reached. Damage softening (decreasing stiffness with increasing damage of the tissue [246]) and generation of micro-defects characterize region *S2*, which is a region that still has increasing resistance to extension. As illustrated in MacLean et al. [235] (Fig. 4 therein) there may be ruptured elastin layers on a microscale that lead to cavities and to the characteristic pattern for micro-defects in the media. The state of damage evolves further until a displacement of about $u = 0.85$ mm, with the limit force of $F_{\max} = 1.76 \pm 0.20$ N (mean±SD, n=8), is reached, and micro-defects coalesced. Consequently, the media dissects, which is indicated by the decreasing force in region *S3*. Our experiments suggest that the primary dissection *S3a* is followed by a peeling like failure mechanism *S3b*, which determines a plateau in the force-displacement curve until it drops to zero (see Fig. 7.8).
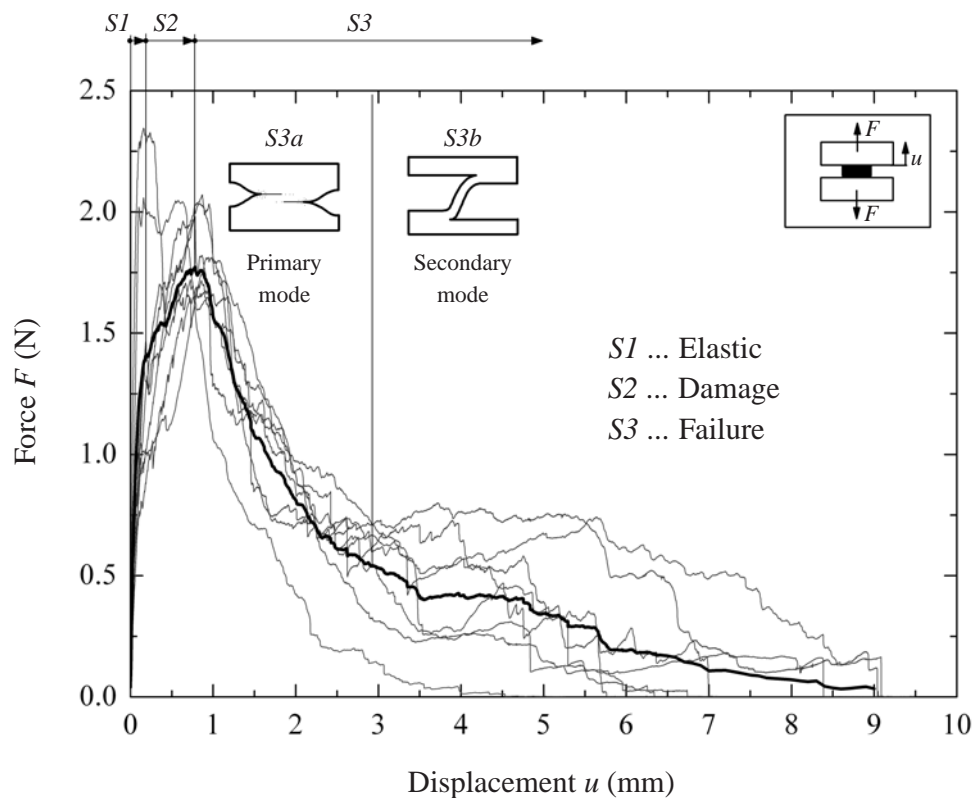
Figure 7.8: Force-displacement behavior for all 8 coin-shaped specimens during the direct tension test. The thick (solid) curve characterizes the arithmetic mean response.

7.3.2 Peeling Test

The applied peeling test caused a slow and controlled dissection propagation, where the force-displacement curve is characterized by a jagged plateau region. In the following the results of the peeling of human AA medias in circumferential and axial directions are presented separately. Figures 7.9 and 7.10 illustrate the measured force/width with respect to the dissection path during the peeling test, where the thick (solid) curves denote the arithmetic means of the individual tests (5 in circumferential and 7 in axial direction), which themselves are illustrated by thin curves.

We fitted the experimental data of the individual experiments to horizontal lines in the force/width-dissection graph, i.e. to constant peeling forces per width, which is motivated by assuming (ideal) rectangular geometries and homogeneous me-
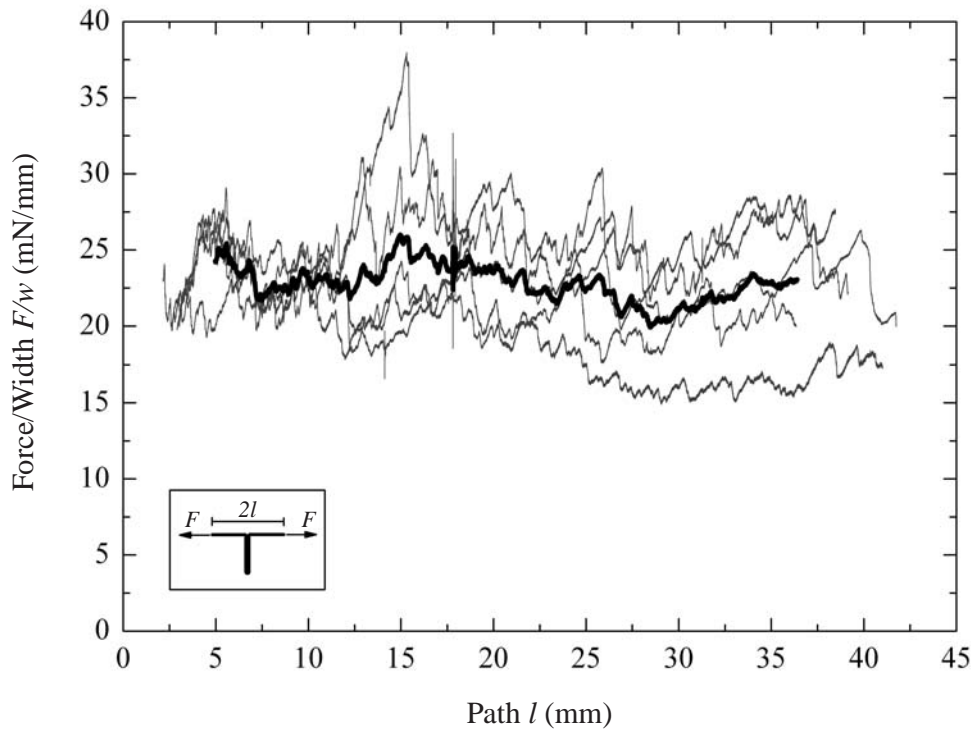
Figure 7.9: Force/width versus dissection path for all 5 circumferential strip specimens during the peeling test. The thick (solid) curve characterizes the arithmetic mean response.
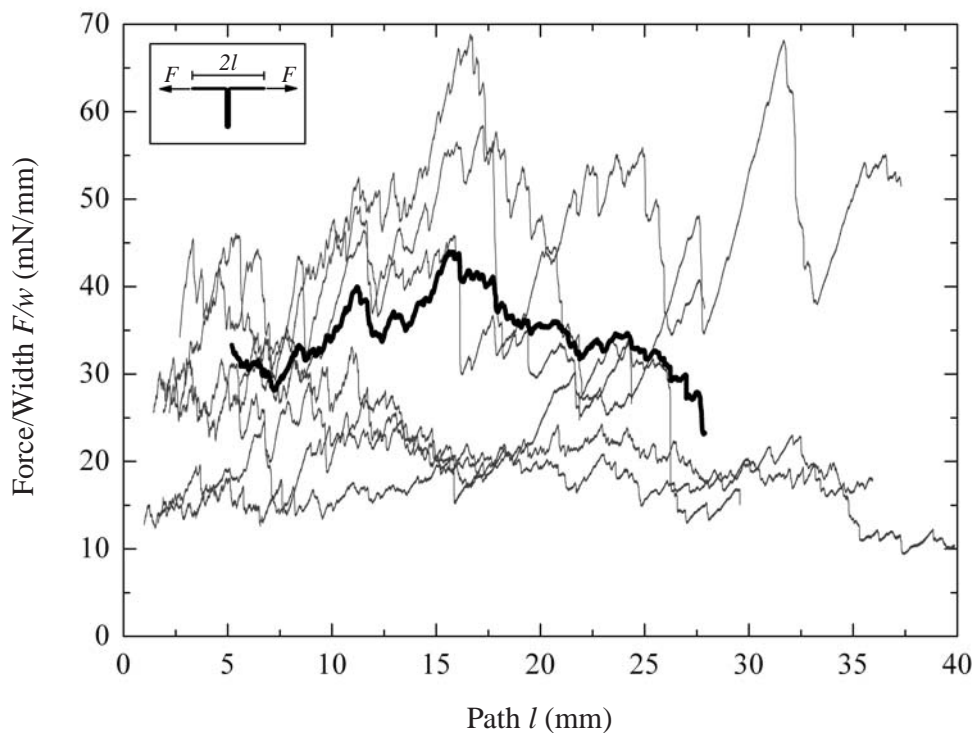
Figure 7.10: Force/width versus dissection path for all 7 axial strip specimens during the peeling test. The thick (solid) curve characterizes the arithmetic mean response.

chanical properties of each specimen. The calculated average resisting forces with their related standard deviations of the individual test specimens in circumferential (*PC I – PC V*) and axial (*PA I – PA VII*) directions are summarized in Table 7.5. As can be seen from these data, and, as already illustrated in Figs. 7.9 and 7.10, there is a smaller scatter of the circumferential test specimens when compared with the axial test specimens, which indicates anisotropic properties of the human aortic media in that respect.

In addition to the investigation of the individual peeling tests, the arithmetic means of the experimental data of the 5 circumferentially and 7 axially oriented test specimens, i.e. the thick (solid) curves in Figs. 7.9 and 7.10, were fitted to horizontal lines in the force/width-dissection graph. These defined the average peeling force/width of $F_{pc} = 22.9 \pm 2.9$ mN/mm (mean±SD, n=5) and of $F_{pa} = 34.8 \pm 15.5$ mN/mm (mean±SD, n=7) (see Table 7.5) of human abdominal medias along the circumferential and axial directions, respectively. The Student's t-test (significance-level of $\alpha = 0.05$) gives a *p*-value of 0.125, which indicates that the force/width values of both tests are not significantly different.

However, the strikingly higher resisting force/width obtained for the axial peeling tests with respect to the circumferential peeling tests is perhaps indicative of anisotropic dissection properties of the human aortic media.

7.3.3 Histological Investigation

As mentioned in Section 7.2.4 eight additional rectangular-shaped strips were prepared and dissected up to about the middle of their lengths, and, consequently, the stress state was 'frozen' in a specifically designed device. Related histological images were prepared.

Figure 7.11(a) shows the media in a kind of 'frozen stress state' which straightens the elastic laminae, and the intermingled collagen fibers and smooth muscle cells might straighten as well. Figure 7.11(b) shows the media embedded under stress-free conditions. The parallel sheets of elastic laminae are attached to each other by fine elastin, collagen fibers and smooth muscle cells, as indicated in the histological images presented in Fig. 7.11. For a detailed explanation of the transmural organization of the arterial media see the electro-microscopical study [64]. We found an

Table 7.5: *Peeling force/width defining the circumferential and axial peeling properties of human AA medias:* PC I – PC V *and* PA I – PA VII *refer to the individual specimens for the circumferential and axial peeling tests, respectively. The values* F_{pc} *and* F_{pa} *denote the arithmetic means of the peeling force/width of the* 5 *circumferentially and the* 7 *axially oriented test specimens, respectively.*

Circumferential peeling		Axial peeling	
Specimen	Force/Width (mN/mm)	Specimen	Force/Width (mN/mm)
PC I	25.2±2.2	*PA I*	37.9±8.2
PC II	22.6±1.8	*PA II*	38.0±5.6
PC III	21.0±1.6	*PA III*	47.6±9.0
PC IV	26.2±2.9	*PA IV*	17.0±3.0
PC V	19.3±2.9	*PA V*	22.8±4.3
–	–	*PA VI*	20.8±5.3
–	–	*PA VII*	59.3±10.9
–	$F_{pc} = 22.9 \pm 2.9$	–	$F_{pa} = 34.8 \pm 15.5$

average of 40 ± 4 (mean±SD, n=8), lamellar units in the human abdominal aortic media of the investigated specimens. Note that collagen fiber bundles and smooth muscle cells are barely seen in these images because of the choice of stain, which accentuates elastin fibers.

The microscopical damage to the media during the peeling in circumferential and axial directions is nicely illustrated in Figs. 7.12(a) and (b), as can be seen by the area at the dissection front. In this area a pronounced cohesive zone has developed, within which fiber bridging might play a dominant role. The elastic laminae are torn apart and the formation of cavities in between them is observed (see Figs. 7.12(c) and (d) for a zoom into the dissection tips). Consequently, under radial (tensile) loading of the medial tissue, interconnected fine elastin fibers, and interlaminar muscle cells are torn loose from their attachments to each other and to adjacent elastin (similar to the study [235]); ruptured fine fibers are evident in the photomicrographs. The observed damage spreads over approximately 6-7 elastic laminae, which is about 15-18% of the thickness of the abdominal aortic media. Note that we could not observe circular-shaped nuclei of the smooth muscle cells within the damage zone, as discovered in the study [230], which is most probably
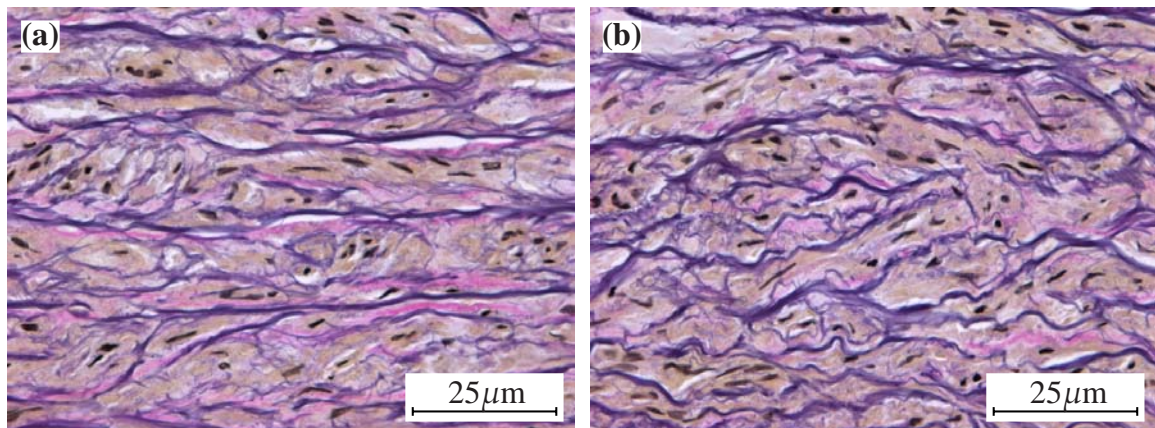
Figure 7.11: Representative histological images of the microstructure of a (a) stretched and an (b) unstretched human aortic media. Elastica van Gieson (EVG) staining, $4\,\mu$m thick sections. Original magnification 800×.

due to the low resolution of the histology.

Microscopical images of the generated dissection surface highlight that peeling in the axial direction creates a remarkably 'rougher' dissection surface compared to that generated by peeling in the circumferential direction (two representative images are shown in Fig. 7.13). In particular, the dissection during the peeling in circumferential direction propagates mainly between adjacent elastic laminae, while the one in the axial direction frequently crosses elastic layers. Interestingly, it sometimes happened that the dissection runs either towards the internal elastic membrane or towards the external elastic membrane during the peeling in the axial direction, which, in a way, mimics the process of aortic dissection, as observed in clinical practice, i.e. where the dissection runs either back into the lumen or outwards into the adventitia. Consequently, it was not possible to dissect the whole specimen. This, however, never happened by peeling rectangular-shaped specimens along the circumferential direction. The histology of the media might explain the observed anisotropic dissection property of the human AA, and the formation of a 'rougher' dissection surface due to peeling in the axial direction, as illustrated in Fig. 7.13. The smooth muscle cells in the media are oriented fairly circumferentially [112] and may provide a more pronounced resistance to the dissection in the axial direction (for example, it is easier to run parallel to the furrows of a ploughed field than across them). Consequently, the creation of
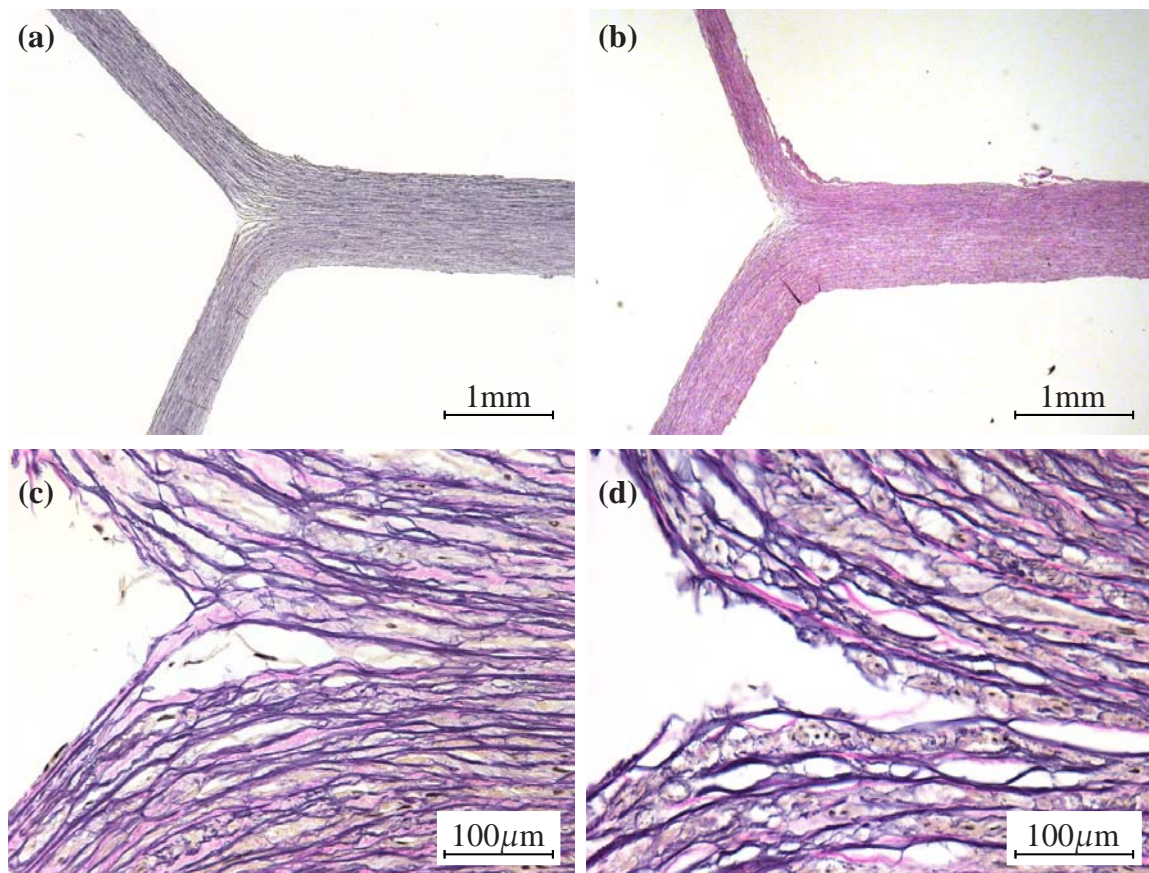
Figure 7.12: Histological images of a representative aortic media during peeling in (a) circumferential and (b) axial directions. Original magnification 20×. Histological images (c) and (d) represent magnifications of the dissection tips and highlight the irreversible mechanism of separation at the micrographic level. Original magnification 400×. Elastica van Gieson (EVG) staining, $4\,\mu$m thick sections.

the 'rougher' dissection surface during peeling of axially oriented test specimens might explain the 'higher' resisting force/width and 'variance' compared to the results from peeling in circumferential direction.

7.4 Discussion

The present study was conducted to explore medial dissection of the human abdominal aorta. Therefore, direct tension and peeling tests are proposed which render defined mechanical problems, and hence allow the quantification of the
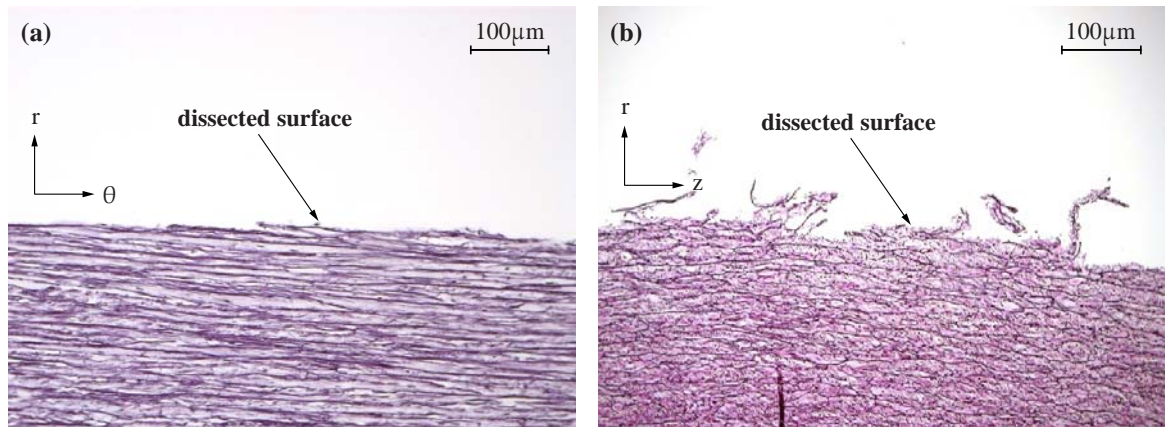
Figure 7.13: Representative histological images illustrating the 'roughness' of the generated dissection surface during peeling in the (a) circumferential and (b) axial directions. Elastica van Gieson (EVG) staining, $4\,\mu$m thick sections. Original magnification 100×.

tissue's dissection properties. The failure mechanisms related to the peeling investigation in terms of localized intra-medial dissection at the microscale level has been demonstrated by related histological investigations.

According to the results from the direct tension test, the development of medial dissection may be characterized within three regions of the force-displacement graph, i.e. region *S1* which we assumed to be elastic, damage accumulation *S2* and localization of damage (failure) *S3*, see Fig. 7.8. It is noted that the recorded force-displacement curve within *S1* remains about linear and does not show stiffness increase at higher strains, as typically known from arterial tissue (see [247], or [89], [248], [199] for overviews). Hence, the tissue might be seen as linear elastic in the radial direction, which is in clear contrast to the elastic properties in circumferential and axial directions. Note that the direct tension tests exhibit average strains in the loading direction within the *S1* region below 10%, and it is most likely that this is too small to activate mechanisms responsible for stiffness increase at higher strains. The final peeling like failure mechanism region, denoted as *S3b*, determines a plateau in the force-displacement curve until it drops to zero, see Fig. 7.8. It seems that the layered structure of the media favors the peeling mechanism along lamellar layers. A dissection within one lamella throughout the whole dissection path did not occur, but we observed outward and inward deviations from the lamellar layers. Consequently, the applied experimental approach, i.e. the direct

tension test leads to multiple dissections between the different medial layers and a peeling-like failure mechanism, as it is illustrated in Fig. 7.5, determines the force-displacement characteristics at larger displacements.

The following is now a brief discussion of the experimental findings of this work with respect to the existing literature, where the radial failure stress and the energy required to propagate a dissection is investigated in detail.

In order to better quantify the results of the direct tension test we assume, mainly for simplicity, a homogeneous stress state to be present. For that case the (average) radial failure stress can be estimated as $F_{max}/(d^2\pi/4) = 140.1 \pm 15.9$ kPa (mean±SD, n=8), where $F_{max} = 1.76 \pm 0.20$ N (mean±SD, n=8), and $d = 4.0$ mm denotes the effective diameter of the circular specimens. It needs to be emphasized that the conducted direct tension tests have caused stress concentrations at the incision of the specimen, and due to its small size this 'edge effect' cannot be neglected. Nevertheless, this approach gives an estimation of the upper limit of the radial failure stress of the investigated human abdominal aortic media, and we may compare the failure stress with the one provided in [235]. That study on porcine thoracic aortas [235] reported a failure of 61.4 ± 4.3 kPa (mean±SD, n=7), which is a value approximately half that determined in our experiments on human AAs. The disagreement may be explained by species differences and high variances.

Regarding the peeling tests, there is an oscillation of the force about some mean 'plateau' level (see Figs. 7.9 and 7.10), which is similar to the results obtained from tearing pig descending thoracic aortas, as provided in [239]. The oscillation is due to an instability inherent in this kind of experiment, which is called 'stick-slip tearing' in rubber mechanics, see, for example, [249]. Based on the given results for the peeling test, we may now estimate the energy required to propagate the medial dissection. According to the performed experiments the external work is found to be $W_c^{ext} = 2.0 F_{pc} l_{pc} = 1.67 \pm 0.33$ mJ/mm (mean±SD, n=5), and $W_a^{ext} = 2.0 F_{pa} l_{pa} = 2.02 \pm 1.41$ mJ/mm (mean±SD, n=7), for the circumferential and axial peeling tests, respectively (F_{pc}, F_{pa} are according to Table 7.5, and l_{pc}, l_{pa} are the current lengths of the specimens in the circumferential and axial directions before separation). Next, we assume that the creation of a new surface due to dissection is the only dissipation present during the test, i.e. the

separated medial tissue behaves fully (hyper)elastic. With this assumption the dissection energy may then be determined by subtracting the elastic stored energy (right before complete separation of the medial strip) from the external work. Moreover, we assume simple tension of the dissected media to be the representative loading mode before complete separation, and hence we neglect inhomogeneities at the clamps and the dissection as well. The average peeling forces and the referential dimensions of the specimens define the first Piola-Kirchhoff stresses $P_{pc} = 4.90 \pm 2.34\,\text{kPa/mm}$ (mean±SD, n=5) and $P_{pa} = 5.02 \pm 3.60\,\text{kPa/mm}$ (mean±SD, n=7), for the circumferential and axial peeling tests, respectively. These stresses are very low so that it can be justified to assume a linear relationship between the first Piola-Kirchhoff stress and the related stretch. Hence, the average elastic energy stored in the circumferential and axial strips during the peeling tests can be estimated as $W_{pc}^{\text{elastic}} = F_{pc}(l_{pc} - L_{pc}) = 0.16 \pm 0.02\,\text{mJ/mm}$ (mean±SD, n=5) and $W_{pa}^{\text{elastic}} = F_{pa}(l_{pa} - L_{pa}) = 0.14 \pm 0.07\,\text{mJ/mm}$ (mean±SD, n=7), respectively. Consequently, the related dissection energy per reference area generated during the peeling of the specimens in circumferential and axial directions may be found as $W_{pc}^{\text{dissect}} = (W_c^{\text{ext}} - W_{pc}^{\text{elastic}})/L_{pc} = 5.1 \pm 0.6\,\text{mJ/cm}^2$ (mean±SD, n=5) and $W_{pa}^{\text{dissect}} = (W_a^{\text{ext}} - W_{pa}^{\text{elastic}})/L_{pa} = 7.6 \pm 2.7\,\text{mJ/cm}^2$ (mean±SD, n=7).

A quantification of the energy required to dissect the aortic media is provided in several works in the literature. For example, one experimental method generates medial dissections by the creation of a bleb due to infusion of a fluid into the media. According to this method the dissection energy is given as $15.9 \pm 0.9\,\text{mJ/cm}^2$ (mean±SD, n=31) for the upper descending thoracic porcine aorta [240], as $1.88 \pm 0.89\,\text{mJ/cm}^2$ (mean±SD, n=17) for the upper abdominal porcine aorta [242], as $11.34 \pm 4.05\,\text{mJ/cm}^2$ (mean±SD, n=17) for the lower abdominal porcine aorta [242], and as $1.65\,\text{mJ/cm}^2$ for the (not further specified) human aorta [241]. Basically, these data are computed by integrating the infusion-pressure volume curves over the infusion volume, i.e. the mechanical energy supplied by the injection into the media. Hence, these data represent the sum of the dissection energy and the elastically stored energy in the media. It is worth noting that the elastically stored energy inherent to the applied experimental method cannot be quantified in a straightforward way. The stored energy needs to be subtracted in order to estimate the dissection energy of the investigated tissues, as done in the present

study. Nevertheless, our quantification of the specific dissection energy falls within the data range presented by the above cited works.

The present investigation indicates that the dissection properties of the human aortic media seem to be anisotropic within the dissection plane, and to the authors' knowledge this has never been reported before. This finding is, however, accompanied by a statistically non-significant difference of the resisting forces between the two peeling directions, and only a small number of specimens have been investigated. In addition, it needs to be emphasized that the shape of the bleb obtained by injecting casting material into the media is circular, as shown in Fig. 4 of [243], which indicates isotropic rather than anisotropic dissection properties of this particular medial tissue. Certainly, more tests are required to identify the anisotropic dissection properties of the human aortic media and, although not always possible, different tests should be performed on the same vessel to look for possible correlations among the tests.

The clinical circumstances of dissection are more varied than the controlled protocol of these experiments. Consequently, these data might not be representative for *in vivo* aortic dissection, where fatigue-like and multiaxial loading is present. However, we think that the data are particularly useful for the estimation of the constitutive response of dissections due to balloon angioplasty, where quasi-static and mainly mode-I loading conditions appear (Gasser and Holzapfel [250]).

8 BIAXIAL MECHANICAL PROPERTIES OF HUMAN CAROTID ARTERIES

Abstract. Specimens of intact wall tubes of human common carotid arteries (CCA), internal carotid arteries (ICA) ($n = 11$, age 77.6 yrs, SD 6.3) and related adventitia and media-intima tubes are mechanically examined. Cyclic, quasi-static extension-inflation tests at different axial stretches are performed on pre-conditioned tube specimens. Stress-free configurations show significant stress releases in the circumferential direction of the intact CCA and ICA walls and in the axial directions of the intact CCA walls and the CCA and ICA adventitias. Mechanical features of all investigated tissues are: strong nonlinearity, pseudo-elastic behavior, small hysteresis. The 'inversion'-feature where the pressure/axial stretch relationship becomes a vertical line is found only for intact walls. Axial 'inversion stretches' are 1.19 (SD 0.06) for CCA, 1.14 (SD 0.06) for ICA, and related external axial forces are 0.43 N (SD 0.15) and 0.30 N (SD 0.22), respectively. Significant negative correlations between age and axial 'inversion stretches' for CCA ($r = -0.67, P = 0.03$) and ICA ($r = -0.29, P = 0.04$) are identified. Adventitias are very compliant at low pressures but change into stiff tubes at high pressures. The burst pressure of the adventitia is beyond 250 kPa. A relatively low burst pressure of approximately 60 kPa is found in the media-intima tubes in which the pressure/circumferential stretch relationships are almost independent of the axial stretches. Stress analyses indicate high anisotropic material properties of all investigated tissues. High circumferential and axial stresses occur in the media-intima tubes at physiological conditions. The obtained results are intended to serve for improving constitutive laws and enhancing our knowledge of arterial function, adaption and remodeling.

8.1 Introduction

Cardiovascular diseases are frequently treated by balloon angioplasty, which is a mechanical procedure during that a vessel is subject to loads far beyond the (usual) physiological domain. It is also widely agreed that the mechanical environment and properties of arteries play an important role in the origin and progression of vascular disease. Therefore, detailed knowledge of their mechanical behavior is essential for the improvement of surgical and non-surgical procedures, as well as for the development of prosthetic materials and artificial tissue equivalents.

The carotid arteries, including the Common Carotid (CCA) and the Internal Carotid Arteries (ICA), are of particular biomedical and clinical interest, since they are prone to atherosclerosis and frequently undergo treatments (usually angioplasty and stenting or carotid endarterectomy) to prevent stroke. Carotid stenosis, or narrowing of one of the major arteries which carries blood to the brain, can cause stroke [251], which is a leading cause of serious, long-term disability and the third leading cause of death, behind disease of the heart and cancer, in the United States [2]. A standard treatment consists of removing the narrowing by procedures such as *carotid endarterectomy* (CEA), *percutaneous transluminal angioplasty* (PTA) or more suitable for carotid arteries *carotid angioplasty with stenting* (CAS). This has changed since the Food and Drug Administration approved the first carotid stent system (Cordis) in July 2004 and the second (Guidant) in August 2004. The system is comprised of a stent and an embolic capture device designed to reduce or trap emboli and clot debris. Angioplasty and stenting is increasingly used to treat carotid lesions, with success rates similar to CEA surgery, while carotid angioplasty without stenting is losing its importance/influence. SAPPHIRE, a large trial comparing CEA and CAS with the *Cordis* stent, found stenting non-inferior to CEA [252]. Moreover, two completed trials comparing endovascular treatment (PTA and CAS) with surgery (CEA) involving 608 patients showed that there were fewer immediate complications with PTA and CAS than with CEA [251].

The CCA is perhaps the most studied, and consequently best understood artery due to the ease in which long specimens free of branches may be excised [89]. Investigations of ICAs are rare, even though plaque formation, and consequently CAS or CEA, occur in the CCA, the ICA and in the carotid bifurcation. Moreover,

most studies available in the literature deal with carotid arteries coming from animals [38, 59, 60, 114, 253–258]. To the authors' knowledge there are few *in vitro* tube studies of human CCA [259, 260] and no *in vitro* tube studies on human ICA available in the literature. Since an artery is a heterogeneous structured composite consisting of three layers with different (visco)elastic properties, a thorough understanding of the behavior requires experimental data on the multiaxial mechanical response of each layer. In particular, there are no *in vitro* tube studies available dealing with the layer-specific mechanical response of human CCA or ICA.

In addition, there is growing experimental evidence that the adventitia plays an important role in various vascular processes such as atherosclerosis, hypertensive remodeling and restenosis after balloon angioplasty [261]. Most biomechanical studies before and also after 1983 used zero-pressure conditions (no-load state) as reference for the analysis, although, 25 years ago, Vaishnav and Vossoughi [20] identified that the load-free configuration of an artery is not a stress-free state.

In documented finite element models of the human carotid bifurcation, mechanical properties of the ICA are assumed to be the same as for the CCA (see, for example, [262] and [263]). Accurate mechanical properties of the ICA will improve the model-prediction and extend the applications of such models.

The aim of this study is to determine the mechanical behavior of human CCA and ICA, and subsequently the adventitial and media-intima composite layers by means of extension-inflation tests at different axial stretches. Moreover, the residual stretches of the adventitia and media-intima tubes and the stress-free configuration of the intact wall, the adventitia and the media-intima composite were determined.

8.2 Materials and Methods

8.2.1 Material and Specimen Preparations

Eleven human CCAs and 10 human ICAs were harvested from 11 human subjects (77.6 ± 6.3 yrs, mean ± SD, ranging from 67 to 86 yrs, 4 female and 7 male). Information about the anamnesis of the carotid arteries investigated is summarized in

Table 8.1: *Anamnesis*

Donor	I	II	III	IV	V	VI	VII	VIII	IX	X	XI
Age (yrs)	82	80	76	83	67	77	84	78	69	71	86
Sex	f	f	m	m	m	f	m	m	m	f	m
Primary disease	MEI	BLC	TAA	CS	NA	FP	HI	DM	RF	BRC	CS
Cause of death	ICP	MET	AR	MI	PAE	GHD	BH	BI	MI	AML	MI
Atherosclerosis:											
Aorta	*h*	*m*	*h*	*h*	*h*	*h*	*h*	*h*	*h*	*h*	*h*
Coronary arteries	*m*	*m*	*h*	*h*	*m*	*h*	*l*	*l*	*m*	*m*	*h*
Cerebral arteries	*m*	-	*m*	*l*	*l*	*m*	*m*	*m*	-	-	*m*
Renal arteries	*l*	*l*	*h*	*m*	*m*	*m*	*m*	*l*	*h*	-	*h*

AML … acute myeloic leukaemia; AR … aneurysm rupture; BH … brain haemorrhage; BI … brain infarction; BLC … bladder carcinoma; BRC … breast carcinoma; CS … coronary sclerosis; DM … diabetes mellitus; FP … fibrinous pericarditis; GHD … global heart dilation; ICP … intracranial pressure; HI … head injury; MEI … media infarction/stroke; MET … metastasis; MI … myocardial infarction; NA … nicotine abuse; PAE … pulmonary artery embolism; RF … renal failure TAA … thoracic aortic aneurysm. Assessment of atherosclerosis is based on autopsy reports (- stands for no atherosclerosis, *l*: low grade, *m*: medium grade, *h*: high grade).

Table 8.1. Only straight segments without palpable circumscribed wall hardening were used. An artery was rejected during preparation if (i) the straight segment showed atherosclerotic plaque formations, or if (ii) eccentric intimal thickening was macroscopically visible. For the present study, the use of autopsy material from human subjects was approved by the Ethics Committee of Medical University Graz. According to the recent published AHA statistics, angioplasty interventions were performed mostly in elderly people aged 65 and older [2]. Thus, the cerebral arteries were required to be aged (around 65+ yrs) and of low/medium grade atherosclerosis (see Anamnesis in Table 8.1).

Immediately after excision, the carotid bifurcation were frozen, and stored at $-80\,°C$. Before mechanical testing, the frozen samples were slowly thawed at $4\,°C$ and then prepared at room temperature $(20\,°C)$. All tests were conducted for one sample within 24 hours after defrosting and all samples were tested within 14 days after excision. The cryopreservation was applied in order to neglect the influence of the muscular response on the mechanical behavior, hence the behavior of the

arterial wall is governed mainly by elastin and collagen components [89].
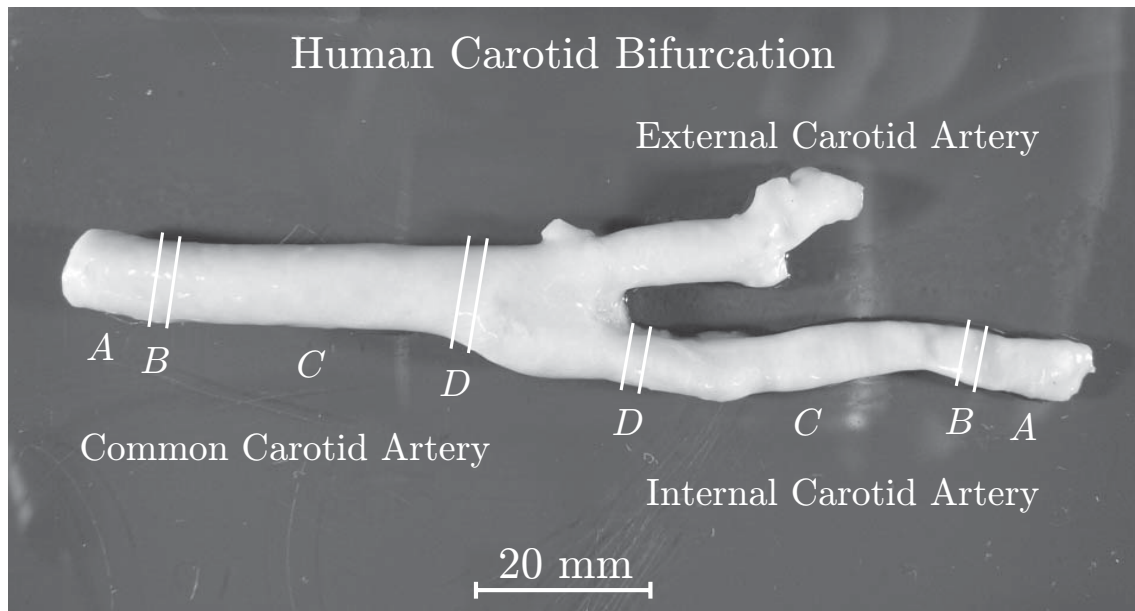
Figure 8.1: Locations of utilized segments in a representative human carotid bifurcation. Segment *A* was used for axial residual stress measurements, *B* for circumferential residual stress and thickness measurements, *C* for tube testing, *D* for thickness measurements of common carotid arteries (CCA), left, and of internal carotid arteries (ICA), right.

Loose connective tissue was carefully removed from the whole carotid bifurcation surface. Two straight arterial segments, one segment of ~50 mm in length from the CCA and one segment from the ICA of ~50 mm in length, were cut out from the carotid bifurcation, as indicated in Fig. 8.1. Three rings were cut from each segment. For the CCA, a ring with ~3 mm in height was cut proximal from the bifurcation for thickness measurement and a ring with ~15 mm in height was cut distal from the bifurcation for determining layer-specific stress-free configurations (see Test Protocol below) and also for thickness measurements (see Fig. 8.1). A similar procedure was applied for the ICA segment but mirrored at the bifurcation. For the axial deformation measurements during tube testing two gage markers (black-colored straw chips) representing the gage length (or region) were glued pointwise with cyanoacrylate adhesive gel in parallel onto the middle part of the arterial segments. Both were orientated transverse to the vessel axis and had a separation distance of ~5 mm. Segments were cannulated at both ends with

specially designed tube connectors matching the vessel diameter and inserted in the testing machine. For a detailed description of the experimental setup, see [69].

8.2.2 Test Protocol

Intact Wall Testing

Extension-inflation tests with continuous recording of transmural pressure (p), axial force (F_z), outer diameter and gage length of the arterial segments were performed at transmural pressures ranging from 0 to 33.3 kPa (250 mmHg) at several axial stretches (λ_z) ranging from 1.0 to 1.3 in increments of 0.05. Since the mechanical behavior of arteries is temperature sensitive [264, 265], specimens were allowed to equilibrate for ~10 min in a 37°C, calcium-free 0.9% NaCl physiological saline solution (PSS) after inserting the cannulated arterial segments in the testing machine. During inflation the axial force was held constant by the testing machine since preliminary isometric tests (arterial segments were forced to keep their lengths) led to buckling of the intact walls and the media-intima tubes. Therefore, the testing machine was controlling the axial stretch of the tube specimens. Buckling of adventitia tube specimens during inflation up to a transmural pressure of ~150 kPa was not observed.

At each increment of axial stretch, the intact wall was pre-conditioned axially and circumferentially by 5 axial stretch cycles ranging from the starting condition (0% axial stretch) to the desired axial stretch, and relaxing back to the initial condition, then by 5 inflation-deflation cycles ranging from 0 to 33.3 kPa (250 mmHg), to ensure a repeatable and reproducible mechanical response. Immediately after pre-conditioning the specimen was inflated and deflated one more time to obtain the 'measuring cycle'. The axial stretching during pre-conditioning was performed quasi-statically (1 mm min^{-1}). The inflation and deflation during the pre-conditioning cycles and the measuring cycle was also performed quasi-statically at 16.7 kPa min^{-1} (125 mmHg min^{-1}).

The unloaded (referential) outer diameter was measured after the pre-conditioning and before the measurement cycle at 0 kPa transmural pressure and 0% axial stretch
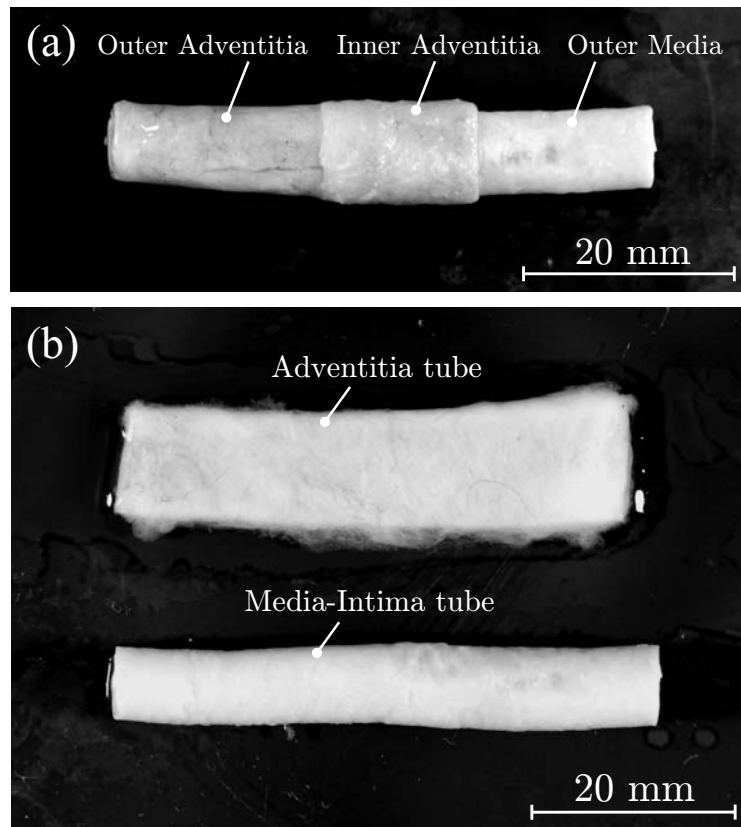
Figure 8.2: Dissection of the intact artery in a 'turtleneck' fashion into an adventitia tube and a media-intima tube (a); the axial retraction of the adventitia tube and the small elongation of the media-intima tube indicate residual stretches within the intact artery wall (b).

($\lambda_z = 1.0$). If the axial load exceeded $2\,\mathrm{N}$ for the CCA or $1\,\mathrm{N}$ for the ICA at high axial stretches (for example, $\lambda_z = 1.25$ or $\lambda_z = 1.3$), the associated tests were not performed to avoid damage to the tissue. These axial loads correspond to an axial first Piola-Kirchhoff stress of about $100\,\mathrm{kPa}$ in the samples with the smallest outer radius and thickness values (CCA: $R = 3.7\,\mathrm{mm}$, $H = 1\,\mathrm{mm}$; ICA: $R = 2.5\ \mathrm{mm}$, $H = 0.8\,\mathrm{mm}$) stemming from preliminary tests. An axial first Piola-Kirchhoff stress of $100\,\mathrm{kPa}$ was assumed to cause no damage to the investigated tissue [75]. After the tests the specimen (vessel) was taken out of the testing machine and submerged in $37\,^\circ\mathrm{C}$ PSS tissue bath.

Table 8.2: *Residual stretches and geometries of all investigated intact walls, separated adventitia and media-intima tube specimens of the CCA and the ICA.*

Artery	Layer	Circumferential residual stretch	Axial residual stretch	R (mm)	H (mm)
CCA	Intact Wall	–	–	4.15 (0.31)	1.17 (0.16)
	Adventitia	1.04 (0.06)	1.08 (0.05)	4.00 (0.28)	0.47 (0.07)
	Media-Intima	1.00 (0.02)	0.98 (0.01)	3.61 (0.13)	0.70 (0.13)
ICA	Intact Wall	–	–	2.67 (0.09)	0.86 (0.06)
	Adventitia	1.04 (0.05)	1.09 (0.06)	2.51 (0.14)	0.33 (0.06)
	Media-Intima	1.00 (0.03)	0.98 (0.01)	2.15 (0.15)	0.53 (0.10)

Values are means (± SD). Circumferential residual stretches calculated as ρ_A/R_A for the adventitia and ρ_{MI}/R_{MI} for the media-intima tube. Axial residual stretches calculated as ζ_A/Z_A for the adventitia and ζ_{MI}/Z_{MI} for the media-intima tube. R and H are the outer radii and the thicknesses of the load-free intact wall (R_W, H_W), the separated load-free adventitias (R_A, H_A) and the media-intima tubes (R_{MI}, H_{MI}) (for abbreviations see Fig. 8.4).

Layer Separation Procedure and Residual Stretches

After ~3 min equilibration in 37 °C PSS and before layer separation a picture considering a gauge for the residual stretch determination was taken. The adventitia could be carefully pulled off in a 'turtleneck' fashion from the underlying media-intima tissue by carefully disconnecting the interconnective fibers (i.e. external elastic membrane fibers and collagen fibers in the media) with an appropriate scalpel. For a representative macroscopic picture of a CCA during dissection see Fig. 8.2(a). This separation was feasible with the aid of a low magnification light microscope (10x) and surgical instruments [38,261,266]. The difference in color and texture between the medial and the adventitial layer was used to separate them from one another. The mesh of collagenous fibers in the adventitia is white-red colored (red due to vasa vasorum), while the mesh of the elastin and muscle fibers in the media appears to be ivory colored [38]. Furthermore, the media is much denser then the adventitia. During the separation the tissue was periodically moistened with PSS. In general, this separation is 'atraumatic' due to the weak adherence of the media to the adventitia [261]. Turtleneck dissection was easier to perform for

elderly arteries than for younger ones. This might be evidence of stronger adherence of the adventitia to the media in younger arteries. Consequently, dissection of young arteries might be more afflicted with tissue damage during dissection. After separation the adventitia retracted immediately in the axial direction which indicates residual stretches (see Fig. **8.2**(b)).

After ~5 min equilibration in 37 °C PSS additional scaled pictures were taken from the adventitia and the media-intima tube. The axial residual stretches of the adventitia and media-intima composite tube were computed as the ratio of the intact wall tube length and the adventitia tube length, and the media-intima composite tube length, respectively. These lengths were determined photogrammetrically from the pictures taken. Analogously, the circumferential residual stretches were computed as the ratio of the intact wall diameter and the adventitia tube diameter, and the media-intima tube diameter, respectively. These diameters were determined by means of the videoextensometer from the load-free tubes inserted in the testing machine.

Adventitia Tube Testing

Analogous to the intact wall, gage markers were attached to the central region of the separated adventitia tube. The adventitia tube was then cannulated, inserted in the testing machine and equilibrated for ~10 min in a 37 °C PSS. Extension-inflation tests of adventitia tubes were performed in two loading domains, named as 'the physiological domain' with transmural pressures ranging from 0 to 33.3 kPa (0 to 250 mmHg) and 'the high-pressure domain' ranging from 0 to 100 kPa (0 to 750 mmHg). At each increment of axial stretch (λ_z), ranging from 1.0 to 1.3 in increments of 0.05, the specimens were pre-conditioned axially, by stretching the tube in the axial direction, and circumferentially by inflating and deflating the tube. Each pre-conditioning procedure was performed cyclically five times. Immediately after pre-conditioning, one cyclic inflation and deflation was performed for the 'measurement cycle'. Tests were first performed in the physiological domain and then in the high-pressure domain.

The unloaded (referential) outer diameter was measured before and after the 'measurement cycle' at $p = 0$ and $\lambda_z = 1.0$.

Media-Intima Composite Tube Testing

The procedure and protocol used for the media-intima composite were analo-
gous to those employed for the intact wall. Since preliminary tests showed that
the media-intima tube can burst at transmural pressures of approximately 60 kPa
(450 mmHg), the media-intima tube was only pressurized from 0 to 20 kPa (0 to
150 mmHg).

Determination of the Stress-free Configuration

Two rings with ~15 mm in height were taken for the determination of the layer-
specific residual stresses, one cut from the proximal end of the CCA (the very left
segments *A* and *B* in Fig. 8.1), and one from the distal end of the ICA (the very
right segments *A* and *B* in Fig. 8.1). A ring with ~3 mm in height (segments *B*
in Fig. 8.1) and, additionally, an 'axial strip' (i.e. a strip whose long sides were
aligned with the vessel axis) (segments *A* in Fig. 8.1) were cut out from these
15 mm rings and glued pointwise with cyanoacrylate adhesive on small plastic
tubes ($\varnothing$ 7 mm), which served as supports in the tissue bath. This procedure
provided load-free suspension of the specimens and allowed proper orientation
of the specimen edges towards a camera. Immediately after insertion in 37 °C PSS,
scaled digital pictures were taken from both the ring and the axial strip, which
appeared roughly as a circular sector. Subsequently, the ring was cut radially. A
release of compressive residual stresses at the inner vessel wall and tensile residual
stresses at the outer surface was observed and the ring deformed roughly to a
circular sector. The time-dependent behavior of the arterial tissue caused changes
in geometrical shapes and the curvatures over time. After 16 hours, no geometric
changes were observed and final pictures were taken from both the circular sector
of the cut ring and the axial strip. Next the adventitia was separated carefully
from the media-intima composite of both specimens along the boundary (i.e. the
external elastic membrane) by means of anatomical instruments and with the aid
of a stereomicroscope. Hence, four strips were obtained, two from the adventitia
and two from the media-intima composite; two of which were oriented axially (i.e.
in parallel to the vessel axis) and two in the circumferential direction. Internal and
external faces of the strips were marked. The procedure performed previously for

the non-separated ring and the axial strip was then repeated for the isolated layer strips. Here, scaled digital pictures were taken after six hours. As a result, a set of pictures was obtained which contained information on the initial geometry of the non-separated specimens and the final geometry of the isolated 'layer-specific' human carotid tissue strips. From these pictures the curvatures of the individual tissue components were determined. The opening angle in the axial strips is not a characteristic quantity for residual deformations since the angle depends on the strip length, and, furthermore, the cut specimens rarely took on the form of circular arcs [34]. For a detailed description of the method used to determine the curvatures of the individual tissue components the reader is referred to [34].

Thickness Measurements

Intact wall thickness. For the intact wall thickness determination, the rings with 3 mm in height from the distal and proximal ends of the CCA and ICA were used (ring segments *B* and *D* in Fig. 8.1). Scaled pictures of the rings cut were taken after ~5 min immersed in PSS at 37 °C. From these scaled pictures the intact wall thickness was measured photogrammetrically at four positions of each ring, averaged regarding the four positions and then averaged regarding the two rings stemming from the same segment. Additionally, the rings were radially cut to get a strip. The average thickness of these strips was measured by means of a videoextensometer to compare it with the photometrical method. For a detailed description of the videoextensometer thickness measurement method (VTMM), see [69, 76].

Adventitial wall thickness. After finishing the high-pressure extension-inflation tests, a ring was cut out from the gage region of the adventitia tube specimen and then radially cut to produce a strip. The average thickness of this strip was measured by means of VTMM.

Media-intima thickness. The same procedure used for the adventitia was used to determine the thickness of the media-intima composite.
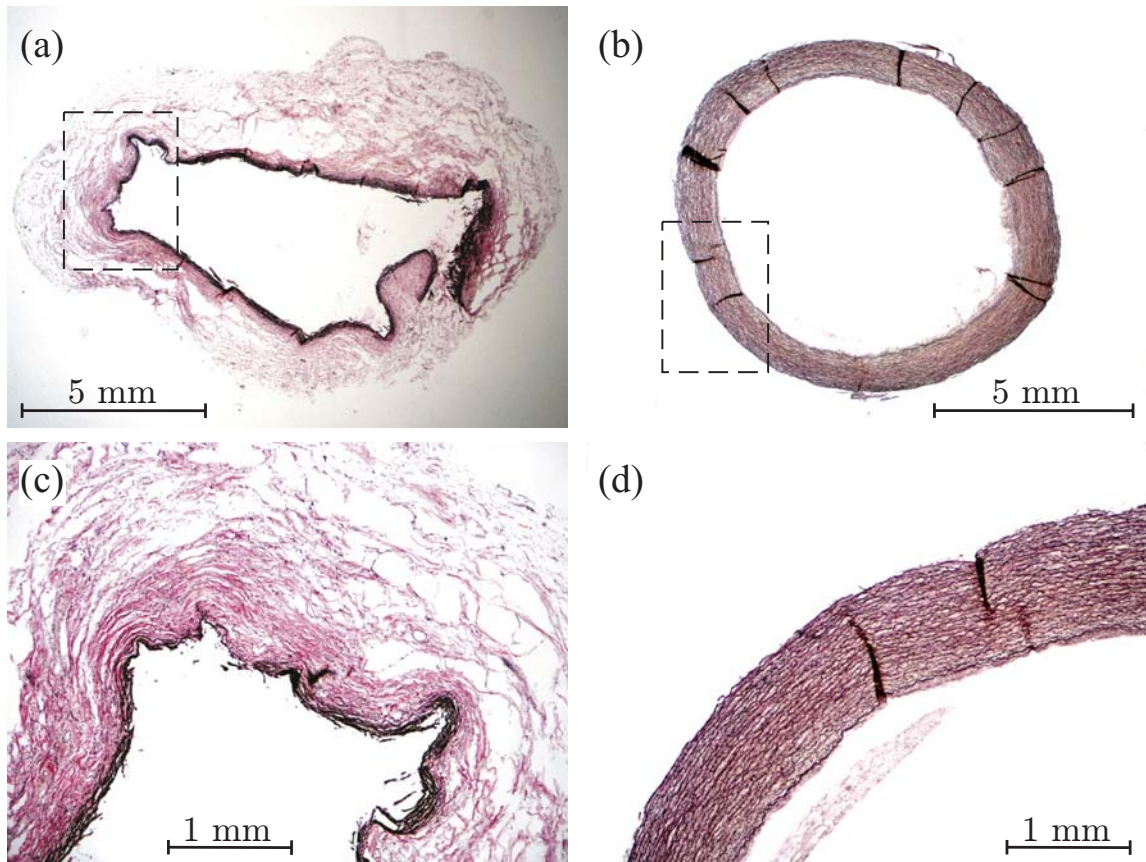
Figure 8.3: Representative histological sections of the adventitia tube (a) and the media-intima tube (b) confirming correct layer-separation of the adventitia from the media-intima tube along the external elastic membrane except for minor fragments of the media attached on the adventitia. Elastica van Giesson (EVG) staining, 4 μm thick sections, original magnification 20$\times$. Histological images (c) and (d) represent higher magnifications of the areas indicated by dashed lines (a) and (b), respectively. The images indicate the 'atraumatic' separation of the adventitia from the underlying media-intima tissue. Superficial elastic lamellae of the media-intima appear ruptured (original magnification 200$\times$).

Histology

Histological investigations were performed to confirm correct and, as much as possible, 'atraumatic' separation of the adventitia from the media-intima composite. In all cases, after the experiments, the gage regions of the adventitia and the media-intima samples were fixed in buffered 4% formaldehyd solution (pH 7.4), embedded in paraffin, sectioned at approx. 4 μm, and stained with Elastica van

Giesson (EVG), see Fig. 8.3. The sections were subsequently examined under a light microscope.

Mechanical Data Analysis

In order to enable analytical calculations of circumferential and axial stresses in the intact wall the adventitia and the media-intima composite, the tube specimens were assumed to be circular cylindrical, thin-walled, homogeneous, incompressible [43] and to have orthotropic behavior [37]. Thus, it is straightforward to compute the average circumferential and axial Cauchy stresses $\sigma_{\theta\theta}$ and σ_{zz} (true stresses) of a loaded tube by means of global equilibrium [139] as

$$\sigma_{\theta\theta} = p\left(\frac{r}{h} - 1\right), \qquad \sigma_{zz} = \frac{p\pi(r-h)^2 + F_z}{h\pi(2r-h)}, \tag{8.1}$$

whereas p is the transmural pressure, r is the outer radius and h is the wall thickness of the loaded tube, while F_z is the axial force. The wall thickness h of the loaded tube can be derived by assuming no volume change in the cylindrical tube during deformation, i.e.

$$[R^2 - (R-H)^2]Z\pi = [r^2 - (r-h)^2]z\pi, \tag{8.2}$$

whereas R, H and Z are the radius, the wall thickness and the gage length of the load-free tube, respectively, and z is the gage length of the loaded tube (see Fig. 8.4 for the kinematics). By substituting the circumferential stretch $\lambda_\theta = r/R$ and the axial stretch $\lambda_z = z/Z$ into the global equilibrium equation (8.1), the average circumferential and axial Cauchy stresses can be expressed as functions of the measured quantities p, F_z, λ_θ, and λ_z:

$$\sigma_{\theta\theta} = \sigma_{\theta\theta}(p, F_z, \lambda_\theta, \lambda_z), \qquad \sigma_{zz} = \sigma_{zz}(p, F_z, \lambda_\theta, \lambda_z). \tag{8.3}$$

These functions contain the unloaded (referential) wall thickness H and the unloaded outer radius R as constants, which have to be determined experimentally.

Note that we made the simplifying assumptions (thin-walled, homogeneous and circular cylindrical tube) to enable analytical estimations of the stresses in the wall
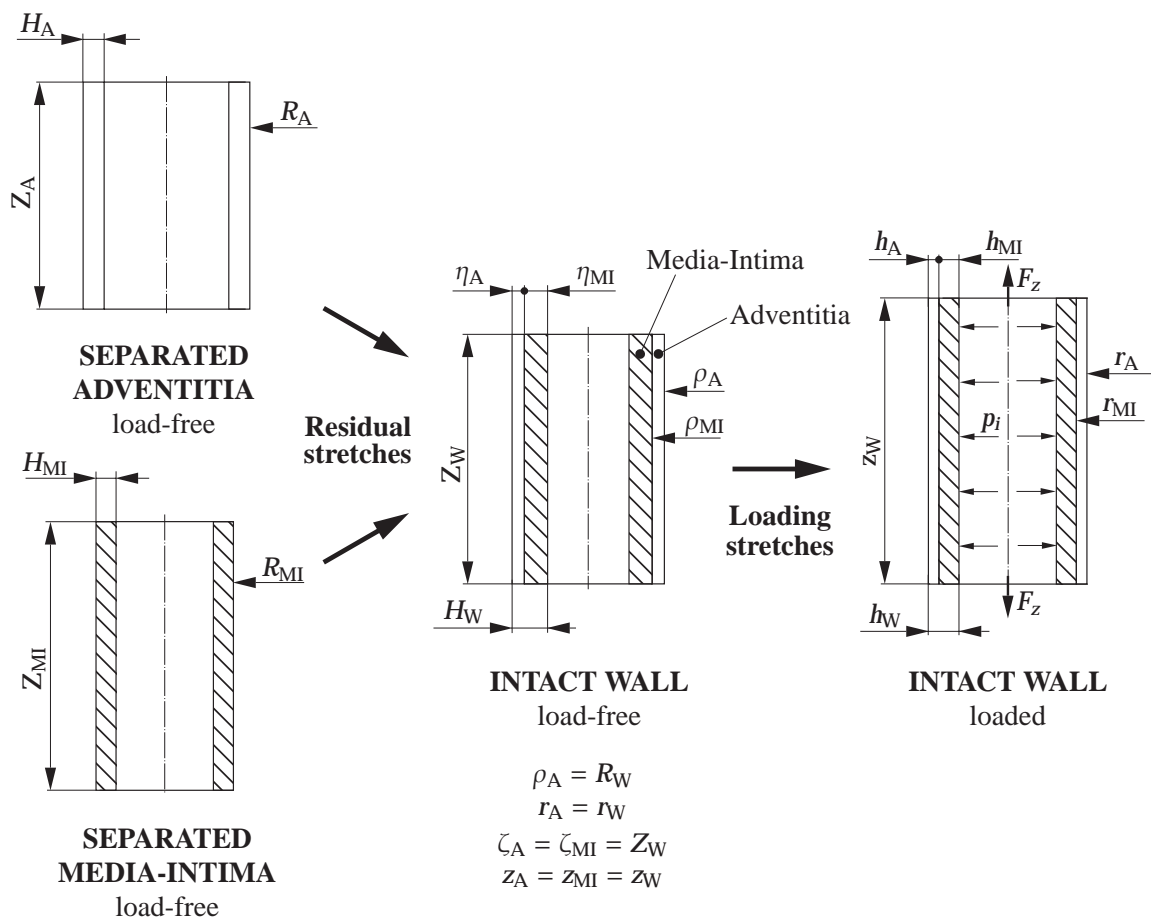
Figure 8.4: Kinematics of the intact wall, and the separated adventitia and the media-intima tubes. For the description of the kinematics of the separated adventitia and the media-intima tubes, two subdeformations are required, whereas for the intact wall one subdeformation is sufficient. For a detailed description of the figure and the parameters, see Section 8.3.1.

and the layers.

Statistics

All data are given as mean ($\pm$ SD). Statistical analyses were performed to test for significant correlations between age and: (i) axial inversion stretch, (ii) external axial inversion force, (iii) circumferential and (iv) axial stretches (at 'physiological conditions', i.e. at 13.3 kPa and at $\lambda_z = 1.05$ to $\lambda_z = 1.10$). We assumed an average axial pre-stretch of the CCA and ICA in the composite of the human neck to be

between $\lambda_z = 1.05$ and $\lambda_z = 1.10$. For this, *Pearson's* correlation coefficients (*r*) were calculated, and *P* values were determined based on *Student's t*-distribution. $P < 0.05$ was considered to be significant. Statistical analyses were performed using the *OriginLab ORIGIN*, Release 7.5, program package.

8.3 Results

8.3.1 Geometry and Kinematics

The kinematics of the intact wall is described by the load-free geometries: outer radius R_W, wall thickness H_W and gage length Z_W, and mapped into the deformed configuration with the related geometries r_W, h_W, z_W, respectively, see Fig. 8.4. The kinematics of the individual layers is described by two subdeformations. First, the kinematics of the considered layers, for example, the adventitial layer is determined by the deformation that occurs between the separated load-free adventitia tube (with R_A, Z_A, H_A) and the load-free configuration of the intact wall. Thereby, the resulted deformed configuration of the adventitia is given by the dimensions ρ_A, ζ_A, η_A. Second, axial stretching and pressurizing the intact wall leads to the deformed configuration of the adventitia (r_A, z_A, h_A). Note that the load-free configuration of the adventitia is not stress-free due to residual stresses within the layer [34]. The kinematics for the media-intima tube are analogous, see Fig. 8.4.

We found significant axial residual stretches after the dissection of the adventitia from the media-intima tube, as summarized in Table 8.2. Remarkably, the circumferential stretch of the adventitias decreased about 1% after 100 kPa of pressurization and 30% of axial stretch in the CCA and ICA, which means that high-pressure loading of the separated adventitias caused almost no remaining stretch. By using the same loading conditions the axial stretch of the adventitias increased about 3% for the CCA, while there was no remaining axial stretch for the ICA. The stretches of the adventitia under loaded condition result as $(\rho_A/R_A)(r_A/\rho_A) = r_A/R_A$, where $\rho_A = R_W$, and $(\zeta_A/Z_A)(z_A/\zeta_A) = z_A/Z_A$, where $\zeta_A = Z_W$. The same applies for the media-intima tube.

Furthermore, the load-free outer radii and thicknesses of the intact walls (R_W, H_W), the separated adventitias (R_A, H_A) and the media-intima tubes (R_{MI}, H_{MI}) for the CCA and the ICA are summarized in Table 8.2.

Table 8.3: *Curvatures in mm^{-1} of the intact wall W, the adventitia A and the media-intima composite MI.*

| | Intact wall W | | | |
| | before cut / after excision | | after 16 h | |
Artery	circ	axial	circ	axial
CCA	0.381 (0.062)	−0.103 (0.096)	0.232 (0.072)	−0.110 (0.077)
ICA	0.562 (0.168)	−0.050 (0.110)	0.179 (0.128)	−0.052 (0.113)

| | Adventitia A | | | |
| | after dissection | | after 6 h | |
Artery	circ	axial	circ	axial
CCA	0.185 (0.062)	−0.142 (0.074)	0.239 (0.038)	−0.125 (0.060)
ICA	0.112 (0.060)	−0.136 (0.093)	0.093 (0.050)	−0.132 (0.091)

| | Media-intima composite MI | | | |
| | after dissection | | after 6 h | |
Artery	circ	axial	circ	axial
CCA	0.158 (0.055)	−0.025 (0.069)	0.169 (0.047)	−0.014 (0.108)
ICA	0.162 (0.072)	−0.052 (0.068)	0.143 (0.036)	−0.053 (0.075)

Values are means (± SD).

8.3.2 Stress-Free Configuration

Mean values and standard deviations (mean and SD) of the curvatures of the intact walls W, i.e. the arterial rings (before the radial cut and after 16 hours), of the axial intact wall strips (immediately after excision and after 16 hours), and of the adventitia A and media-intima composite MI strips (immediately after dissection and after 6 hours) of the CCA and the ICA are summarized in Table 8.3. The configurations of the circumferential and the axial strips after 16 hours and 6 hours, respectively, are assumed to be stress-free. For the case that histology confirmed correct layer separation, the curvatures of the adventitia and the media-intima composite strips are also documented. Approximately 80% of the adventitia specimens
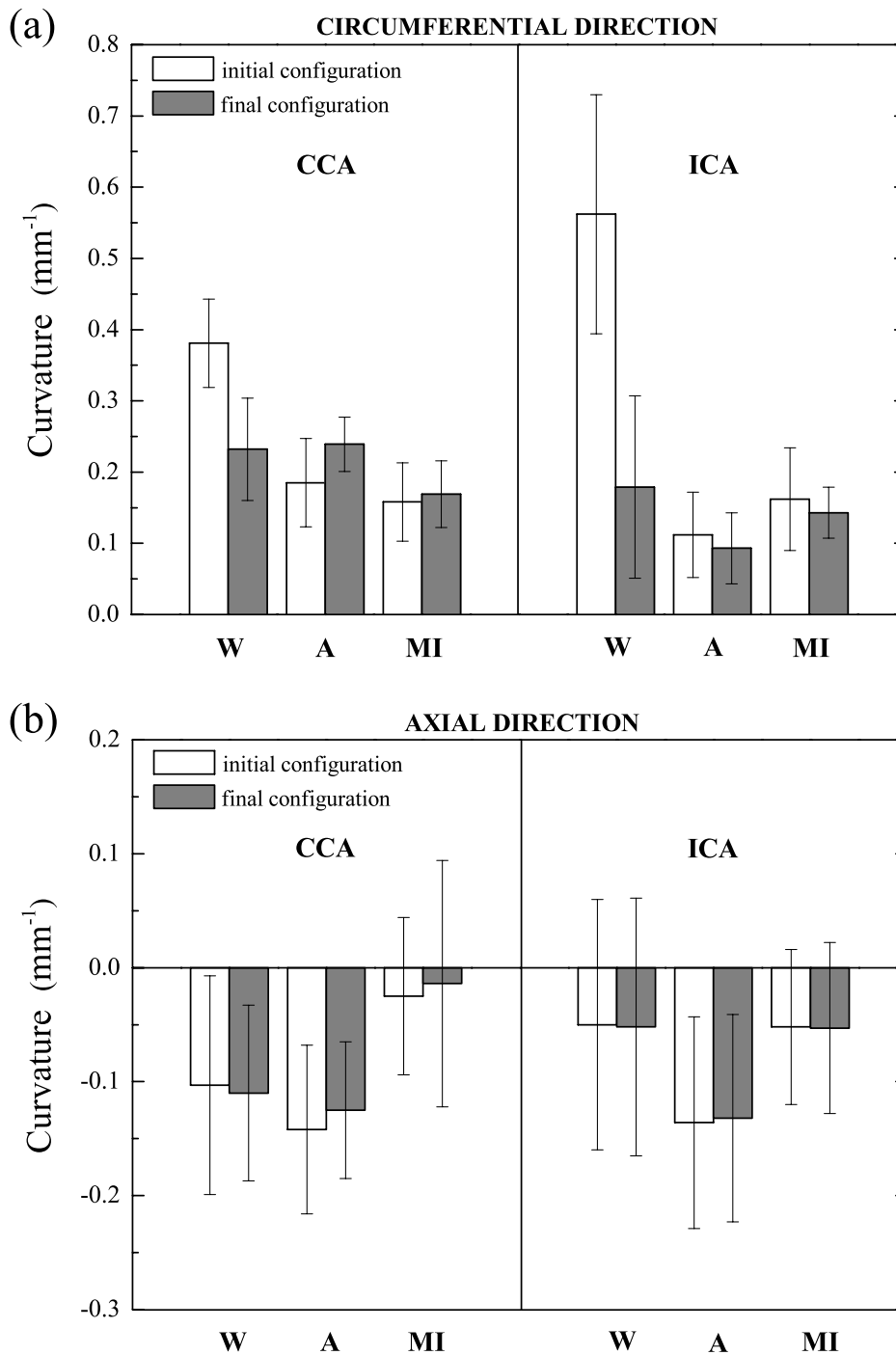
Figure 8.5: Column plots of the curvatures (mean values and SD) for **CCA** (left) and **ICA** (right): intact wall **W**, i.e. arterial rings before radial cut, intact wall strips in the circumferential (a) and axial direction (b) 16 hours after cut; adventitia **A** and media-intima composite **MI** strips in the circumferential (a) and axial direction (b) immediately after dissection and 6 hours after dissection (gray columns). White columns indicate the initial configuration, i.e. before radial cut of the ring and immediately after dissection of the layer strips. Gray columns indicate the final configuration, i.e. 16 hours after cut of the intact wall strips and 6 hours after dissection of the layer strips.

and all of the media-intima specimens were confirmed to be correctly separated and included in the subsequent analysis. For a more detailed illustration of the difference between the curvatures of the intact wall and the layers, and between the orientations, column plots of the curvature values of Table 8.3 are displayed in Fig. 8.5. In general, the curvature values of the circumferential oriented strips were always positive, whereas the axially oriented strips showed mainly negative curvature values. As expected, the intact walls in the circumferential direction show a significant decrease of the curvature after radial cutting of the rings of the CCA ($P = 0.003$) and ICA ($P = 0.002$), which indicated a release of residual stresses. The circumferential oriented adventitia of the CCA ($P = 0.079$) and ICA ($P = 0.746$), as well as the circumferential oriented media-intima composite strips of the CCA ($P = 0.149$) and ICA ($P = 0.598$), showed no significant change 6 hours after dissection. Moreover, all strips oriented in the axial direction of the CCA and ICA showed no significant change 16 and 6 hours after dissection as clearly evident in column plot Fig. 8.5(b). This indicates a fast residual stress release in the axial oriented specimens within from the excision of the specimen from the compound to the first scaled digital picture taken. Significant stress release in the axial direction is observed in the intact walls of the CCA and the adventitia of the CCA and ICA, if the initial curvature was assumed to be 1 (i.e. straight cylinder of the tube specimen).

8.3.3 Load-Deformation Behavior

Representative mechanical responses of a pre-conditioned intact wall, adventitia and media-intima obtained from a CCA and an ICA are shown in Figs. 8.6–8.11.

Intact Wall

For the intact wall, the circumferential and axial stretches resulting from the applied pressure (0–33.3 kPa) was plotted for axial stretches ranging from 1.0–1.2 for the CCA and 1.0–1.25 for the ICA (see Figs. 8.6 and 8.7). The curves exhibit nearly elastic behavior (small hysteresis). Typically for soft collagenous tissue, load-deformation behavior is strongly nonlinear with pronounced stiffening at higher

(a)

(b)

Figure 8.6: Representative mechanical responses of an intact CCA. Circumferential stretch-pressure (a) and axial stretch-pressure (b). Each curve is related to a specific axial stretch. The 0%-check (dotted line), performed after '1.20 axial stretch loading', shows no significant difference from the initial '1.0 axial stretch' cycle (solid line). Likewise, the fifth loading cycle (solid lines) of the '1.15 and 1.20 axial stretch loading' resembles the corresponding first loading cycles (dotted lines).
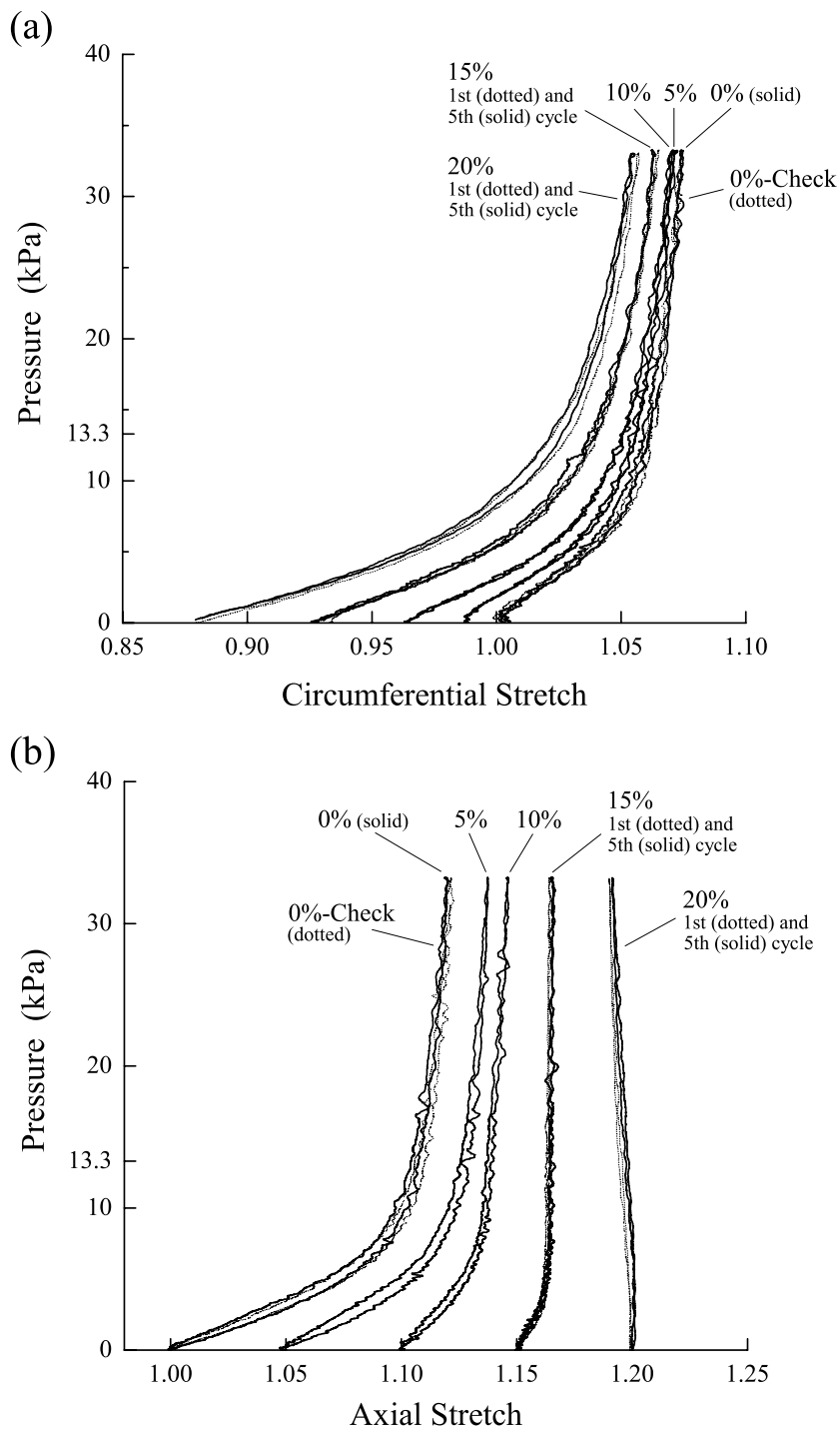
(a)

(b)
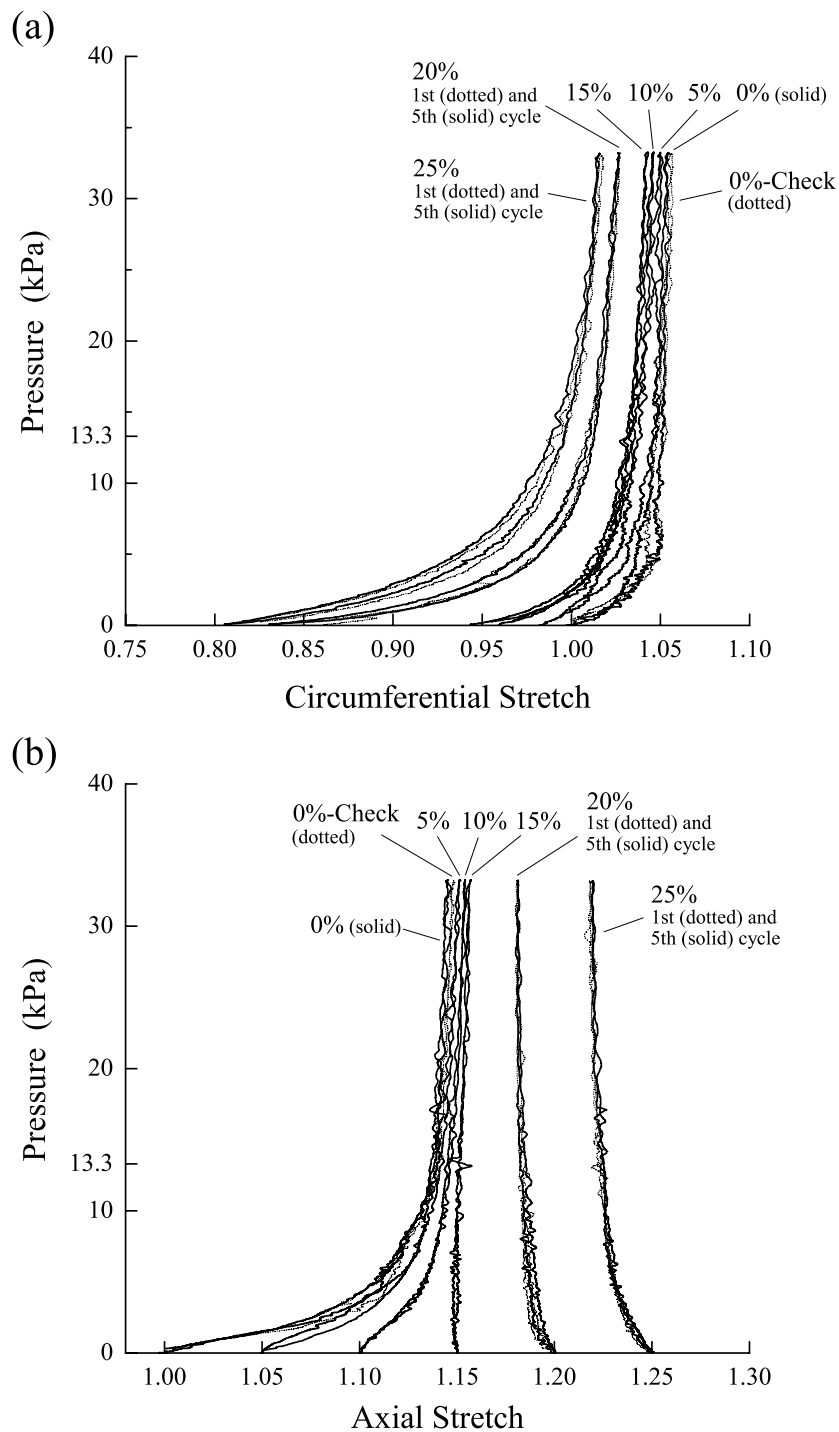
Figure 8.7: Representative mechanical responses of an intact ICA. Circumferential stretch-pressure (a) and axial stretch-pressure (b). Each curve is related to a specific axial stretch. The fifth loading cycle (solid lines) of the '1.20 and 1.25 axial stretch loading' resembles the corresponding first loading cycles (dotted lines).

pressures. During cyclic pre-conditioning, there were only minimal changes in the mechanical response, indicated by the small shift between the initial loading cycles (indicated by dotted curves) and the final cycles (solid curves). For reasons of clarity, this is only shown for curves with the highest axial stretches in the Figs. 8.6–8.11. Moreover, pre-conditioning was typically finished after only three to four inflation-deflation cycles. We investigated whether the axial stretch has any influence on the pre-conditioning behavior of the investigated tissues. Remarkably, we found significant linear correlations between the axial stretch and the 'stress-softening' during pre-conditioning (axial stretch-difference of the initial and the final pre-conditioning cycle) in the circumferential direction ($r = 0.817$, $P = 0.047$) for the CCA and ($r = −0.883$, $P = 0.047$) for the ICA. Thus, with increasing axial stretch, the CCAs in the circumferential direction experienced an increasing 'stress softening', whereas the ICAs experienced an increasing 'stress hardening' with increasing axial stretch. No significant linear correlations were observed between the axial stretch and the pre-conditioning behavior in the axial direction.

Another remarkable feature can be seen in the axial stretch-pressure plots (Figs. 8.6(b) and 8.7(b)). Up to a certain axial stretch the slopes of the curves are positive, then they become slightly negative (i.e. the vessel contracts axially with increasing pressure). Thus, at a particular axial stretch (i.e. the '*inversion stretch*' with a related external axial force), the length of the specimen is independent of the pressure. The inversion stretches are not indicated in Figs. 8.6(b) and 8.7(b) since their exact values are not known, but for the particular specimen in the Figs. 8.6(b) and 8.7(b) they are about 1.18 for the CCA and 1.15 for the ICA. On average, we found axial inversion stretches of 1.19 (SD 0.06) for the CCAs ($n = 11$) and 1.14 (SD 0.06) for the ICAs ($n = 10$), and associated average external axial forces were determined to be 0.43 N (SD 0.15) for the CCA and 0.30 N (SD 0.22) for the ICA, respectively.

Adventitia

The mechanical response of the adventitia for the CCA and ICA is only shown for the high pressure domain (see Figs. 8.8 and 8.9), since the mechanical behavior in the low pressure domain was very similar, and, therefore, captured by the high pressure behavior. Briefly, the adventitia in the low pressure domain exhibit nearly

Figure 8.8: Representative mechanical responses of the adventitia of the CCA. Circumferential stretch-pressure (a) and axial stretch-pressure (b). Each curve is related to a specific axial stretch. The fifth loading cycle (solid lines) of the '1.25 and 1.30 axial stretch loading' resembles the corresponding first loading cycles (dotted lines).
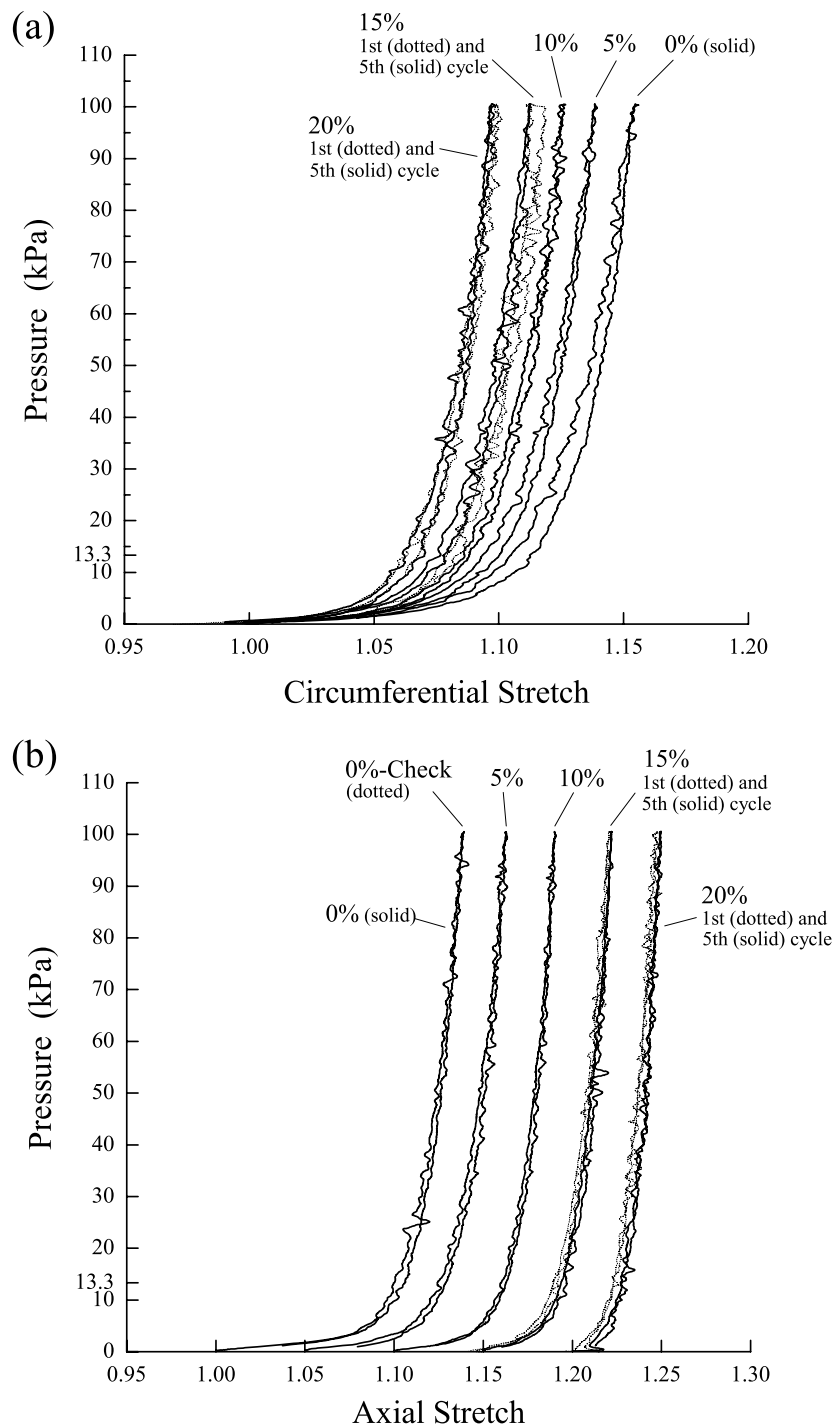
Figure 8.9: Representative mechanical responses of the adventitia of the ICA. Circumferential stretch-pressure (a) and axial stretch-pressure (b). Each curve is related to a specific axial stretch. The fifth loading cycle (solid lines) of the '1.15 and 1.20 axial stretch loading' resembles the corresponding first loading cycles (dotted lines).

elastic behavior with small hysteresis, nonlinearity and pronounced stiffening at higher pressures. Remarkably, even in the high pressure domain (up to 100 kPa) the adventitia showed nearly elastic behavior with only small hysteresis. Furthermore, no signs of material damage were observed during high pressure loadings. Interestingly, at high pressures (above 33.3 kPa) the slopes of the curves in the axial stretch-pressure plots (Figs. 8.8(b) and 8.9(b)) seem to be nearly linear and independent of the axial stretch applied, whereas at low pressures (below 10 kPa) the axial distensibility is rapidly decreasing with increasing axial stretch. Additionally, some specimens were inflated up to a transmural pressure of 250 kPa (i.e. 2.5 bar or 36.3 psi) to observe ultimate tensile strength properties of the adventitia tissue. At pressures up to 250 kPa no rupture of the adventitia tube occurred. For a transmural pressure of 250 kPa we computed (using Eqs. 8.1–8.3) the circumferential stress ($\sigma_{\theta\theta} = 4.2$ MPa), and the axial stress ($\sigma_{zz} = 1.6$ MPa) at a circumferential and axial stretch of $\lambda_\theta = 1.32$ and $\lambda_z = 1.07$, respectively. Remarkably, this led to the same characteristic behavior as experiments performed with 100 kPa. In particular, the circumferential and axial stretch-pressure plots of the 250 kPa cycle showed nearly elastic behavior with no observable damage signs, i.e. the ultimate tensile stresses of the investigated adventitia were beyond the above-computed stresses. The '*inversion*' feature (vertical line in the axial stretch-pressure plots discussed for the intact wall) was *not* observed for the adventitia tubes of CCA and ICA. Significant linear correlation between axial stretch and pre-conditioning behavior was not observed for the adventitia tubes.

Media-Intima

The media-intima (composite) tubes of the CCA and ICA showed mechanical behaviors similar to the intact walls (similar shapes of the curves, nearly elastic behavior, nonlinearity and small hysteresis). However, in contrast to the intact wall, the MI tube in the axial direction showed *no* inversion feature (i.e. no vertical line), not even at high axial stretches of 1.25. Furthermore, the mechanical response expressed through the circumferential stretch-pressure relation seems to be (almost) independent of the axial stretch (see, for example, Figs. 8.10(a), 8.11(a), 8.16(a) and 8.17(a)). Whereas, the axial stretch-pressure behavior of the media-intima showed an increase in stiffening with increasing axial stretch similar to the

(a)

(b)
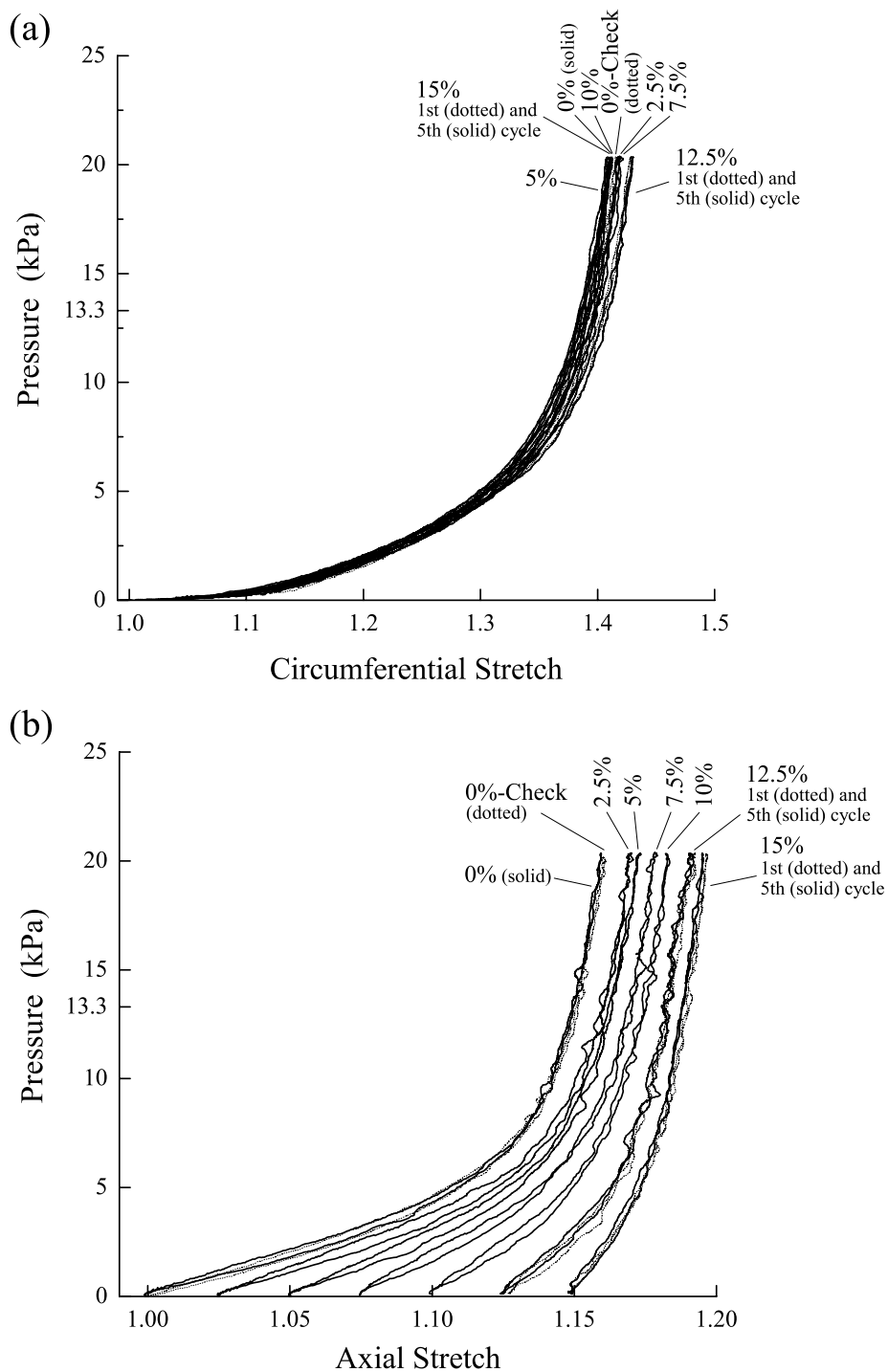
Figure 8.10: Representative mechanical responses of the media-intima composite of the CCA. Circumferential stretch-pressure (a) and axial stretch-pressure (b). Each curve is related to a specific axial stretch. The fifth loading cycle (solid lines) of the '1.125 and 1.15 axial stretch loading' resembles the corresponding first loading cycles (dotted lines).
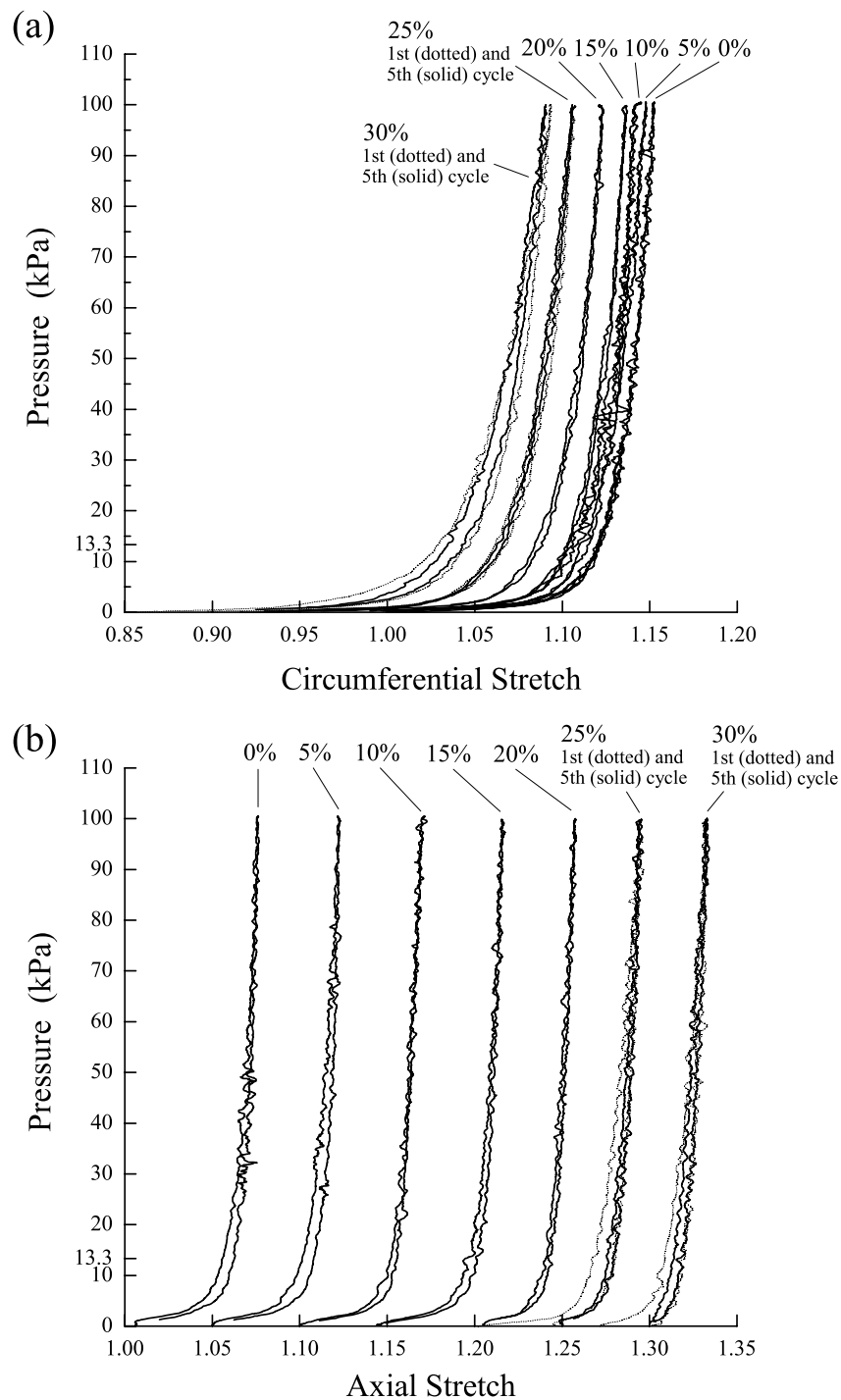
(a)

(b)
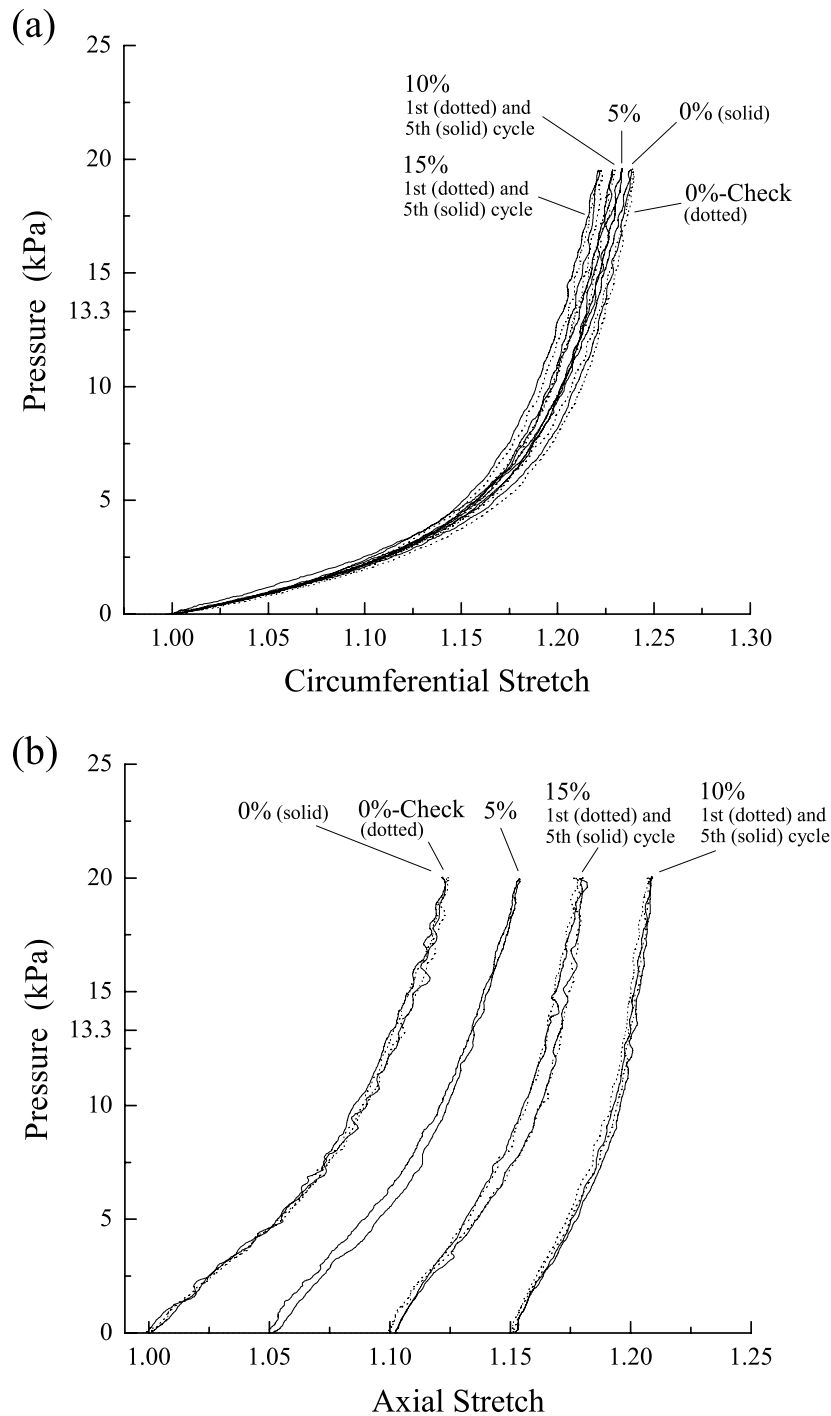
Figure 8.11: Representative mechanical responses of the media-intima composite of the ICA. Circumferential stretch-pressure (a) and axial stretch-pressure (b). Each curve is related to a specific axial stretch. The fifth loading cycle (solid lines) of the '1.10 and 1.15 axial stretch loading' resembles the corresponding first loading cycles (dotted lines).

intact wall. Moreover, the MI tubes of the CCA and the ICA showed similar characteristic behavior, only the ICA MI tubes seem to be consistently stiffer than the associated CCA MI tubes (see, for example, the representative Figs. 8.10 and 8.11). At preliminary MI tube tests it happened that the media-intima tube ruptured at pressures of approximately 60 kPa (450 mmHg). For this pressure and an assumed axial *in situ* stretch of 1.1 (10%), we computed the circumferential and axial stress in the media-intima tube as $\sigma_{\theta\theta} = 0.6$ MPa and $\sigma_{zz} = 0.3$ MPa, respectively. Significant linear correlations between axial stretch and pre-conditioning behavior was not observed for the media-intima tubes.

For all investigated tissues (intact wall, adventitia and media-intima composite for the CCA and the ICA), rotations of the axial gage markers on the specimens were not observed, which suggests *orthotropic material symmetry*, whereas the torsional rigidity of the tube connectors was assumed to be negligible. Moreover, a '0%-control' cycle (shown in Figs. 8.6-8.11) which was performed after the highest axial stretch test, almost resembled the initial 0%-curve.

8.3.4 Stress Analysis

By means of Eq. (8.3), average circumferential and axial stresses of the intact wall, the adventitia and the media-intima composite of both the CCA and ICA were computed for the following 13 pressure values: 1.5, 2, 3, 6.7, 9, 10, 13.3, 15, 18, 20, 22, 26.6, and 30 kPa (11, 15, 23, 50, 68, 75, 100, 113, 135, 150, 165, 200, 225 mmHg), at axial stretches ranging from 0% to 20% with 5% increments (1.0 to 1.2) for the intact wall and the adventitia, and from 0% to 10% with 5% increments (1.0 to 1.1) for the media-intima composite. Figures 8.12-8.17 show the calculated mean circumferential and axial stresses (± SD indicated by bars; axial stretch of 0% indicated by squares, 5% by circles, 10% by triangles, 15% by upside down triangles and 20% by rhombuses) in regard to the applied transmural pressure (ranging 0–33.3 kPa).

In general, circumferential and axial stresses increase with increasing axial stretch, but that is more pronounced in the axial direction. Since we use the Laplace law

Figure 8.12: Mean circumferential (a) and axial stresses (b) ($\pm$ SD indicated by bars) subjected to transmural pressure of the CCA intact walls at different axial stretches (0–20%). Different symbols for the mean stresses and increasing bar width for the SD with increasing axial stretch are used.

(a)

(b)
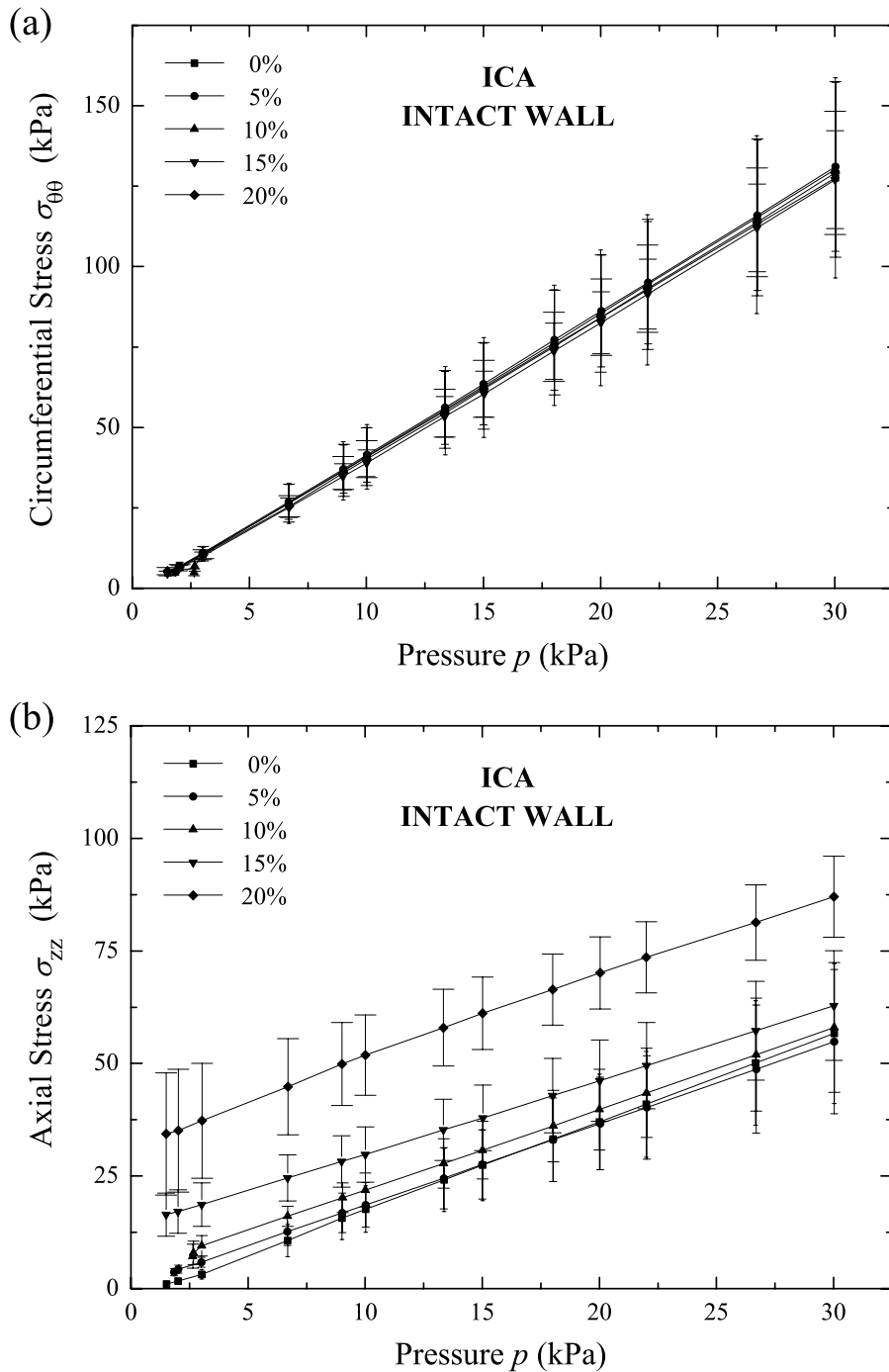
Figure 8.13: Mean circumferential (a) and axial stresses (b) (± SD, indicated by bars)
           subjected to transmural pressure of the ICA intact walls at different
           axial stretches (0–20%). Different symbols for the mean stresses and
           increasing bar width for the SD with increasing axial stretch are used,
           respectively.

Table 8.4: *Circumferential and axial stresses in the investigated tubes of the CCAs and ICAs at mean physiological pressure and different axial stretches.*

						CCA				
	circumferential					axial				
λ_z	W	A	A_w	MI	MI_w	W	A	A_w	MI	MI_w
1.00	49.0 (5.8)	135.0 (4.3)	142.3 (3.1)	120.9 (24.0)	119.2 (26.6)	17.7 (7.8)	26.9 (4.3)	27.8 (6.7)	58.2 (10.7)	57.4 (11.9)
1.05	52.5 (7.2)	140.5 (24.1)	142.4 (29.8)	125.2 (22.1)	123.3 (24.8)	21.1 (8.0)	46.7 (8.8)	47.4 (5.5)	82.5 (3.6)	82.1 (3.5)
1.10	55.3 (8.5)	140.2 (24.2)	140.2 (28.8)	128.6 (20.6)	126.7 (23.5)	28.3 (13.7)	76.7 (23.3)	76.8 (19.6)	96.7 (10.4)	96.4 (11.5)
1.15	59.8 (10.1)	146.4 (41.0)	139.0 (47.7)	–	–	31.4 (4.3)	74.8 (11.1)	78.9 (11.9)	–	–
1.20	63.5 (4.3)	172.9 (15.4)	168.1 (23.3)	–	–	52.5 (2.8)	88.5 (24.4)	90.0 (19.0)	–	–
						ICA				
	circumferential					axial				
λ_z	W	A	A_w	MI	MI_w	W	A	A_w	MI	MI_w
1.00	55.2 (13.8)	76.3 (14.2)	76.6 (9.9)	134.7 (9.1)	130.2 (8.8)	24.1 (7.0)	20.0 (15.7)	21.0 (15.2	64.0 (4.3)	61.8 (4.2)
1.05	56.1 (11.3)	83.3 (17.7)	84.0 (15.7)	138.3 (9.3)	133.7 (9.0)	24.5 (6.8)	33.4 (11.5)	33.6 (13.2)	65.8 (4.4)	63.5 (4.3)
1.10	55.6 (12.1)	85.1 (18.4)	85.9 (17.0)	141.6 (9.5)	136.9 (9.2)	27.8 (5.5)	42.2 (8.5)	43.5 (11.3)	67.5 (4.5)	65.1 (4.4)
1.15	53.3 (6.3)	97.2 (24.2)	98.7 (19.3)	–	–	35.2 (6.8)	55.0 (27.9)	55.6 (12.9)	–	–
1.20	54.4 (7.4)	111.5 (11.2)	108.5 (18.5)	–	–	58.0 (8.5)	62.5 (16.0)	62.5 (23.3)	–	–

Circumferential $\sigma_{\theta\theta}$ and axial σ_{zz} stresses of the CCAs and ICAs at mean physiological pressure $p = 13.3$ kPa (100 mmHg) and different axial stretches ($\lambda_z=1.0$, 1.05, 1.1, 1.15, 1.2) in the intact wall W, the adventitia tube with (A_w) and without (A) consideration of residual stretches, and the media-intima composite tube with (MI_w) and without (MI) consideration of residual stretches.

(8.1), the relationship between pressure and stress is linear, and the circumferential stress is twice as high as the related axial stress at 0% axial stretch. However, for the intact wall, the adventitia and the media-intima composite we found *circumferential-to-axial stress slope ratios* (CASSRs) higher than two (2.8 for the intact wall, 5.3 for the adventitia and 2.4 for the media-intima composite), which suggests anisotropy for that tubes. The adventitia of the ICA showed a high CASSR as well, and hence a highly anisotropic behavior. Surprisingly, the intact wall and the media-intima composite of the ICA showed CASSRs close to two (2.2 and 2.1, respectively), which would suggest isotropic behavior. By increasing the axial stretch to 20%, the CASSR decreases to 1.7 for the intact wall, to 2.2 for the adventitia and to 2.1 for the media-intima composite for the CCA. The ICA adventitia and media-intima showed decreasing CASSR, from 3.7 to 2.1 and 2.10 to 2.09, respectively. Interestingly, the ICA intact wall showed only a slight increase of CASSR (from 2.2 to 2.4) with axial stretch up to 20%.

(a)

(b)

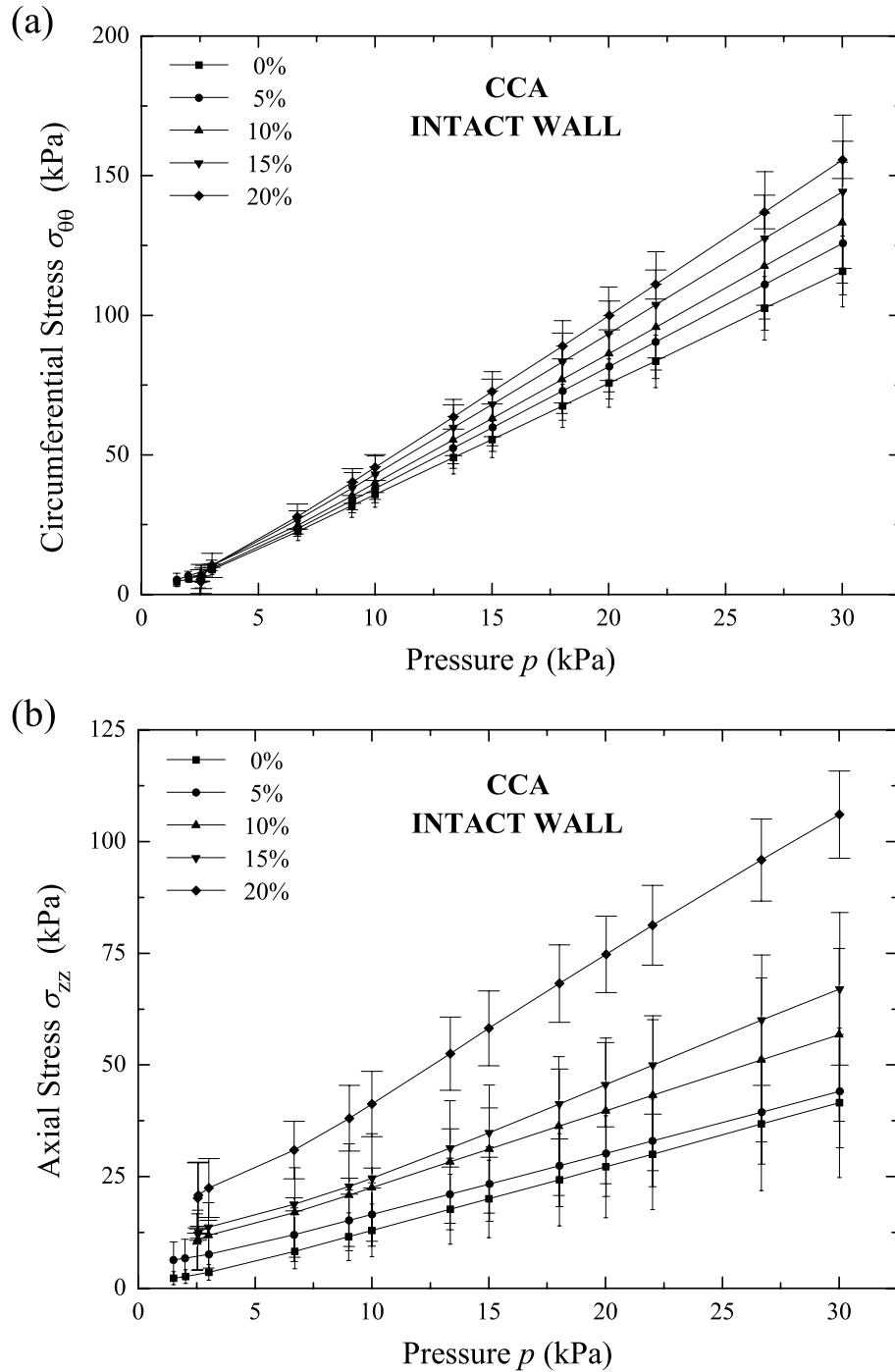

Figure 8.14: Mean circumferential (a) and axial stresses (b) (± SD, indicated by bars) subjected to transmural pressure of the CCA adventitias at different axial stretches (0–20%). Different symbols for the mean stresses and increasing bar width for the SD with increasing axial stretch are used. Dashed lines with gray SD bars illustrate mean stresses and SD without consideration of residual stretches. * indicates consideration of residual stretches.

(a)

(b)
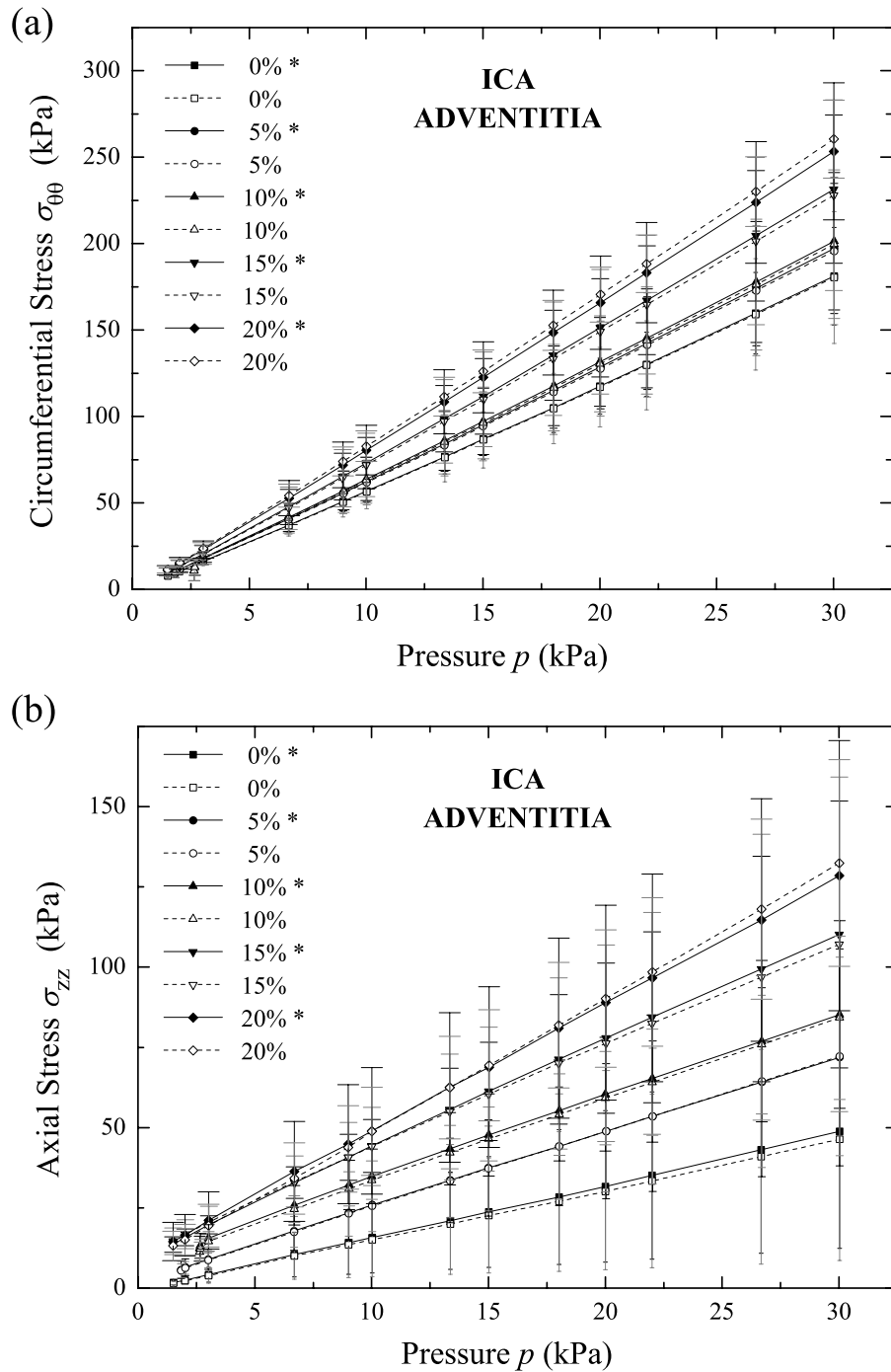
Figure 8.15: Mean circumferential (a) and axial stresses (b) (± SD, indicated by bars) subjected to transmural pressure of the ICA adventitias at different axial stretches (0–20%). Different symbols for the mean stresses and increasing bar width for the SD with increasing axial stretch are used, respectively. Dashed lines with gray SD bars illustrate mean stresses and SD without consideration of residual stretches. * indicates consideration of residual stretches.

The stresses in the intact wall and the media-intima composite are similar in the CCA and ICA for both directions (circumferential and axial), whereas the stresses in the adventitia of the CCA in the circumferential direction are significantly higher than the associated stresses in the ICA. The stresses in the adventitia of the CCA in the axial direction were not significantly higher.

To study the influence of the residual stretches on the stress states in the adventitia tubes and the media-intima tubes, additional stress calculations were performed with residual stretches omitted. Dashed lines with gray SD bars illustrate the associated data (see Figs. 8.14, 8.16, 8.15 and 8.17). For a better illustration of the influence of the residual stretches on the circumferential and axial stresses of the investigated tubes (W, A and MI) of the CCA and the ICA, stresses (mean (SD)) were computed for the mean physiological blood pressure of 13.3 kPa (100 mmHg) and for different axial stretches ranging from 0–20% (see Table 8.4).

In particular, at low axial stretches (0% and 5%), the CCA adventitia showed a slight increase in mean circumferential stresses if residual stretches were considered. At 10% axial stretch the residual stretches show no influence on the circumferential stresses, and at higher axial stretches (15% and 20%) the circumferential stresses start to decrease. At a particular point, which we call the *reverse point*, the influence of both the residual stretches and the axial stretch on the circumferential stresses reverses. Before this point the circumferential stresses were slightly increased, and afterwards they were slightly decreased if residual stretches are considered. The mean axial stresses of the CCA adventitia are for all axial stretches slightly increased if residual stretches are considered. The ICA adventitia showed a behavior similar to the CCA adventitia, but the *reverse point* is located at an axial stretch of 15–20%. The stresses in the media-intima tubes always decrease slightly if residual stretches are considered. Interestingly, there seems to be no influence from the axial stretch and the orientations (circumferential or axial) on the stresses in the media-intima composite.

In all cases, the above mentioned residual stretch dependent stress analysis were not significant due to the high SD observed in the tissues. However, some trend-setting assessments can be made.
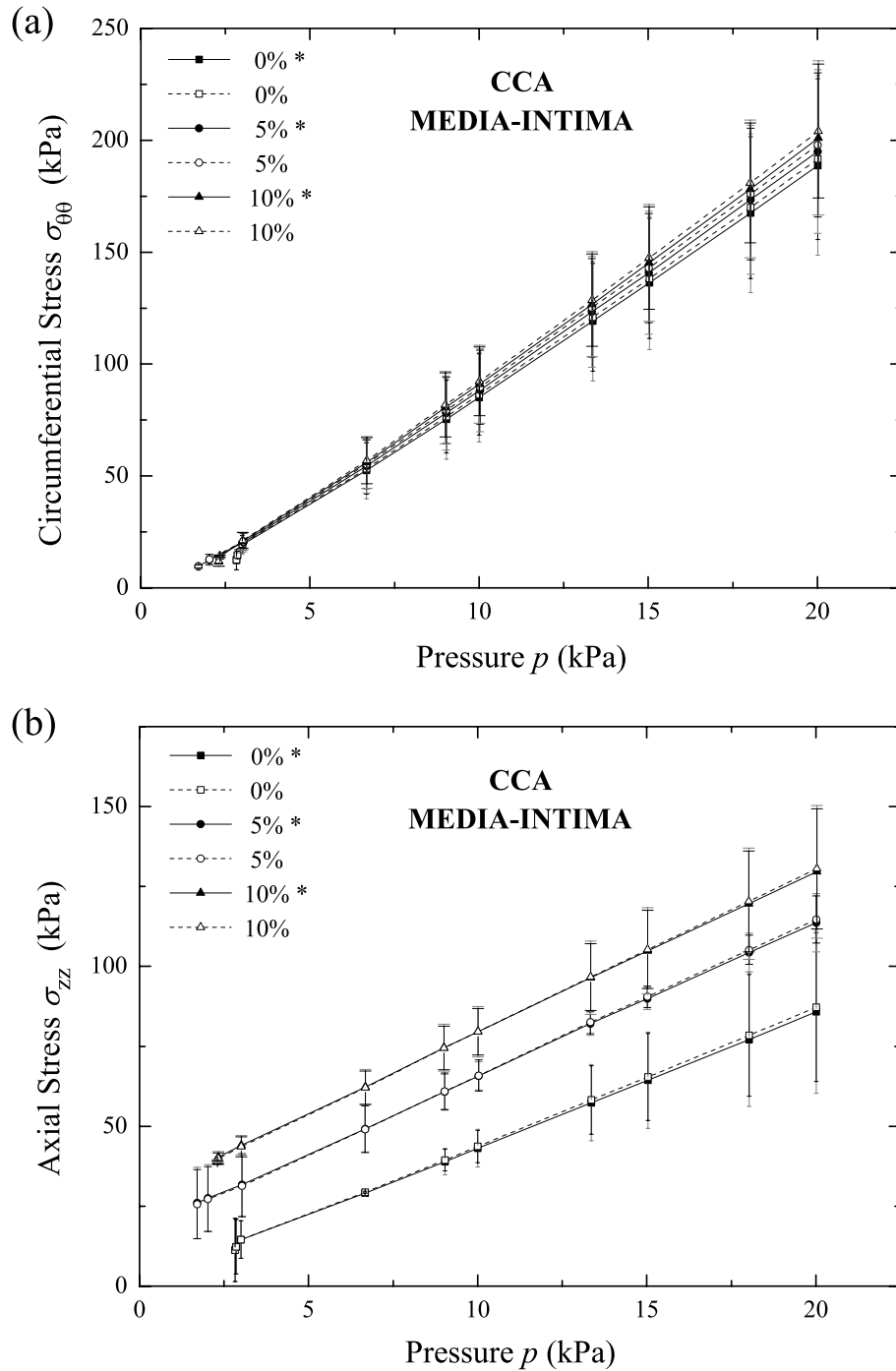
Figure 8.16: Mean circumferential (a) and axial stresses (b) (± SD, indicated by bars) subjected to transmural pressure of the CCA media-intima composites at different axial stretches (0–10%). Different symbols for the mean stresses and increasing bar width for the SD with increasing axial stretch are used, respectively. Dashed lines with gray SD bars illustrate mean stresses and SD without consideration of residual stretches. * indicates consideration of residual stretches.

(a)

(b)
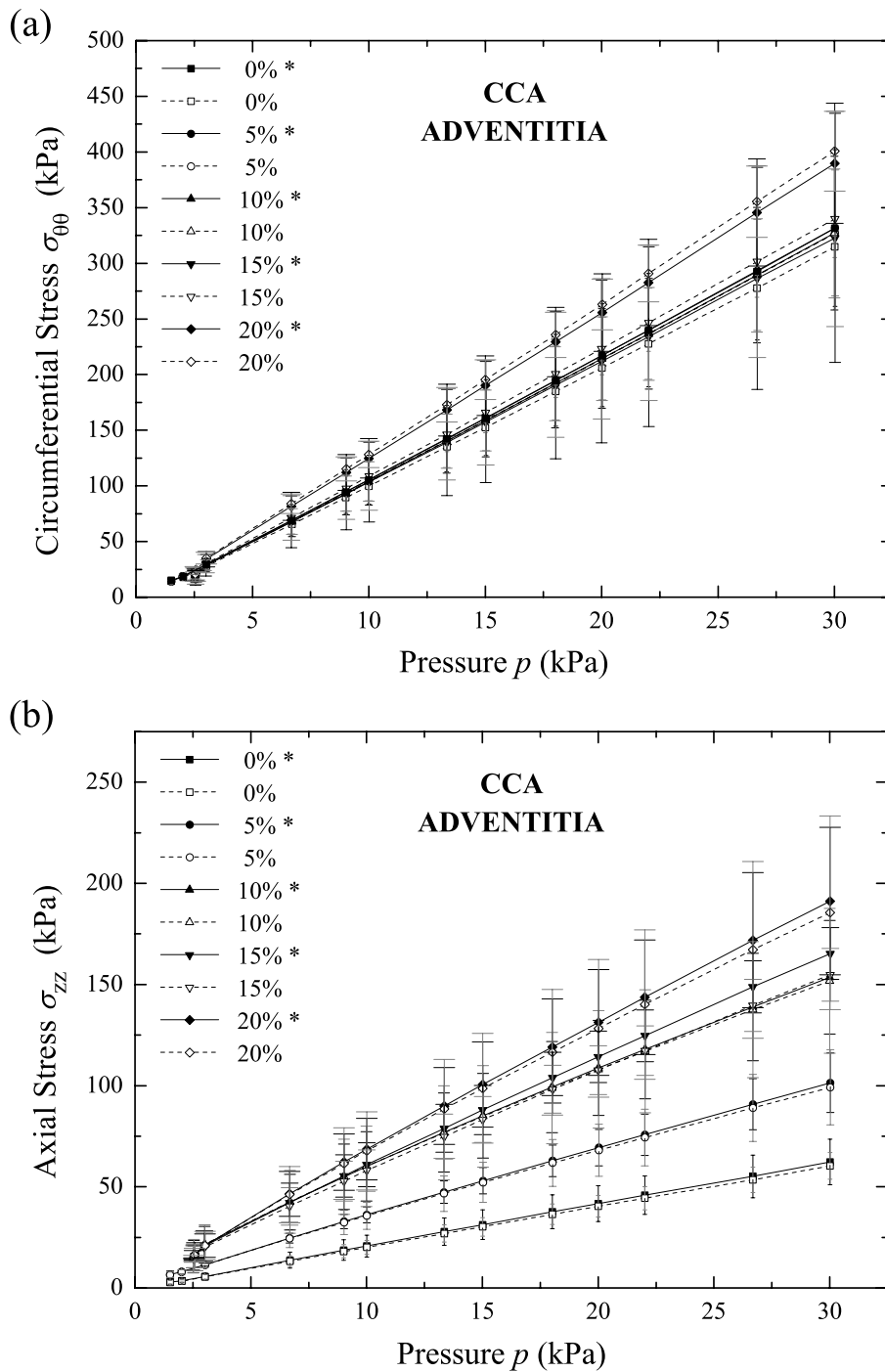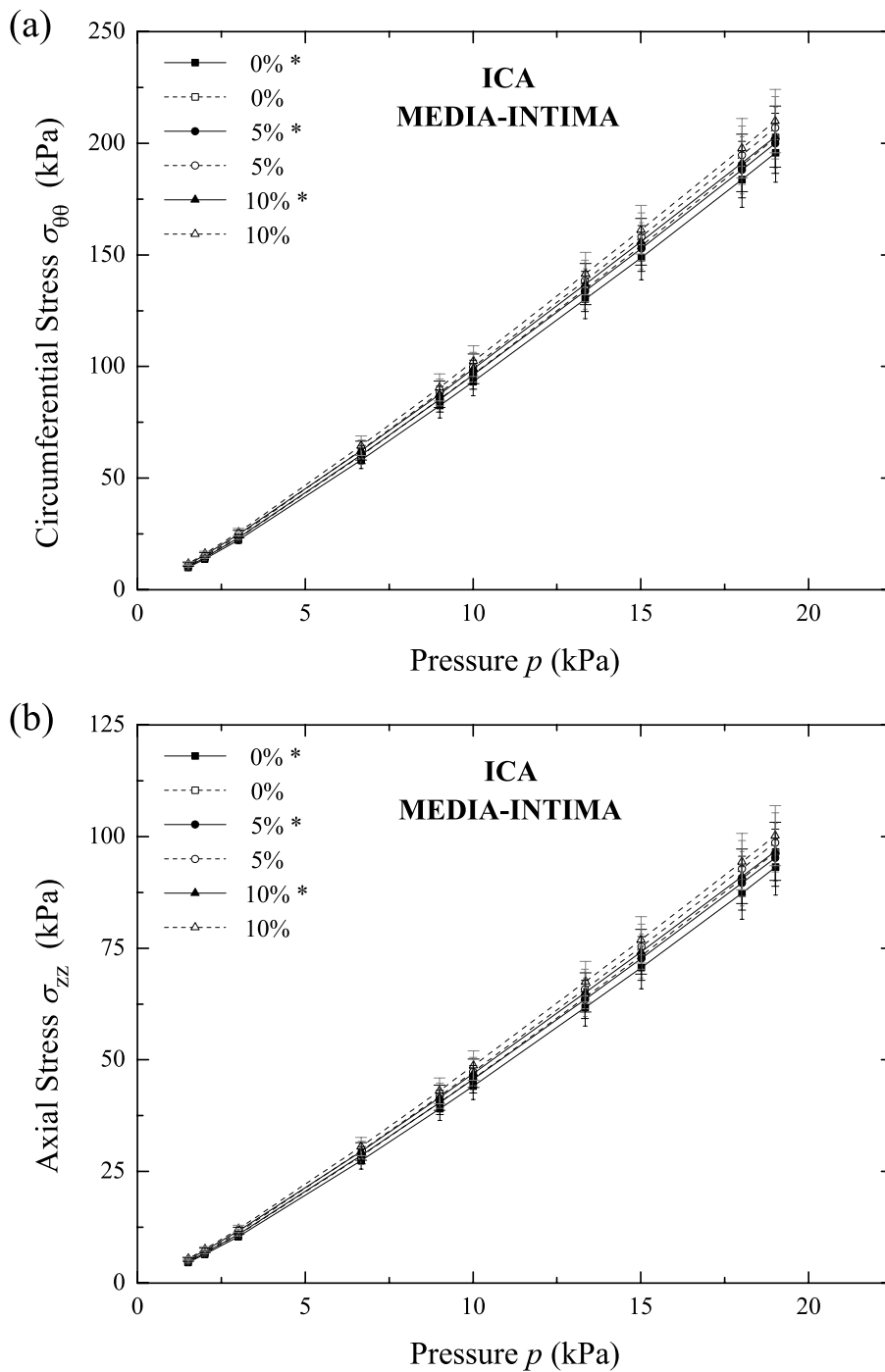

Figure 8.17: Mean circumferential (a) and axial stresses (b) (± SD, indicated by bars) subjected to transmural pressure of the ICA media-intima composites at different axial pre-stretches (0–10%). Different axial pre-stretches, different symbols for the mean stresses and increasing bar width for the SD with increasing axial stretch are used, respectively. Dashed lines with gray SD bars illustrate mean stresses and SD without consideration of residual stretches. * indicates consideration of residual stretches.

8.3.5 Histological Investigations

The histological investigations confirmed that the adventitia was properly re-moved. The media-intima tube showed 1–4 ruptured elastic lamellae on the outer surface, but the integrity of the remaining media-intima composite (intact intima, intact elastic lamellae) was confirmed. Microphotographs of representative sec-tions are shown in Fig. 8.3.

8.3.6 Statistics

Statistical analysis were performed to test significant correlations between age and (i) axial inversion stretch, (ii) external axial inversion force, (iii) circumferential stretches and (iv) axial stretches (at physiological conditions, i.e. at a pressure of 13.3 kPa and at an axial stretch of $\lambda_z = 1.05$ and $\lambda_z = 1.10$). We assumed the axial stretch of the CCA and ICA to be between $\lambda_z = 1.05$ and $\lambda_z = 1.10$ in the human body.

We found significant negative correlations between age and axial 'inversion stretches' for the intact wall of the CCA ($r = -0.67, P = 0.03$) and for the intact wall of the ICA ($r = -0.29, P = 0.04$). Interestingly, no significant correlations were found between age and external axial inversion forces for the intact wall of the CCA ($r = 0.26, P = 0.46$) and for the ICA ($r = 0.45, P = 0.26$). Inversion stretch behavior was not observed for the adventitia or for the media-intima tubes. Finally, no sig-nificant correlations between age and circumferential or axial stretches at physio-logical conditions were found for the intact wall, the adventitia or the media-intima composite in the CCA and the ICA.

8.4 Discussion

An important area in vessel biomechanics is the determination of the mechani-cal loads and the associated deformations and stresses that occur in the arterial wall. Most studies on vessel wall mechanics investigate animal arterial tissues and consider arterial walls as single-layer homogeneous structures. However, in understanding of factors like age, gender, risk factors and anamnesis, mechanical

data originating from human tissues are more informative (vital) than those from animal tissues. Moreover, arterial walls are heterogenous three-layered composites with significantly different histological, physiological and biomechanical features. Thus, a better understanding of their mechanical functions requires layer-specific data.

8.4.1 Geometry

The average *ratios of outer diameter to wall thickness* (DTR) were 7.1 for the intact wall of the CCA and 6.2 for the intact wall of the ICA. This corresponds well to 8.9 for human CCAs obtained from angiographic measurements of 22 adults (34 to 77 yrs) [262, 267]. The value, however, differs significantly for the ICA where a DTR of 13 was reported [262, 267]. For young human CCA a DTR of 3.8 ($n = 7$, age: 21–35 yrs) was reported [259], which is clearly smaller than those found for the DTR of the CCA in the present study. Furthermore, animal CCAs showed smaller DTRs; 5.4 for sheeps [257] and 5.0 for porcine ($n = 26$) [268], which may lead to the conclusion that the DTRs of CCAs of young humans and (young) animals are smaller than those from elderly man. The DTR of the adventitia tubes were determined to be 17.0 and 15.2 for the CCA and the ICA respectively, which justifies the thin-wall approach adopted, while such high DTRs were not found for the intact wall and the media-intima tube of the CCA and ICA (see Table 8.2). No comparable data for carotids are available in the literature. Only a DTR value of 22.7 for human femoral adventitia tubes, which is a similar finding, was found in the literature [69].

The unloaded average thicknesses for the intact wall were determined to be 1.17 mm (SD 0.16) for the CCA and 0.86 mm (SD 0.06) for the ICA. Animal CCA thicknesses found in the literature were similar for sheeps, 0.98 mm (SD 0.18), [257], and smaller for porcine, 0.64 mm (SD 0.09), [268]. Unfortunately, no comparable data for carotid adventitias were found in the literature. However, the thickness of human femoral adventitias was stated as 0.41 mm (SD 0.09) ($n = 11$, age: 79.3 yrs (SD 8.2), [69], which is similar to the CCA adventitia thickness of 0.47 mm (SD 0.07) of our study. The *media-intima composite thickness* (MIT) was determined to be 0.70 mm (SD 0.13) for the CCA and 0.53 mm (SD 0.10) for the ICA. The MIT for

aged human CCA found in the literature was 0.72 mm (SD 0.15) ($n = 22$, age 61 yrs (SD 7)) [269], which correlates very well with our findings. A value of 0.64 mm (SD 0.14) for younger human CCA (mean age 42.4 mm (SD 16.5), $n = 69$, with ages ranging from 16 to 75 yrs) is reported in [270]. No data were found for the MIT of the ICA. A fundamental difference between human and animal arteries is that not only the adventitia and the media but also the intima exhibited considerable thickness and mechanical strength [73, 76].

8.4.2 Residual Stretches and Stress-Free Configuration

For the first time, the present study reports data on significant residual stretches of the adventitia and the media-intima composite in an arterial wall composite (see Table 8.2).

Significant residual stress release in the circumferential direction was observed only for the intact wall of the CCA and ICA. Six hours after separation a small residual stress release was observed in the layers oriented in the circumferential direction, which might indicate that residual stress release of the adventitia and media-intima already occurs in the composite of the intact wall during stress release after cutting. On average, all axially oriented strips showed small changes (similar negative curvatures) from the initial (~3 min after cut) to the final configuration (16 and 6 hours after, respectively), which indicates that the residual stress release in axially oriented strips occurs almost immediately (within ~3 min) after cutting from the remaining arterial compound. By assuming zero curvature (i.e. initial configuration in the arterial compound is a straight cylinder), significant stress release in the axial direction was observed in the intact walls of the CCA and the adventitia of the CCA and ICA (see Table 8.3).

We identified an average circumferential curvature of 0.232 mm^{-1} (SD 0.072) for the intact wall of the CCA, and 0.179 mm^{-1} (SD 0.128) for the intact wall of the ICA. This corresponds very well to the opening angle of 130° (SD 15) or to the curvature of 0.224 mm^{-1} (SD 0.026) for human CCAs ($n = 8$) published by Delfino et al. 1996 [271]. However, a larger average curvature 0.282 mm^{-1} (SD 0.049) ($n = 8$) or 116° (SD 20) was found for human ICAs [271]. Opening angles for CCAs of rats (84° (SD 12)) and sheeps (85° (SD 27)) were clearly smaller than

opening angles of human CCAs [257, 258], which may indicate age-dependency of residual stresses [212]. Unfortunately, no data about residual stresses of the ICA were found in the literature. Human aortic adventitias remained flat in the circumferential ($-0.003\,\text{mm}^{-1}$ (SD 0.029)) and axial ($0.0\,\text{mm}^{-1}$ (SD 0.040)) direction [34], which was not the case for human CCAs and ICAs investigated here (see Fig. 8.5). Furthermore, the study by Holzapfel et al. [34] has shown that residual deformations are three dimensional and cannot be described by a single parameter such as 'the' opening angle. Therefore, their quantification and modeling require consideration of both stretching and bending, which are highly layer-specific and axially dependent. Our study confirmed this finding. To our knowledge, this is the first study where 'layer-specific' residual stresses in the circumferential and axial direction of human CCAs and ICAs are reported.

8.4.3 Load-Deformation Behavior, Stress Analysis, and Implications for Vascular Physiology

Common features of all investigated tissues are: strong nonlinearity, pseudo-elastic behavior, small hysteresis. During cyclic pre-conditioning there were only minimal changes in the mechanical response and pre-conditioning was finished after only three to four inflation-deflation cycles. Furthermore, all tissues (except the media-intima of the CCA in the circumferential direction, Fig. 8.10(a)) showed a decrease in circumferential stretches with increasing axial stretches, which indicates the 'crosstalk' between both directions. Remarkably, all investigated 'layer' tubes showed no obvious damage since the '0%-control' cycle, which was performed after the last load cycle, resembled the initial 0%-curve. Moreover, no rotation of the gauge markers during inflation suggests *orthotropic material symmetry*.

We observed the 'inversion feature' of the axial stretch-pressure curves at higher axial stretches only for the intact walls. At this 'inversion stretch', the axial stretch and force are relatively independent of the transmural pressure. This feature is supposed to be characteristic of all arteries [89]. For animal arteries the axial *in situ* stretch is approximately equal to the '*inversion stretch*' [62, 272], whereas aged human arteries showed significantly smaller axial *in situ* stretches than '*inversion stretches*' [73]. To answer the crucial question whether or not the measured axial *in*

situ stretch equals the axial *in vivo* stretch at mean arterial pressure, we performed *in situ* inflation tests on human iliac arteries. Based on these findings, we concluded that the '*physical operating range*' was between the axial *in situ* stretch and the '*inversion stretch*' [73]. From an energy-minimizing point of view, it would be best if the axial *in vivo* stretch in arteries equals approximately the 'inversion stretch' (i.e. arteries do no 'axial work' during the cardiac cycle). However, this energetically-optimized vessel function was neither confirmed nor disproved in the above mentioned studies. We found average axial '*inversion stretches*' of 1.14 (SD 0.06) for all investigated CCAs ($n = 11$) and 1.19 (SD 0.06) for the ICAs ($n = 10$), and related average external axial forces of 0.43 N (SD 0.15) for the CCAs and 0.30 N (SD 0.22) for the ICAs, respectively. Statistical analysis showed significant negative correlations between age and axial '*inversion stretches*' for the CCAs ($r = -0.67$, $P = 0.03$) and for the ICAs ($r = -0.29$, $P = 0.04$). Interestingly, no significant correlations were found between age and external axial inversion forces for the CCAs ($r = 0.26$, $P = 0.46$) and for the ICAs ($r = 0.45$, $P = 0.26$).

The mechanical data generated in this study emphasize the adventitia and the media-intima composite as 'layers' with different mechanical properties, and hence different mechanical functions. Particularly, the adventitia is very compliant at low pressures but carries significant loads under physiological conditions. At higher blood pressures, it becomes the mechanically dominated wall component due to its pronounced stiffening behavior, and, consequently, the adventitia is most appropriate for sensing hypertensive states [69]. These insights support the hypothesis of an adventitia-dependent regulation of the arterial smooth muscle tone. The adventitia is suggested to consist of many potential mechanical sensory and regulatory constituents, such as the adipose tissue, fibroblasts, macrophages, vasa vasorum and terminal nerve fibers. Perivascular adventitial adipose tissue is suggested to release a transferable adventitium–derived relaxing factor in vascular smooth muscle cells [208]. Another study suggested that visceral periadventitial adipose tissue controls arterial tone by inducing vasorelaxation via K_V channel activation in vascular smooth muscle cells [273]. Adventitial fibroblasts may be transfected via adenoviral vectors to produce nitric oxide (NO) upon receptor or nonreceptor activation. This single molecule NO is responsible for regulatory processes such as anti-inflammatory, mitogenic, and contractile activities of the

vessel wall as well as the homeostatic process within the vessel lumen [274]. In this regard, it has been shown that NO produced by fibroblasts in the adventitia causes effective vessel relaxation [275]. Furthermore, the endothelial cells in the intima of the vasa vasorum may react on elevated mechanical stresses with specific paracrine activity, which could affect the entire vessel wall [69]. Additionally, from the sympathetic and vagal efferent nerve terminals, released neurotransmitters may act on vascular smooth muscle directly or through release of endothelium-derived NO [276]. It has been demonstrated recently that adventitia removal influenced arterial wall viscosity and elasticity in *in vivo* studies, possible by a smooth muscle-dependent mechanism since it was not present in *in vitro* studies [207]. On the other hand, adventitia is suggested to play a key role in the development of atherosclerosis from early intimal hyperplasia to calcification of chronic vascular lesions [276]. Thus therapies that focus on the adventitial contribution to the development of atherosclerosis and restenosis may have strong clinical promise [276].

The adventitias investigated in the present study changed into extremely stiff tubes at pressures exceeding the physiological range (see Figs. 8.8, 8.9, 8.14, 8.15). This suggests that overstretch of the media and intima is strongly restricted by the adventitia. Because of this pronounced stiffening, the difference between a 'safe' and a 'dangerous' balloon diameter during balloon angioplasty is very small. If the nominal diameter of the balloon is too large, the adventitia faces extremely high pressures, which finally might cause even rupture [69].

The biaxial mechanical behavior of human carotid media-intima tubes have, to our knowledge, never been published before. The courses and shapes of the stretch-pressure curves are similar to those of the intact arterial wall (see Figs. 8.12–8.17). However, until the highest performed axial stretch of the media-intima tube (1.25), no '*inversion*' feature (vertical line in the axial stretch-pressure plots) was observed. Interestingly, the diameter change during pressurization of the media-intima tube seems to be independent of the axial stretch. The relatively low burst pressure of approximately 60 kPa of the media-intima tube may lead to damage or rupture of the MI tube during high pressure loading of the intact wall, for example, during balloon angioplasty. Therefore, our results emphasize a proper choice of the balloon diameter for a safe and effective angioplasty procedure. Our

circumferential stretch-pressure results correspond to diameter-pressure curves of media-intima tubes from bovine carotid arteries [38]. However, the study [38] documents a dependency of the diameter-pressure behavior on the axial pre-stretch, and significant bigger hysteresis. Remarkably, high circumferential and axial stresses occurred in the media-intima tube at mean physiological pressure (13.3 kPa).

A fundamental prerequisite of the present study was a relatively atraumatic separation technique for the separation of the intact wall in an intact adventitial tube and an intact media-intima tube in a turtle-neck fashion. Correct layer separation was confirmed by light microscope inspection during the separation process, and by histological analysis after testing.

8.4.4 Study Limitation

Only separation of the intact wall tube in an intact adventitia tube and an intact media-intima composite tube was feasible.

Mechanical dissection of the adventitial layer from the media-intima composite may cause structural damage. However, this seems not to be the case in view of the mechanical strength of the adventitia and the relatively ease of dissection. The media-intima tubes did show rupture of medial lamellar layers on the outer surface of the media, which, to some aspect, might have influenced the mechanical behavior. However, the number of ruptured medial layers could be limited to three or four. The influence of the connection between adventitia tissue and the media-intima tissue was not examined in the present study.

The wall thickness H of the intact wall in the load-free tube was determined photogrammetrically from two rings which were taken from the ends of each segment. Since the shape of the vessel is not a perfect cylindrical tube, this may cause errors. Future developments should allow us to determine the wall thickness or the inner diameter directly at the center of the specimen. An accurate thickness measurement is crucial for stress computations. Reliable thickness measurements of highly deformable thin structures such as adventitias are especially difficult, and hence more likely to be afflicted with errors. Finally, a relatively small number of

arterial specimens were investigated so that an anamnesis-dependent conclusion could not be drawn.

The separation of the vessel wall into major 'layers' is, however, a step toward modeling the next level of hierarchy in the structure. Each 'layer' can be described by a unique set of material parameters and an appropriate nonlinear, anisotropic constitutive model. A more detailed investigation and determination of the microstructure and the mechanical behavior of the constituents (collagen fibers, elastin, smooth muscle cells, macrophages, etc.), and the combination with the macroscopic behavior of arteries will lead to better, constituent-based, multi-scaled and structure-based constitutive models. With this knowledge a more satisfactory description of arterial walls, their functionality, adaption and remodeling will be feasible.

9 3D MODELING OF THE MECHANICAL RESPONSE OF HUMAN CAROTID ARTERIES

Abstract.   Aged human arteries consist of three mechanical distinct layers: adventitia, media, intima. Experimental data from a series of biaxial tests (axial extension and inflation) on the intact carotid artery (common and internal) walls, and subsequently, their corresponding layer-dissected intact adventitia and media-intima composite tubes were fitted to an established novel, three-dimensional, and structure-based strain energy function (SEF). The zero stress states of the investigated tubes are considered by the kinematic formulation in the fitting process. Therefore, the obtained constitutive (material) parameters include the zero stress state and the mechanical behavior of the utilized tissues. The SEF used is suitable to describe the different mechanical properties of the investigated tubes at different local axial stretches and pressure loading domains. For all samples the two structure-based parameters reveal strong anisotropy with more alignment of the collagen fibers in the circumferential direction, and therefore, higher stiffness in the circumferential direction. Contour plots of the SEF against the circumferential and axial stretch were convex, which is a fundamental prerequisite for the use in finite-element codes. The validated 3D constitutive model will serve as a foundation for the formulation of layer-specific boundary value problems in human carotid physiology and pathology.

9.1 Introduction

Constitutive models or strain energy functions (SEFs) based on the theory of nonlinear continuum mechanics are preferably used to describe the mechanical properties of biological soft tissues including arteries. Experimental load-deformation data can be approximated by a SEF, which is characterized by constitutive (material) parameters. These parameters are usually determined by fitting the experi-

mental data to an appropriate SEF by considering the material mechanics theory and kinematics. One important motivation for such studies is that stresses and strains are believed to trigger the onset of atherosclerosis, the most common disease of the arterial walls. Disease of the arterial wall or cardiovascular disease is the number one cause of death globally and is projected to remain the leading cause of death [277]. An estimated 17.5 million people died from cardiovascular disease in 2005, representing 30% of all global deaths. Of these deaths, 7.6 million were due to heart attacks and 5.7 million were due to stroke. If appropriate action is not taken, by 2015, an estimated 20 million people will die from cardiovascular disease every year, mainly from heart attacks and strokes [277].

In general, *in vitro* (human) arteries (and the underlying major layers intima I, media M and adventitia A) display highly nonlinear pseudo-elastic [139] and anisotropic mechanical behavior over finite strains with the formation of small hysteresis [75, 76, 80]. The nonlinear (exponential) stiffening (common to all biological tissues) is based on the recruitment of the (load bearing) collagen fibers, which also leads to the characteristic anisotropic behavior of arteries [140, 195]. In addition to the *in vitro* characteristics, *in vivo* the artery is a pre-stretched material under an internal pressure load [134]. *In vivo* arteries are in an activated state due to nerve stimulated smooth muscle cells, but in this study we focus only on the passive state. Arteries can be regarded as incompressible materials, since they do not change their volume within the physiological range of deformation [43]. Moreover, the load-free configuration of an artery and their arterial layers is not a stress-free state, i.e. they contain residual stresses [20]. The existence of residual stress is manifest in the springing open of an arterial ring when it is cut in the radial direction [18, 139]. It is of crucial importance to identify these residual stresses in order to predict reliably the state of stress in the arterial tissue [21, 22, 134]. A novel study showed pronounced residual stress releases in the circumferential and axial direction [34]. Furthermore in that study [34], layer strips (A, M, I) showed pronounced contraction and elongation in the circumferential and axial direction after layer-dissection of the intact wall strips. This feature was referred to as residual stretches in the layers. For a more detailed description of the mechanical features and the mechanical behavior of human arteries and its underlying layers, the reader is referred to [75, 76, 80] and references therein.

Due to the above mentioned diversity and complexity of the arterial wall mechanics, a systematic study of the mechanical behavior of arteries based on the continuum theory of large deformation elasticity (by incorporating the histological structure and the (complex) kinematics of the artery and its underlying layers) is justified.

In the past, most SEF's which are able to describe the typical mechanical characteristics of the arterial wall (i.e. nonlinear, anisotropy, finite strains), were purely phenomenological [22, 39, 139, 262]. Even though these SEFs succeeded in describing the material properties of soft tissue, most have been subjected to limitations, e.g. they incorporate many parameters, are overly simplified, do not incorporate structural parameters, or violate laws of physics or thermodynamics for ill-chosen parameters [278]. Ideally, a SEF should make use of histologically available information to offer a better description of the wall deformation under load [278]. Appropriate arterial SEF's incorporating the histology structure are first discussed in [133, 278–281].

In this study the arterial wall and layers (A, M, I) are mechanically viewed as a composite material existing of an isotropic material (or matrix) containing predominantly highly distensible elastin, and embedded in this isotropic matrix, anisotropic components mainly contributed by stiff collagen fibers with a given orientation and dispersion. This model is based on histological investigations, since elastin and collagen content seem to have influences on vessel mechanics [282, 283].

A short overview of the histology of the arterial layers will be given. In healthy young arteries the inner layer *tunica intima* or, intima I for short, is very thin (consists only of a single layer of endothelial cells lining the arterial wall) and makes an nonsignificant contribution to the mechanical properties of the arterial wall. The healthy but aged intima consists of several very thin mainly collagenous layers with different orientations and distributions [120, 121], because of this intima thickening with age (*arteriosclerosis*) the mechanical contribution may become significant [76]. This process is called homogeneous diffuse intimal hyperplasia, which is the result of a nonatherosclerotic process [130]. In contrast, pathological changes of the intimal components may be associated with *atherosclerosis*, where fatty substances,

calcium, collagen fibers, cellular waste products and fibrin deposit into the arterial wall [130].

The middle arterial layer *tunica media* or, media M for short, consists of several medial layers, where smooth muscle cells are embedded in an elastin and collagen fibril network. These collagen fibrils are orientated and distributed mainly around the circumferential direction [284].

The outer layer *tunica adventitia* or, adventitia A for short, consists mainly of fibroblasts, fibrocytes and thick bundles of collagen fibrils forming collagen fibers. The collagen fibers in the unloaded artery are wavy and arranged in helical structures and serve to reinforce the arterial wall [134]. The adventitia is less stiff in the load-free configuration and at low pressures (loads) than the media, but at higher pressure levels becomes a 'jacket-like' tube which prevents the artery from overstretch and rupture, due straightening and stretching of the collagen fibers. For a more detailed description of the arterial histology the reader is referred to [134].

To overcome most of the above-mentioned shortcomings associated with SEF's, the SEF used in this paper incorporates histological structure information of the artery and their layers, such as the existence of an isotropic matrix, fiber orientations and their distributions. Hence, our SEF consists of an isotropic and an anisotropic part. The isotropic part of the SEF represents the equally distributed elastic elastin fiber matrix, whereas the anisotropic part represents the collagen fiber families with specific orientations and three-dimensional distributions.

For the kinematics, we consider the artery as an incompressible thick-walled (circular) cylindrical tube appropriate for extension and inflation. For simplification, we assume no torsion of the artery during extension and inflation, which can be assumed in the case of an healthy straight artery, i.e. circular cylindrical tube, and the assumption of cylindrical orthotropic symmetry. The assumption of cylindrical orthotropic symmetry of an artery is generally accepted in the literature [134]. In the formulation of the kinematics (theoretical framework) important kinematic features of the artery and the layers, such as the circumferential and axial residual stresses of the vessel wall and the layer tubes, and the circumferential and axial residual stretches of the layer tubes are taken into account.

A sophisticated three-dimensional mechanical model is necessary for meaningful analysis of the stresses and strains in the arterial wall. Therefore, the objective of this study was to develop a theoretical framework, which involves the kinematics and the biaxial mechanical response of human aged healthy carotid arteries and their associates adventitia (A) and media-intima composite (M-I), to determine more reliable constitutive parameters based on a novel and validated structure-based three-dimensional SEF.

9.2 Materials and Methods

9.2.1 Material

Eleven human common carotid arteries and 10 human internal carotid arteries from 11 human subjects (76.8 ± 6.3 yrs, mean $\pm$ SD, ranging from 67 to 86 yrs, 4 female and 7 male) were excised during autopsy within 24 h from death. The arteries were required to have at most medium atherosclerotic plaque formations (see Anamnesis Tab. 1 in [80]). The plaque grade estimations were made under examination by experienced pathologists. For this study, the use of autopsy material from human subjects was approved by the Ethics Committee of the Medical University of Graz (Graz, Austria).

9.2.2 Mechanical Testing

Extension-inflation tests, with continuous recording of transmural pressure (p), axial force (F_z), outer diameter and gage length of the intact artery walls, were performed at transmural pressures ranging from 0 to 33 kPa (250 mmHg) at several local axial stretches (λ_z) ranging from 1.0 to 1.3 in increments of 0.05. Specimens were immersed in a 37°C, calcium-free 0.9% NaCl physiological saline solution (PSS) during testing.

Thereafter, the intact artery wall was dissected into an adventitia and a media-intima tube, which were also tested separately. For the adventitia, the same testing protocol used for the intact artery wall was applied, and then, a similar testing protocol but with a higher pressurization (up to 100 kPa) was performed. For the

media-intima tube only a cyclic pressurization of 20 kPa was applied, because of its inherent low rupture pressure obtained in preliminary tests.

The circumferential and axial residual stretches of the adventitia and the media-intima tubes were determined photogrammetrically (from pictures taken), because after separation the adventitia showed an obvious contraction in the axial direction.

Moreover, stress-free configurations in the circumferential and axial directions (in terms of curvatures, circumferences and lengths, respectively) of the intact artery wall, the adventitia and the media-intima tube were determined. Thicknesses of the intact artery wall, the adventitia and the media-intima were also determined.

Finally, histological investigations were performed to confirm correct and as much as possible 'atraumatic' separation of the adventitia from the media-intima composite.

Brief summary of the testing results

Common mechanical features of all investigated tissues are: strong nonlinearity, pseudo-elastic behavior and small hysteresis. The so-called 'inversion'-feature (i.e., negative slopes of the axial stretch-pressure curves at higher axial stretches) was observed only for the intact walls. Adventitias were very compliant at low pressures but carried significant loads under physiological conditions. The adventitias became very stiff tubes at pressures exceeding the physiological range. Stress analyses indicated highly anisotropic material properties of all investigated tissues. In addition, high circumferential and axial stresses occurred in the media-intima tube at physiological conditions. For a more detailed description of the testing methods employed and the testing results the reader is referred to [80].
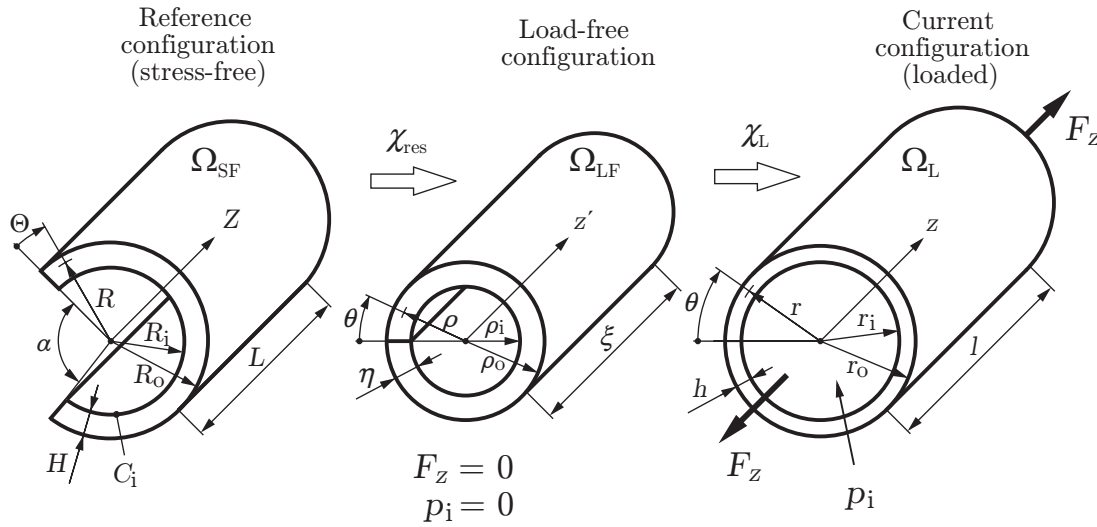
Figure 9.1: Kinematics of the intact wall. An intact arterial ring in the (stress-free) reference configuration Ω_{SF} (with released circumferential residual stresses), the load-free configuration Ω_{LF} (with incorporated residual stresses but without external loadings), and the (loaded) current configuration Ω_{L} by applying internal pressure p_{i} and axial force F_{z}.

9.2.3 Theoretical Framework

Kinematics of an Intact Artery Wall Tube: Combined Bending, Extension and Inflation

We consider the intact artery as an incompressible thick-walled cylindrical tube subjected to extension and inflation. We assume that there is no torsion loading on the tube. It is known that the load-free configuration, Ω_{LF}, in which the artery is excised from the body and not subjected to any loads is not a stress-free (or strain-free) reference configuration Ω_{SF} [20]. Thus, the arterial ring springs open when cut in a radial direction and an axially oriented strip bent away from the vessel axis [34, 80]. We assume that the open sector is the undeformed (stress-free and fixed) reference configuration Ω_{SF}, as depicted in Fig. 9.1. Thus, in terms of cylindrical coordinates (R, Θ, Z), the geometrical region of the stress-free configuration of the tube Ω_{SF} is defined by:

$$R_{\text{i}} \leq R \leq R_{\text{o}}, \ 0 \leq \Theta \leq (2\pi - \alpha), \ 0 \leq Z \leq L, \tag{9.1}$$

where R_{i}, R_{o}, α and L denote the inner and outer radii, the opening angle and the length of the 'stress-free' (split) tube, respectively. Note that the opening angle α

identified in Fig. 9.1 differs from the definition normally used (see, for example, Fung and Liu [205]).

The deformation χ takes Ω_{SF} into the current (loaded) configuration Ω_L. χ is the composition of the deformations χ_{res} and χ_L, as indicated in the Fig. 9.1, where χ_{res} generates the load-free configuration Ω_{LF} associated with residual stresses, while χ_L is associated with axial elongation and inflation, and leads to the final (current) configuration Ω_L. Particulary, the deformation χ_{res} maps the stress-free configuration Ω_{SF} into the load-free configuration Ω_{LF}. In terms of cylindrical coordinates (ρ, θ', z'), the geometry of the load-free configuration is:

$$\rho_i \leq \rho \leq \rho_o, \ 0 \leq \theta' \leq 2\pi, \ 0 \leq z' \leq \xi, \tag{9.2}$$

where ρ_i, ρ_o and ξ denote the inner and outer radii, and the length of the unloaded (but not stress-free) configuration Ω_{LF}, respectively.

Due to the incompressibility condition the inner radius of the load-free tube ρ_i leads to:

$$\rho_i = \sqrt{\rho_o^2 - \frac{R_o^2 - R_i^2}{k\lambda_{z,\mathrm{res}}}}, \quad \theta = k\Theta, \quad z' = \lambda_{z,\mathrm{res}}Z \tag{9.3}$$

with

$$k = \frac{2\pi R_i}{C_i} = \frac{2\pi}{\kappa_{R_i} C_i}, \tag{9.4}$$

where the parameter k, defined by $k = 2\pi/(2\pi - \alpha)$, is a convenient measure of the opening angle α in the stress-free configuration [133]. k is calculated from the photometrically determined values, the inner curvature $\kappa_{R_i} = 1/R_i$ and the inner arc length (circumference) C_i (see also [34] and [80]). The axial stretch due to the axial residual stresses (i.e. bent away from the vessel axis) $\lambda_{z,\mathrm{res}}$ is (approximately) computed by the ratio ξ_i/L_i, where ξ_i and L_i are the lengths of the unloaded inner tube and the length of the inner portion of the excised stress-free axial strip (see [34] and [80]), respectively. Both lengths ξ_i and L_i are determined from axial residual stress (deformation) measurements (see [34]), and are stated in Table 3 in [80].
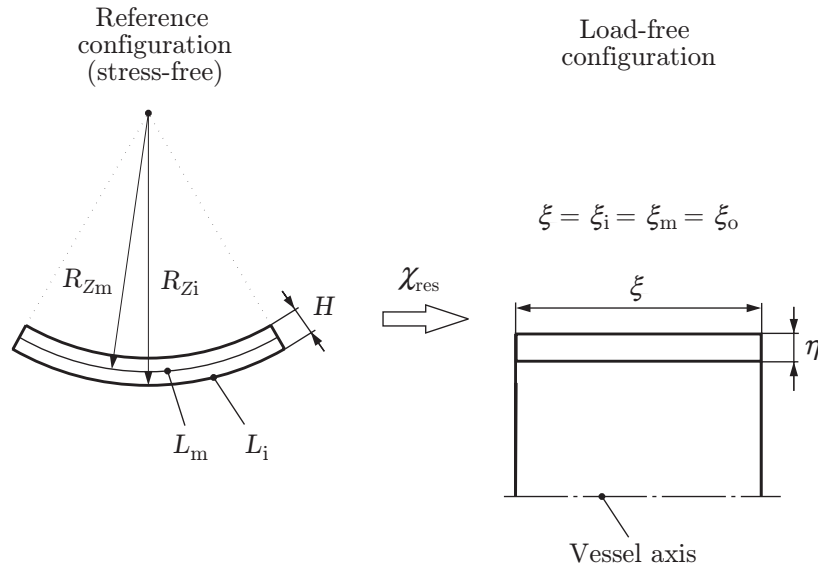
Figure 9.2: Kinematics of the reference configuration of an axial strip, assumed to be stress-free after residual stress release, mapped into the load-free configuration, where the axial strip is constrained to be straight in the compound of the arterial (layer) ring, see also Fig. 2 in [34].

From the left part of Fig. 9.2 we can derive for the ratio of the lengths and radii:

$$\frac{L_\mathrm{m}}{R_{Z_\mathrm{m}}} = \frac{L_\mathrm{i}}{R_{Z_\mathrm{i}}}, \tag{9.5}$$

where L_m and L_i are the arc lengths of the middle and inner portion of the stress-free axial strip, respectively, and R_{Z_m} and R_{Z_i} are the corresponding (associated) middle and inner arc radii of the stress-free axial strip, respectively.

Furthermore, with $R_{Z_\mathrm{m}} = R_{Z_\mathrm{i}} - H/2$ and $R_{Z_\mathrm{i}} = 1/\kappa_{Z_\mathrm{i}}$ it follows for L_i:

$$L_\mathrm{i} = \frac{L_\mathrm{m}}{1 - \frac{H\kappa_{Z_\mathrm{i}}}{2}}, \tag{9.6}$$

where κ_{Z_i} is the inner curvature of the stress-free axial strip prepared for the axial residual stress measurements [34].

With the assumptions $L_\mathrm{m} = \xi_\mathrm{m}$ and $\xi_\mathrm{i} = \xi_\mathrm{m} = \xi_\mathrm{a} = \xi$, it follows for $\lambda_{z,\mathrm{res}} = \xi_\mathrm{i}/L_\mathrm{i}$:

$$\lambda_{z,\mathrm{res}} = 1 - \frac{H\kappa_{Z_\mathrm{i}}}{2}. \tag{9.7}$$

The deformation χ_L takes the load-free configuration Ω_{LF} into the current (loaded) configuration Ω_L (see Fig. 9.1). In terms of cylindrical coordinates (r, θ, z), the geometry of the current (loaded) configuration is:

$$r_i \leq r \leq r_o, \ 0 \leq \theta \leq 2\pi, \ 0 \leq z \leq l, \tag{9.8}$$

where r_i, r_o and l denote the inner and outer radii and the length of the loaded tube, respectively.

During loading χ_L with the incompressibility condition, and hence no volume change, it follows for the inner radius of the loaded tube r_i:

$$r_i = \sqrt{r_o^2 - \frac{\rho_o^2 - \rho_i^2}{\lambda_z}}, \tag{9.9}$$

where $\lambda_z = l/\xi$.

Furthermore, for $\chi = \chi_L \circ \chi_{res}$, it follows with Eq. (9.3):

$$r_i = \sqrt{r_o^2 - \frac{R_o^2 - R_i^2}{k\lambda_{z,res}\lambda_z}}, \tag{9.10}$$

where the outer radius of the loaded tube may be expressed as $r_o = \rho_o \lambda_\theta$, and λ_θ and λ_z are the (measured) circumferential and the axial stretch of the loaded tube with respect to the configuration Ω_{LF}.

Now, r_i can be expressed solely as a function of the (indirectly) measured circumferential stretch λ_θ and axial stretch λ_z of the tube, and R_o, R_i, k and $\lambda_{z,res}$ as constants according to:

$$r_i = \sqrt{\rho_o^2 \lambda_\theta^2 - \frac{R_o^2 - R_i^2}{k\lambda_{z,res}\lambda_z}}. \tag{9.11}$$

Kinematics of the Adventitia and the Media-intima Tube

The same procedure used for the intact tube can also be applied for the kinematics of the adventitia and the media-intima tube. However, when the adventitia tube is removed from the media-intima tube, residual stretches between the adventitia
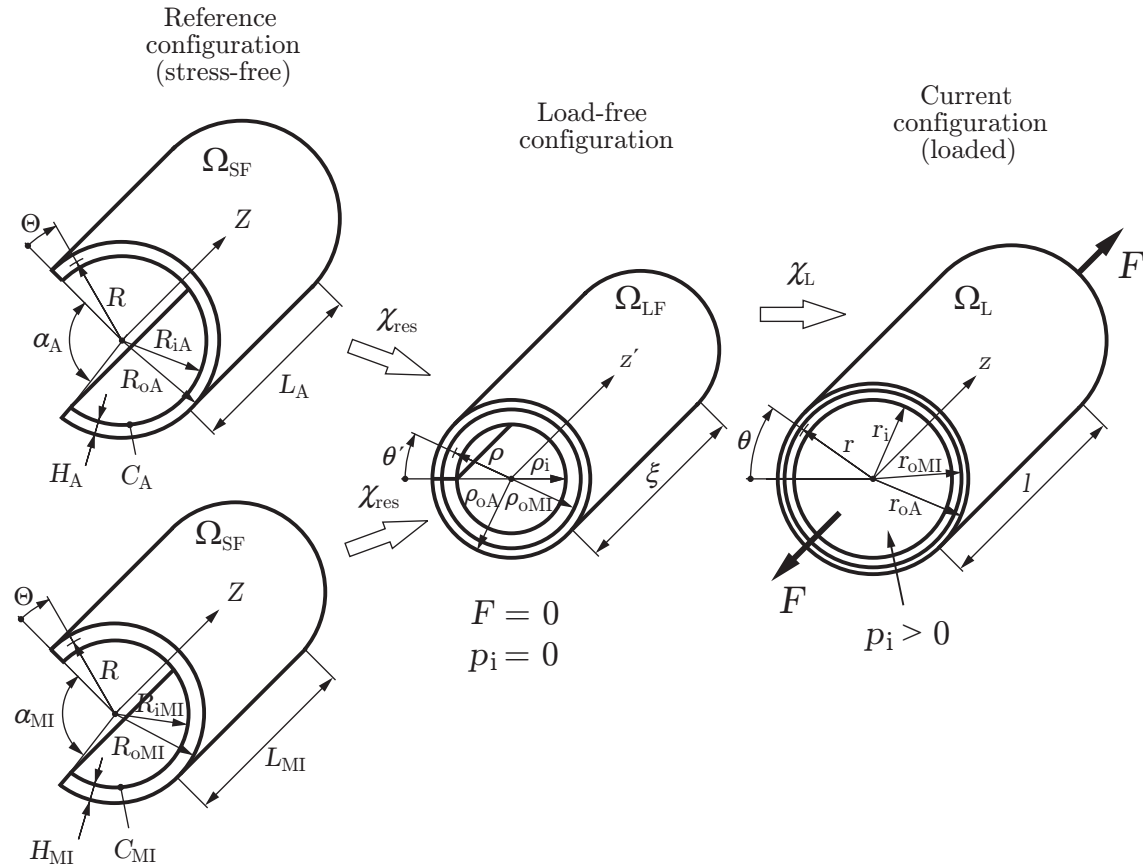
Figure 9.3: Kinematics of the adventitia and the media-intima tube. Similar to the intact wall, where two subdeformations (χ_{res} and χ_{L}) are applied to bring the (stress-free) reference configuration Ω_{SF} over the load-free configuration Ω_{LF} to the (loaded) current configuration Ω_{L}.

and media-intima tube are released and can (have to) be taking into account (see Fig. 9.3). Average circumferential and axial residual stretches of the adventitia and media-intima tubes are stated in Table 2 in [80].

Therefore, an additional step between Ω_{SF} and Ω_{LF} is necessary, as depicted in Fig. 9.3. In this step the circumferential and the axial residual stretches are considered.

For r_{i} of the adventitia and the media-intima tube it follows that:

$$r_{\mathrm{i}} = \sqrt{(\rho_{\mathrm{o}}\lambda_{\theta,\mathrm{rs}}\lambda_{\theta})^2 - \frac{R_{\mathrm{o}}^2 - R_{\mathrm{i}}^2}{k\lambda_{\mathrm{z,res}}\lambda_{\mathrm{z,rs}}\lambda_{\mathrm{z}}}}. \tag{9.12}$$

where $\lambda_{\theta,\mathrm{rs}}$ and $\lambda_{z,\mathrm{rs}}$ denote the circumferential and the axial residual stretch, respectively. The circumferential residual stretch can be computed as $\lambda_{\theta,\mathrm{rs}} = \rho_{\mathrm{oA}}/\rho_{\mathrm{o}}$ for the adventitia and $\lambda_{\theta,\mathrm{rs}} = \rho_{\mathrm{oMI}}/\rho_{\mathrm{o}}$ for the media-intima tube, respectively. The axial residual stretch can be computed as $\lambda_{z,\mathrm{rs}} = \xi_{\mathrm{A}}/\xi$ for the adventitia and $\lambda_{z,\mathrm{rs}} = \xi_{\mathrm{MI}}/\xi$ for the media-intima tube, respectively.

Equilibrium Equations

In the absence of body forces the equilibrium equations are

$$\mathrm{div}\,\sigma = \mathbf{0}, \tag{9.13}$$

where $\mathrm{div}(\bullet)$ denotes the spatial divergence of the spatial field $(\bullet)$. Note that in cylindrical coordinates (r, θ, z), due to geometrical and constitutive symmetry, the only non-trivial component of (9.13) is:

$$\frac{\mathrm{d}\sigma_{rr}}{\mathrm{d}r} + \frac{(\sigma_{rr} - \sigma_{\theta\theta})}{r} = 0. \tag{9.14}$$

From this equation and the boundary condition $\sigma_{rr}|_{r=r_o} = 0$ on the outer surface of the tube, the radial Cauchy stress σ_{rr} may be calculated as:

$$\sigma_{rr}(\xi) = \int_{\xi}^{r_{\mathrm{o}}} (\sigma_{rr} - \sigma_{\theta\theta}) \frac{\mathrm{d}r}{r}, \quad r_{\mathrm{i}} \leq \xi \leq r_{\mathrm{o}}. \tag{9.15}$$

The internal pressure $p_{\mathrm{i}} = -\sigma_{rr}|_{r=r_i}$ can be obtained in the from:

$$p_{\mathrm{i}} = \int_{r_{\mathrm{i}}}^{r_{\mathrm{o}}} (\sigma_{\theta\theta} - \sigma_{rr}) \frac{\mathrm{d}r}{r}. \tag{9.16}$$

In view of the additive split of the Cauchy stress tensor σ into volumetric and isochoric parts by using the decomposition $(\sigma_{\theta\theta} = p + \overline{\sigma}_{\theta\theta}$ and $\sigma_{rr} = p + \overline{\sigma}_{rr})$, where p is the hydrostatic pressure and becomes an indeterminate *Lagrange multiplier* in

the description of incompressible materials, it follows for (9.16):

$$p_i = \int_{r_i}^{r_o} (\bar{\sigma}_{\theta\theta} - \bar{\sigma}_{rr}) \frac{dr}{r}, \tag{9.17}$$

where $\bar{\sigma}_{\theta\theta}$ and $\bar{\sigma}_{rr}$ denote the isochoric parts of the normal components of the Cauchy stress in the circumferential and radial direction, respectively.

For static equilibrium, the sum of the (measured) axial force (F_z) and the pressure force ($p_i \pi r_i^2$) equals the integral of axial stress over the vessel wall cross section:

$$F_z + p_i \pi r_i^2 = 2\pi \int_{r_i}^{r_o} \sigma_{zz} r dr, \tag{9.18}$$

where σ_{zz} denotes the principal stress in the axial direction.

By using the decompositions $\sigma_{zz} = p + \bar{\sigma}_{zz}$, $\sigma_{\theta\theta} = p + \bar{\sigma}_{\theta\theta}$ and $\sigma_{rr} = p + \bar{\sigma}_{rr}$, and the use of the expression (9.16), it follows for the measured force:

$$F_z = \pi \int_{r_i}^{r_o} (2\bar{\sigma}_{zz} - \bar{\sigma}_{\theta\theta} - \bar{\sigma}_{rr}) r dr, \tag{9.19}$$

where $\bar{\sigma}_{zz}$ denotes the isochoric parts of the normal component of the Cauchy stress in the axial direction.

Strain-Energy Function

In order to model the general mechanical characteristics of the arterial tissues we use the strain-energy function Ψ (per unit volume) [76]:

$$\Psi = \frac{\mu}{2}(I_1 - 3) + \frac{k_1}{k_2}(\exp\{k_2[(1-\rho)(I_1 - 3)^2 + \rho(I_4 - 1)^2]\} - 1) \tag{9.20}$$

with:

$$I_1 = \lambda_r^2 + \lambda_\theta^2 + \lambda_z^2 \quad \text{and} \quad I_4 = \lambda_\theta^2 \cos^2\varphi + \lambda_z^2 \sin^2\varphi, \tag{9.21}$$

where $\mu > 0$ and $k_1 > 0$ are stress-like parameters, $k_2 > 0$ and $\rho \in [0,1]$ are dimensionless parameters, and I_1 and $I_4 > 1$ are invariants [133]. The parameter φ in (9.21) is the angle between the fiber reinforcement (orthotropy) and the circumferential direction in the individual 'layers', which, therefore, acts as a *geometrical parameter*. Since the structural orientation of the individual 'layers' was not investigated the parameter φ is here used as a phenomenological variable. The dimensionless parameter ρ ranges between zero and one and is a measure of the 'degree of anisotropy'. If $\rho = 0$ the second term of Eq. (9.20) reduces to an pure isotropic (rubber-like) model, similar to that proposed in [142]. If $\rho = 1$ the second term in Eq. (9.20) reduces to an pure anisotropic model proposed in [134]. Furthermore, ρ can be interpreted as a dispersion (structure) parameter, which represents the three-dimensional fiber distribution around the preferred fiber-direction in an integral sense [285]. This model is already implemented in the finite element systems ANSYS (ANSYS Inc., Canonsburg, Pennsylvania, USA) and ADINA (ADINA R&D Inc., Watertown, Massachusetts, USA).

For incompressible hyperelastic materials the three principal Cauchy stresses $\overline{\sigma}_{\mathrm{rr}}$, $\overline{\sigma}_{\theta\theta}$ and $\overline{\sigma}_{\mathrm{zz}}$ may be expressed according to [133]:

$$\sigma_{aa} = -p + \overline{\sigma}_{aa}, \qquad \overline{\sigma}_{aa} = \lambda_a \frac{\partial \Psi}{\partial \lambda_a}, \qquad a = r, \theta, z, \tag{9.22}$$

where p is an indeterminate Lagrange multiplier, and $\overline{\sigma}_{aa}$ denote the isochoric parts of the stress components σ_{aa}.

Hence, from Eq. (9.17), (9.22), the strain-energy function (9.20) and the properties (9.21) for the invariants I_1 and I_4 we get an explicit expression for the internal pressure, i.e.:

$$p_{\mathrm{i}} = 4 \int_{r_{\mathrm{i}}}^{r_{\mathrm{o}}} (\lambda_\theta^2 - \lambda_r^2) \left(\frac{\mu}{2} + k_1(1-\rho)(I_1-3) \exp\{k_2[(1-\rho)(I_1-3)^2 + \rho(I_4-1)^2]\} \right)$$

$$- (\lambda_\theta^2 \cos^2\varphi)\rho(I_4-1) \exp\{k_2[(1-\rho)(I_1-3)^2 + \rho(I_4-1)^2]\}\frac{1}{r}\mathrm{d}r. \tag{9.23}$$

In an analogous manner, the use of Eqs. (9.20)–(9.22) and (9.19) yields the measured

axial force F_z, i.e.:

$$F_z = 4\pi \int_{r_i}^{r_o} (2\lambda_z^2 - \lambda_\theta^2 - \lambda_r^2)\left(\frac{\mu}{2} + k_1(1-\rho)(I_1-3)\exp\{k_2[(1-\rho)(I_1-3)^2 + \rho(I_4-1)^2]\}\right)$$

$$- (2\lambda_z^2\cos^2\varphi - \lambda_\theta^2\cos^2\varphi)\rho(I_4-1)\exp\{k_2[(1-\rho)(I_1-3)^2 + \rho(I_4-1)^2]\}r\mathrm{d}r, \quad (9.24)$$

with $r_i = ((\rho_o\lambda_\theta)^2 - (R_o^2 - R_i^2)/(k\lambda_{z,\mathrm{res}}\lambda_z))^{0.5}$ according to (9.11) and $r_o = \rho_o\lambda_\theta$ for the intact wall, and with $r_i = ((\rho_o\lambda_{\theta,\mathrm{rs}}\lambda_\theta)^2 - (R_o^2 - R_i^2)/(k\lambda_{z,\mathrm{res}}\lambda_{z,\mathrm{rs}}\lambda_z))^{0.5}$ according to (9.12) and $r_o = \rho_o\lambda_{\theta,\mathrm{rs}}\lambda_\theta$ for the adventitia and media-intima tube, where λ_r, λ_θ, and λ_z are the principal stretches of the deformation (when there is no shear) associated with the radial, circumferential, and axial directions, respectively. Each arterial tissue sample was regarded to be incompressible [43], which requires that $\lambda_r\lambda_\theta\lambda_z = 1$, and therefore, λ_r can be expressed by:

$$\lambda_r = \frac{1}{\lambda_\theta\lambda_z}. \quad (9.25)$$

Now with (9.25), the internal pressure p_i, i.e. (9.23), and the (measured) axial force F, i.e. (9.24), can be expressed as functions of the (indirectly) measured quantities $\lambda_\theta = r_o/\rho_o$ and $\lambda_z = l/\xi$, and a set $\{\mu, k_1, k_2, \varphi, \rho\}$ of constitutive parameters, i.e.:

$$p_i = p_i(\lambda_\theta, \lambda_z, \mu, k_1, k_2, \varphi, \rho), \quad F_z = F_z(\lambda_\theta, \lambda_z, \mu, k_1, k_2, \varphi, \rho). \quad (9.26)$$

For the intact artery wall, these two functions contain six constants, which must be determined experimentally: the radial and the axial curvature κ_{R_i} and κ_{Z_i}, respectively, the inner arc length (circumference) C_i and the wall thickness H in the stress-free configuration Ω_{SF}, and furthermore, the outer radius ρ_o and the length ξ in the load-free configuration Ω_{LF}. From these six constants all other needed values can be computed: $R_i = 1/\kappa_{R_i}$, $k = 2\pi/\kappa_{R_i}C_i$, $R_o = R_i + H$, $\lambda_{z,\mathrm{res}} = 1 - H\kappa_{Z_i}/2$, $\lambda_\theta = r_o/\rho_o$ and $\lambda_z = l/\xi$, with r_o and l as measured quantities.

In summary, for the adventitia and the media-intima tube, five additional constants must be determined experimentally: The outer radii and the lengths Ω_{SF} of the adventitia in the stress-free configuration, denoted as R_{oA} and Z_A respectively, and of the media-intima tube denoted as R_{oMI} and Z_{MI} respectively, and finally

the outer radius of the unloaded media-intima tube ρ_{oMI}.

Determination of the Constitutive Parameters

The five parameters $(\mu, k_1, k_2, \varphi, \rho)$ in Eqs. (9.20), (9.21) are obtained by means of a nonlinear least-square regression (Levenberg-Marquardt algorithm [286]). We minimize the 'objective function':

$$E^2 = \sum_{j=1}^{n} \left\{ \left[w_p \left(p_{ij}^{\mathrm{mod}} - p_{ij}^{\mathrm{exp}} \right) \right]^2 + \left[w_F \left(F_{zj}^{\mathrm{mod}} - F_{zj}^{\mathrm{exp}} \right) \right]^2 \right\}, \tag{9.27}$$

where n is the number of considered data points, and w_p and w_F are weighting factors for the internal pressure and the axial force, respectively, while p_{ij}^{mod} and F_{zj}^{mod} are the internal pressure and the axial force predicted by the function Ψ for the j-th data record ('mod' stands for model), and p_{ij}^{exp} and F_{zj}^{exp} are the associated experimentally measured internal pressure and axial force ('exp' stands for experiment), respectively.

The weighting factors are determined to equate contributions (values) of the internal pressure and the axial force terms in the objective function (9.27). Therefore, the mean value of the axial forces is used as weighting factor w_p and the mean value of the internal pressures is used as weighting factor w_F. For the fitting process 18 representative data points were chosen from the final (i.e., preconditioned) loading cycle of each test data set. Only data points on the loading branches were considered. This is justified by the small hystereses between loading and unloading branches observed for all arterial tissues investigated (as can be seen in Figs. 6-11 in [80]).

Statistical Analysis

As a measure for the correlation relation between the model and the experimental internal pressure and axial force values the (linear) correlation coefficients $r(p_i)$ and

r(*F*) were calculated as:

$$r(p_i) \quad = \quad \frac{\sum_{j=1}^{n}(p_{ij}^{exp} - \overline{p_i^{exp}})(p_{ij}^{mod} - \overline{p_i^{mod}})}{\sqrt{\sum_{j=1}^{n}(p_{ij}^{exp} - \overline{p_i^{exp}})^2 \sum_{j=1}^{n}(p_{ij}^{mod} - \overline{p_i^{mod}})^2}}, \tag{9.28}$$

and

$$r(F_z) \quad = \quad \frac{\sum_{j=1}^{n}(F_{zj}^{exp} - \overline{F_z^{exp}})(F_{zj}^{mod} - \overline{F_z^{mod}})}{\sqrt{\sum_{j=1}^{n}(F_{zj}^{exp} - \overline{F_z^{exp}})^2 \sum_{j=1}^{n}(F_{zj}^{mod} - \overline{F_z^{mod}})^2}}, \tag{9.29}$$

where an overbar denotes average value. The correlation coefficients measure only the degree of linear correlation between the experimentally determined internal pressure and axial force values respectively, and those derived from the strain-energy function. However, even a total correlation ($r = 1$) might be afflicted with misfits. For example, there could be a large constant difference between the associated internal pressure or axial force values.

Therefore, a second error measure, which is based on the objective function E^2 (Eq. 9.27) was calculated to evaluate the 'goodness of fit'. This error measure for p_i and F is defined by:

$$\varepsilon_{p_i} = \frac{100}{p_{i,ref}} \sqrt{\frac{E_{p_i}^2}{n-q}}, \qquad \varepsilon_{F_z} = \frac{100}{F_{z,ref}} \sqrt{\frac{E_{F_z}^2}{n-q}}, \tag{9.30}$$

where $E_{p_i}^2$ and $E_{F_z}^2$ are the final 'objective function' values (or weighted mean squared error) of the internal pressure and axial force, respectively, n is the number of data points considered, q is the number of parameters in the strain-energy function (which in the case is five). Hence $n-q$ is the number of degrees of freedom, while $p_{i,ref}$ and $F_{z,ref}$ are the mean values of the internal pressure and axial force values, respectively. Thus, the error measures ε_{p_i} and ε_{F_z} are the percentages of the root-mean-square errors (per statistical degree of freedom) between the experimental and model determined internal pressures and axial forces respectively, normalized in regard to $p_{i,ref}$ and $F_{z,ref}$, respectively.

Table 9.1: *Constitutive parameters (μ,k_1,k_2,φ,ρ) of the SEF (Eq. 9.20) obtained from the experimental data of the intact wall, the adventitia, and media-intima composite of the CCA [80]. Furthermore, associated correlation coefficients ($r(p_i)$ and $r(F_z)$) and error measures (ε_{p_i} and ε_{F_z}) are stated.*

| Donor | Neck side | Constitutive parameters | | | | | r | | ε, % | |
		μ, kPa	k_1, kPa	k_2	$\varphi,°$	ρ	p_i	F_z	p_i	F_z
				Intact wall						
I	l	70.2	99.9	26.4	11.5	1.0	0.970	0.970	8.8	12.2
II	l	46.0	32.7	12.1	19.9	1.0	0.933	0.992	13.3	4.2
II	r	38.7	9.7	19.6	18.9	0.5	0.987	0.941	5.7	13.3
IV	l	34.2	15.5	199.2	17.1	0.8	0.964	0.922	10.6	13.3
V	l	2.2	14.2	64.5	30.3	1.0	0.973	0.955	8.1	14.4
V	r	28.2	8.0	15.1	10.5	0.6	0.983	0.965	6.5	12.5
VI	l	82.1	43.6	120.1	24.2	0.5	0.964	0.963	9.3	12.4
VI	r	54.8	2.9	20.3	31.2	1.0	0.951	0.918	10.3	14.2
VII	r	73.1	5.1	116.8	14.0	0.7	0.956	0.945	11.6	11.2
VIII	r	54.8	13.0	91.5	26.1	0.9	0.995	0.909	3.3	14.1
IX	r	4.9	68.2	71.8	20.9	0.6	0.961	0.983	9.9	8.6
Mean		44.5	28.4	68.9	20.4	0.8	0.967	0.951	8.9	11.9
SD		26.2	30.8	59.3	7.0	0.2	0.018	0.027	2.8	3.0
				Adventitia (33 kPa domain)						
II	l	0.0	875.2	146.3	41.2	0.8	0.913	0.908	15.4	15.6
II	r	70.5	61.2	32.8	15.9	0.9	0.939	0.925	12.6	13.3
V	l	95.4	8.5	328.3	38.2	1.0	0.920	0.947	13.0	11.2
V	r	60.0	1.6	41.5	23.9	0.9	0.973	0.973	9.8	15.1
VI	l	34.7	52.2	88.9	26.6	0.7	0.980	0.995	7.1	10.5
VI	r	61.6	28.7	85.8	21.8	0.6	0.989	0.973	5.9	6.2
VIII	r	95.1	238.8	45.3	42.9	0.9	0.939	0.914	13.8	26.5
Mean		59.6	180.9	109.8	30.1	0.8	0.950	0.948	11.1	12.6
SD		33.8	316.6	104.0	10.6	0.1	0.030	0.034	3.6	3.6
				Adventitia (100 kPa domain)						
II	l	129.5	506.8	76.8	38.3	0.8	0.962	0.935	9.6	12.8
II	r	217.3	40.6	11.9	19.7	0.9	0.925	0.886	15.6	16.0
V	r	0.0	110.5	43.9	24.9	0.9	0.922	0.903	13.6	15.1
VI	l	98.7	20.9	49.7	21.0	0.7	0.991	0.960	4.8	11.1
VI	r	120.6	23.5	40.8	19.5	0.7	0.950	0.924	8.4	13.4
VIII	r	184.2	39.4	39.2	19.7	0.9	0.984	0.984	7.6	11.4
Mean		138.2	178.4	48.4	25.9	0.8	0.961	0.938	11.9	16.1
SD		77.1	226.4	22.8	8.7	0.1	0.030	0.036	6.3	7.7
				Media-Intima						
II	l	134.6	10.3	18.8	8.8	0.7	0.983	0.881	6.4	14.1
IV	l	106.8	26.5	23.0	3.5	0.9	0.970	0.850	8.5	16.3
V	r	128.9	25.9	21.5	6.8	0.7	0.985	0.894	5.9	13.7
VI	r	118.9	36.1	2.8	8.5	1.0	0.999	0.879	1.9	18.0
Mean		122.3	24.7	16.5	6.9	0.8	0.984	0.876	5.7	15.5
SD		12.2	10.7	9.3	2.4	0.2	0.012	0.019	2.8	2.0

Neck side: l … left; r … right.

Table 9.2: *Constitutive parameters (μ,k_1,k_2,φ,ρ) of the SEF (Eq. 9.20) obtained from the experimental data of the intact wall, the adventitia, and media-intima composite of the ICA [80]. Furthermore, associated correlation coefficients ($r(p_i)$ and $r(F_z)$) and error measures (ε_{p_i} and ε_{F_z}) are stated.*

| Donor | Neck side | Constitutive parameters | | | | | r | | ε, % | |
		μ, kPa	k_1, kPa	k_2	$\varphi,°$	ρ	p_i	F_z	p_i	F_z
				Intact wall						
III	l	43.8	93.6	79.6	17.2	0.7	0.925	0.941	9.4	8.5
IV	l	23.7	7.5	12.2	11.6	0.8	0.919	0.905	9.9	12.3
V	r	24.6	13.4	29.9	7.3	0.6	0.951	0.952	10.9	8.9
VI	l	22.9	87.8	109.6	19.3	0.7	0.955	0.980	10.9	10.5
VI	r	3.8	1.2	42.9	19.8	0.7	0.964	0.902	9.1	13.2
VII	r	12.4	93.4	96.9	21.8	0.7	0.970	0.973	8.5	8.3
VIII	r	35.7	1.3	63.1	34.6	0.9	0.947	0.950	11.4	15.6
IX	r	31.8	39.8	80.9	21.3	0.9	0.930	0.910	11.6	13.3
X	r	25.6	20.4	68.7	26.8	0.7	0.950	0.940	10.5	11.7
XI	r	7.4	4.5	45.7	22.4	0.8	0.962	0.904	9.5	15.7
Mean		29.7	27.8	64.2	22.0	0.8	0.944	0.929	10.1	12.3
SD		24.1	36.6	32.6	9.1	0.1	0.019	0.026	1.0	3.0
				Adventitia (33 kPa domain)						
VI	r	0.0	15.9	75.5	40.7	1.0	0.926	0.897	13.1	17.8
VII	r	0.3	51.5	38.9	20.4	0.7	0.972	0.905	8.2	13.1
VIII	r	11.3	475.3	63.2	41.6	0.9	0.936	0.930	13.8	15.7
IX	l	3.0	43.2	44.9	29.8	0.8	0.950	0.920	13.4	17.6
X	r	5.7	17.0	76.7	41.3	1.0	0.934	0.912	14.6	18.9
XI	r	149.5	69.9	304.6	16.8	1.0	0.956	0.909	12.3	15.7
Mean		28.3	112.1	100.6	31.8	0.9	0.946	0.912	12.6	16.5
SD		59.5	179.1	101.1	11.2	0.1	0.017	0.012	2.3	2.1
				Adventitia (100 kPa domain)						
VI	r	0.0	16.4	55.6	22.4	0.9	0.951	0.890	11.0	19.6
VII	r	0.0	48.2	35.5	29.8	0.7	0.990	0.914	4.9	15.0
VIII	r	0.0	526.6	346.5	30.5	0.9	0.913	0.873	14.9	17.8
X	r	0.0	29.2	48.3	45.4	0.9	0.928	0.908	12.3	15.6
XI	r	0.7	659.5	4.0	0.0	0.8	0.926	0.895	10.4	14.8
Mean		0.1	256.0	98.0	25.6	0.8	0.942	0.896	10.7	16.6
SD		0.3	311.5	140.3	16.6	0.1	0.030	0.016	3.7	2.1
				Media-Intima						
IX	r	0.7	17.0	7.6	12.4	0.6	0.999	0.893	1.5	14.8
X	r	36.2	14.2	26.6	10.2	0.8	0.950	0.870	6.2	17.9
XI	r	15.8	32.7	17.8	6.7	0.9	0.932	0.895	8.5	13.7
Mean		17.6	21.3	17.3	9.8	0.8	0.960	0.886	5.4	15.5
SD		17.8	10.3	9.5	2.9	0.2	0.035	0.014	3.6	2.2

Neck side: l … left; r … right.

9.3 Results

The three-dimensional SEF used (Eq. 9.20) [76] provides a suitable model for the extension-inflation experiments on aged human carotid arteries and their associated 'layers' (adventitia and media-intima composite) [80]. The SEF is suitable to describe the experiment at different pressure domains and axial stretches: 20 kPa domain (for the media-intima composite), 33.3 kPa domain (for the intact wall and the adventitia), and 100 kPa domain (for the adventitia); and axial stretches ranging from 1.0 to 1.3, respectively.

Constitutive parameters of the intact arteries, and their associated adventitia tubes and media-intima composite tubes of the CCA and ICA are summarized in Table 9.1 and 9.2, respectively. For the determination of one set of constitutive parameters (μ,k_1,k_2,φ,ρ) experimental data corresponding to axial stretches ranging from at least λ_z = 1.0-1.15 in increments of 0.05 were considered in the fitting process. Figures 9.4-9.9 show representative circumferential stretch-pressure and axial stretch-pressure plots, where experimental data are compared with numerical results obtained from the SEF (Eq. 9.20). All of the strain-energy functions determined are convex, which is a fundamental prerequisite for the use in finite-element codes [71]. In average the anisotropic parameter ρ ranges only from 0.8-0.9 and the phenomenological determined geometrical parameter φ, the fiberangle, is always smaller than $45°$, which reveals strong anisotropy with higher stiffness in the circumferential direction. In Table 9.1 and 9.2 correlation coefficients ($r(p_i)$ and $r(F_z)$) and the error measures (ε_{p_i} and ε_{F_z}) are given.

To compare the mechanical behavior of the different utilized tubes (W, A, MI), the circumferential $\sigma_{\theta\theta}$ and axial σ_{zz} stresses are plotted in Fig. 9.10 and 9.11 for three different axial stretches λ_z=1.05, 1.1, 1.15 against the circumferential stretch λ_θ. We assume an axial *in vivo* stretch of about $\lambda_{z,iv}$=1.1 of the human CCA and ICA, since $\lambda_{z,iv}$ was determined to 1.07 of an 73-year-old male ICA [287]. Since the plots of the ICA are very similar to those of the CCA, we do not show the ICA plots. The plots of the CCA and the ICA show increasing stiffness with increasing axial stretch and considerable differences in the mechanical response between the tubes. In particular, in the circumferential direction up to a certain stress the media-intima is stiffer than the intact wall and thereafter the intact wall becomes
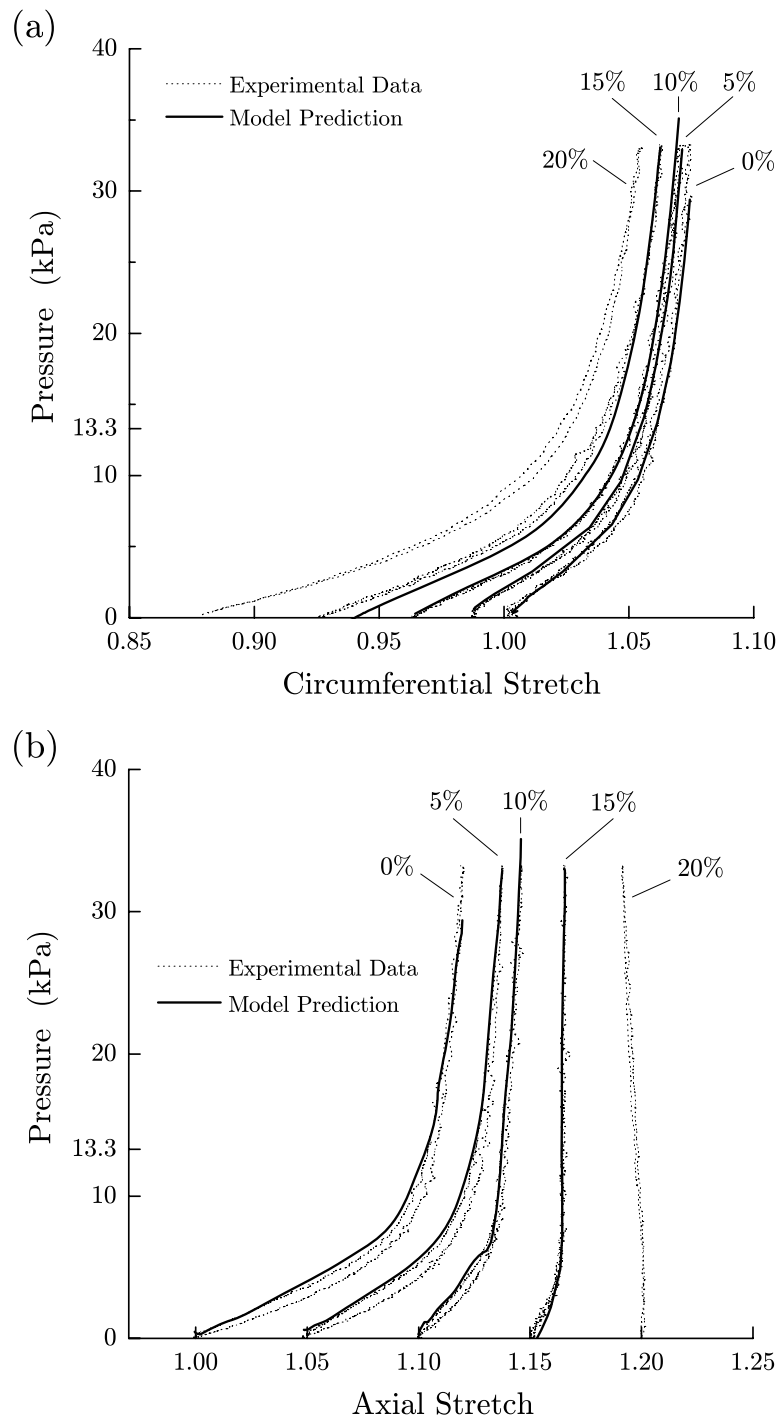
(a)

(b)

Figure 9.4: Representative pressure-circumferential stretch (a) and pressure-axial stretch plot (b) of the intact wall of the CCA obtained from donor *VIII*. Experimental inflation-deflation data (dotted lines) at different axial stretches (ranging from 0-20%) are compared with calculated data predicted by the SEF (9.20) (solid lines).
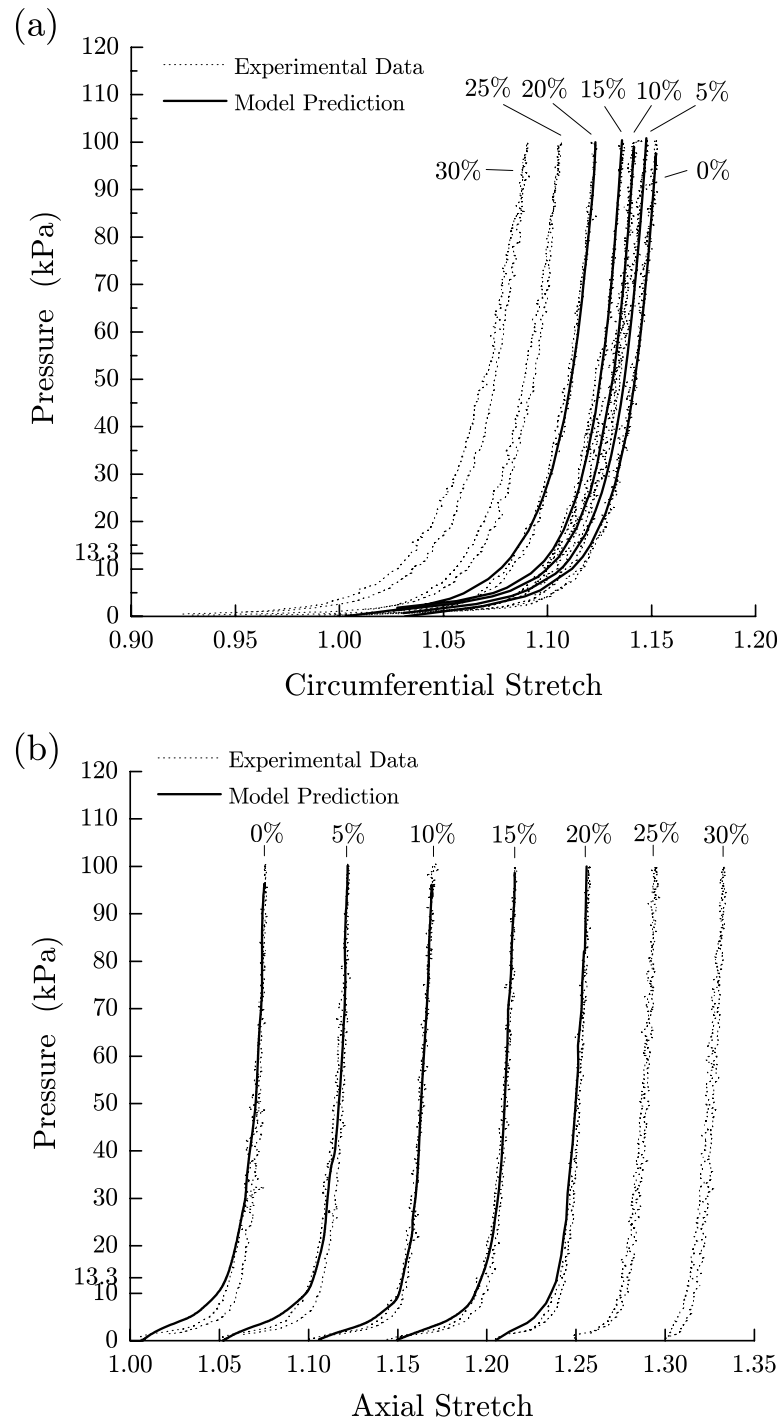
Figure 9.5: Representative pressure-circumferential stretch (a) and pressure-axial stretch plot (b) of the adventitia of the CCA obtained from donor *VIII*. Experimental inflation-deflation data (dotted lines) at different axial stretches (ranging from 0-30%) are compared with calculated data predicted by the SEF (9.20) (solid lines).

Figure 9.6: Representative pressure-circumferential stretch (a) and pressure-axial stretch plot (b) of the media-intima of the CCA obtained from donor *VIr*. Experimental inflation-deflation data (dotted lines) at different axial stretches (ranging from 0-15%) are compared with calculated data predicted by the SEF (9.20) (solid lines).
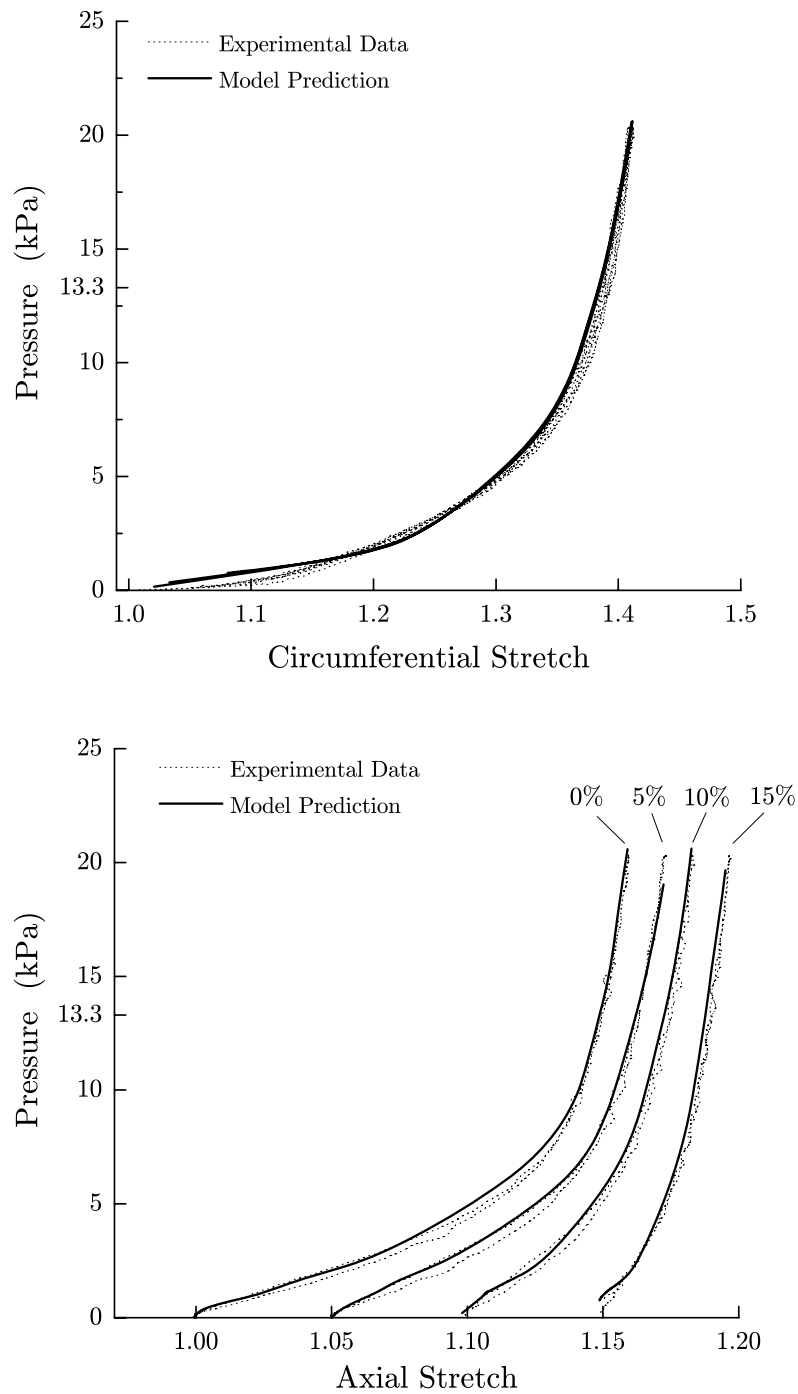
stiffer. Similar behavior was observed for the tubes in the axial direction, but with more pronounced dependency on the axial stretch (see Fig. 9.11).

9.4 Discussion

In this study, the constitutive parameters for a three-dimensional model of the intact wall, and the adventitia and media-intima 'layers' of the CCA and ICA were determined on the basis of (biaxial) extension-inflation tests (see Figs. 4-9 in [80] and Figs. 9.4-9.9). It was demonstrated that the constitutive parameters can be determined with consideration of residual stresses and stretches in the kinematic formulations. The provided constitutive parameters already include the significant (and important) residual stresses and stretches observed in load-free arterial tubes [80, 134]. The 3D model involves only a small number of constitutive parameters, so that a Levenberg-Marquardt algorithm avoids problems of non-uniqueness associated with their sensitivity to small changes in the data [23, 135].

Comparison with Previous Studies

Previous mechanical *in vitro* studies of human carotid arteries were not based on experimental data of individual layers [259, 265, 288], moreover, there is not a single mechanical tube study on the ICA intact wall or associate layers. This is the first study which provide constitutive parameters of the intact wall, and the associated 'layers' adventitia and media-intima of the human carotid arteries (CCA and ICA) in 3D model based on comprehensive experimental data [80].

Mechanical Behavior and Model Representation

The mechanical behavior and associated model representations of the investigated layers (W,A,MI) are shown in Figs. 9.4-9.9. Mechanical features of all investigated 'layers' are strong nonlinearity, pseudo-elastic behavior, and small hysteresis. At high axial stretches only the intact walls showed the inversion feature, where the tube axially contracts with increasing internal pressure. Adventitias are very compliant at low pressures but change into stiff tubes at high pressures. The mechanics of the media-intima tubes seem to be almost independent of the applied axial stretches.

Figure 9.7: Representative pressure-circumferential stretch (a) and pressure-axial stretch plot (b) of the intact wall of the ICA obtained from donor *VII*. Experimental inflation-deflation data (dotted lines) at different axial stretches (ranging from 0-15%) are compared with calculated data predicted by the SEF (9.20) (solid lines).

(a)

(b)
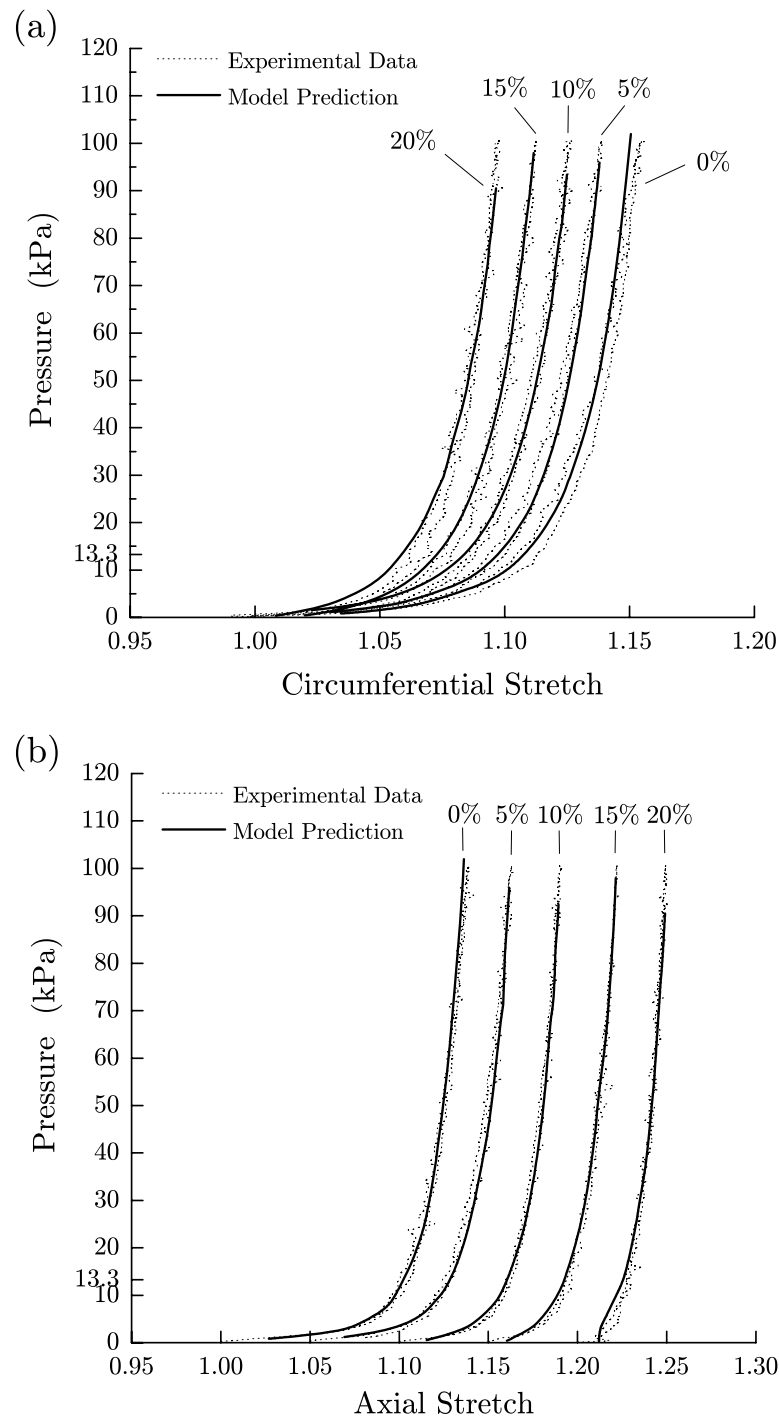
Figure 9.8: Representative pressure-circumferential stretch (a) and pressure-axial stretch plot (b) of the adventitia of the ICA obtained from donor *VII.* Experimental inflation-deflation data (dotted lines) at different axial stretches (ranging from 0-20%) are compared with calculated data predicted by the SEF (9.20) (solid lines).
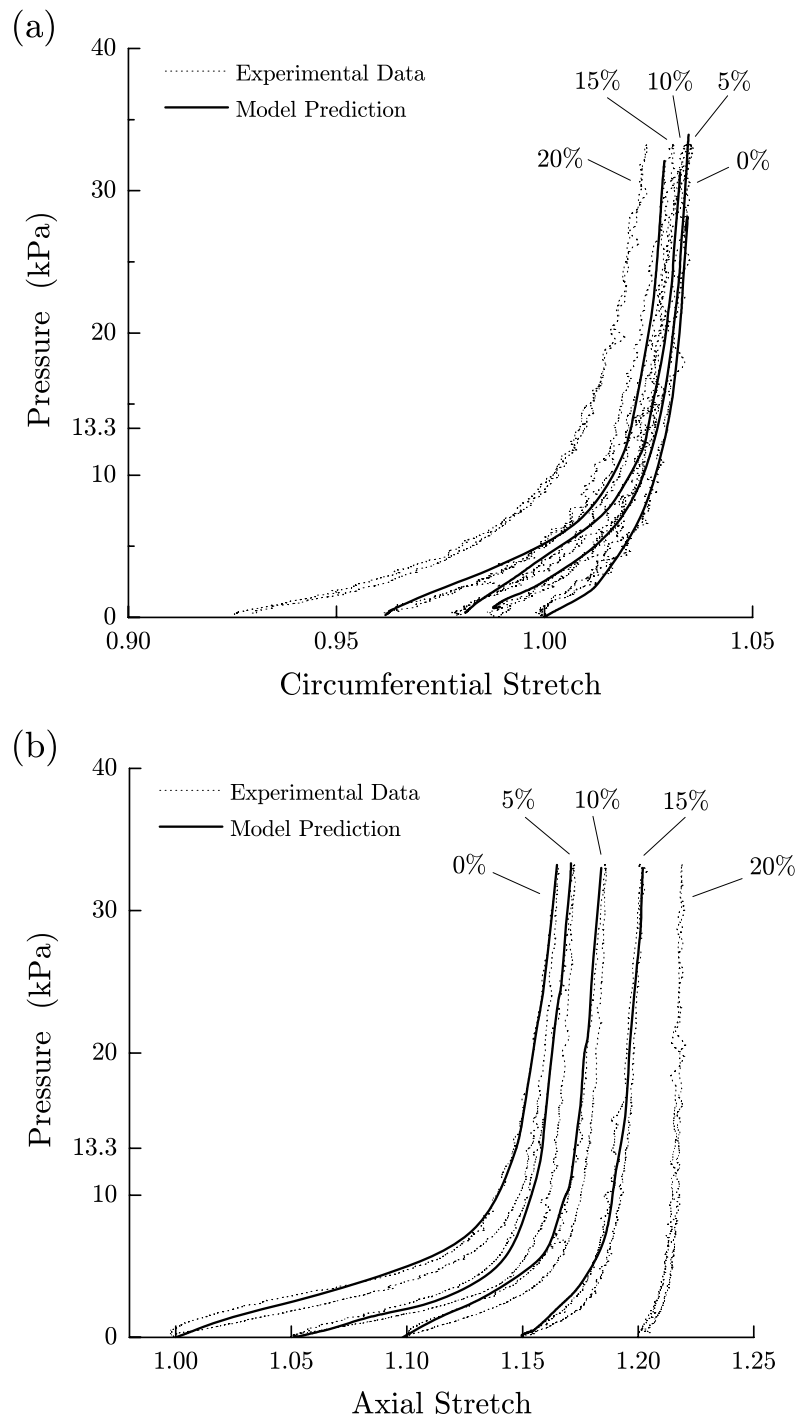
Figure 9.9: Representative pressure-circumferential stretch (a) and pressure-axial stretch plot (b) of the media-intima of the ICA obtained from donor *IX r.* Experimental inflation-deflation data (dotted lines) at different axial stretches (ranging from 0-15%) are compared with calculated data predicted by the SEF (9.20) (solid lines).
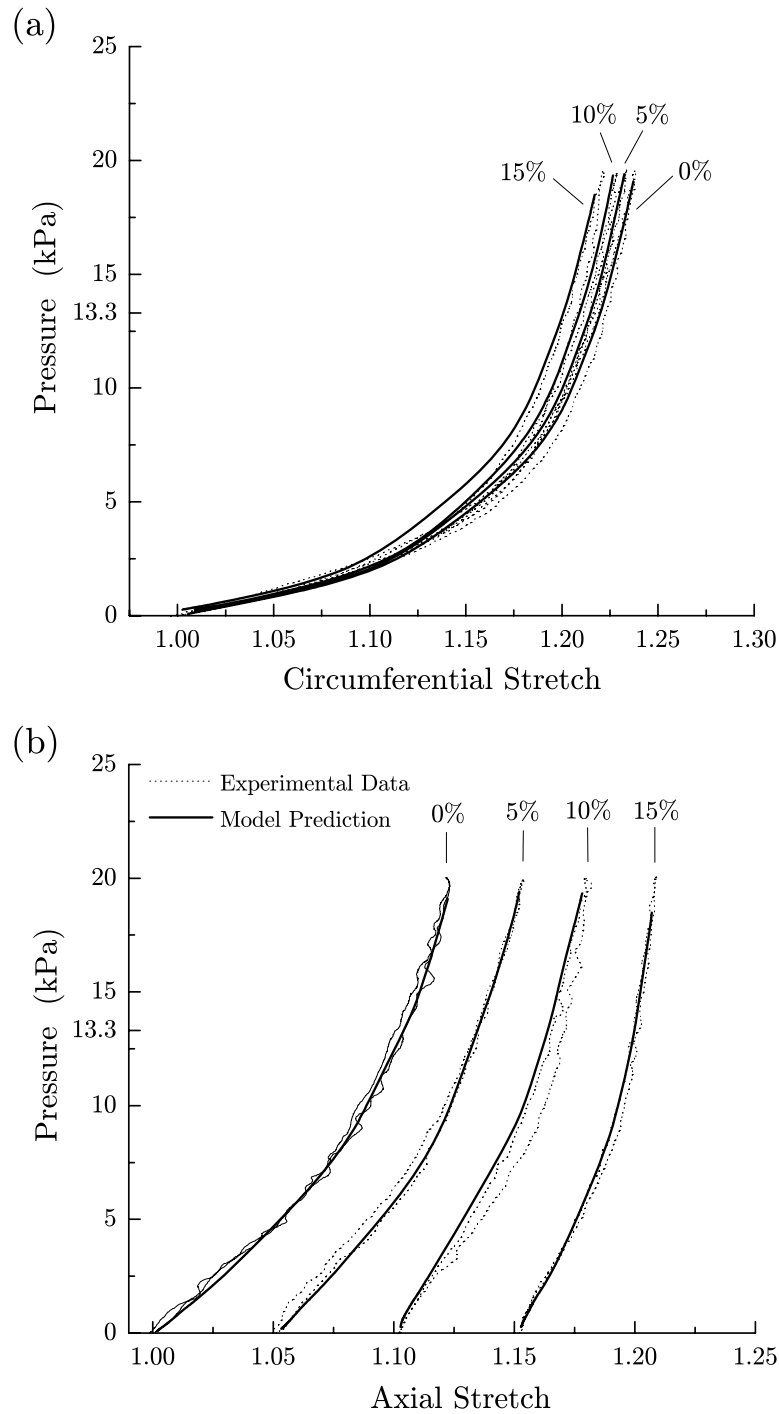
Interestingly, for every specimen of every layer the phenomenological determined fiber angle φ was smaller than $45°$, the mean values even smaller than $32°$, which indicates more stiffness in the circumferential direction due to collagen fibers orientation mainly in the circumferential direction. Smallest fiber angles were observed for media-intima of the CCA and ICA ($\overline{\varphi} < 10°$), which is consistent with other findings for the medial collagen organization in human arteries [166, 168]. The parameter k_2 (is a quantity for the average stiffness in the high loading domain) and the fiber angle φ of the CCA adventitia in the 100 kPa domain were always smaller than those of the adventitia in the 33 kPa domain (see Table 9.1). This indicates that high-pressure loading might have caused material softening of the CCA adventitias. This phenomenon could be explained by successive recruitment of collagenous fibers in the outer adventitial layers, which are initially less organized than those in the inner layers [71]. This phenomenon was not observed for the ICA. For all 'layers' the mean value of the dimensionless anisotropy parameter ρ was about 0.8 with a small standard deviation SD of 0.2, which indicate highly anisotropic materials. Both the correlation coefficients close to 1, as well as the small 'error measure' values in Tab. 9.1 and 9.2 indicate good correlation between the model and the experimental data for all arterial 'layers' (Figs. 9.4-9.9).

By taking the mean values of the five constitutive parameters for each 'layer', we obtain a kind of 'average model', which reflects the mean of all mechanical data obtained from the human CCA and ICA specimens. Although the variances among individual specimens are large, the mechanical characteristics become more clear, and this allows a comparative study of the mechanics of the different investigated 'layers'. The mean model response of the individual layers shown in Figs. 9.10 and 9.11 show that the adventitia stiffens most rapidly, whereas the slope of the stress-stretch relation is larger for the media-intima than the intact wall up to a certain stress (stretch), and thereafter the intact wall becomes stiffer than the media-intima.

The influence of the axial stretch on the stress-stretch relation for the CCA can be seen in Figs. 9.10 and 9.11. The stress-stretch curves shift significantly leftward and become stiffer when axial stretch increases. This shift was more pronounced in the σ_z-λ_θ plot (Fig. 9.11) than in the σ_θ-λ_θ plot (Figs. 9.10). Similar behavior was observed for the ICA 'layers'.

Figure 9.10: Circumferential stress-circumferential stretch model response representing the mean of all mechanical data of the intact wall, the adventitia (33kPa domain), and the media-intima composite of the CCA. Mean constitutive parameters are from Table 9.1. Data correspond to axial stretch ratios λ_z=1.05, 1.1, 1.15.
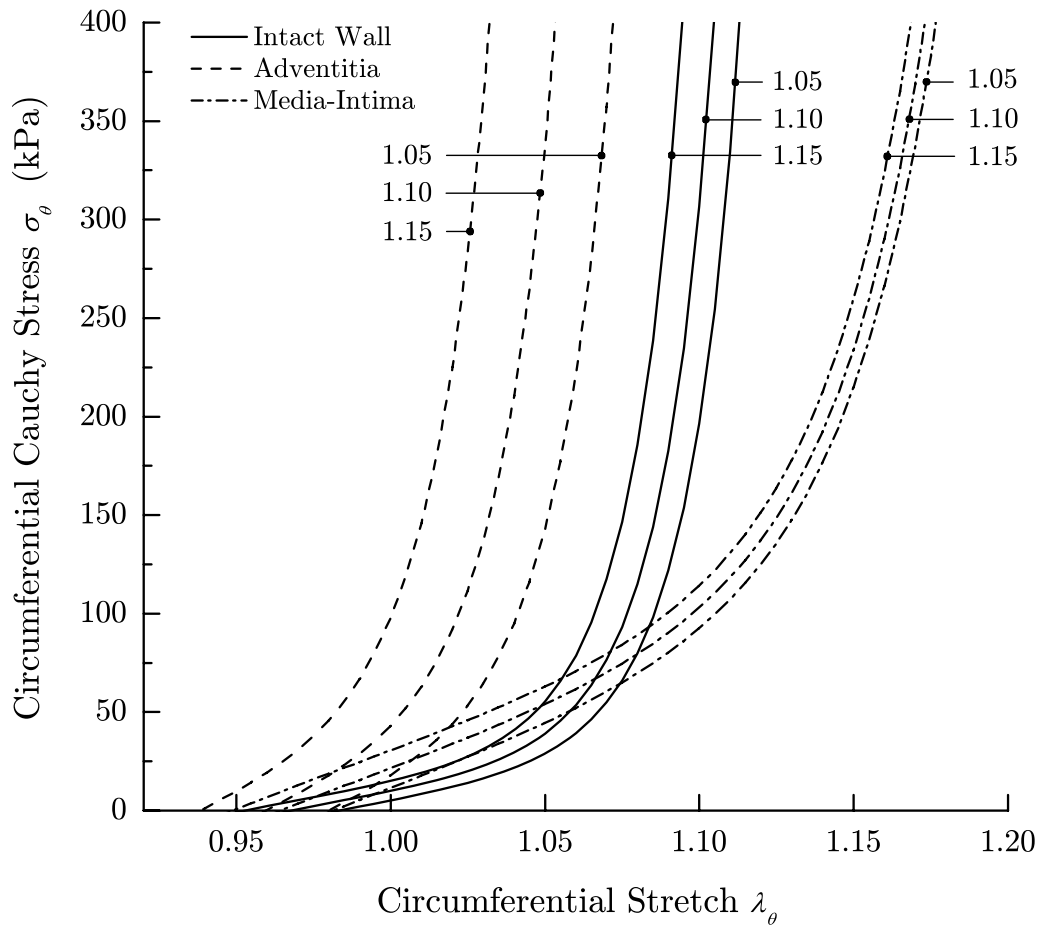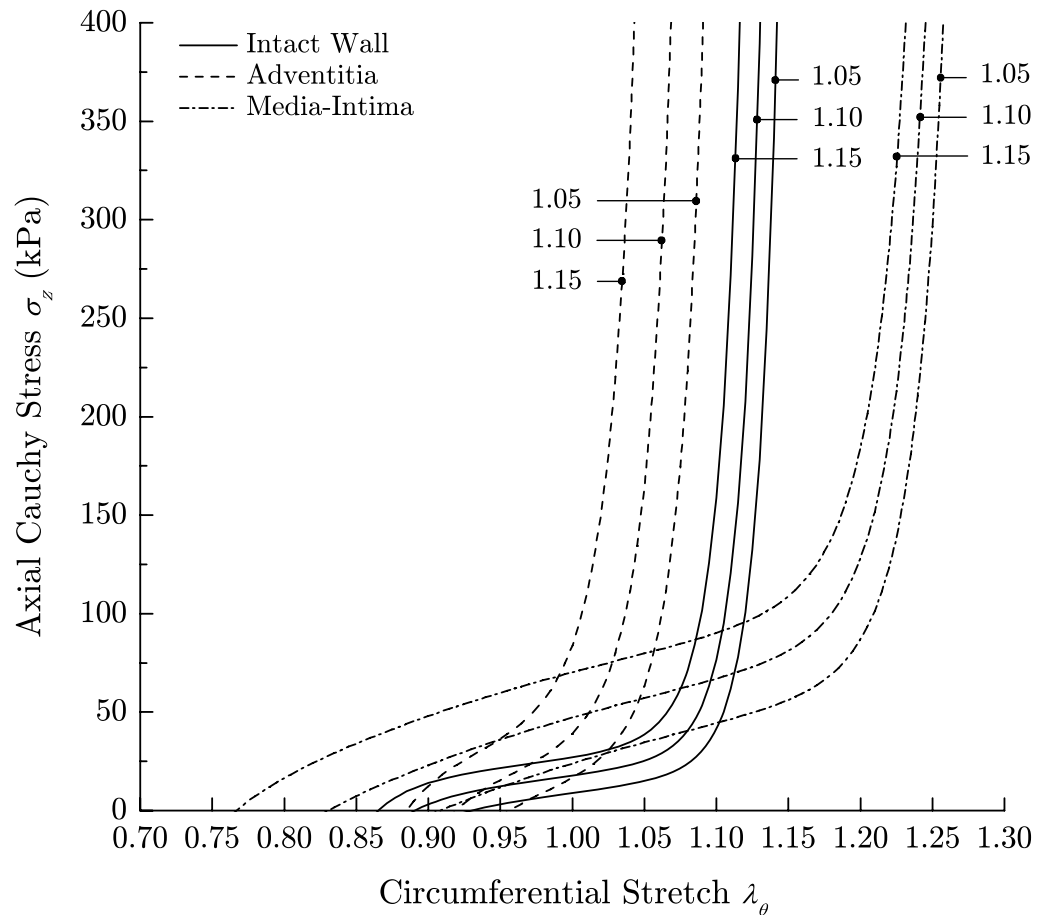
Figure 9.11: Axial stress-circumferential stretch model response representing the mean of all mechanical data of the intact wall, the adventitia (33kPa domain), and the media-intima composite of the CCA. Mean constitutive parameters are from Table 9.1. Data correspond to axial stretch ratios λ_z=1.05, 1.1, 1.15.

Parameter Estimation

The 'objective functions' (and error functions) were minimized to determine the constitutive parameters. In this study, the internal pressure and external (measured) axial force were used as the minimized objective functions. In isometric tests, where the length of tubes was held constant, at higher pressures we observed buckling of the intact wall and the media-intima tube, and therefore, distorted axial stretch measurements. As a consequence we let the machine control the external axial force to be approximately constant. Hence, the goodness of fit was generally better for the internal pressure than for the external axial force (see Table 9.1 and 9.2).

Convexity of the Strain Energy Function

The values of the constitutive parameters for the SEF expressed in Eqs. (9.20) and (9.21) must be such that the strain energy is convex, i.e. the material must be stable under loading [134]. In order to validate this demand we plot for every specimen several contours of the strain-energy against the circumferential and axial stretches. All SEF contours of all specimens were determined to be convex.

Limitations

The assumption of incompressibility may lead to an underestimation of stresses because a stress-induced fluid extrusion, in particular the looser outer adventitial parts would be associated with smaller cross sections and thus higher stresses. However, if there is a fluid exchange during cyclic loading, it must occur very fast because the observed hysteresis are small (see Figs. 9.4-9.9).

Only a relatively small number of samples were investigated, so that a meaningful correlation between constitutive parameters and different 'layers' could not be quantified.

Since the collagen fiber orientation and associated distribution in the tissues were not determined experimentally, we handled φ and ρ as fitting parameters, and therefore, as phenomenological determined parameters. In future works experimentally determined collagen fiber orientations and associated distributions will lead to more unique and reliable constitutive parameters, and a better description of biological soft tissues.

The constitutive parameters and associate SEF stated in this study are intended to serve as a basis for finite element simulations of clinical intervention methods and related problems, and thus to help in identifying possible improvements or solutions.

REFERENCES

[1] S. Petersen, V. Peto, M. Rayner, J. Leal, R. Luengo-Fernandez, and A. Gray. *European Cardiovascular Disease Statistics, 2005 Edition.* British Heart Foundation Health Promotion Research Group and Department of Public Health, University of Oxford, 2005.

[2] W. Rosamond, K. Flegal, K. Furie, A. Go, K. Greenlund, N. Haase, S. M. Hailpern, M. Ho, V. Howard, B. Kissela, S. Kittner, D. Lloyd-Jones, M. McDermott, J. Meigs, C. Moy, G. Nichol, C. O'Donnell, V. Roger, P. Sorlie, J. Steinberger, T. Thom, M. Wilson, Y. Hong, American Heart Association Statistics Committee, and Stroke Statistics Subcommittee. *Heart Disease and Stroke Statistics – 2008 Update*, volume 117. A Report From the American Heart Association Statistics Committee and Stroke Statistics Subcommittee, 2008.

[3] J. C. Palmaz, R. R. Sibbitt, S. R. Reuter, F. O. Tio, and W. J. Rice. Expandable intraluminal graft: a preliminar study. Work in progress. *Radiology*, 156:73–77, 1985.

[4] J. C. Palmaz, R. R Sibbit, S. R. Reuter, F. Garcia, and F. O. Tio. Expandable intrahepatic portacaval shunt stents: early experience in the dog. *Am. J. Roentgenology*, 145:821–825, 1985.

[5] J. C. Palmaz, R. R. Sibbitt, F. O. Tio, S. R. Reuter, J. E. Peters, and F. Garcia. Expandable intraluminal vascular graft: a feasibility study. *Surgery*, 99:199–205, 1986.

[6] J. C. Palmaz, S. A. Windeler, F. Garcia, F. O. Tio, R. R Sibbitt, and S. R. Reuter. Atherosclerotic rabbit aortas: expandable intraluminal grafting. *Radiology*, 160:173–176, 1986.

[7] J. C. Palmaz, D. T. Kopp, H. Hayashi, R. A. Schatz, G. Hunter, F. O. Tio, O. Garcia, R. Alvarado, C. Rees, and S. C. Thomas. Normal and stenotic renal

arteries: experimental balloon-expandable intraluminal stenting. *Radiology*, 164:705–708, 1987.

[8] B. L. van der Hoeven, N. M. Pires, H. M. Warda, P. V. Oemrawsingh, B. J. van Vlijmen, P. H. Quax, M. J. Schalij, E. E. van der Wall, and J. W. Jukema. Drug-eluting stents: results, promises and problems. *Int. J. Cardiol.*, 99:9–17, 2005.

[9] J. A. G. Rhodin. Architecture of the vessel wall. In R. M. Berne, editor, *Handbook of Physiology, Section 2, Volume 2*. Am Physiol Soc, Bethesda, 1979.

[10] J. Hulthe and B. Fagerberg. Circulating oxidized LDL is associated with sub-clinical atherosclerosis development and inflammatory cytokines (air study). *Arterioscler. Thromb. Vasc. Biol.*, 22:1162–1167, 2002.

[11] H. C. Stary, B. Chandler, J. R. Guyton, W. Insull, M. E. Rosenfeld, S. A. Schaffer, C. J. Schwartz, W. D. Wagner, and R. W. Wissler. A definition of initial, fatty streak, and intermediate lesions of atherosclerosis. A report from the committee on vascular lesions of the council on arteriosclerosis, american heart association. *Arterioscler. Thromb.*, 14:840–856, 1994.

[12] H. C. Stary, A. B. Chandler, R. E. Dinsmore, V. Fuster, S. Glagov, W. Insull Jr., M. E. Rosenfeld, C. J. Schwartz, W. D. Wagner, and R. W. Wissler. A definition of advanced types of atherosclerotic lesions and a histological classification of atherosclerosis. A report from the Committee on Vascular Lesions of the Council on Arteriosclerosis, American Heart Association. *Circulation*, 92:1355–1374, 1995.

[13] A. C. Newby and A. B. Zaltsman. Fibrous cap formation or destruction – the critical importance of vascular smooth muscle cell proliferation, migration and matrix formation. *Cardiovasc. Res.*, 41:345–360, 1999.

[14] P. Libby. Current concepts of the pathogenesis of the acute coronary syndromes. *Circulation*, 104:365–372, 2001.

[15] M. J. Davies. Going from immutable to mutable atherosclerotic plaques. *Am. J. Cardiol.*, 88 (Supl):2F–9F, 2001.

[16] E. J. Marey. Pressione et vitesse du sang. *Physiologique Experimentale*, 1876.

[17] C. S. Roy. The elastic properties of the arterial wall. *J. Physiol.*, 3:125–159, 1880–82.

[18] D. H. Bergel. *The visco-elastic properties of the arterial wall.* PhD thesis, University of London, 1960.

[19] Y. C. Fung. On the foundations of biomechanics. *J. Appl. Mech.*, 50:1003–1009, 1983.

[20] R. N. Vaishnav and J. Vossoughi. Estimation of residual strains in aortic segments. In C. W. Hall, editor, *Biomedical Engineering II: Recent Developments*, pages 330–333. Pergamon Press, New York, 1983.

[21] C. J. Chuong and Y. C. Fung. On residual stress in arteries. *J. Biomech. Eng.*, 108:189–192, 1986.

[22] K. Takamizawa and K. Hayashi. Strain energy density function and uniform strain hypothesis for arterial mechanics. *J. Biomech.*, 20:7–17, 1987.

[23] Y. C. Fung. *Biomechanics. Mechanical Properties of Living Tissues.* Springer-Verlag, New York, 2nd edition, 1993.

[24] R. Skalak, G. Dasgupta, M. Moss, E. Otten, P. Dullemeijer, and H. Vilmann. Analytical description of growth. *J. Theor. Biol.*, 94:555–577, 1982.

[25] R. Skalak, S. Zargaryan, R. K. Jain, P. A. Netti, and A. Hoger. Compatibility and the genesis of residual stress by volumetric growth. *J. Math. Biol.*, 34:889–914, 1996.

[26] A. Sani, C. Berry, and S. Greenwald. Effect of age and sex on residual stress in the aorta. *J. Vasc. Res.*, 32:398–405, 1995.

[27] Y. C. Fung and S. Q. Liu. Strain distribution in small blood vessels with zero-stress state taken into consideration. *Am. J. Physiol.*, pages H544–H552, 1992.

[28] S. Q. Liu and Y. C. Fung. Zero-stress states of arteries. *J. Biomech. Eng.*, 110:82–84, 1988.

[29] H. C. Han and Y. C. Fung. Species dependence of the zero-stress state of aorta: Pig versus rat. *J. Biomech. Eng.*, 113:446–451, 1991.

[30] S. Q. Liu and Y. C. Fung. Influence of stz-induced diabetes on zero-stress states of rat pulmonary and systemic arteries. *Diabetes*, 41:136–146, 1992.

[31] H. C. Han and Y. C. Fung. Longitudinal strain of canine and porcine aortas. *J. Biomech. Eng.*, 28:637–641, 1995.

[32] J. Vossoughi, Z. Hedjazi, and F. S. Borris II. Intimal residual stress and strain in large arteries. In N. A. Langrana, M. H. Friedman, and E. S. Grood, editors, *Proceedings of the ASME Summer Bioengineering Conference*, pages 434–437, New York, 1993. ASME BED-Vol. 24.

[33] S. E. Greenwald, J. E. Moore, Jr., A. Rachev, T. P. C. Kane, and J.-J. Meister. Experimental investigation of the distribution of residual strains in the artery wall. *J. Biomech. Eng.*, 119:438–444, 1997.

[34] G. A. Holzapfel, G. Sommer, M. Auer, P. Regitnig, and R. W. Ogden. Layer-specific 3D residual deformations of human aortas with non-atherosclerotic intimal thickening. *Ann. Biomed. Eng.*, 35:530–545, 2007.

[35] N. Stergiopulos, A. Pannatier, A. Rachev, S. E. Greenwald, and J.-J. Meister. Assessment of mechanical homogeneity of the arterial wall by an artery-inversion test. *Cardiovasc. Engrg.*, 1:31–36, 2001.

[36] T. Matsumoto, T. Goto, and M. Sato. Microscopic residual stress caused by the mechanical heterogeneity in the lamellar unit of the porcine thoracic aortic wall. *JSME Intern. J. A*, 47:341–348, 2004.

[37] D. J. Patel and D. L. Fry. The elastic symmetry of arterial segments in dogs. *Circ. Res.*, 24:1–8, 1969.

[38] W.-W. von Maltzahn, R. G. Warriyar, and W. F. Keitzer. Experimental measurements of elastic properties of media and adventitia of bovine carotid arteries. *J. Biomech.*, 17:839–847, 1984.

[39] C. J. Chuong and Y. C. Fung. Three-dimensional stress distribution in arteries. *J. Biomech. Eng.*, 105:268–274, 1983.

[40] G. A. Holzapfel and H. W. Weizsäcker. Biomechanical behavior of the arterial wall and its numerical characterization. *Comp. Biol. Med.*, 28:377–392, 1998.

[41] R. W. Lawton. The thermoelastic behavior of isolated aortic strips of the dog. *Circ. Res.*, 2:344–353, 1954.

[42] P. B. Dobrin and A. A. Rovick. Influence of vascular smooth muscle on contractile mechanics and elasticity of arteries. *Am. J. Physiol.*, 217:1644–1651, 1969.

[43] T. E. Carew, R. N. Vaishnav, and D. J. Patel. Compressibility of the arterial wall. *Circ. Res.*, 23:61–68, 1968.

[44] R. H. Cox. Three-dimensional mechanics of arterial segments *in vitro*: methods. *J. Appl. Phys.*, 36:381–384, 1974.

[45] R. H. Cox. Arterial wall mechanics and composition and the effects of smooth muscle activation. *Am. J. Physiol.*, 229:807–812, 1975.

[46] R. H. Cox. Effects of norepinephrine on mechanics of arteries *in vitro*. *Am. J. Physiol.*, 23:420–425, 1976.

[47] R. H. Cox. Mechanics of canine iliac artery smooth muscle *in vitro*. *Am. J. Physiol.*, 230:462–470, 1976.

[48] R. H. Cox. Passive mechanics and connective tissue composition of canine arteries. *Am. J. Physiol.*, 234:H533–H541, 1978.

[49] R. H. Cox. Regional variation of series elasticity in canine arterial smooth muscles. *Am. J. Physiol.*, 234:H542–H551, 1978.

[50] R. H. Cox. Comparison of carotid artery mechanics in the rat, rabbit and dog. *Am. J. Physiol.*, 234:H280–H288, 1978.

[51] R. H. Cox. Differences in mechanics of arterial smooth muscle from hindlimb arteries. *Am. J. Physiol.*, 235:H649–H656, 1978.

[52] R. H. Cox and D. K. Detweiler. Arterial wall properties and dietary atherosclerosis in the racing greyhound. *Am. J. Physiol.*, 236:H790–H797, 1979.

[53] R. H. Cox. Changes in arterial wall properties during development and maintenance of renal hypertension. *Am. J. Physiol.*, 242:H477–H484, 1982.

[54] R. H. Cox. Comparison of arterial wall mechanics using ring and cylindrical segments. *Am. J. Phys.*, 244:H298–H303, 1983.

[55] P. B. Dobrin and J. M. Doyle. Vascular smooth muscle and the anisotropy of dog carotid artery. *Circ. Res.*, 27:105–119, 1970.

[56] P. B. Dobrin. Isometric and isobaric contraction of carotid arterial smooth muscle. *Am. J. Physiol.*, 225:659–663, 1973.

[57] P. B. Dobrin. Mechanical properties of arteries. *Physiol. Rev.*, 58:397–460, 1978.

[58] P. B. Dobrin. Vascular mechanics. In J. T. Shepherd and F. M. Abboud, editors, *Handbook of Physiology. Section 2: The Cardiovascular System*, volume III, pages 65–102. American Physiological Society, Bethesda, 1983.

[59] P. B. Dobrin and T. R. Canfield. Elastase, collagenase, and the biaxial elastic properties of dog carotid artery. *Am. J. Physiol.*, 247:H124–H131, 1984.

[60] P. B. Dobrin. Biaxial anisotropy of dog carotid arteriy: estimation of circumferential elastic modulus. *J. Biomech.*, 19:351–358, 1986.

[61] P. Van Loon, W. Klip, and E. L. Bradley. Length-force and volume-pressure relationships of arteries. *Biorheology*, 14:181–201, 1977.

[62] H. W. Weizsäcker, H. Lambert, and K. Pascale. Analysis of the passive mechanical properties of rat carotid arteries. *J. Biomech.*, 16:703–715, 1983.

[63] J. M. Clark and S. Glagov. Structural integration of the arterial wall. *Laboratory Investigation*, 40:587–602, 1979.

[64] J. M. Clark and S. Glagov. Transmural organization of the arterial media: The lamellar unit revisited. *Arteriosclerosis*, 5:19–34, 1985.

[65] W.-W. von Maltzahn, D. Besdo, and W. Wiemer. Elastic properties of arteries: A nonlinear two-layer cylindrical model. *J. Biomech.*, 14:389–397, 1981.

[66] R. P. Vito and H. Demiray. A two layered model for arterial wall mechanics. In *Proceedings of the 35th Annual conference on Engineering in Medicine and Biology (ACEMB)*, Pennsylvania, PA. September 22-24, 1982.

[67] H. Demiray and R. P. Vito. A layered cylindrical shell model for an aorta. *Int. J. Eng. Sci.*, 29:47–54, 1991.

[68] C. A. J. Schulze-Bauer. Biomechanische Eigenschaften humaner Ilikalarterien. Diplomarbeit, Karl-Franzens-Universiät Graz, Juli 2000.

[69] C. A. J. Schulze-Bauer, P. Regitnig, and G. A. Holzapfel. Mechanics of the human femoral adventitia including high-pressure response. *Am. J. Physiol. Heart Circ. Physiol.*, 282:H2427–H2440, 2002.

[70] C. A. J. Schulze-Bauer, H. Amenitsch, and G. A. Holzapfel. SAXS investigation of layer-specific collagen structures in human aortas during tensile testing. In *European Materials Research Society Spring Meeting, E-MRS 2002 SPRING MEETING - Synchrotron Radiation and Materials Science (Symposium I)*, Strasbourg, France, 2002.

[71] C. A. J. Schulze-Bauer, P. Regitnig, and G. A. Holzapfel. Mechanics of the human femoral adventitia including high-pressure response. *Am. J. Physiol. Heart Circ. Physiol.*, 282:H2427–H2440, 2002.

[72] G. Sommer. Layer-specific mechanical response of human coronary arteries. Master's thesis, Graz University of Technology, 2003. In German.

[73] C. A. J. Schulze-Bauer, C. Mörth, and G. A. Holzapfel. Passive biaxial mechanical response of aged human iliac arteries. *J. Biomech. Eng.*, 125:395–406, 2003.

[74] F. Schmid. Layer-specific investigation of the mechanical behavior of the human femoral artery. Master's thesis, Graz University of Technology, 2003. In German.

[75] G. A. Holzapfel, G. Sommer, and P. Regitnig. Anisotropic mechanical properties of tissue components in human atherosclerotic plaques. *J. Biomech. Eng.*, 126:657–665, 2004.

[76] G. A. Holzapfel, G. Sommer, C. T. Gasser, and P. Regitnig. Determination of the layer-specific mechanical properties of human coronary arteries with non-atherosclerotic intimal thickening, and related constitutive modelling. *Am. J. Physiol. Heart Circ. Physiol.*, 289:H2048–2058, 2005.

[77] F. Schmid, G. Sommer, M. Rappolt, C. A. J. Schulze-Bauer, P. Regitnig, G. A. Holzapfel, P. Laggner, and H. Amenitsch. In situ tensile testing of human aortas by time-resolved small angle X-ray scattering. *Synchro. Rad.*, 12:727–733, 2005.

[78] F. Schmid, G. Sommer, M. Rappolt, P. Regitnig, G.A. Holzapfel, P. Laggner, and H. Amenitsch. Bidirectional tensile testing cell for in situ small angle X-ray scattering investigations of soft tissue. *Nuclear Instruments and Methods in Physics Research Section B: Beam Interactions with Materials and Atoms*, B 246:262–268, 2006.

[79] G. Sommer, T. C. Gasser, P. Regitnig, M. Auer, and G. A. Holzapfel. Dissection of the human aortic media: an experimental study. *J. Biomech. Eng.*, 130:021007–1–021007–12, 2008.

[80] G. Sommer, P. Regitnig, L. Koeltringer, and G. A. Holzapfel. Biaxial mechanical properties of intact and layer-dissected human carotid arteries at physiological and supra-physiological loadings. *Am. J. Physiol. Heart Circ. Physiol.*, 2008. Submitted.

[81] V. Fuster, editor. *Assessing and modifying the vulnerable atherosclerotic plaque. American Heart Association.* Futura publishing company, Armonk, 2002.

[82] C. M. Kramer. Magnetic resonance imaging to identify the high-risk plaque. *Am. J. Cardiol.*, 90:15L–17L, 2002.

[83] R. Virmani, A. P. Burke, F. D. Kolodgie, and A. Farb. Pathology of the thin-cap fibroatheroma: a type of vulnerable plaque. *J. Invas. Cardiol.*, 16:267–272, 2003.

[84] R. W. Kavey, S. R. Daniels, R. M. Lauer, D. L. Atkins, L. L. Hayman, and K. Taubert. American heart association guidelines for primary prevention of atherosclerotic cardiovascular disease beginning in childhood. *Circulation*, 107:1562–1566, 2003.

[85] M. Rayner and S. Petersen. *European cardiovascular disease statistics 2000.* British Heart Foundation (BHF), London, 2000.

[86] G. A. Holzapfel, M. Stadler, and C. A. J. Schulze-Bauer. A layer-specific three-dimensional model for the simulation of balloon angioplasty using magnetic resonance imaging and mechanical testing. *Ann. Biomed. Eng.*, 30:753–767, 2002.

[87] P. D. Richardson. Biomechanics of plaque rupture: progress, problems, and new frontiers. *Ann. Biomed. Eng.*, 30:524–536, 2002.

[88] N. V. Salunke and L. D. T. Topoleski. Biomechanics of atherosclerotic plaque. *Crit. Rev. Biomed. Eng.*, 25:243–285, 1997.

[89] J. D. Humphrey. *Cardiovascular Solid Mechanics. Cells, Tissues, and Organs.* Springer-Verlag, New York, 2002.

[90] C. L. Lendon, A. D. Briggs, G. V. R. Born, M. C. Burleigh, and M. J. Davies. Mechanical testing of connective tissue in the search for determinants of atherosclerotic plaque cap rupture. *Biochem. Soc. Trans.*, 16:1032–1033, 1988.

[91] G. V. R. Born and P. D. Richardson. Mechanical properties of human atherosclerotic lesions. In S. Glagov, W. P. Newman, and S. A. Schaffer, editors, *Pathology of Human Atherosclerotic Plaques*, pages 413–423. Springer-Verlag, New York, 1990.

[92] C. L. Lendon, M. J. Davies, G. V. R. Born, and P. D. Richardson. Atherosclerotic plaque caps are locally weakened when macrophages density is increased. *Atherosclerosis*, 87:87–90, 1991.

[93] R. T. Lee, A. J. Grodzinsky, E. H. Frank, R. D. Kamm, and F. J. Schoen. Structure-dependent dynamic mechanical behavior of fibrous caps from human atherosclerotic plaques. *Circulation*, 83:1764–1770, 1991.

[94] R. T. Lee, S. G. Richardson, H. M. Loree, A. J. Grodzinsky, S. A. Gharib, F. J. Schoen, and N. Pandian. Prediction of mechanical properties of human atherosclerotic tissue by high-frequency intravascular ultrasound imaging. *Arterioscler. Thromb.*, 12:1–5, 1992.

[95] B. N. McCord. *Fatigue of atherosclerotic plaque.* Ph.D. Thesis, Department of Mechanical Engineering, Georgia Institute of Technology, GA, 1992.

[96] G. L. Lendon, M. J. Davies, P. D. Richardson, and G. V. R. Born. Testing of small connective tissue specimens for the determination of the mechanical behaviour of atherosclerotic plaques. *J. Biomed. Eng.*, 15:27–33, 1993.

[97] H. M. Loree, A. J. Grodzinsky, S. Y. Park, L. J. Gibson, and R. T. Lee. Static circumferential tangential modulus of human atherosclerotic tissue. *J. Biomech.*, 27:195–204, 1994.

[98] L. D. T. Topoleski, N. V. Salunke, J. D. Humphrey, and W. J. Mergner. Composition- and history-dependent radial compressive behavior of human atherosclerotic plaque. *J. Biomed. Mater. Res. A*, 35:117–127, 1997.

[99] L. D. T. Topoleski and N. V. Salunke. Mechanical behavior of calcified plaques: a summary of compression and stress-relaxation experiments. *Z. Kardiol.*, 89: Suppl. 2:II/85–II/91, 2000.

[100] N. V. Salunke, L. D. T. Topoleski, J. D. Humphrey, and W. J. Mergener. Compressive stress-relaxation of human atherosclerotic plaque. *J. Biomed. Mater. Res. A*, 55:236–241, 2001.

[101] H. C. Stary. *Atlas of Atherosclerosis: Progression and Regression.* The Parthenon Publishing Group, Boca Raton, London, New York, Washington, D.C., 2nd edition, 2003.

[102] C. A. J. Schulze-Bauer and G. A. Holzapfel. Determination of constitutive equations for human arteries from clinical data. *J. Biomech.*, 36:165–169, 2003.

[103] G. A. Holzapfel, C. A. J. Schulze-Bauer, and M. Stadler. Mechanics of angioplasty: Wall, balloon and stent. In J. Casey and G. Bao, editors, *Mechanics in Biology*, New York, 2000. The American Society of Mechanical Engineers (ASME). AMD-Vol. 242/BED-Vol. 46, pp. 141–156.

[104] L. L. Demer. A skeleton in the atherosclerosis closet. *Circulation*, 92:2029–2032, 1995.

[105] H. M. Loree, R. D. Kamm, R. G. Stringfellow, and R. T. Lee. Effects of fibrous cap thickness on peak circumferential stress in model atherosclerotic vessels. *Circ. Res.*, 71:850–858, 1992.

[106] H. M. Loree, B. J. Tobias, L. J. Gibson, R. D. Kamm, D. M. Small, and R. T. Lee. Mechanical properties of model atherosclerotic lesion lipid pools. *Arterioscler. Thromb.*, 14:230–234, 1994.

[107] S. D. Williamson, Y. Lam, H. F. Younis, H. Huang, S. Patel, M. R. Kaazempur-Mofrad, and R. D. Kamm. On the sensitivity of wall stresses in diseased arteries to variable material properties. *J. Biomech. Eng.*, 125:147–155, 2003.

[108] P. D. Richardson, M. J. Davies, and G. V. R. Born. Influence of plaque configuration and stress distribution on fissuring of coronary atherosclerotic plaques. *Lancet*, 2(8669):941–944, 1989.

[109] R. B. Hickler. Aortic and large artery stiffness: Current methodology and clinical correlations. *Clinical Cardiology*, 13:317–322, 1990.

[110] P. R. Moreno, K. R. Purushothaman, V. Fuster, and W. N O'Connor. Intimo-medial interface damage and adventitial inflammation is increased beneath disrupted atherosclerosis in the aorta: Implications for plaque vulnerability. *Circulation*, 105:2504–2511, 2002.

[111] P. A. Berberian and S. Fowler. The subcellular biochemistry of human arterial lesions. i. biochemical constituents and marker enzymes in diseased and un-affected portions of human aortic specimens. *Exp. and Molecular Patholology*, 30:27–40, 1979.

[112] J. A. G. Rhodin. Architecture of the vessel wall. In D. F. Bohr, A. D. Somlyo, and H. V. Sparks, editors, *Handbook of Physiology, The Cardiovascular System*, volume 2, pages 1–31. American Physiolgial Society, Bethesda, Maryland, 1980.

[113] G. C. Cheng, H. M. Loree, R. D. Kamm, M. C. Fishbein, and R. T. Lee. Distribution of circumferential stress in ruptured and stable atherosclerotic lesions: A structural analysis with histopathological correlation. *Circulation*, 87:1179–1187, 1993.

[114] D. J. Patel and J. S. Janicki. Static elastic properties of the left coronary circumflex artery and the common carotid artery in dogs. *Circ. Res.*, 27:149–158, 1970.

[115] B. S. Gow, D. Schonfeld, and D. J. Patel. The dynamic elastic properties of the canine left circumflex coronary artery. *J. Biomech.*, 7:389–395, 1974.

[116] T. Kang, J. Resar, and J. D. Humphrey. Heat-induced changes in the mechanical behavior of passive coronary arteries. *J. Biomech. Eng.*, 117:86–93, 1995.

[117] S. J. Bund, A. A. Oldham, and A. M. Heagerty. Mechanical properties of porcine small coronary arteries in one-kidney, one-clip hypertension. *J. Vasc. Res.*, 33:175–180, 1996.

[118] X. Lu, J. Yang, J. B. Zhao, H. Gregersen, and G. S. Kassab. Shear modulus of porcine coronary artery: contributions of media and adventitia. *Am. J. Physiol. Heart Circ. Physiol.*, 285:1966–1975, 2003.

[119] X. Lu, A. Pandit, and G. S. Kassab. Biaxial incremental homeostatic elastic moduli of coronary artery: two-layer model. *Am. J. Physiol. Heart Circ. Physiol.*, 287:H1663–1669, 2004.

[120] C. Velican and D. Velican. Study of coronary intimal thickening. *Atherosclerosis*, 56:331–344, 1985.

[121] P. B. Canham, H. M. Finlay, J. G. Dixon, D. R. Boughner, and A. Chen. Measurements from light and polarised light microscopy of human coronary arteries fixed at distending pressure. *Cardiovasc. Res.*, 23:973–982, 1989.

[122] B. S. Gow and C. D. Hadfield. The elasticity of canine and human coronary arteries with reference to postmortem changes. *Circ. Res.*, 45:588–594, 1979.

[123] K. Hayashi, Y. Igarashi, and K. Takamizawa. Mechanical properties and hemodynamics in coronary arteries. In *New Approaches in Cardiac Mechanics*, K. Kitamura and H. Abè and K. Sagawa (Eds), Tokyo, 1986. Gordon and Breach. 285–294.

[124] P. D. Richardson and S. M. Keeny. Anisotropy of human coronary artery intima. Proc 15th Ann NorthEast Bioengineering Conference, 1989. 205–206.

[125] D. V. Carmines, J. H. McElhaney, and R. Stack. A piece-wise non-linear elastic stress expression of human and pig coronary arteries tested *in vitro*. *J. Biomech.*, 24:899–906, 1991.

[126] I. Ozolanta, G. Tetere, B. Purinya, and V. Kasyanov. Changes in the mechanical properties, biochemical contents and wall structure of the human coronary arteries with age and sex. *Med. Eng. Phys.*, 20:523–533, 1998.

[127] C. J. van Andel, P. V. Pistecky, and C. Borst. Mechanical properties of porcine and human arteries: implications for coronary anastomotic connectors. *Ann. Thorac Surg.*, 76:58–65, 2003.

[128] A. Kastrati, A. Schömig, S. Elezi, H. Schühlen, J. Dirschinger, M. Hadamitzky, A. Wehinger, J. Hausleiter, H. Walter, and F.J. Neumann. Predictive factors of restenosis after coronary stent placement. *J. Am. Coll. Cardiol.*, 30:1428–1436, 1997.

[129] J. Hausleiter, M. Sebastian, A. N. Li, C. K. Abbey, H. Honda, R. Makkar, J. S. Whiting, and N. Eigler. A porcine coronary stent model of increased neointima formation in the left anterior descending coronary artery. *Z. Kardiol.*, 91:614–619, 2002.

[130] H. C. Stary, D. H. Blankenhorn, A. B. Chandler, S. Glagov, W. Jr. Insull, M. Richardson, M. E. Rosenfeld, S. A. Schaffer, C. J. Schwartz, W. D. Wagner, and R. W. Wissler. A definition of the intima of human arteries and of its atherosclerosis-prone regions. A report from the committee on vascular lesions of the council on arteriosclerosis, American Heart Association. *Circulation*, 85:391–405, 1992.

[131] The national heart, lung, and blood institute coronary artery surgery study (cass). *Circulation*, 63(6 Pt 2):I1–I81, 1981.

[132] R. W. Ogden. *Non-linear Elastic Deformations.* Dover, New York, 1997.

[133] G. A. Holzapfel. *Nonlinear Solid Mechanics. A Continuum Approach for Engineering.* John Wiley & Sons, Chichester, 2000.

[134] G. A. Holzapfel, T. C. Gasser, and R. W. Ogden. A new constitutive framework for arterial wall mechanics and a comparative study of material models. *J. Elasticity*, 61:1–48, 2000.

[135] G. A. Holzapfel, T. C. Gasser, and R. W. Ogden. Comparison of a multi-layer structural model for arterial walls with a Fung-type model, and issues of material stability. *J. Biomech. Eng.*, 126:264–275, 2004.

[136] G. A. Holzapfel, M. Stadler, and T. C. Gasser. Changes in the mechanical environment of stenotic arteries during interaction with stents: Computational assessment of parametric stent design. *J. Biomech. Eng.*, 127:166–180, 2005.

[137] S. H. Kang, H. K. Park, C. W. Lee, J. J. Kim, M. K. Hong, S. W. Park, and S. J. Park. Impaired flow-mediated vasodilation of epicardial coronary artery in vasospastic angina. *J. Korean Med. Sci.*, 13:591–596, 1998.

[138] I. Gradus-Pizlo, B. Bigelow, Y. Mahomed, S. G. Sawada, K. Rieger, and H. Feigenbaum. Left anterior descending coronary artery wall thickness measured by high-frequency transthoracic and epicardial echocardiography includes adventitia. *Am. J. Cardiol.*, 91:27–32, 2003.

[139] Y. C. Fung, K. Fronek, and P. Patitucci. Pseudoelasticity of arteries and the choice of its mathematical expression. *Am. J. Physiol.*, 237:H620–H631, 1979.

[140] M. R. Roach and A. C. Burton. The reason for the shape of the distensibility curve of arteries. *Canad. J. Biochem. Physiol.*, 35:681–690, 1957.

[141] D. Mohan and J. W. Melvin. Failure properties of passive human aortic tissue I - uniaxial tension tests. *J. Biomech.*, 15:887–902, 1982.

[142] H. Demiray. A note on the elasticity of soft biological tissues. *J. Biomech.*, 5:309–311, 1972.

[143] J. Pache, A. Kastrati, J. Mehilli, H. Schühlen, F. Dotzer, J. Hausleiter, M. Fleckenstein, F. J. Neumann, U. Sattelberger, C. Schmitt, M. Muller, J. Dirschinger, and A. Schömig. Intracoronary stenting and angiographic results: strut thickness effect on restenosis outcome (ISAR-STEREO-2) trial. *J. Am. Coll. Cardiol.*, 41:1283–1288, 2003.

[144] C. Rogers, D. Y. Tseng, J. C. Squire, and E. R. Edelman. Balloon-artery interactions during stent placement: a finite element analysis approach to pressure, compliance and stent design as contributors to vascular injury. *Circ. Res.*, 84:378–383, 1999.

[145] A. König, T. M. Schiele, J. Rieber, K. Theisen, H. Mudra, and V. Klauss. Influence of stent design and deployment technique on neointima formation and vascular remodeling. *Z. Kardiol.*, 91:98–102, 2002.

[146] WHO World Health Organisation. *World Health Report 2004*. World Health Organisation, Geneva, Switzerland, 2004.

[147] S. Petersen and V. Peto and M. Rayner. *Coronary heart disease statistics 2004 edition*. British Heart Foundation, London, England, 2004.

[148] Statistik Austria. *Jahrbuch der Gesundheitsstatistik 2006*. Statistik Austria, Vienna, Austria, 2008.

[149] M. Fleisch and B. Meier. Management and outcome of stents in 1998: long-term outcome. *Cardio. Rev.*, 7:215–218, 1999.

[150] E. Mosler, W. Folkhardand E. Knorzer, H. Nemetschek-Gansler, T. Nemetschek, and M. H. Koch. Stress-induced molecular rearrangement in tendon collagen. *J. Mol. Biol.*, 182:589–596, 1985.

[151] N. Sasaki, N. Shukunami, N. Matsushima, and Y. Izumi. Time-resolved X-ray diffraction from tendon collagen during creep using synchrotron radiation. *J. Biomech.*, 32:285–292, 1999.

[152] P. Fratzl, K. Misof, I. Zizak, G. Rapp, H. Amenitsch, and S. Bernstorff. Fibrillar structure and mechanical properties of collagen. *J. Struct. Biol.*, 122:119–122, 1998.

[153] R. Puxkandl, I. Zizak, O. Paris, J. Keckes, W. Tesch, S. Bernstorff, P. Purslow, and P. Fratzl. Viscoelastic properties of collagen: synchrotron radiation investigations and structural model. *Philos. T. Roy. Soc. B*, 357:191–197, 2002.

[154] T. J. Wess, A.P. Hammersley, L. Wess, and A. Miller. A consensus model for molecular packing of type I collagen. *J. Struct. Biol.*, 122:92–100, 1998.

[155] J. P. Orgel, A. Miller, T. C. Irving, R. F. Fischetti, A. P. Hammersley, and T. J. Wess. The in situ supermolecular structure of type I collagen. *Structure*, 9:1061–1069, 2001.

[156] D. A. D. Parry and A. S. Craig. Electron microscope evidence for an 80 Å unit in collagen fibrils. *Nature*, 282:213–215, 1979.

[157] D. A. D. Parry. The molecular and fibrillar structure of collagen and its relationship to the mechanical properties of connective tissue. *Biophys. Chem.*, 29:195–209, 1988.

[158] P. P. Castellani, M. Morocutti, M. Franchi, A. Ruggeri, A. Bigi, and N. Roveri. Stress-induced molecular rearrangement in tendon collagen. *Cell Tissue Res.*, 234:735–743, 1983.

[159] M. Marchini, M. Morocutti, A. Ruggeri, M. H. Koch, A. Bigi, and N. Roveri. Differences in the fibril structure of corneal and tendon collagen. an electron microscopy and X-ray diffraction investigation. *Connect. Tissue Res.*, 15:269–281, 1986.

[160] P. P. Purslow, T. J. Wess, and D. W. L. Hukins. Collagen orientation and molecular spacing during creep and stress-relaxation in soft connective tissues. *J. Exp. Biol.*, 201:135–142, 1998.

[161] N. Roveri, A. Ripamonti, C. Pulga, G. Jeronimidis, P. P. Purslow, D. Volpin, and L. Gotte. Mechanical behaviour of aortic tissue as a function of collagen orientation. *Makromol. Chem.*, 181:1999–2007, 1980.

[162] A. Bigi, A. Ripamonti, and N. Roveri. X-ray investigation of the orientation of collagen fibres in aortic media layer under distending pressure. *Int. J. Biol. Macromol.*, 3:287–291, 1981.

[163] G. Re, A. Bigi, S. A. Dalla, A. Incerti, and N. Roveri. Collagen fibre reorientation around a crack in biaxially stretched aortic media. *Boll. Soc. Ital. Biol. Sper.*, 55:2149–2152, 1979.

[164] G. Re, A. Bigi, A. Incerti, and N. Roveri. Collagen fiber orientation in the tunica media of the aorta as a function of intraluminal pressure. *Boll. Soc. Ital. Biol. Sper.*, 56:263–267, 1980.

[165] G. Re, A. Bigi, A. Incerti, and N. Roveri. Roentgenographic study of the structural organization of the collagen fibers in the tunica media of the aorta. *Boll. Soc. Ital. Biol. Sper.*, 56:268–272, 1980.

[166] P. B. Canham, E. A. Talman, H. M. Finlay, and J. G. Dixon. Medial collagen organization in human arteries of the heart and brain by polarized light microscopy. *Conn. Tiss. Res.*, 26:121–134, 1991.

[167] P. B. Canham, P. Whittaker, S. E. Barwick, and M. E. Schwab. Effect of pressure on circumferential order of adventitial collagen in human brain arteries. *Can. J. Physiol. Pharmacol.*, 70:296–305, 1992.

[168] H. M. Finlay, L. McCullough, and P. B. Canham. Three-dimensional collagen organization of human brain arteries at different transmural pressures. *J. Vasc. Res.*, 32:301–312, 1995.

[169] H. M. Finlay, P. Whittaker, and P. B. Canham. Collagen organization in the branching region of human brain arteries. *Stroke*, 29:1595–1601, 1998.

[170] A. J. Rowe, H. M. Finlay, and P. B. Canham. Collagen biomechanics in cerebral arteries and bifurcations assessed by polarizing microscopy. *J. Vasc. Res.*, 40:406–415, 2003.

[171] F. H. Silver, I. Horvath, and D. J. Foran. Time-resolved X-ray diffraction from tendon collagen during creep using synchrotron radiation. *Crit. Rev. Biomed. Eng.*, 29:279–301, 2001.

[172] P. P. Purslow, A. Bigi, A. Ripamonti, and N. Roveri. Collagen fibre reorientation around a crack in biaxially stretched aortic media. *Int. J. Biol. Macromol.*, 6:21–25, 1984.

[173] H. Amenitsch, M. Rappolt, M. Kriechbaum, H. Mio, P. Laggner, and S. Bernstorff. First performance assessment of the small-angle X-ray scattering beamline at ELETTRA. *Synchro. Rad.*, 5:506–508, 1998.

[174] S. Bernstorff, H. Amenitsch, and P. Laggner. High-throughput asymmetric double-crystal monochromator of the SAXS beamline at ELETTRA. *Synchro. Rad.*, 5:1215–1221, 1998.

[175] A. Bigi and N. Roveri. *Handbook on Synchrotron Radiation*. Elsevier Science Publishers B.V., Amsterdam, Holland, 4th edition, 1991.

[176] A. P. Hammersley, S. O. Svensson, A. Thompson, H. Graafsma, Å. Kvick, and J. P. Moy. Calibration and correction of distortions in two-dimensional detector systems. *Rev. Scientific Instruments*, 66:2729–2733, 1995.

[177] J. S. Lee. Speckle suppression and analysis for synthetic aperture radar images. *Optical Engineering*, 25:636–643, 1986.

[178] W. Folkhard, D. Christmann, W. Geercken, E. Knorzer, M. H. Koch, E. Mosler, H. Nemetschek-Gansler, and T. Nemetschek. Twisted fibrils are a structural principle in the assembly of interstitial collagens, chordae tendineae included. *Z. Naturforsch. A*, 42:1303–1306, 1987.

[179] K. Misof, G. Rapp, and P. Fratzl. A new molecular model for collagen elasticity based on synchrotron X-ray scattering evidence. *BIOPJ*, 72:1376–1381, 1997.

[180] G. A. Holzapfel. Biomechanics of soft tissue. In J. Lemaitre, editor, *The Handbook of Materials Behavior Models. Volume III, Multiphysics Behaviors, Chapter 10, Composite Media, Biomaterials*, pages 1049–1063, Boston, 2001. Academic Press.

[181] N. Sasaki and S. Odajima. Stress-strain curve and Young's modulus of a collagen molecule as determined by the X-ray diffraction technique. *J. Biomech.*, 29:655–658, 1996.

[182] E. T. Thostenson, Z. F. Ren, and T.W. Chou. Advances in the science and technology of carbon nanotubes and their composites: A review. *Compos. Sci. Technol.*, 61:1899–1912, 2001.

[183] P. Fratzl. Small–angle scattering in materials science – a short review of applications in alloys, ceramics and composite materials. *J. Appl. Cryst.*, 36:397–404, 2003.

[184] D. M. Wright, V. C. Duance, T. J. Wess, C. M. Kielty, and P. P. Purslow. The supramolecular organisation of fibrillin-rich microfibrils determines the mechanical properties of bovine zonular filaments. *J. Exp. Biol.*, 202:3011–3020, 1999.

[185] F. Eberli, S. Windecker, and B. Meier. In V. Hombach, editor, *Interventionelle Kardiologie, Angiologie und Kardiovaskularchirurgie: Technik, Klinik, Therapie.* Plenum Press, Stuttgart–New York, 2001.

[186] Messphysik Material Testing. `http://www.messphysik.com`, *A-8280 Fürstenfeld, Austria*, 2005.

[187] H. Amenitsch, S. Bernstorff, M. Kriechbaum, D. Lombardo, H. Mio, M. Rappolt, and P. Laggner. Performance and first results of the elettra high-flux beamline for small-angle X-ray scattering. *J. Appl. Cryst.*, 30:872–876, 1997.

[188] T. C. Huang, H. Toraya, T. N. Blanton, and Y. Wu. X-ray powder diffraction analysis of silver behenate, a possible low-angle diffraction standard. *J. Appl. Cryst.*, 26:180–184, 1993.

[189] A. P. Hammersley. Fit2d: An introduction and overview. *ESRF Internal Report*, 1997.

[190] G. Rajkumar, H. A. AL-Khayat, F. Eakins, A. He, C. Knupp, and J. M. Squire. Fibrefix a new integrated CCP13 software package. *Fibre Diffraction Review*, 13, 2005.

[191] L. A. Feigin and D. I. Svergun. In H.-P. Fink, editor, *Structure analysis by small-angle X-ray and neutron scattering*, volume XIII. Plenum Press, New York/London, 1987.

[192] J. Liao, L. Yang, J. Grashow, and M. S. Sacks. Molecular orientation of collagen in intact planar connective tissues under biaxial stretch. *Acta Biomaterialia*, 1:45–54, 2005.

[193] D. H. Bergel. The properties of blood vessels. In Y. C. Fung, N. Perrone, and M. Anliker, editors, *Biomechanics: Its Foundations and Objectives*, pages 105–139. Prentice-Hall, Englewood Cliffs, New Jersey, 1972.

[194] J. D. Humphrey and F. C. P. Yin. Constitutive relations and finite deformations of passive cardiac tissue: II. Stress analysis in the left ventricle. *Circ. Res.*, 65:805–817, 1989.

[195] W. W. Nichols and M. F. O'Rourke. *McDonald's Blood Flow in Arteries. Theoretical, Experimental and Clinical Principles*, chapter 4, pages 73–97. Arnold, London, 4th edition, 1998.

[196] D. J. Patel and R. N. Vaishnav. *Basic Hemodynamics and its Role in Disease Processes.* University Park Press, Baltimore, 1980.

[197] R. P. Vito. A note on arterial elasticity. *J. Biomech.*, 6:561–564, 1973.

[198] H. W. Weizsäcker and J. G. Pinto. Isotropy and anisotropy of the arterial wall. *J. Biomech.*, 21:477–487, 1988.

[199] G. A. Holzapfel and R. W. Ogden, editors. *Mechanics of Biological Tissue.* Springer-Verlag, Heidelberg, 2006.

[200] K. Takamizawa and K. Hayashi. Uniform strain hypothesis and thin-walled theory in arterial mechanics. *Biorheology*, 25:555–565, 1988.

[201] R. W. Ogden and C. A. J. Schulze-Bauer. Phenomenological and structural aspects of the mechanical response of arteries. In J. Casey and G. Bao, editors, *Mechanics in Biology*, New York, 2000. The American Society of Mechanical Engineers (ASME). AMD-Vol. 242/BED-Vol. 46, pp. 125–140.

[202] Y. C. Fung and S. Q. Liu. Relationship between hypertension, hypertrophy, and opening angle of zero-stress state of arteries following aortic constriction. *J. Biomech. Eng.*, 111:325–335, 1989.

[203] A. Badrek-Amoudi, C. K. Patel, T. P. C. Kane, and S. E. Greenwald. The effect of age on residual strain in the rat aorta. *J. Biomech. Eng.*, 118:440–444, 1996.

[204] T. Matsumoto, K. Hayashi, and K. Ide. Residual strain and local strain distributions in the rabbit atherosclerotic aorta. *J. Biomech.*, 28:1207–1217, 1995.

[205] Y. C. Fung and S. Q. Liu. Change of residual strains in arteries due to hypertrophy caused by aortic constrictions. *Circ. Res.*, 65:1340–1349, 1989.

[206] J. Vossoughi. Longitudinal residual strains in arteries. In *Proceedings of the 11th Southern Biomedical Engineering Conference*, Memphis, TN, 1992. October 2–4, 1992, pp. 17–19.

[207] E. I. Cabrera Fischer, D. Bia, J. M. Camus, Z. Zocalo, E. Forteza, and R. L. Armentano. Adventitia–dependent mechanical properties of brachiocephalic ovine arteries in *in vivo* and *in vitro* studies. *Acta Physiol. (Oxf.)*, 188:103–111, 2006.

[208] M. Löhn, G. Dubrovska, B. Lauterbach, F. C. Luft, M. Gollasch, and A. M. Sharma. Periadventitial fat releases a vascular relaxing factor. *FASEB J.*, 16:1057–1063, 2002.

[209] A. Rachev and S. E. Greenwald. Residual strains in conduit arteries. *J. Biomech.*, 36:661–670, 2003.

[210] T. Matsumoto and K. Hayashi. Stress and strain distribution in hypertensive and normotensive rat aorta considering residual strain. *J. Biomech.*, 118:62–73, 1996.

[211] R. C. Gonzalez and R. E. Woods. *Digital Image Processing*. Addison Wesley, New York, 1992.

[212] A. Saini, C. Berry, and S. Greenwald. Effect of age and sex on residual stress in the aorta. *J. Vasc. Res.*, 32:398–405, 1995.

[213] M. J. Thubrikar, P. Agali, and F. Robicsek. Wall stress as a possible mechanism for the development of transverse intimal tears in aortic dissections. *J. Med. Eng. Technol.*, 23:127–134, 1999.

[214] I. A. Khan and C. K. Nair. Clinical, diagnostic, and management perspectives of aortic dissection. *Chest*, 122:311–328, 2002.

[215] A. G. Archer, P. L. Choyke, R. K. Zeman, C. E. Green, and M. Zuckerman. Aortic dissection following coronary artery bypass surgery: diagnosis by CT. *Cardiovasc. Intervent. Radiol.*, 9:142–145, 1986.

[216] D. Richens, K. Kotidis, M. Neale, C. Oakley, and A. Fails. Rupture of the aorta following road traffic accidents in the United Kingdom 1992–1999. The results of the co-operative crash injury study. *Eur. J. Cardio-thorac.*, 23:143–148, 2003.

[217] S. Wicky, P. Capasso, R. Meuli, A. Fischer, L. von Segesser, and P. Schnyder. Spiral CT aortography: an efficient technique for the diagnosis of traumatic aortic injury. *Eur. Radiol.*, 8:828–833, 1998.

[218] I. Mészáros, J. Mórocz, J. Szlávi, J. Schmidt, L. Tornóci, L. Nagy, and L. Szép. Epidemiology and clinicopathology of aortic dissection. *Chest*, 117:1271–1278, 2000.

[219] N. T. Kouchoukos and D. Dougenis. Surgery of the thoracic aorta. *N. Engl. J. Med.*, 336:1876–88, 1997.

[220] J. Auer, R. Berrent, and B. Eber. Aortic dissection: Incidence, natural history and impact of surgery. *J. Clin. Basic Cardiol.*, 3:151–154, 2000.

[221] D. W. Losordo, K. Rosenfield, A. Pieczek, K. Baker, M. Harding, and J. M. Isner. How does angioplasty work? Serial analysis of human iliac arteries using intravascular ultrasound. *Circulation*, 86:1845–1858, 1992.

[222] K. M. Detre, D. R. Holmes Jr., R. Holubkov, M. J. Cowley, M. G. Bourassa, D. P. Faxon, G. R. Dorros, L. G. Bentivoglio, K. M. Kent, and R. K. Myler. Incidence and consequences of periprocedural occlusion: The 1985-1986 National Heart, Lung, and Blood Institute Percutaneous Transluminal Coronary Angioplasty Registry. *Circulation*, 82:739–750, 1990.

[223] R. Agarwal, U. Kaul, V. Dev, S. Sharma, and P. Venugopal. The morphology of coronary arterial dissection occurring subsequent to angioplasty and its influence on acute complications. *Int. J. Cardiol.*, 31:59–64, 1991.

[224] M. S. Huber, J. F. Mooney, J. Madison, and M. R. Mooney. Use of a morphologic classification to predict clinical outcome after dissection from coronary angioplasty. *Am. J. Cardiol.*, 68:467–471, 1991.

[225] T. R. Cripps, J. M. Morgan, and A. F. Rickards. Outcome of extensive coronary artery dissection during coronary angioplasty. *Br. Heart J.*, 66:3–6, 1991.

[226] R. S. Saber, W. D. Edwards, K. R. Bailey, T. W. McGovern, R. S. Schwartz, and D. R. Holmes Jr. Coronary embolization after balloon angioplasty or thrombolytic therapy: An autopsy study of 32 cases. *J. Am. Coll. Cardiol.*, 22:1283–1288, 1993.

[227] S. P. Jain, A. Jain, T. J. Collins, S. R. Ramee, and C. J. White. Predictors of restenosis: a morphometric and quantitative evaluation by intravascular ultrasound. *Am. Heart J.*, 128:664–673, 1994.

[228] A. J. Black, D. L. Namay, A. L. Niederman, N. J. Lembo, G. S. Roubin, J. S. Douglas Jr., and S. B. King 3rd. Tear or dissection after coronary angioplasty. Morphologic correlates of an ischemic complication. *Circulation*, 79:1035–1042, 1989.

[229] H. Wolinsky and S. Glagov. A lamellar unit of aortic medial structure and function in mammals. *Circ. Res.*, 20:90–111, 1967.

[230] A. S. M. Tam, M. C. Sapp, and M. R. Roach. The effect of tear depth on the propagation of aortic dissections in isolated porcine thoracic aorta. *J. Biomech.*, 31:673–676, 1998.

[231] C. van Baardwijk and M. R. Roach. Factors in the propagation of aortic dissection in canine thoracic aortas. *J. Biomech.*, 20:67–73, 1987.

[232] T. C. Gasser and G. A. Holzapfel. Modeling the propagation of arterial dissection. *Eur. J. Mech. A/Solids*, 25:617–633, 2006.

[233] D. A. Vorp, M. L. Raghavan, S. C. Muluk, M. S. Makaroun, D. L. Steed, R. Shapiro, and M. W. Webster. Wall strength and stiffness of aneurysmal and nonaneurysmal abdominal aorta. *Ann. N.Y. Acad. Sci.*, 800:274–276, 1996.

[234] M. Adham, J. P. Gournier, J. P. Favre, E. De La Roche, C. Ducerf, J. Baulieux, X. Barral, and M. Pouyet. Mechanical characteristics of fresh and frozen human descending thoracic aorta. *J. Surg. Res.*, 64:32–34, 1996.

[235] N. F. MacLean, N. L. Dudek, and M. R. Roach. The role of radial elastic properties in the development of aortic dissections. *J. Vasc. Surg.*, 29:703–710, 1999.

[236] D. A. Vorp, B. J. Schiro, M. P. Ehrlich, T. S. Juvonen, M. A. Ergin, and B. P. Griffith. Effect of aneurysm on the tensile strength and biomechanical behavior of the ascending thoracic aorta. *Ann. Thorac Surg.*, 800:1210–1214, 2003.

[237] D. Mohan and J. W. Melvin. Failure properties of passive human aortic tissue II - biaxial tension tests. *J. Biomech.*, 16:31–44, 1983.

[238] M. Groenink, S. E. Langerak, E. Vanbavel, E. E. van der Wall, B. J. M. Mulder, A. C. van der Wall, and J. A. E. Spaan. The influence of aging and aortic stiffness on permanent dilation and breaking stress of the thoracic descending aorta. *Cardiovasc. Res.*, 43:471–480, 1999.

[239] P. P. Purslow. Positional variations in fracture toughness, stiffness and strength of descending thoracic pig aorta. *J. Biomech.*, 16:947–953, 1983.

[240] M. W. Carson and M. R. Roach. The strength of the aortic media and its role in the propagation of aortic dissection. *J. Biomech.*, 23:579–588, 1990.

[241] I. M. Tiessen and M. R. Roach. Factors in the initiation and propagation of aortic dissections in human autopsy aortas. *J. Biomech. Eng.*, 115:123–125, 1993.

[242] M. R. Roach and S. H. Song. Variations in strength of the porcine aorta as a function of location. *Clin. Invest. Med.*, 17:308–318, 1994.

[243] M. R. Roach, J. C. He, and R. G. Kratky. Tear propagation in isolated, pressurized porcine thoracic aortas. *Canad. J. Cardiol.*, 15:569–575, 1999.

[244] J. S. Robertson and K. V. Smith. An analysis of certain factors associated with the production of experimental dissection of the aortic media, in relation to the pathogenesis of dissection aneurysm. *J. Path. Bact.*, 60:43–49, 1948.

[245] A. E. Hirst and V. J. Johns. Experimental disection of media of aorta by pressure: Its relation to spontanous dissecting aneurysm. *Circ. Res.*, 10:897–903, 1962.

[246] L. M. Kachanov. *Introduction to Continuum Damage Mechanics.* Martinus Nijhoff Publishers, Dordrecht, The Netherlands, 1986.

[247] R. N. Vaishnav, J. T. Young, J. S. Janicki, and D. J. Patel. Nonlinear anisotropic elastic properties of the canine aorta. *Biophys. J.*, 12:1008–1027, 1972.

[248] G. A. Holzapfel and R. W. Ogden, editors. *Biomechanics of Soft Tissue in Cardiovascular Systems.* Springer-Verlag, Wien – New York, 2003.

[249] H. W. Greensmith and A. G. Thomas. Rupture of rubber III. determination of tear properties. *J. Polymer Science*, 18:189–200, 1955.

[250] T. C. Gasser and G. A. Holzapfel. Modeling plaque fissuring and dissection during balloon angioplasty intervention. *Ann. Biomed. Eng.*, 35:711–723, 2007.

[251] L. J. Coward, R. L. Featherstone, and M. M. Brown. Percutaneous transluminal angioplasty and stenting for carotid artery stenosis (review). *The Cochrane Database of Systematic Reviews 2004*, 2:1–18, 2006.

[252] J. S. Yadav, M. H. Wholey, R. E. Kuntz, P. Fayad, B. T. Katzen, G. J. Mishkel, T. K. Bajwa, P. Whitlow, N. E. Strickman, M. R. Jaff, J. J. Popma, D.B. Snead, D. E. Cutlip, B. G. Firth, and K. Ouriel. Protected carotid–artery stenting versus endarterectomy in high–risk patients. *N. Engl. J. Med.*, 351:1493–1501, 2004.

[253] R. H. Cox. Anisotropic properties of the canine carotid artery *in vitro*. *J. Biomech.*, 8:293–300, 1975.

[254] A. M. Brant, M. F. Teodori, R. L. Kormos, and H. S. Borovetz. Effect of variations in pressure and flow on the geometry of isolated canine carotid arteries. *J. Biomech.*, 20:831–838, 1987.

[255] V. Berczi, P. Toth, A. G. Kovach, and E. Monos. Biomechanical properties of canine vertebral and internal carotid arteries. *Acta Phys. Hungar.*, 75:133–145, 1990.

[256] B. E. Johnson and A. Hoger. The use of strain energy to quantify the effect of residual stress on mechanical behaviour. *Math. Mech. Solids*, 3:447–470, 1998.

[257] W. C. P. M. Blondel, J. Didelon, G. Maurice, J.-P. Carteaux, X. Wang, and J.-F. Stoltz. Investigation of 3-d mechanical properties of blood vessels using a new in vitro tests system: Results on sheep common carotid arteries. *IEEE T. Biomed. Eng.*, 48:442–451, 2001.

[258] J. Zhao, J. Day, Z. F. Yuan, and H. Gregersen. Regional arterial stress–strain distributions referenced to the zero–stress state in the rat. *Am. J. Physiol. Heart Circ. Physiol.*, 282:622–629, 2002.

[259] B. S. Gupta and V. A. Kasyanov. Biomechanics of human common carotid artery and design of novel hybrid textile compliant vascular grafts. *J. Biomed. Mater. Res. A*, 24:341–349, 1997.

[260] V. Kasyanov, I. Ozolanta, B. Purinya, A. Ozols, and V. Kancevich. Compliance of a biocomposite vascular tissue in longitudinal and circumferential directions as a basis for creation of artificial substitutes. *Mech. Comp. Mat.*, 39:347–358, 2003.

[261] C. A. J. Schulze-Bauer, M. Auer, R. Stollberger, P. Regitnig, M. Sonka, and G. A. Holzapfel. Assessment of plaque stability by means of high-resolution MRI and finite element analyses of local stresses and strains. In *CD-ROM Conference Proceedings, 2002 IEEE International Symposium on Biomedical Imaging: Macro to Nano*, Washington D.C., USA, July 7–10 2002.

[262] A. Delfino, N. Stergiopulos, J. E. Moore Jr., and J.-J. Meister. Residual strain effects on the stress field in a thick wall finite element model of the human carotid bifurcation. *J. Biomech.*, 30:777–786, 1997.

[263] K. Perktold and G. Rappitsch. Computer simulation of local blood flow and vessel mechanics in a compliant carotid artery bifurcation model. *J. Biomech.*, 28:845–856, 1995.

[264] J. D. Humphrey. Continuum thermomechanics and the clinical treatment of disease and injury. *Appl. Mech. Rev.*, 56:231–260, 2003.

[265] G. V. Guinea, J. M. Atienza, M. Elices, P. Aragoncillo, and K. Hayashi. Thermomechanical behavior of human carotid arteries in the passive state. *Am. J. Physiol. Heart Circ. Physiol.*, 288:2940–2945, 2005.

[266] A. Pandit, X. Lu, C. Wang, and G. S. Kassab. Biaxial elastic material properties of porcine media and adventitia. *Am. J. Physiol. Heart Circ. Physiol.*, 288:H2581–H2587, 2005.

[267] B. K. Bharadvaj, R. F. Mabon, and D. P. Giddens. Steady flow in a model of the human carotid bifurcation. Part I – flow visualization. *J. Biomech.*, 15:349–362, 1982.

[268] S. Roy, P. Silacci, and N. Stergiopulos. Biomechanical properties of decellularized porcine common carotid arteries. *Am. J. Physiol. Heart Circ. Physiol.*, 289:1567–1576, 2005.

[269] J. M. Meinders, L. Kornet, and A. P. G. Hoeks. Assessment of spatial inhomogeneities in intima media thickness along an arterial segment using its dynamic behavior. *Am. J. Physiol. Heart Circ. Physiol.*, 285:384–391, 2003.

[270] A. Schmeißer and W. G. Daniel. Therapeutische Neoangiogenese. *Z. Kardiol.*, 88:241–244, 1999.

[271] A. Delfino. *Analysis of stress field in a model of a human carotid bifurcation.* PhD thesis, Federal Institute of Technology, Lausanne, Switzerland, 1996.

[272] P. van Loon, W. Klip, and E. L. Bradley. Length-force and volume-pressure relationships in arteries. *Biorheology*, 14:181–201, 1977.

[273] St. Verlohren, G. Dubrovska, S. Tsang, K. Essin, F. C. Luft, Y. Huang, and M. Gollasch. Visceral periadventitial adipose tissue regulates arterial tone of mesenteric arteries. *Hypertension*, 44:271–276, 2004.

[274] V. Fuster, P. R. Moreno, Z. A. Fayad, R. Corti, and J. J. Badimon. Atherothrombosis and high–risk plaque: Part I: evolving concepts. *J. Am. Coll. Cardiol.*, 46:937–954, 2005.

[275] M. Tsutsui, H. Onoue, Y. Iida, L. Smith, T. O'Brien, and Z. S. Katusic. Adventitia–dependent relaxations of canine basilar arteries transduced with recombinant eNOS gene. *Am. J. Physiol. Heart Circ. Physiol.*, 276:H1846–H1852, 1999.

[276] D. D. Gutterman. Adventitia–dependent influences on vascular function. *J. Biomed. Mater. Res. A*, 277:1265–1272, 1999.

[277] The world health report 2007 - a safer future: global public health security in the 21st century. `http://www.who.int/whr/2007/en/`, 2007.

[278] M. A. Zulliger, P. Fridez, K. Hayashi, and N. Stergiopulos. A strain energy function for arteries accounting for wall composition and structure. *J. Biomech.*, 37:989–1000, 2004.

[279] K. Hayashi. Experimental approaches on measuring the mechanical properties and constitutive laws of arterial walls. *J. Biomech. Eng.*, 115:481–488, 1993.

[280] J. D. Humphrey. An evaluation of pseudoelastic descriptors used in arterial mechanics. *J. Biomech. Eng.*, 121:259–262, 1999.

[281] J. D. Humphrey. Continuum biomechanics of soft biological tissues. *Proc. R. Soc. Lond. A*, 459:1–44, 2003.

[282] S. E. Greenwald and C. L. Berry. The effect of alterations of scleroprotein content on the static mechancial properties of the arterial wall. *Adv. in Physiological Science*, 8:203–212, 1980.

[283] F. L. Wuyts, V. J. Vanhuyse, G. J. Langewouters, W. F. Decraemer, E. R. Raman, and S. Buyle. Elastic properties of human aortas in relation to age and atherosclerosis: A structural model. *Phys. Med. Biol.*, 40:1577–1597, 1995.

[284] H. Wolinsky and S. Glagov. Structural basis for the static mechanical properties of the aortic media. *Circ. Res.*, 14:400–413, 1964.

[285] T. C. Gasser, R. W. Ogden, and G. A. Holzapfel. Hyperelastic modelling of arterial layers with distributed collagen fibre orientations. *J. R. Soc. Interface*, 3:15–35, 2006.

[286] D. W. Marquardt. An algorithm for least-squares estimation of nonlinear parameters. *SIAM J. Appl. Math.*, 11:431–441, 1963.

[287] B. D. Stemper, N. Yoganandan, and F. A. Pintar. Methodology to study intimal failure mechanics in human internal carotid arteries. *J. Biomech.*, 38:2491–2496, 2005.

[288] Z. J. Samila and S. A. Carter. The effect of age on the unfolding of elastin lamellae and collagen fibers with stretch in human carotid arteries. *Can. J. Physiol. Pharmacol.*, 59:1050–1057, 1981.

Monographic Series TU Graz

Computation in Engineering and Science

Vol. 1 Steffen Alvermann
**Effective Viscoelastic Behaviour
of Cellular Auxetic Materials**
2008
ISBN 978-3-902465-92-4

Vol. 2 Sendy Fransiscus Tantono
**The Mechanical Behaviour of a Soilbag
under Vertical Compression**
2008
ISBN 978-3-902465-97-9

Vol. 3 Thomas Rüberg
Non-conforming FEM/BEM Coupling in Time Domain
2008
ISBN 978-3-902465-98-6

Vol. 4 Dimitrios E. Kiousis
**Biomechanical and Computational Modeling of
Atherosclerotic Arteries**
2008
ISBN 978-3-85125-023-7

Vol. 5 Lars Kielhorn
**A Time-Domain Symmetric Galerkin BEM
for Viscoelastodynamics**
2009
ISBN 978-3-85125-042-8

Vol. 6 Gerhard Unger
**Analysis of Boundary Element Methods
for Laplacian Eigenvalue Problems**
2009
ISBN 978-3-85125-081-7

Vol. 7 Gerhard Sommer
**Mechanical Properties of Healthy and Diseased
Human Arteries**
2010
ISBN 978-3-85125-111-1